Four-variable Partial Wave Analysis of $\pi^+ p$ Single Pion Production Channels from Threshold to 1700 MeV

by

Wlodzimierz Anthony Christopher Mier-Jedrzejowicz

A thesis submitted for the degree of
Doctor of Philosophy of the University of London

Department of Physics
Imperial College
LONDON SW7

September 1978

ABSTRACT

Author: W.A.C. Mier-Jedrzejowicz

Title: Four-variable Partial Wave Analysis of π^+p single pion production channels from threshold to 1700 MeV.

This thesis describes reactions of positive π mesons at around 1 GeV/c momentum with protons in a bubble chamber, studied by the author.

Bubble chamber film at 4 energies was analysed, and Data Summary Tapes were generated. Differential cross-sections for elastic data were fitted, and accurate channel cross-sections were calculated.

An energy-independent partial wave analysis of the major inelastic channels in this energy range, $\pi^+p\pi^o$ and $\pi^+\pi^+n$ was performed, using the generalised isobar model and the maximum likelihood method. Data were fitted at 9 centre of mass energies between 1.4 and 1.7 GeV; this included 2 energies which had been processed by the author and which lay in the middle of the energy range. Extensive checks of the analysis programs were made and are described. Ambiguous solutions were found at every energy; continuum ambiguities are discussed, and a continuity analysis is described. Cross-sections and Argand diagrams are presented for a continuous solution which shows clearly resonant behaviour in the S31, P33 and D33 waves. The behaviour of the important P31 wave is discussed.

Calculations of contributions from incoherent one-pion-exchange effects leading to I=2 $\pi\pi$ states were added to the analysis programs. The data were re-fitted, giving results that do not differ seriously from those without one-pion-exchange; kinematics projections in the $\pi^+\pi^+n$ channel are improved, some of the Argand diagrams become more continuous, no additional resonances are found, nor do any vanish. The parameters of the effective range potential used to describe the I=2 one-pion-exchange were found to be nearly constant over the energy range, and their significance is discussed.

Resonance parameters and signs are presented, and compared with the results of other analyses, and with the predictions of symmetry schemes.

To my Mother and Grandmother

Ad maiorem Dei gloriam

Table of Contents

Abstract 2

Table of Contents 4

List of Tables 8

List of Figures 10

Acknowledgements 12

Chapter I Overview of this π^+p experiment

I.1 Introduction 13

I.2 Historical Context 15

I.3 $\pi\pi N$ analyses 16

Chapter II Film measuring and D.S.T. making

II.1 Introduction 21

II.2 Data Taking 21

II.2.1 The Film 21

II.2.2 Optical Constants 23

II.2.3 Beam momentum and magnetic field 25

II.2.4 Film measuring 26

II.3 Program Processing 27

II.3.1 Pre-kinematics programs 27

II.3.2 Kinematics and Geometry programs 29

II.3.3 Hypothesis selection and D.S.T. creation 31

II.4 Momenta other than 800 and 850 MeV/c 33

II.5 Checking the D.S.T.'s 35

Chapter III Cross-sections, elastic analysis and Dalitz Plots

III.1 Introduction 45

III.2 Separation of channels 45

III.3 Cross-section calculations 49

III.3.1 Total cross-sections 49

III.3.2 Channel-dependent corrections 49

III.3.3 Cross-sections 59

III.4 Elastic Analysis 62

III.4.1 Elastic corrections 62

III.4.2 Elastic results 66

III.4.3 Backward elastic cross-sections 75

III.5 Dalitz plots 77

Chapter IV 4-variable Fitting Formalism

IV.1 Introduction 86

IV.2 $\pi\pi$N Formalism 87

IV.2.1 The Isobar Model 87

IV.2.2 Notation and Deler-Vallades Formalism 88

IV.2.3 Other Parametrisations 98

IV.2.4 Expressions for Cross-sections 100

IV.3 Maximum Likelihood Formalism 103

Chapter V Data Fitting and Results

V.1 Introduction 108

V.2 Preparation of Data for Fitting 110

V.3 Calculation of Normalisation Integrals 114

V.4 Data Fitting 117

V.4.1 Choice of Waves 117

V.4.2 Likelihood calculation and fitting routines 122

V.4.3 Performing the fits 127

V.4.4 Error Calculations 134

V.5 Results 137

V.5.1 Ability to reproduce Monte Carlo data 137

V.5.2 Reproduction of the experimental data 139

V.6 Validity of The Isobar Model 157

Chapter VI Obtaining a 9-Energy Solution

VI.1 Introduction 162

VI.2 Comparing different solutions at one energy 162

VI.3 Ambiguities and Continuity 167

VI.3.1 Discrete ambiguities and the continuum ambiguity 167

VI.3.2 Continuity 169

VI.4 Using continuity to choose a 9-energy solution 172

VI.4.1 The continuity search formalism 172

VI.4.2 Performing the continuity search 176

VI.5 Results, Argand Diagrams amd discussion 186

Chapter VII One Pion Exchange Effects and Final Results

VII.1 Introduction 201

VII.2 Formalism of I=2 $\pi\pi$ effects 203

VII.2.1 Formalism of I=2 $\pi\pi$ 203

VII.2.2 Inclusion in Likelihood Calculations 210

VII.3 Performing the Fits 213

VII.3.1 Programming the likelihood function 213

VII.3.2 Data fitting and error calculations 216

VII.3.3 Reproduction of experimental data 218

VII.4 Continuity search and results 228

VII.4.1 Continuity search and s-channel results 228

VII.4.2 I=2 $\pi\pi$ results 251

VII.5 Discussion of partial wave analysis results 259

VII.5.1 Discussion of the results of this analysis 259

VII.5.2 Comparison with other analyses 271

VII.5.3 Comparison with theory 276

VII.6 Concluding Remarks 291

Appendix A Argand diagrams from non-OPE fits 295

Appendix B Argand diagrams from refit with OPE 304

References 313

List of Tables

I.1 Details of first I.C./W.C. film 19

I.2 Details of Oxford film 19

I.3 Details of second I.C./W.C. film 20

I.4 Details of third I.C./W.C./Cambridge film 20

II.1 Numbers of events on D.S.T.'s 38

II.2 Mean beam parameters and cuts imposed 39

II.3 Beam Stretch Functions 40

II.4 850 MeV/c stretches at the different laboratories 40

III.1 Numbers of events and cross-sections 55-56

III.2 Cuts and elastic fit parameters 65

III.3 Elastic differential cross-sections in the c.m.s. 69

III.4 Elastic fit Legendre coefficients 70

IV.1 Symbols used in $\pi p \to \pi\pi N$ formulæ 90-91

IV.2 List of waves 92

V.1 Summary description of bins used in energy-independent fits 112

V.2 Probabilities of finding different minima at 750 MeV/c 132

V.3 Summary of fitting runs 133

V.4 $\pi\pi N$ Cross-sections in different waves 154

VI.1 Results of a standard CHI run 178

VI.2 RANCOM limits 179

VI.3 Results of CHI with various parameters of ΔSD1 and ΔDS3 183

List of Tables contd.

VI.4 Results of CHI tied to various waves 184

VI.5 Results of CHI with various numbers of waves 185

VI.6 T-matrix elements 196-200

VII.1 Standard CHI run results 230

VII.2 Results of CHI with various ΔSD1 and ΔDS3 parameters 231

VII.3 Results of CHI tied to various waves 233-235

VII.4 Results of CHI with various numbers of waves 236

VII.5 T-matrix elements 243-247

VII.6 $\pi\pi$N cross-sections in different waves 250

VII.7 Scattering length and effective range values 254

VII.8 I=2 s-wave phase shifts 257

VII.9 Resonance parameters and ratings 269

VII.10 Signs and diameters on Argand diagrams 270

VII.11 $\{70, 1^-\}$ signs 284

VII.12 Positive parity multiplets 290

List of Figures

I.1 π^+p cross-sections 14

I.2 Typical Bubble Chamber photographs 17

II.1 Film measuring and processing flowchart 22

II.2 Beam track momentum dip and azimuth at 850 MeV/c 41

II.3 Beam stretch functions at 850 MeV/c 42

II.4 Elastic event probabilities at 1250 MeV/c 43

II.5 3-body event probabilities at 1250 MeV/c 43

II.6 Coplanarity function at 850 MeV/c 44

III. 1 Missing masses^2 and energies of elastic events at 850 MeV/c 47

III.2 Missing masses^2 and energies of elastic and $\pi^+p\pi^o$ events at 850 MeV/c 48

III.3 Elastic cross-sections 57

III.4 $\pi^+p\pi^o$ cross-sections 58

III.5 $\pi^+\pi^+n$ cross-sections 59

III.6 $\pi^+\pi^+p\pi^-$ cross-sections 60

III.7 $\pi^+p\eta$ cross-sections 61

III.8 ΣK cross-sections 61

III.9 Elastic θ and ϕ distributions 63

III.10 Elastic differential cross-sections 67-68

III.11 Elastic fit Legendre coefficients 71-73

III.12 Backward elastic differential cross-sections 76

III.13 $\pi^+p\pi^o$ Dalitz plot and projections at 800 MeV/c 78

III.14 $\pi^+\pi^+n$ Dalitz plot and projections at 800 MeV/c 79

III.15 $\pi^+p\pi^o$ Dalitz plot at 850 MeV/c 80

III.16 $\pi^+\pi^+n$ Dalitz plot at 850 MeV/c 81

List of Figures contd.

III.17 $\pi^+ p \pi^0$ Dalitz plot at 1150 MeV/c 82

III.18 $\pi^+ \pi^+ n$ Dalitz plot at 1150 MeV/c 83

III.19 $\pi^+ p \pi^0$ Dalitz plot at 1250 MeV/c 84

III.20 $\pi^+ \pi^+ n$ Dalitz plot at 1250 MeV/c 85

IV.1 Schematic diagram of a $\pi p \to \pi\pi N$ reaction 90

V.1 The steps in finding a solution 109

V.2 Histograms of c.m.s. energies 111

V.3 Higher moments in Δ moments analysis 120

V.4 Results of fits to Monte Carlo data 138

V.5 Fit projections compared to original data 140-149

V.6.a $\pi\pi N$ cross-sections in different waves 152

V.6.b Enlarged P31 cross-sections 153

V.7 Fitted $\pi^+ \pi^+ n$ cross-sections 156

V.8 Fits in different regions of the Dalitz plot 159-160

VI.1 Range of reduced likelihoods at each momentum 166

VI.2 Continuity paths on an Argand diagram 174

VI.3 ΔSD1 and ΔDS3 Argand diagrams with errors 187

VI.4 Argand diagrams for the larger waves 191-195

VII.1 t-channel diagram 205

VII.2 O.P.E. refit projections 219-227

VII.3 Argand diagrams for the larger waves 238-242

VII.4 $\pi\pi N$ cross-sections in different waves 248

VII.5 Enlarged P31 cross-sections 249

VII.6 I=2 O.P.E. cross-section contributions to $\pi\pi N$ cross-sections 252

VII.7 I=2 scattering lengths 255

VII.8 I=2 s-wave phase shifts 258

VII.9 Enlarged sections of P33 Argand diagrams 266

ACKNOWLEDGEMENTS

First of all, I thank Professor I. Butterworth for letting me study in the High Energy Physics Group, and my supervisor, Dr. Keith Barnham, who was always ready with suggestions and relevant preprints or reprints. My thanks go to all the physicists who have worked on the π^+p experiment, but particularly to those with whom I worked directly, Rob Stevens, Andy White, Simon Orebi Gann, Steve Glickman, and Neil and Penny Baggett.

The $\pi\pi N$ analysis groups have kept their analyses independent, but we do meet and discuss methods and results. I would like to thank all those whom I met and who gave me help and advice on such occasions, particularly Jean Dolbeau and Ron Longacre.

Many others at Imperial College, not directly involved with the experiment helped me. My special thanks to Dr. D. Miller for help with optical constants, to Dr. Mike Mermikides for explaining CERN programs, and to Betty Moynihan and Geoff Fayers for help with the PDP10 computer. I am especially grateful to Juli and Ghysaline for measuring much of my part of the film, and to Janet, Marg, Pat and Christine for doing the paperwork and for their kind words, but I also thank everyone else involved with measuring and bookkeeping. Pat Hurst's work in co-ordinating the film measuring has been invaluable. The staff of the RHEL IBM computer were very helpful, particularly in running the fitting programs.

Linda Gold deserves sincere thanks and praise for patiently typing this thesis. A general thank-you for their help and support goes to all my other friends, at I.C. and beyond, whose names I cannot fit in here. My thanks to the Science Research Council who supported me for three years, and I thank Professor J. Dungey for allowing me to finish this thesis while I worked for him.

Finally, and especially, I thank my mother and father, my brother and sister, for not only tolerating but also actively supporting my writing of this thesis.

CHAPTER I

Overview of this $\pi^+ p$ Experiment

I.1 Introduction

This thesis describes the author's work in a $\pi^+ p$ bubble chamber experiment with incident beam momenta of around 1 GeV/c. The experiment was already several years old when the author joined it - film had been taken in 3 separate runs, and theses and publications had been produced describing the earlier work. The author was in fact the last Ph.D. student to join the experiment. This first chapter of the thesis therefore describes the experiment as a whole and serves to put the author's work and the rest of the thesis into context.

The original motivation for the work was the need to provide a high statistics bubble chamber experiment on $\pi^+ p$ interactions in the resonance region around 1.5 - 1.6 GeV centre of mass energy. Recent interest in the predictions of various SU(6) schemes and Melosh transformations made partial wave analysis of this data all the more important. Analysis of the inelastic channels is particularly necessary since only they can give information on the signs of resonances. Only bubble chamber experiments can give full data on inelastic interactions at all angles, and the 3-body channels in $\pi^+ p$ at this energy take up nearly all the inelastic cross-section (see Fig. I.1). The majority of this thesis describes a partial wave analysis of $\pi^+ p \pi^\circ$ and $\pi^+ \pi^+ n$ channels at 9 incident beam momenta.

It must be stressed that this sort of analysis is vital if a good understanding of SU(6) is to be obtained. Theories extending from SU(6) to include the 4 or more quarks required

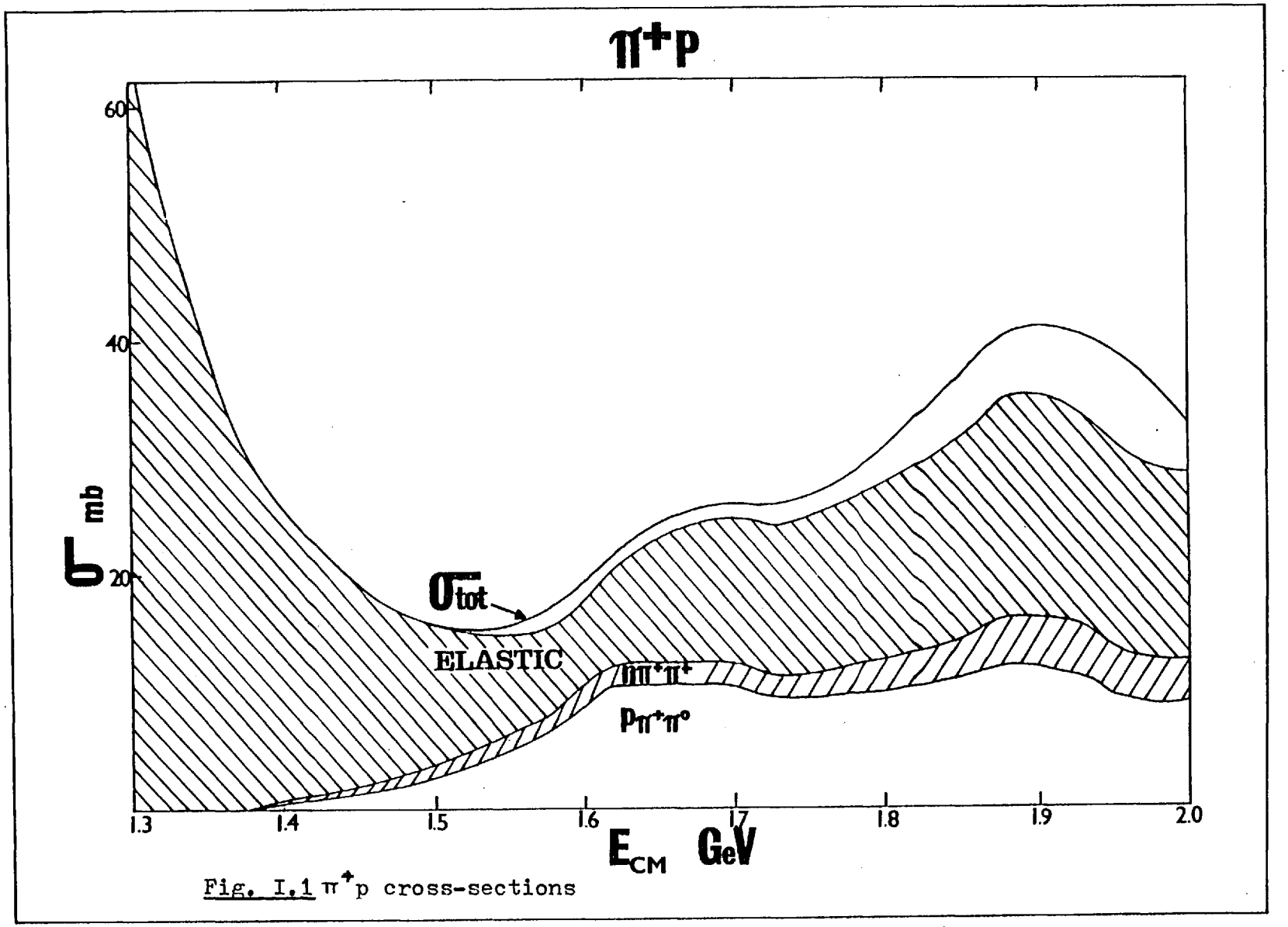

Fig. I.1 $\pi^+ p$ cross-sections

to explain recent results will also be helped by such improvements in the understanding of SU(6).

I.2 Historical Context

From the time when it was realised in the mid-1960's that the resonance regions in π^+p, π^-p, K^-p etc. concealed more than a very simple resonance structure, the need for high statistics experiments to examine these structures in detail was obvious. One such experiment was a collaboration between Imperial College and Westfield College - this took π^+p bubble chamber photographs at four incident momenta in the Saclay 81 cm. bubble chamber exposed to π^+ mesons from the Rutherford Laboratory K1 beam line. Table I.1 gives details of this exposure. A number of papers and theses describing analysis of this data have been published (see refs. 1, 2, 3, 4, 5, 9, 12). At the same time a group from Oxford used the same experimental setup to make exposures at slightly lower beam momenta. Table I.2 gives details, and references 6, 7, 8 describe analysis of that data.

The energy range of the Imperial College/Westfield College collaboration was extended upwards and downwards in 2 further sets of exposures taken in 1968 and 1970, and the collaboration was joined by Cambridge University in 1970. Both these exposures used the Rutherford Laboratory K9 beam line and the 1.5 m. British National Hydrogen Bubble Chamber. Table I.3 gives details of the second exposure, and references 9, 10, 12 describe its analysis. Table I.4 gives details of

the third exposure; reference 11 describes some of the Cambridge processing at these energies. Chapters II and III of this thesis describe processing of the majority of the film at these energies through to the DST stage. Figure I.2 shows 3 typical bubble chamber photographs from the third exposure.

I.3 $\pi\pi N$ Analyses

As mentioned above, all this data was taken for use in partial wave analyses with high statistics at a number of closely spaced energies. The number of such π^+p elastic analyses has been increasing steadily in recent years and their results together with those from other elastic channels are in general agreement with SU(6) theories. Problems still remain; see the Proceedings of the Oxford Conference on Baryon Resonances for a recent summary (ref. 13), or Rosner (ref.14) for an older, but more detailed view of the field. The number of analyses of the inelastic channels is however still very small. Only 2 other groups have performed analyses on the same scale as the Imperial/Westfield one. The SLAC - LBL group collected data from various sources, including the Oxford data described above. Their publications (ref. 15) give their results together with the sources of their data and references to earlier analyses that used parts of that data. The Saclay group (ref. 16) used mostly their own data, but also some other data including that from Oxford. Saclay too give a list of earlier analyses of some of their data. Both groups analyse the $p\pi^-\pi^0$, $n\pi^+\pi^-$, and $p\pi^+\pi^0$ final states. SLAC - LBL have a gap of 100 MeV in their centre of mass energy range, and Imperial/Westfield data was used to check their continuation across this gap (ref. 17).

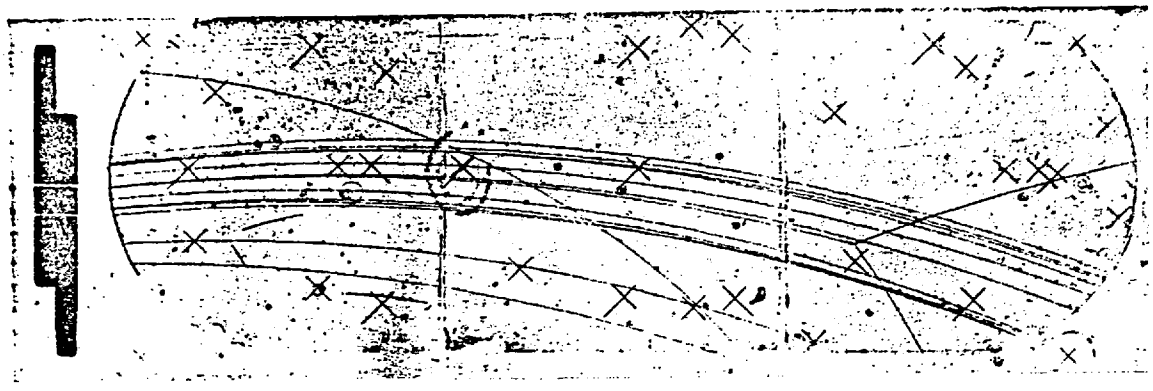

$\pi^+ p \rightarrow \pi^+ p$

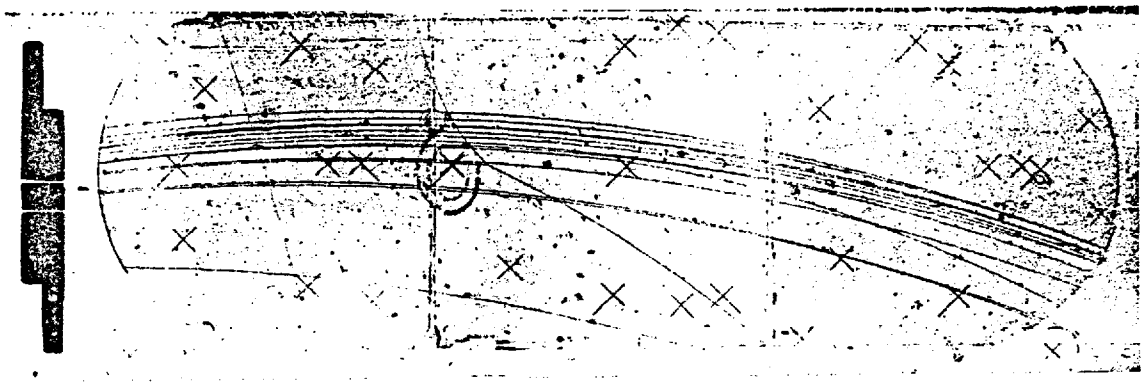

$\pi^+ p \rightarrow \pi^+ p \pi^o$

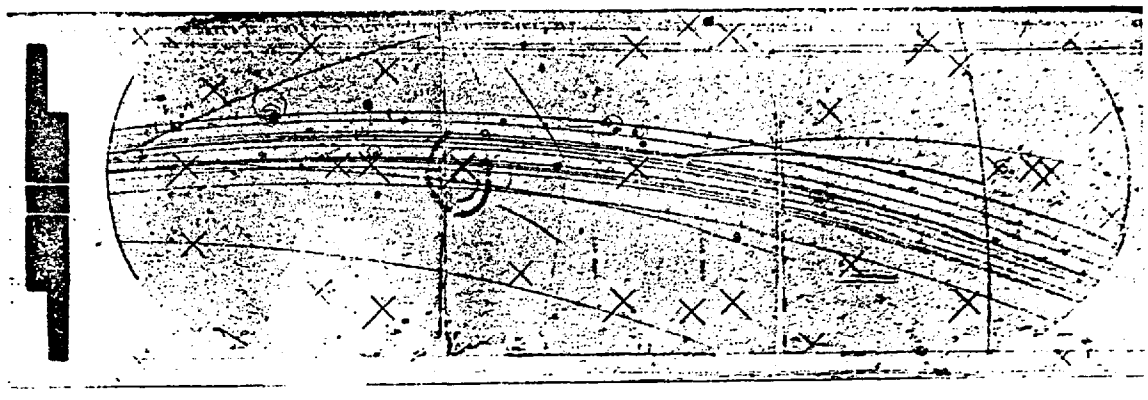

$\pi^+ p \rightarrow \pi^+ \pi^+ n$

Figure I.2 Typical bubble chamber photographs

The Imperial/Westfield group has been analysing $\pi^+ p \pi^0$ and $\pi^+\pi^+ n$ data since 1972. We combine the ubiquitous Oxford data, 2 energies processed by the author (one in the SLAC - LBL gap), and the 4 energies from our first run to give 9 energies with good statistics for a 4-variable maximum likelihood fit using the isobar model. Benefitting from our earlier experience and that of the other 2 groups we have checked and refined our basic fitting program, in particular by the addition of one-pion-exchange calculations. The techniques used and the results obtained are described in chapters IV to VII of this thesis.

Nominal beam momentum MeV/c	Total no. of events on DST	No. of π^+p events	No. of $\pi^+p\pi^0$ events	No. of $\pi\pi n$ events
895	11856	4776	5946	1004
945	15516	6712	7236	1272
995	15151	7100	6517	1284
1040	13704	6548	5714	1163

Film taken in 1966 in the Saclay 80 cm. bubble chamber using the Rutherford K1 beam line.
The nominal beam momenta were originally 905, 955, 1005, 1050 MeV/c but were in fact called 895, 945, 995, 1040 from very early on.
Details in ref. 1, see also refs. 2, 3, 5.

Table I.1 Details of first I.C./W.C. film

Nominal beam momentum MeV/c	Total no. of events on DST	No. of π^+p events	No. of $\pi^+p\pi^0$ events	No. of $\pi\pi n$ events
600	20536	19560	802	174
650	4327	3980	274	72
700	13705	11401	1911	383
750	7765	5457	1960	331
800	6568	3757	2336	426

Film taken in 1966 in the Saclay 80 cm. bubble chamber using the Rutherford K1 beam line.
Details from ref. 6, see also refs. 7, 8.

Table I.2 Details of Oxford film

Nominal beam momentum MeV/c	Total no. of events on DST	No. of π^+p events	No. of $\pi^+p\pi^o$ events	No. of $\pi\pi n$ events	Remarks
1100	6341	2917	2443	576	
1200	9308	4363	3256	803	
1300	11716	5186	3822	1063	
1400	18319	8093	5903	2018	
1450	3397	1532	1091	376	Only Cambridge data on DST
1500	8268	3684	2576	1046	Only Cambridge data on DST
1550					Abandoned
1600					Not processed

Film taken in 1968 in the 1.5 m British National Bubble chamber using the Rutherford K9 beam line.

Details in ref. 9, see also ref. 10 and Chapter 2 of this thesis.

Table I.3 Details of second I.C./W.C. film

Nominal Beam momentum MeV/c	Total no. of events on DST	No. of π^+p events	No. of $\pi^+p\pi^o$ events	No. of $\pi\pi n$ events
800	7042	3916	2520	492
850	9029	4009	4136	715
1150	9669	4650	3627	827
1250	17200	8036	6069	1482

Film taken in 1970 in the 1.5 m British National Bubble chamber using the Rutherford K9 beam line.

Details in this thesis, see also ref. 11

Table I.4 Details of third I.C./W.C./Cambridge film

CHAPTER II

Film taking, Measuring and Processing

II.1 Introduction

The film from the third data taking run described in Chapter I was divided equally between Cambridge, Imperial College and Westfield College. Reference 11 gives a general description of how the Cambridge film was processed. The Westfield film was measured at Westfield, but the measurements were processed at Imperial College, and all remeasurements of it were made and processed at Imperial College. The processing of all the Imperial College third run film was the author's responsibility, and when the Westfield College film was passed to Imperial College, its processing was also undertaken by the author. This chapter describes the steps taken to create Data Summary Tapes (D.S.T.'s) from this film. A flow chart describing this processing is provided in Figure II.1. The conversion of our bubble chamber film to D.S.T.'s is well documented in earlier publications (refs. 1, 9, 12), so only those items that differed from earlier work or caused trouble are described here in detail.

II.2 Data Taking

II.2.1 The Film

As mentioned in I.2, the film was taken in the British National 1.5 metre bubble chamber, using the K9 beam line at Rutherford Laboratory. This line was designed primarily for higher energy $K^{\pm}$ beams, so there was considerable trouble in obtaining a suitable beam momentum and intensity, particularly at the 2 lower momenta in this run. Indeed, an extra yoke magnet was used at the beam entry point to swing the beam into the chamber. Furthermore, the

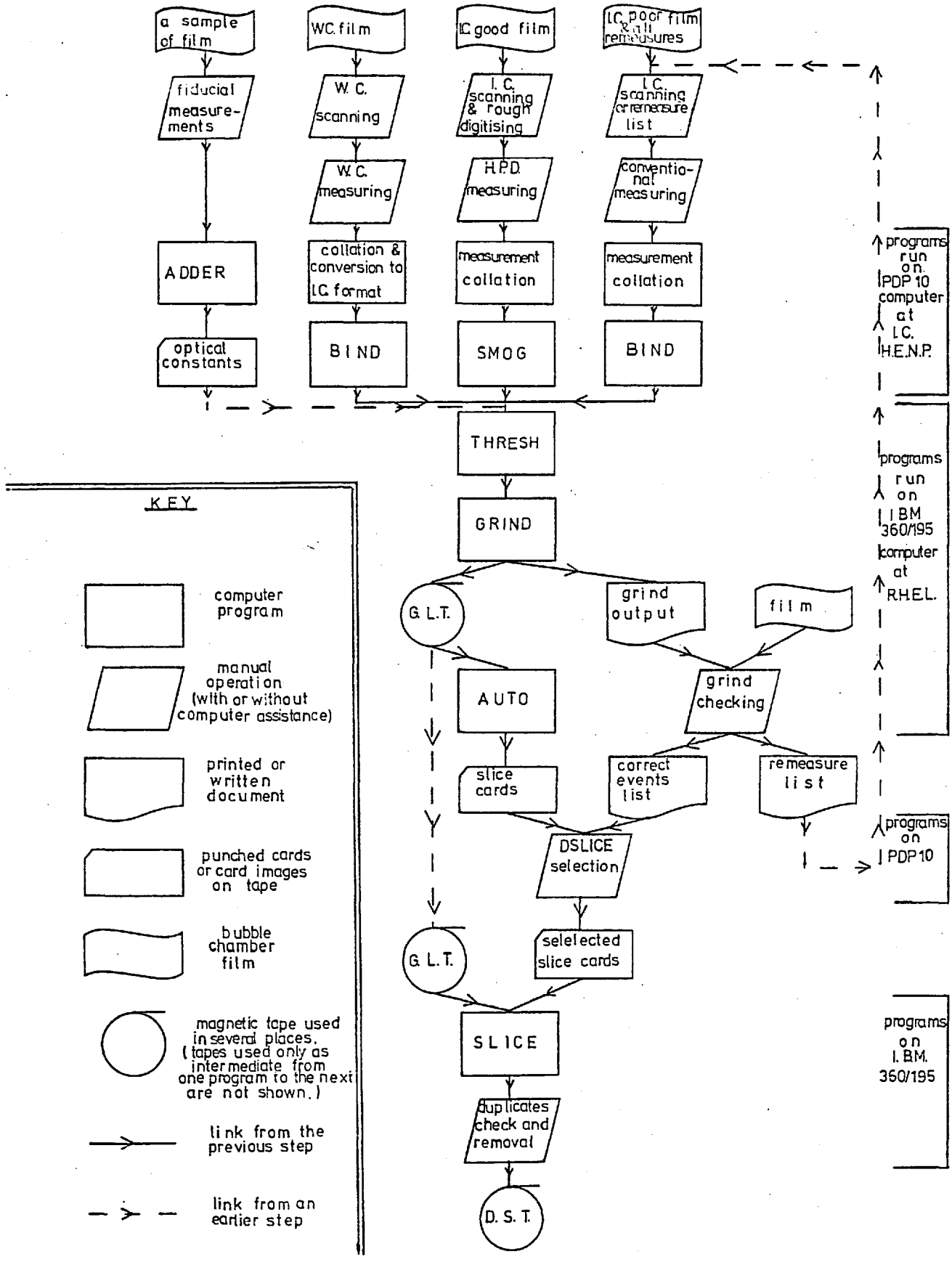

Figure II.1 Film measuring and processing flowchart

B.N.H.B.C. had been taken apart for tests with a track sensitive target just before this run (one or two interesting events found at the scanning stage were ascribed to π^+ interactions with neon). When the chamber was reassembled for normal use, a new magnetic field map was not taken, nor was the central field value measured. Because of the reassembling, new optical constants were determined for the film, and the magnetic field value was reassessed.

II.2.2 Optical Constants

The geometry programs (see Section II.3.2) require optical constants describing the layout of the bubble chamber and cameras. As the bubble chamber was unlikely to have been reassembled in exactly its previous position, new optical constants were determined for this run, as follows.

After each run in the bubble chamber, the 3 cameras are replaced by telescopes which measure the relative displacements of three fiducial marks on the back window of the bubble chamber with respect to three marks on the front window. This data and information on nominal positions of fiducial marks on front and back windows, cooling factors, and depth of the chamber, are input to program TELESCOPE (ref. 18). TELESCOPE uses these inputs to calculate, by a least squares fit, the co-ordinates and relative rotation of the back window with respect to the front window. The author made minor alterations to TELESCOPE and used it to calculate the co-ordinates and rotation for this run.

The positions of 17 fiducial marks on all 3 views were measured on 300 frames each on 3 rolls of film taken during this run, and on 70 frames on a fourth roll. Program HPDEDT (ref. 18) was used to calculate from these measurements an average set of

fiducial measurement values with errors. This was done by a process of repeated calculation of mean values and rejection of poor measurements, controlled by an operator.

Program ADDER (ref. 19) was then used to calculate the optical constants for this run. The results from HPDEDT, the co-ordinates and rotation from TELESCOPE, and nominal values for other optical constants are input to ADDER. (For a full description of the optical constants, see the THRESH and GRIND write-ups, ref. 20). These numbers are used to calculate distances between nominal positions and measured positions of fiducial marks, ADDER then uses the CERN minimising program MINUIT (ref. 20) to minimise a function of these distances by varying a selected combination of the input numbers. At the end of its calculations, ADDER outputs optical constants ready for use in the geometry programs.

It was feared that problems with holding the film flat in the cameras might necessitate the use of several different sets of optical constants for different rolls in this run, but after a few runs of ADDER, a set that was consistent for all the rolls was calculated.

A valuable tool for checking optical constants lies in the use of the stretch function. For a variable X with standard deviation σ, the stretch function is defined to be

$$S_X = \frac{X_{fitted} - X_{measured}}{(\sigma_M^2 - \sigma_F^2)}$$

For any normally distributed variable X, S_X should have a normal distribution with a mean of zero, and a standard deviation of one. This was used to check the optical constants.

Events measured on the rolls used for determining optical constants were processed by the geometry and kinematics programs using the new optical constants and those from the second (1968) run. Events which fitted as elastic scatters with four constraints (i.e. 4C fits - those elastic events for which all measurements are accepted) were chosen, and stretch functions were plotted for the inverse of the momentum, the dip, and the azimuth of beam tracks and outgoing tracks. (The inverse of the momentum is used since this is normally distributed, whereas the momentum is not). Significant deviations from a zero mean indicate asymmetries due to incorrect values of the beam momentum (see Section II.2.3) or to incorrect optical constants. Deviations from a standard deviation close to one indicate wrong estimates of measurement errors.

The stretch functions obtained using the new optical constants showed a significant improvement as compared to those from the values for the 1968 run. Several sets of new optical constants were tried; none gave ideal values and distributions, but this could not be expected in view of problems with the film (see Sections II.2.3 and II.2.4). The set chosen gave good stretches in momentum and azimuth and worse but acceptable values in dip, which was the variable most affected by the film problems. Figure II.3 shows the stretch functions for beam tracks at 850 MeV/c, and Table II.3 gives the function values at all four momenta. Beam tracks are chosen since they are most sensitive to optical constant problems and useful in checking the incident momentum (see Section II.2.3).

II.2.3 Beam momentum and magnetic field

The magnetic field in the bubble chamber was produced by the normal 1.5 m chamber magnet, and an additional magnet was used to

swing the beam into the chamber.† The field bends the tracks of charged particles in the chamber and so makes it possible to measure their momenta, but an accurate measurement requires a map of the field to be used together with a central field value. The central field value in the chamber was not directly measured, but a record of the currents in the magnets was kept, and from the properties of the magnets a central field value was calculated to within 0.1 Kgauss in 11 Kgauss. It was also necessary to check if the dismantling and reassembling of the chamber had seriously affected the field mapping. A few test runs of the kinematics and geometry programs were made, using the original field map and slightly differing central magnetic field values in steps of 0.03 Kgauss. Missing momenta and stretch functions for the beam momentum were plotted; they did not differ seriously. Runs with a field value of 11.05 Kgauss were slightly the best, and this was taken as the central field value. The stretch functions (Fig.II.3,Table II.3) are reasonable, so the old field map was taken to be sufficiently accurate.

II.2.4 Film measuring

The film from the 1970 run was stored for several years before it was measured. During this time the film emulsion dried out so that much of the film could not be measured on an automatic measuring machine (H.P.D.). Some of the film was kept close to an H.P.D. and was sprayed with oil when this broke down at one time. Both problems caused considerable difficulty when processing of the film in this

---

† Note. When this was set up, the beam momentum had to be rechecked. A part roll of film was taken, developed, measured, and processed by the kinematics programs in 24 hours. This gave an approximate value of the beam momentum, and made it possible to adjust the momentum to the required value.

state was entrusted to the author.

The automated measuring process developed for this experiment (ref. 12) was found to be unusable for most of this film. Rolls not measured on the H.P.D., and those with a failure rate of over 50% on the H.P.D. were measured on the moving stage conventional measuring machines at Imperial College, and on rough digitising tables at Westfield College. Parts of the film covered with oil could not be measured on the conventional machines either. A full printout for every event was produced by GRIND (see Section II.3.2) and every event was checked by eye, at first by physicists, later by trained scanners under physicists' supervision. Successful fits were marked as such on the listing, and a remeasure list of bad measurements and failed measurements was made up by hand. All remeasuring was done on conventional machines at Imperial College, and the remeasures were checked in the same manner. No further full remeasure passes were made, since test passes showed that this would not significantly improve the numbers of events, mainly because of the poor quality of the film. The next sections describe the computer program processing of these measurements.

II.3 Program Processing

II.3.1 Pre-kinematics programs

Film measuring on the H.P.D., and on conventional measuring tables, is carried out in interaction with an on-line computer program. For H.P.D. measuring, the film must first be scanned and rough digitised, to create a list of what the H.P.D. must measure. This scanning and rough digitising was done in one pass of the film; as usual only events within a specified fiducial volume, and with beam tracks following the normal beam trajectory were accepted.

The rough digitisation data was then tidied and used to control H.P.D. measuring. Measurements from the H.P.D. are merged by the program SMOG (ref. 21) for input to THRESH.

For conventional measurements the film was scanned and measured in one pass; events outside the fiducial volume or off-beam were again rejected. If the film had been tried on the H.P.D. and failed to measure well, or if it was being remeasured, the H.P.D. or remeasure lists were used. Remeasure lists described events that had failed on the first measure, and events that were seen during GRIND checking but had not been measured at all. The program BINDG (ref. 21) was used to reformat these measurements for input to THRESH.

Westfield College measurements were originally punched to paper tape, then copied to magnetic tape in a format suitable for processing at Westfield College. A program (STAPED) written by the author was used to edit these tapes at Imperial College; it removed bad measurements, inserted end-of-file marks, and referred suspect events to the operator for checking. The edited tape was then reformatted to I.C. format using a conversion program rewritten by the author. This program also printed information concerning these events that BINDG required. Output from this program and the printed information (roll number and measuring machine number) were then input to BINDG, giving a THRESH input tape.

All this work, except for the creation of tapes by Westfield College, was done on the Imperial College High Energy Physics Group PDP10 computer.

II.3.2 Kinematics and Geometry Programs

The CERN kinematics and geometry programs THRESH and GRIND (ref. 20) lay next in the program chain. At the earlier stages of the experiment they were run on the University of London Computing Centre (U.L.C.C.) CDC-6600 computer, which had served the group well at that time. By the time of this run it was considerably overloaded with work; jobs took up to a week to run, and there was a significant probability of tapes and printed output being lost. Our versions of THRESH and GRIND were therefore transferred onto the Rutherford Laboratory IBM 360/195 computer in 1973. Initially there were problems with program rewriting and compatibility between different computers; the author had to make changes in THRESH and GRIND subroutines when further problems were found during production runs. The programs then worked well and turnaround times went down to about one day on the new computer, but it was 6 months before all problems had been sorted out.

The operations of THRESH and GRIND are well known, and their use in this experiment has been described in references 1, 9 and 12, so only the following points relevant to the present work will be made.

Optical Constants and Magnetic Field. The numbers whose values and calculation are described in section II.2 were used throughout for this run. Different bubble chamber fiducial marks were used for HPD measurements, for conventional measurements at Imperial College, and for conventional measurements made at Westfield College, so the lists of fiducial mark positions in the optical constants had to differ

accordingly. Beam track and secondary track profiles and stretch functions were plotted during processing to check for possible problems.

GRIND beam block. GRIND allows the use of a beam block - a mean beam momentum, dip and azimuth at the point where the beam enters the bubble chamber, together with estimated errors on these, and rates of change as the beam moves through the chamber. These values are used for events with a badly measured beam track, and to swing beam measurements towards the mean values (unless the measurement is more than a defined number of standard deviations away from the mean). They are particularly useful for experiments with a high beam momentum, where it is difficult to get accurate measurements of the beam tracks because they are nearly straight.

For the run being measured, the beam momenta were so low that beam tracks curved considerably and could be measured well, so the beam block would be most useful for events with a badly measured beam. Because the beam line was pushed to its lowest limits, and the extra magnet was used, the spread of momenta was wider than is normal. Swinging measured values towards the mean may have moved them too far from their true values, and replacing bad measurements with mean values could have given wrong results. It was therefore possible that the imposition of a beam block would not be justifiable.

A beam block was calculated by the author for 0.85 GeV/c film, using only elastic events fitted with 4 constraints. A previous thesis (ref. 9) by Rob Stevens gives details of such calculations. GRIND was run with and without this

beam block, and the results showed that it would indeed be better not to use a beam block. It is better to lose a few events with badly measured beam tracks than to introduce events with an incorrect beam momentum and direction. This applies to all the momenta of this run, and GRIND was used throughout without a beam block.

At the end of this stage in the processing, there exists a GRIND library Tape (G.L.T.) containing all possible hypotheses for each event that passed succesfully through THRESH and GRIND, and limited information on other measured events. There is also a GRIND output printed listing describing each event. This is the listing, mentioned in II.2.4, used for checking all measurements. Comments written on this listing either state which hypothesis is correct, or mark the event for remeasuring.

II.3.3 Hypothesis Selection and D.S.T. Creation

The Data Summary Tape (D.S.T.) at each momentum is made up by selecting the correct hypotheses from all G.L.T.'s at that momentum, changing their formats, and writing them all to the D.S.T. This is done by the CERN program SLICE (ref. 20). SLICE is provided with a deck of SLICE cards, one for each acceptable event hypothesis. It tidies these up, then compares them with the relevant G.L.T. and writes corresponding event hypotheses to the D.S.T. in a specified format.

Production of SLICE cards, originally punched by hand from notes on GRIND listings, has been increasingly automated. For film from the second run of this experiment a special

version of program AUTO, described in references 9 and 12 was used to produce SLICE cards automatically, leaving the need for a much smaller amount of manual intervention. This version of AUTO ran only on the U.L.C.C. CDC computers, and used ionization information from H.P.D. measurements. A different version of AUTO was adapted for use on the R.H.E.L. IBM computer; this together with the lack of ionization information for conventionally measured film resulted in much less efficient decision-making, and in some cases wrong hypotheses were chosen. For the third run of film AUTO was therefore used only to produce SLICE cards for all hypotheses accepted by GRIND.

These cards were not punched, but were written to a magnetic tape on the IBM computer at R.H.E.L. A separate program, DSLICE, was developed by Simon Orebi Gann to display SLICE cards on-line on the Imperial College H.E.N.P. PDP10 computer. DSLICE copied the card images off the tape onto a disk, then displayed all acceptable hypotheses for an event on a light-penning visual display unit, one event at a time. An operator used the light-pen to indicate the hypothesis that had been marked as correct on a GRIND listing, or to reject all hypotheses, At the end of a run, DSLICE wrote out the selected SLICE card images to tape. This method was faster and more convenient than punching SLICE cards by hand, or going through cards punched by a computer.

The DSLICE output tape was sent back to R.H.E.L. and reformatted by another program SREAD. SLICE was then run with this tape of SLICE card images, and with the corresponding G.L.T. as inputs, producing a D.S.T. Up to this stage, the events from each separate roll of film, and from first

measures and remeasures were kept on separate files on the tapes. The separate D.S.T. files were now merged into one large file for all events at the given energy, and reformatted again into the final D.S.T. format.

Before the D.S.T. could be used, it was necessary to check for duplicate events. An event may have been measured twice, or two SLICE cards may have been unintentionally selected for the same event, and it was necessary to remove these duplicates. A program, RED, written by the author checked the whole D.S.T. frame by frame. If two events on the same frame were less than 1 cm. apart in the bubble chamber, a warning was printed giving details of both. In some cases there were 2 genuine events close together but 5 to 10 duplicate events were found per roll. These were removed by another program, REJ.

Cambridge D.S.T.'s were changed to the Imperial College format, checked for duplicates too, and added to the I.C./W.C. data to give the final D.S.T.'s.

II.4 Momenta other than 800 and 850 MeV/c

As the 800 and 850 MeV/c D.S.T.'s were needed for the 3-body partial wave analysis described further on, and indeed lay in the middle of its energy range, they were made up before the 1150 and 1250 D.S.T.'s . The program chain used on the 360 computer was developed on the 800 and 850 film, and then used on other film. It worked for that too, but it is worth making the following comments concerning these and other higher energy D.S.T.'s

1. The $\pi^+ p \to \Sigma K$ channel, below threshold at 800 and 850 MeV/c is open at the higher energies. ΣK events were scanned and measured with no special problems.

2. At 1.15 GeV/c, only 9 rolls of film had been taken instead of 12 as at the other energies of this run. Furthermore, Westfield College lost 2 of their rolls (the third was processed entirely at I.C.), so additional emphasis was placed on getting events at this energy through the I.C. processing chain. This was not helped by a bug on a conventional table used to remeasure this film - events measured by short people failed very frequently, whereas those measured by tall measurers had the usual pass rate. This was in no way channel-dependent, and a third measure of some film confirmed this without significantly improving the statistics.

3. The standard deviation on the dip stretch functions was slightly worse at 1.15 and 1.25 than at .8 and .85, but still within acceptable limits. This was seen by Imperial College and by Cambridge. See Table II.3.

4. The I.C. remeasures at 1.4 GeV/c, mentioned in reference 9, were completed by the author and added to the 1.4 D.S.T.

5. Of the remaining energies from the second run (table I.3), 1.55 and 1.6 were abandoned because of proton contamination of the beam, though the film still exists. 1.5 was processed only by Cambridge, 1.45 was processed by Cambridge, Westfield (who had the largest part of the 1.45 film) measured this energy but did not process it. Imperial College measured and

processed part of the 1.45 film, then decided that it needed new optical constants. The author obtained and checked these in the same manner as is described in section II.2.2, but shortage of staff and lack of scanning tables prevented completion of processing. The present situation is therefore that only Cambridge D.S.T.'s exist at 1.45 and 1.5 GeV/c.

II.5 Checking the D.S.T.s

Before the tapes are used for cross-section calculations and other physics analysis, their quality needs to be assessed. This section gives the numbers of events on the D.S.T.s and shows plots that allow the quality of the data to be checked. Most of these checks were made using the CERN program SUMX (ref. 20).

The total numbers of events on the D.S.T.s , the numbers of events from each laboratory, and the numbers of events per roll of film measured at each laboratory, are shown in Table II.1. It can be seen that the effort to get as many events processed as possible at I.C. was successful.

Figure II.2 shows beam track momentum, dip, and azimuth plots from the 850 MeV/c D.S.T., for 4-C elastic events. The momentum shows a wide spread about a well-defined peak; as described in II.3.2, I.C. and W.C. did not pull measurements in towards a mean value. Cambridge did pull theirs in, and rejected events that were too far to pull in reasonably. The beam dip and azimuth plots show the expected distributions. In order to obtain reliable results, particularly in the calculation of cross-sections, cuts were imposed to remove off-beam events.

The cuts used at 850 MeV/c are drawn in on Figure II.2, and Table II.2 gives the values of the cuts imposed at all four momenta. All the remaining plots and event numbers in this chapter and the next are for events within the cuts.

Figure II.3 shows stretch functions at 850 MeV/c, and Table II.3 gives stretch function values for all four momenta. Table II.4 gives stretch functions separately for I.C., W.C., and Cambridge measurements at 850 MeV/c. Stretches have already been discussed in connection with their use to check optical constants. The Imperial College optical constants had been calculated with the assumption that stretches on the dip would be worst because of film problems. The Cambridge optical constants were calculated to obtain the best balance between the three measurements, and the results in Table II.4 clearly reflect this difference in approaches. The stretches from the combined D.S.T.s are quite acceptable.

Figures II.4 and II.5 show distributions of probabilities for elastic and 3-body events. These are essentially flat, with a peak at low probabilities. This is as expected, and has been discussed in previous theses (refs. 1, 9 and 12). 1250 MeV/c data is used here, the distributions at the other momenta are similar.

Figure II.6 shows the distribution of the coplanarity function

$$p_{\pi_i} \wedge (p_{\pi_f} \wedge p_{p_f})$$

for 4-C events at 850 MeV/c. Momentum conservation demands that this be zero, otherwise the incident pion and outgoing particles would not lie in a single plane. It can be seen that this quantity is close to zero, and peaks at zero.

These plots and tables show that the data has been well measured, and that no serious overall systematic problems exist. The numbers of events are sufficient for cross-section calculations. The problems with the I.C. film have been overcome; they made measuring it more difficult, but the data from it is trustworthy.

Momentum (MeV/c)	800	850	1150	1250
Total number of events	7042	9029	9669	17200
I.C.				
Number of events	2970	3465	4795	6327
Events per roll	743	990	1598	1582
W.C.				
Number of events	1732	2798	1869	5545
Events per roll	577	933	1869	1386
Cambridge				
Number of events	2340	2766	3005	5328
Events per roll	585	692	1002	1184

Table II.1

Numbers of events on D.S.T.s

Nominal Momentum P_{lab} MeV/c	800	850	1150	1250
lower momentum cut	766	818	1110	1214
upper momentum cut	804	848	1170	1276
Mean momentum within cuts	785	833	1140	1246
lower dip cut (radians)	-.0420	-.0380	-.0180	-.0160
upper dip cut	.0400	.0440	.0220	.0240
mean dip λ within cuts .	.0022	.0047	.0042	.0046

Table II.2

Mean beam parameters and cuts imposed

Nominal Momentum MeV/c	800	850	1150	1250
$1/P_{lab}$				
Mean	-.051	.037	-.037	-.164
Standard deviation	1.079	0.996	0.998	0.981
dip				
Mean	-.207	-.231	-.201	-.091
Standard deviation	1.140	1.184	1.280	1.325
Azimuth				
Mean	-.060	-.006	.060	.091
Standard deviation	1.007	1.023	1.042	1.027

Table II.3

Beam stretch functions

Laboratory	I.C.	W.C.	Cambridge
$1/P_{lab}$			
Mean	.055	-.068	.033
Standard deviation	0.921	0.739	1.116
Dip			
Mean	-.497	-.019	.020
Standard deviation	1.101	1.029	1.230
Azimuth			
Mean	-.118	.042	.127
Standard deviation	1.021	0.751	1.050

Table II.4

850 MeV/c stretches at the different laboratories

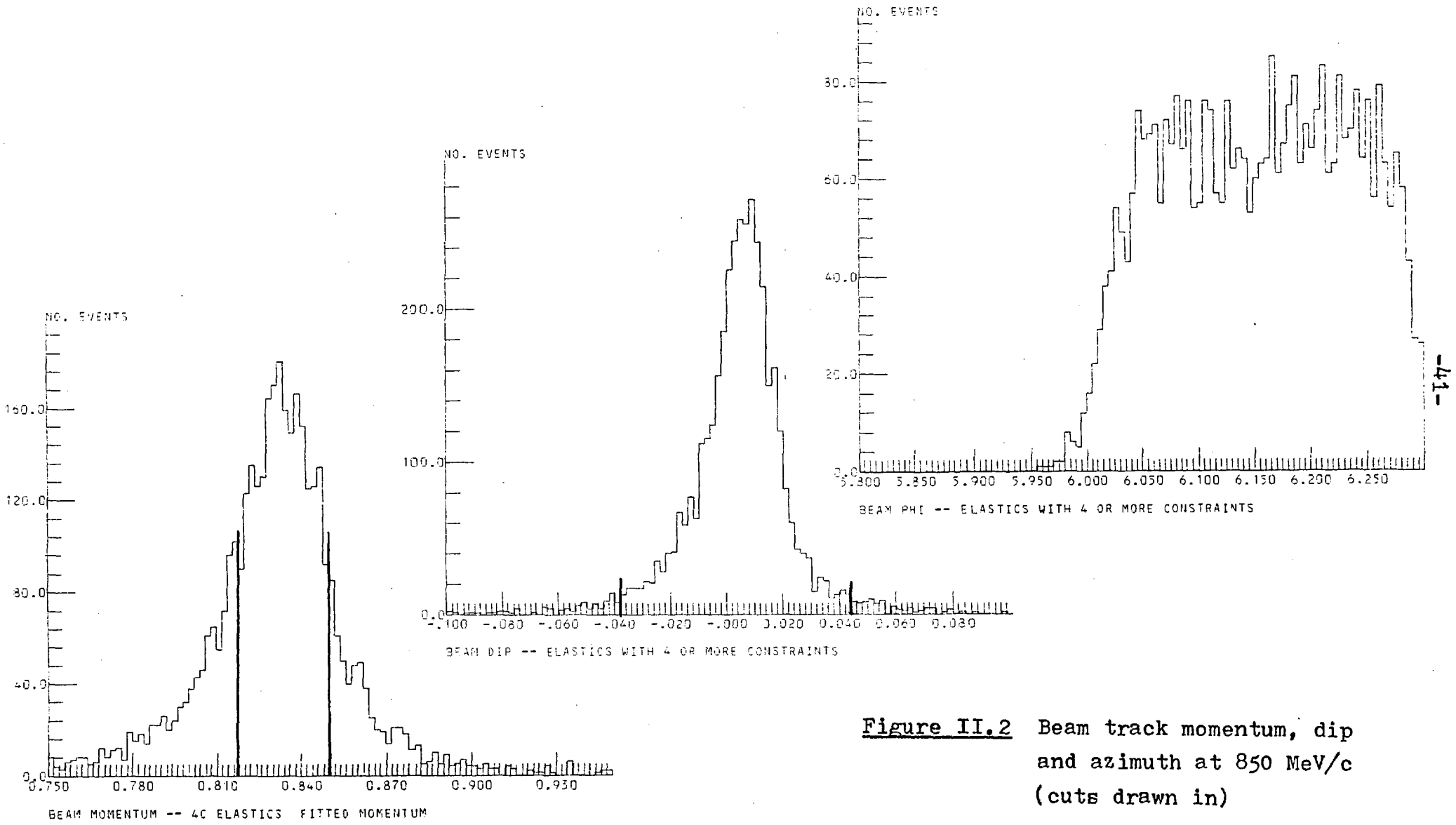

Figure II.2 Beam track momentum, dip and azimuth at 850 MeV/c (cuts drawn in)

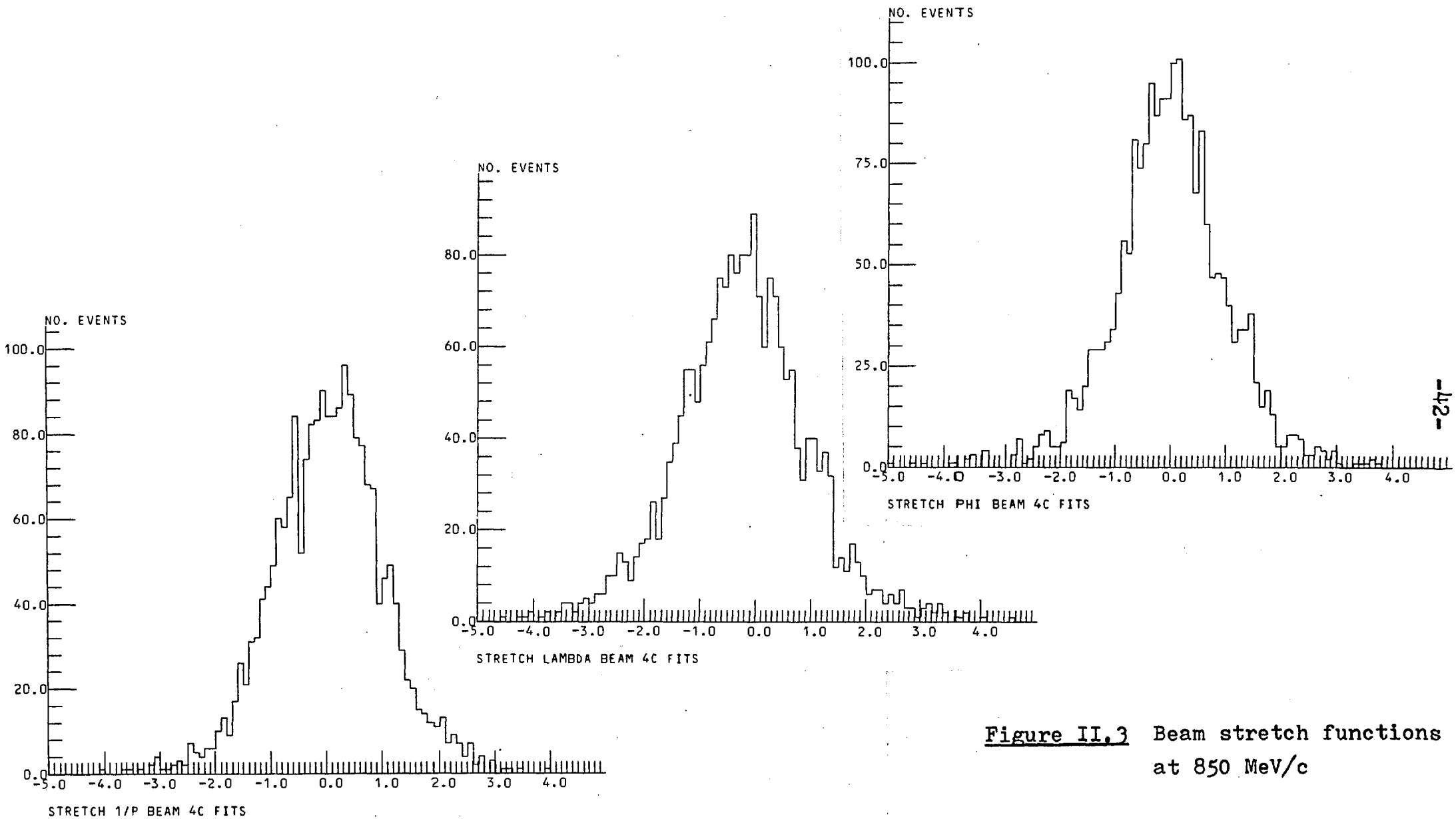

Figure II.3 Beam stretch functions at 850 MeV/c

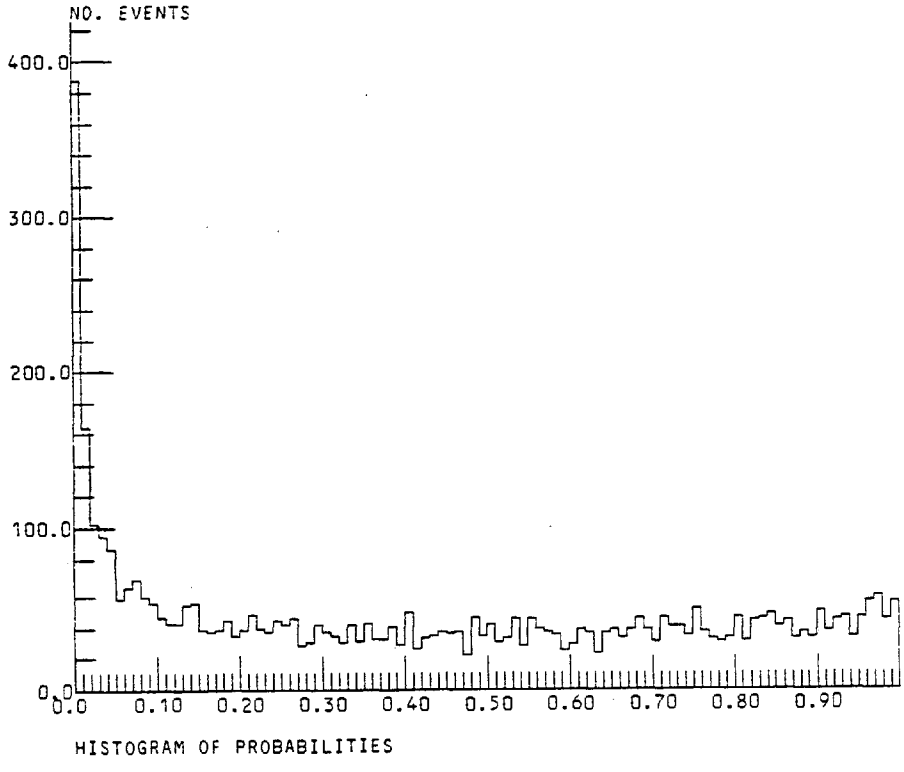

Figure II.4 Elastic event probabilities at 1250 MeV/c

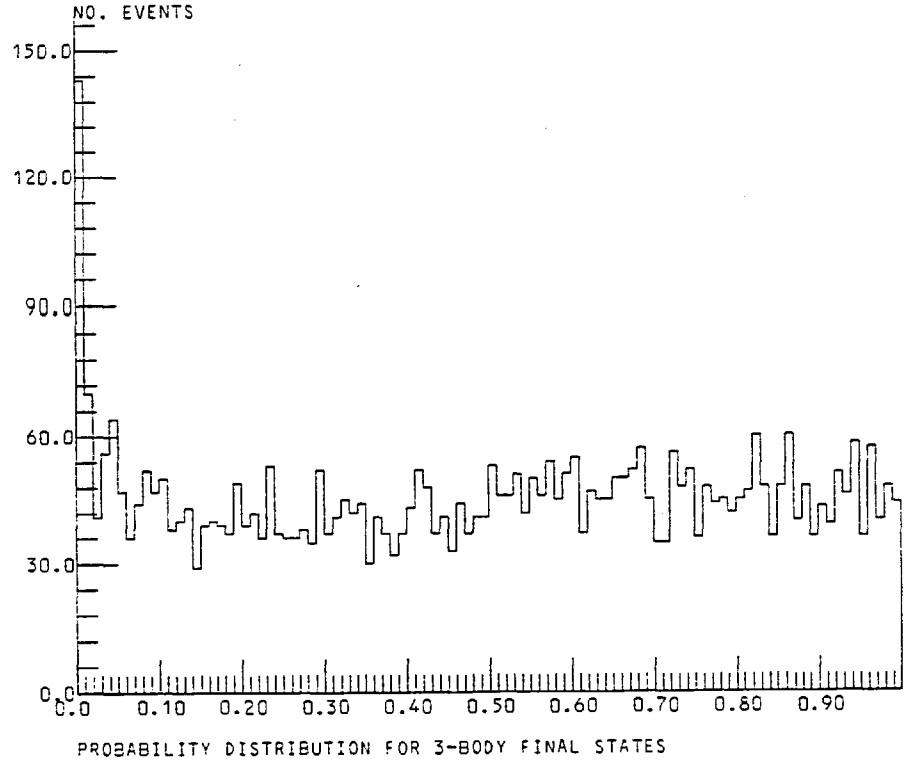

Figure II.5 3-body event probabilities at 1250 MeV/c

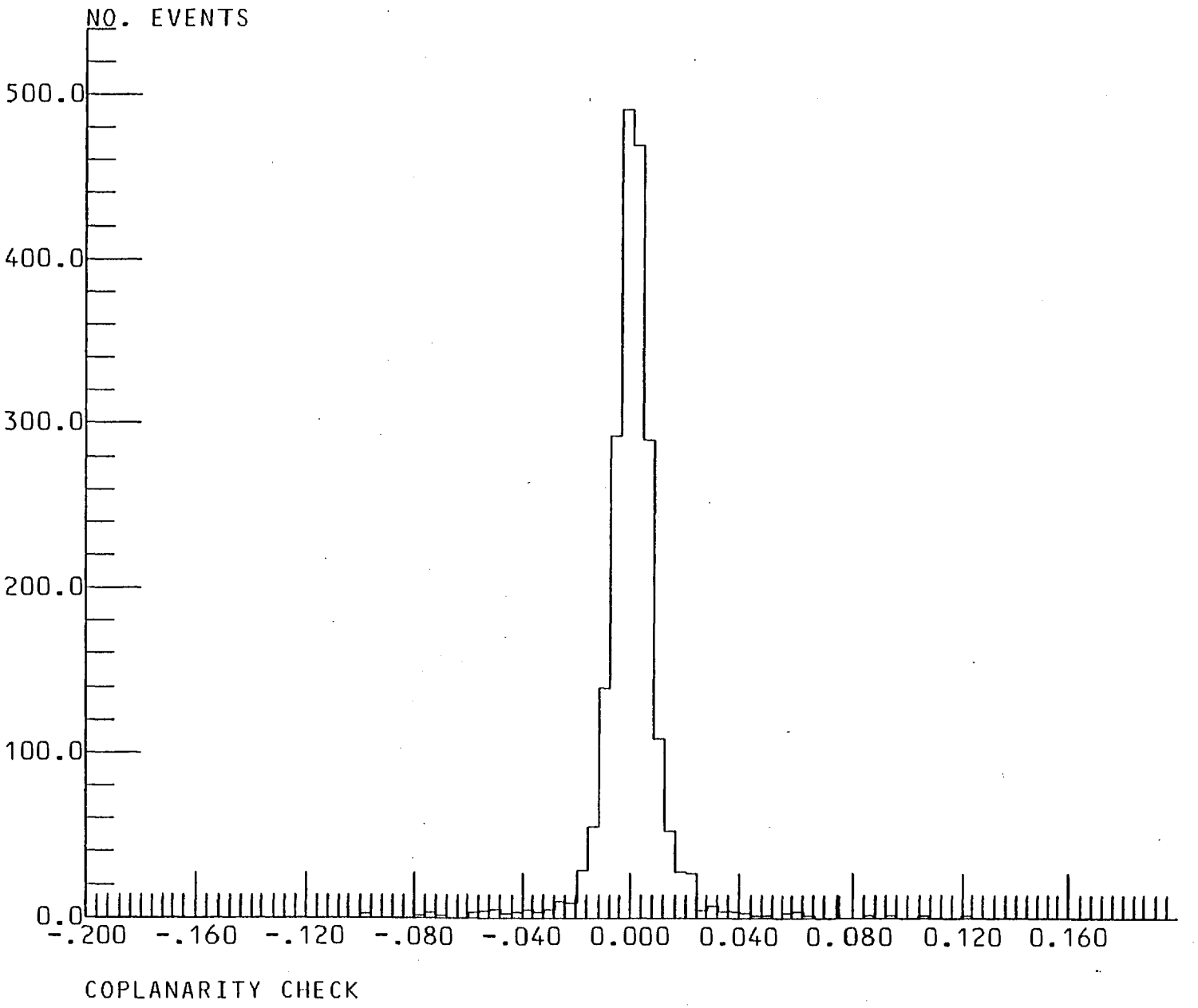

Figure II.6 Coplanitary function at 850 MeV/c

CHAPTER III

Cross-sections, Elastic Analysis and Dalitz Plots

III.1 Introduction

This chapter discusses the problems of separating different channels, and making channel-dependent corrections, then presents the calculated cross-sections in each channel. Corrections for scanning losses in the elastic channel are discussed in particular, and the elastic data is analysed in terms of a Legendre polynomial series. The elastic analysis provides values of the backward elastic differential cross-sections, and these are discussed. Dalitz plots from the four D.S.T.s are also presented.

III.2 Separation of channels

The four reactions that contribute most to the cross-sections at our energies are -

$$\pi^+p \rightarrow \pi^+p \qquad 3.1$$

$$\rightarrow \pi^+p\pi^o \qquad 3.2$$

$$\rightarrow \pi^+\pi^+n \qquad 3.3$$

$$\rightarrow \pi^+p\pi^+\pi^- \qquad 3.4$$

The elastic events, 3.1, are used in the elastic analysis, and must be corrected for scanning losses. The inelastic events, 3.2, 3.3, are to be used in the 3-body analysis. It is therefore particularly important to separate these channels cleanly. Of the other channels, ΣK was identified by the decay of the Σ, and other neutral particle production

was identified by deciding whether missing mass squared was inconsistent with hypotheses 3.1 to 3.4. These channels contribute little to the cross-section, so misidentification would have a minimal effect.

The channel 3.4 was immediately identified by the additional tracks. Channels 3.2 and 3.3 were initially separated by the kinematics programs, in cases of possible doubt the GRIND printout was compared with the film, and a decision was made on the basis of track ionisation. Only one or two events per roll could not be definitely identified in this way. Separation of channels 3.1 and 3.3 should be unambiguous on kinematic grounds; if an event could be a candidate for both channels, it was usually badly measured and was remeasured, otherwise the elastic hypothesis was accepted - earlier work in this experiment had shown that the elastic hypothesis was correct where it was possible (refs. 1, 9, 12).

The most difficult separation is that of channels 3.1 and 3.2. GRIND could usually make a choice on the basis of kinematics, doubtful events were checked, and remeasured if they had large errors, or assigned to the elastic channel. Figure III.1 shows a plot of missing mass squared (x-axis) versus missing energy, and projections for elastic events alone at 850 MeV/c. Figure III.2 shows plots of the same quantities for events assigned to channels 3.1 and 3.2. There is no evidence of contamination of either channel by the other. It should also be noted that the missing mass squared and energy (x-projection and y-projection respectively) in the elastic channel both peak close to zero.

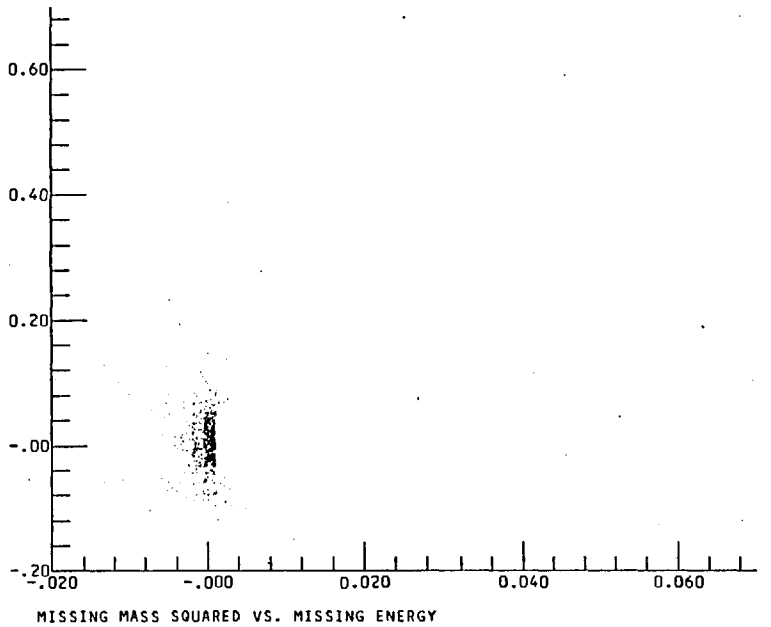

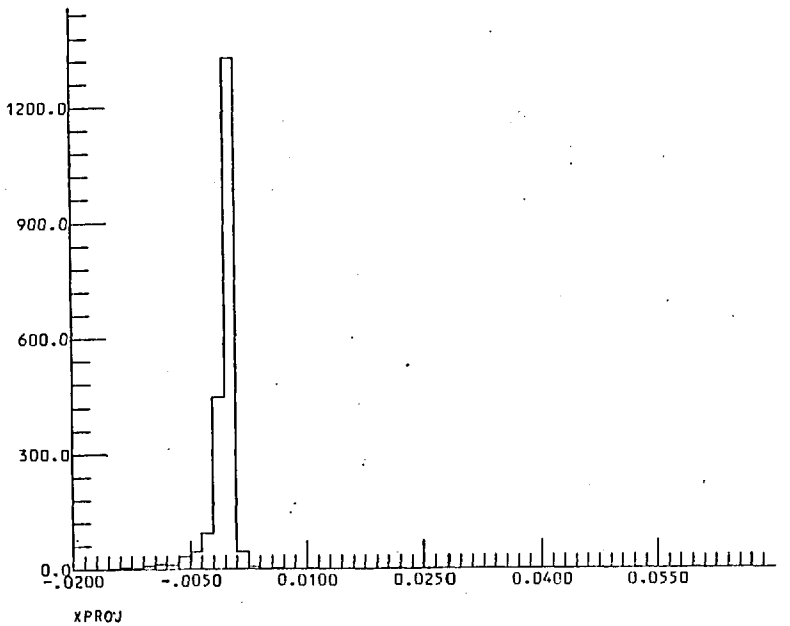

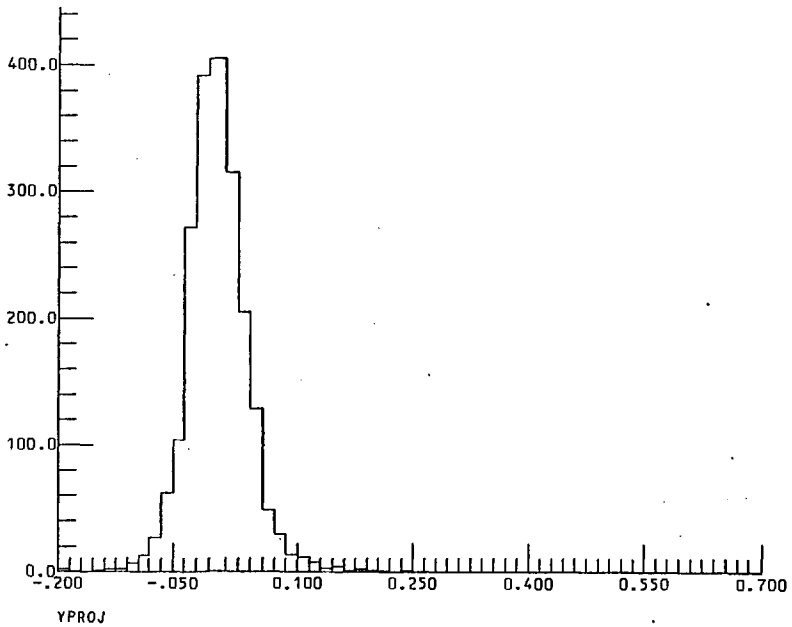

Figure III.1 Missing masses and energies of $\pi^+ p$ events

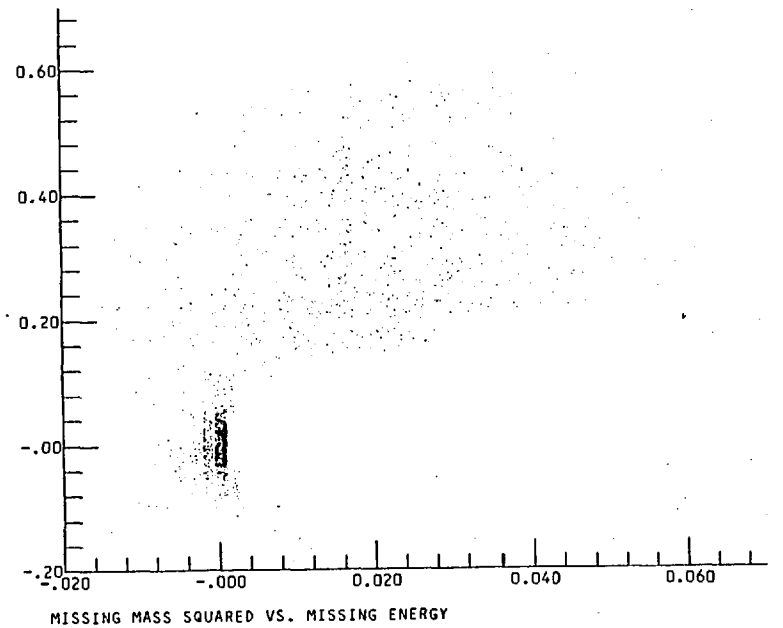

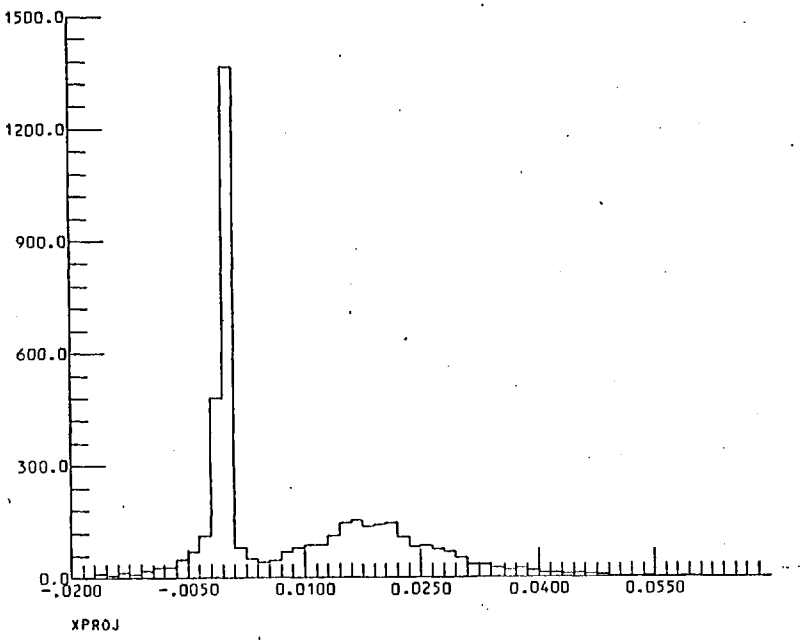

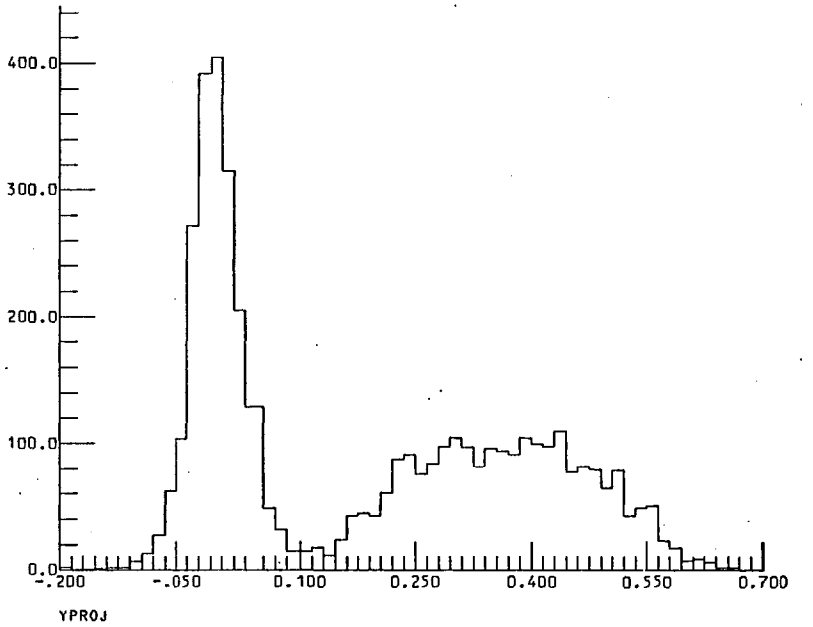

Figure III,2 Missing masses and energies of π^+p and $\pi^+p\pi^o$ events

The important channels therefore appear to be cleanly separated, so that accurate cross-sections can be calculated.

III.3 Cross-section Calculations

III.3.1 Total cross-sections

In all film-taking runs for this experiment, there was some muon contamination of the beam. V. Tayler (ref. 2) estimated 5-8%, but no exact values were obtained. All cross-sections have therefore been calculated by normalising to the total π^+p cross-sections of Carter et al (ref. 22). The author fitted 30 points of the Carter et al data by Chebyshev polynomials using the Harwell program PEIIAD(ref. 23). Fits of increasing order were made until fitted values were the same to better than one part in 10^3 at three consecutive orders. Cross-sections from the 14th. order fit were then calculated at the mean momenta of the D.S.T.s, and the errors were taken to be those on the nearest Carter et al data point. These total cross-sections are given in Table III.1.

III.3.2 Channel-dependent corrections

Channel-dependent problems and differences in programs or in handling certain channels at the different institutions must be checked for, and corrected where necessary. Cambridge used RHEL kinematics programs, not the CERN ones, so program-dependent faults could be checked by comparing Cambridge results with those of I.C. and W.C. Numbers of events before and after correction are given in Table III.1. There were no

significant differences between I.C. and W.C. event distributions in different channels, so I.C. and W.C. event numbers are given in one column, and Cambridge event numbers are given separately. The numbers of events in Tables III.1 and II.2 show that about 90% of Cambridge events were within the beam cuts, compared with only about 50% of the I.C. and W.C. events. This is a reflection of the fact that Cambridge pulled their measured quantities in towards mean values, whereas I.C. and W.C. did not.

i) Elastic events

Events where the pion scatters in nearly the forward direction, or where the reaction plane is approximately perpendicular to the plane of the bubble chamber cameras tend to be missed during scanning, and are difficult to measure. Corrections for these losses were made during the elastic analysis, described in Section III.4. Inelastic channels are not significantly affected by such errors, so this correction is applied only in the elastic channel.

ii) 3-body and multineutral channels

Events whose final state contains a π^+ and a p but whose missing mass (mm) is not compatible with zero may be badly measured elastics, $\pi^+ p \pi^o$, $\pi^+ p \eta^o$, or $\pi^+ p$ multineutral events. Similarly, events with two π^+ tracks may be $\pi^+ \pi^+ n$ or $\pi^+ \pi^+$ multineutrals. Multineutral events are usually written $\pi^+ p(mm)$ and $\pi^+ \pi^+ (mm)$ where (mm) represents the missing mass of the neutral particles. The separation of the $\pi^+ p$, $\pi^+ p \pi^o$ and $\pi^+ \pi^+ n$ events has already been discussed; these are the largest channels, and the ones of major interest to this

experiment. Errors in the multineutral and $\pi^+ p\eta^o$ channels can only affect the major channels by a few percent, but are worth correcting so as to give corrected cross-sections in the multineutral and $\pi^+ p\eta^o$ channels.

The uncorrected event numbers in Table III.1 show that Cambridge had fewer multineutral events than I.C. and W.C. An added complication lay in that Cambridge did not distinguish $\pi^+ p\eta^o$ events from $\pi^+ p(mm)$. The differences between Cambridge and I.C./W.C. cannot be attributed entirely to statistical fluctuations; they are much too large, particularly in the $\pi^+ p\eta^o$ and $\pi^+ p(mm)$ channels, and at the higher momenta. A detailed consideration of these channels is therefore necessary.

Firstly, consider which events can be found in the multineutral channels, and where they would lie on a plot of missing mass. Genuine multineutral events should be assigned to this channel, and should cluster around multineutral masses,- the mass of 2, 3 or more π^o mesons in the $\pi^+ p(mm)$ channel, or $n\pi^o$, $n\pi^o\pi^o$ etc. in the $\pi^+\pi^+(mm)$ channel. $\pi^+ p\pi^o$, $\pi^+ p\eta^o$ and $\pi^+\pi^+ n$ events should not be found in the multineutral channel, unless very badly measured, however a few badly measured elastic events, whose missing mass is below that of a π^o, but is incompatible with zero may also be found in the $\pi^+ p(mm)$ channel. There may also be a background of very badly measured events, whose missing mass is not identifiable as any of the above, but which would mostly be badly measured multineutrals. The kinematic decision on

whether the missing mass can be that of a single pion or neutron depends on estimated errors. If errors are underestimated, then some poorly measured $\pi^+p\pi^o$ and $\pi^+\pi^+n$ events will be misidentified as multineutrals, whereas overestimated errors lead to genuine multineutral events being fitted as 3-body events. Underestimated errors will therefore give a large background in a missing mass plot, whereas overestimated errors will remove the peaks at multineutral masses, leaving only a background of badly measured events.

Missing mass squared plots were made separately for I.C./W.C. events, and for Cambridge events, The I.C./W.C. π^+p(mm) plots showed distinct peaks at masses of $\pi^o\pi^o$, $\pi^o\pi^o\pi^o$ and $4\pi^o$, with very little background. The Cambridge plots, in contrast, showed no peaks, only a very few scattered events, and in particular no η^o peak was seen. The $\pi^+\pi^+$(mm) plots at the two lower momenta showed only a small background, but at the upper momenta I.C./W.C. showed a peak near the mass of $n\pi^o$, whereas the Cambridge data showed no peak. These plots, and the fact that Cambridge pulled their measurements towards fitted values, led to the belief that the I.C./W.C. data was correct, and the Cambridge data needed correcting. The numbers of events in Table III.1 have been corrected accordingly, and where events have been added to the Cambridge $\pi^+p\eta^o$, π^+p(mm) and $\pi^+\pi^+$(mm) channels, they have been subtracted from the $\pi^+p\pi^o$ and $\pi^+\pi^+n$ channels. At 800 MeV/c, the I.C./W.C. π^+p(mm) channel contained a group of 9 events with missing mass very close to zero - these

were taken to be mis-assigned elastic events and were therefore added to the numbers of elastic events.

Plots were also made of the cosine of the π^+ scattering angle in the π^+p(mm) channel. The distribution of events showed that they did not all come from one kinematic region. This adds to confidence in the assumption that the problems were due to an overestimate of the errors, which would not preferentially affect a special kinematic region. The careful checks and corrections made lead to confidence in the calculated $\pi^+p\pi^o$, π^+p(mm) and $\pi^+\pi^+$(mm) cross-sections.

iii) 4-prongs

Where ambiguities occured between $\pi^+p\pi^+\pi^-$ and $\pi^+p\pi^+\pi^-\gamma$, the 4-C fit was always chosen. In the case of ambiguities between $\pi^+p\pi^+\pi^-\gamma$ and $\pi^+p\pi^+\pi^-\pi^o$, the hypothesis with the higher probability was chosen. At the two upper momenta, a higher proportion of I.C. and W.C. $\pi^+p\pi^+\pi^-$ events failed than in other channels, so the numbers of events were corrected for this.

iv) ΣK

The earlier Imperial College runs had considerable trouble with this channel. The version of GRIND used on the 360 computer for the third run was much less troublesome, but a larger fraction of events failed in this channel than in others. A correction based on an estimate of this larger failure rate and on a comparison with Cambridge results has been applied.

III.3.3 Cross-sections

The last columns of Table III.1 give cross-sections calculated from the corrected numbers of events and from the total cross-sections. Errors are calculated as follows : $\sqrt{N}$ errors are assumed on the uncorrected numbers of events, they are scaled up to account for corrections, then these errors are combined with the errors on the total cross-sections and a $\sqrt{N}$ error on the total number of events to give the error on each calculated cross-section.

Cross-sections for the π^+p channel are shown in Figure III.3. Results from this thesis, from momenta previously analysed by our experiment, and from the Oxford experiment (refs. 6, 7, 8) are shown together with results from other experiments. Our statistics are good, so our errors are small compared to most earlier experiments. Figures III.4, III.5, III.6, III.7 show cross-sections for $\pi^+p\pi^o$, $\pi^+\pi^+n$, $\pi^+p\pi^+\pi^-$ and $\pi^+p\eta^o$ respectively. Our $\pi^+p\pi^o$ and $\pi^+\pi^+n$ results are in agreement with earlier work, and the errors are small. $\pi^+p\eta^o$ results have larger errors because this is a small channel, and we had some trouble, as already discussed. The Oxford group originally doubled the number of 4-prong events that they observed when they calculated their cross-sections. In Figure III.6 we have shown the values they later gave in reference 6, and these are in good agreement with ours. Figure III.8 compares our ΣK cross-sections with those of other experiments; our statistics are again small, but the agreement is reasonable.

channel	I.C. and W.C. events	Cambridge events	Corrected number of events	Cross-section (mb)
800 MeV/c				
π^+p	1287	1180	2651 ± 53	8.46 ± .23
$\pi^+p\pi^o$	855	802	1657 ± 40	5.29 ± .16
$\pi^+\pi^+n$	179	142	321 ± 18	1.02 ± .06
π^+pmm	18	8	17 ± 4	0.05 ± .01
$\pi^+\pi^+mm$	3	6	9 ± 3	0.03 ± .01
$\pi^+p\pi^+\pi^-$	14	16	30 ± 5	0.10 ± .02
			Total cross-section	14.95 ± .18
850 MeV/c				
π^+p	1254	862	2224 ± 48	7.40 ± .21
$\pi^+p\pi^o$	1370	913	2274 ± 48	7.57 ± .21
$\pi^+\pi^+n$	235	163	398 ± 20	1.32 ± .07
π^+pmm	26	8	43 ± 7	0.14 ± .02
$\pi^+\pi^+mm$	4	5	9 ± 3	0.03 ± .01
$\pi^+p\pi^+\pi^-$	28	18	46 ± 7	0.15 ± .02
$\pi^+p\pi^+\pi^-mm$	1	0	1 ± 1	.003 ± .003
			Total cross-section	16.62 ± .18

Table III.1.a

Numbers of events and cross-sections at 800 and 850 MeV/c

Channel	I.C. and W.C. events	Cambridge events	Corrected number of events	Cross-section (mb)
1150 MeV/c				
π^+p	1632	1243	3058 ± 57	13.75 ± .32
$\pi^+p\pi^\circ$	1184	975	2124 ± 46	9.55 ± .25
$\pi^+\pi^+n$	292	231	502 ± 22	2.26 ± .10
$\pi^+p\eta^\circ$	17	0	30 ± 7	0.13 ± .03
π^+pmm	36	6	64 ± 10	0.29 ± .05
$\pi^+\pi^+mm$	32	4	57 ± 10	0.26 ± .05
$\pi^+p\pi^+\pi^-$	90	97	221 ± 16	0.99 ± .07
$\pi^+p\pi^+\pi^-\pi^\circ$	6	4	10 ± 3	0.04 ± .01
$\pi^+p\pi^+\pi^-\gamma$	1	1	2 ± 1	.009 ± .004
ΣK	14	13	29 ± 6	0.13 ± .03
		Total cross-section		27.42 ± .18
1250 MeV/c				
π^+p	2530	2248	5051 ± 73	15.55 ± .29
$\pi^+p\pi^\circ$	1883	1749	3479 ± 59	10.71 ± .22
$\pi^+\pi^+n$	443	474	841 ± 29	2.59 ± .09
$\pi^+p\eta^\circ$	123	0	231 ± 21	0.71 ± .07
π^+pmm	77	23	145 ± 15	0.45 ± .05
$\pi^+\pi^+mm$	98	10	184 ± 18	0.57 ± .06
$\pi^+p\pi^+\pi^-$	234	222	473 ± 22	1.43 ± .07
$\pi^+p\pi^+\pi^-\pi^\circ$	13	11	26 ± 5	0.08 ± .02
$\pi^+p\pi^+\pi^-\gamma$	9	18	28 ± 5	0.09 ± .02
$\pi^+p\pi^+\pi^-mm$	0	1	1 ± 1	.003 ± .003
$\pi^+\pi^+\pi^+\pi^-n$	1	2	3 ± 2	.009 ± .006
ΣK	22	39	83 ± 11	0.26 ± .03
		Total cross-section		32.46 ± .46

Table III.1.b Numbers of events and cross-sections at 1150 and 1250 MeV/c

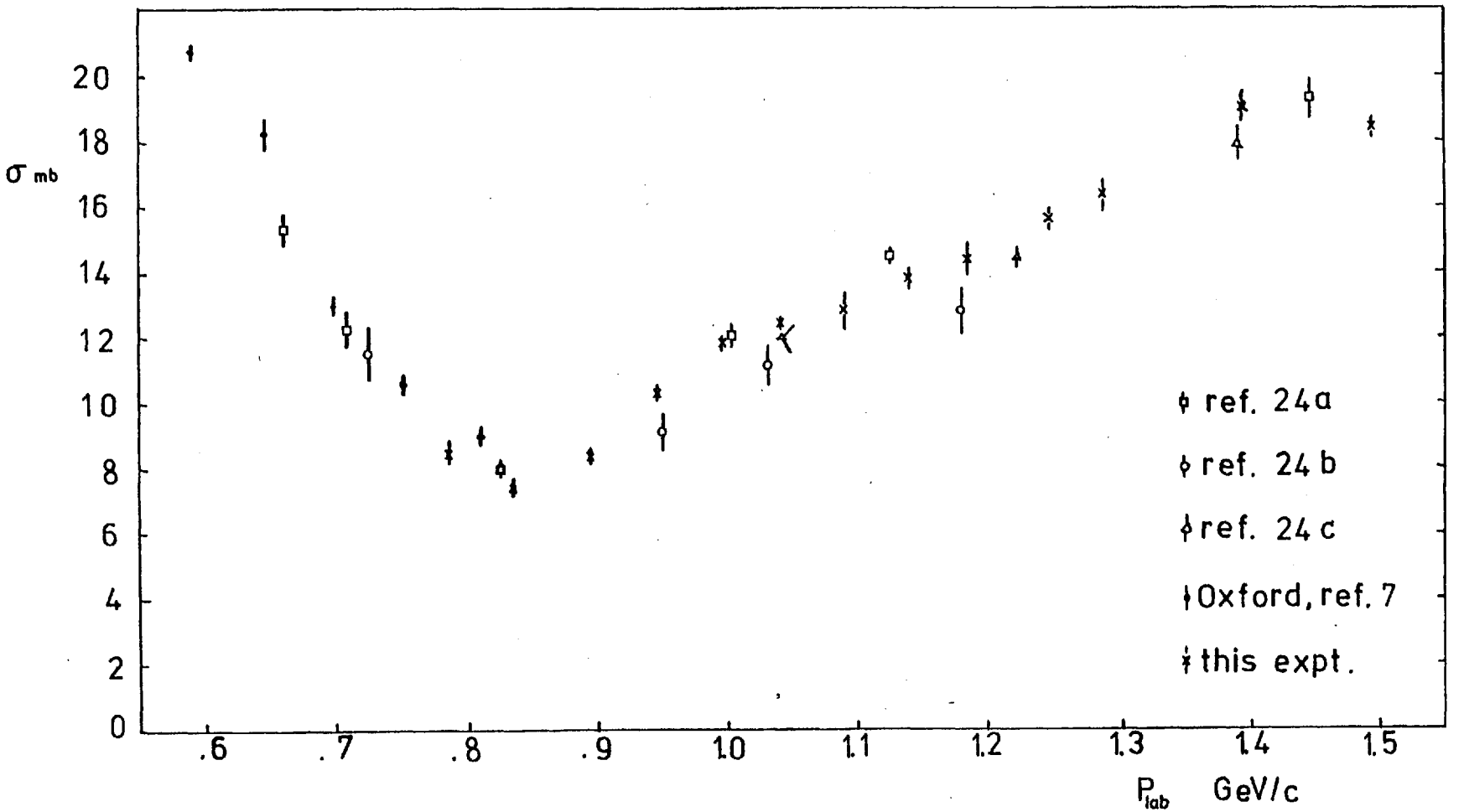

Figure III.3 π^+p Elastic cross-sections

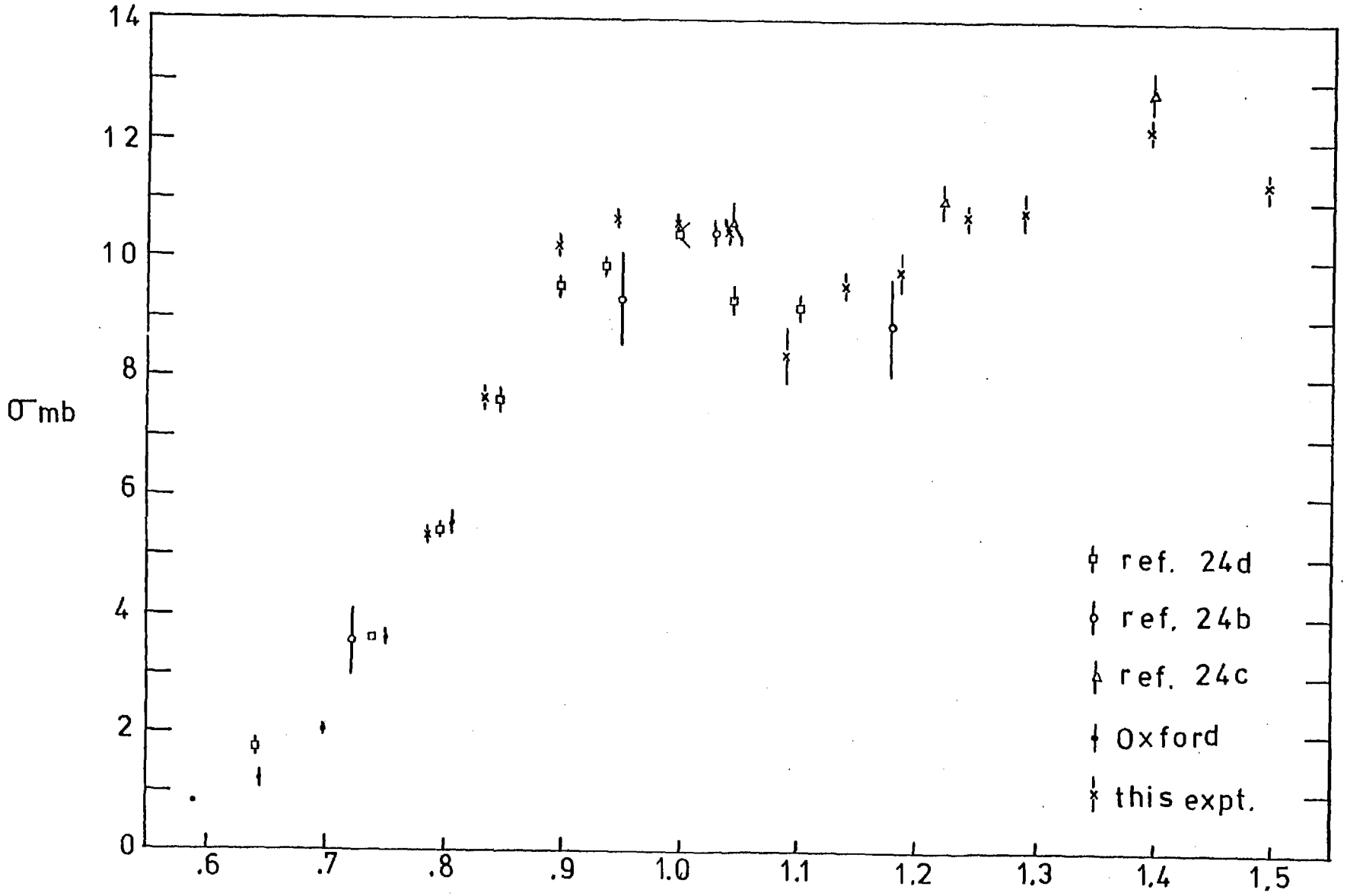

Figure III.4 $\pi^+ p \pi^o$ cross-sections

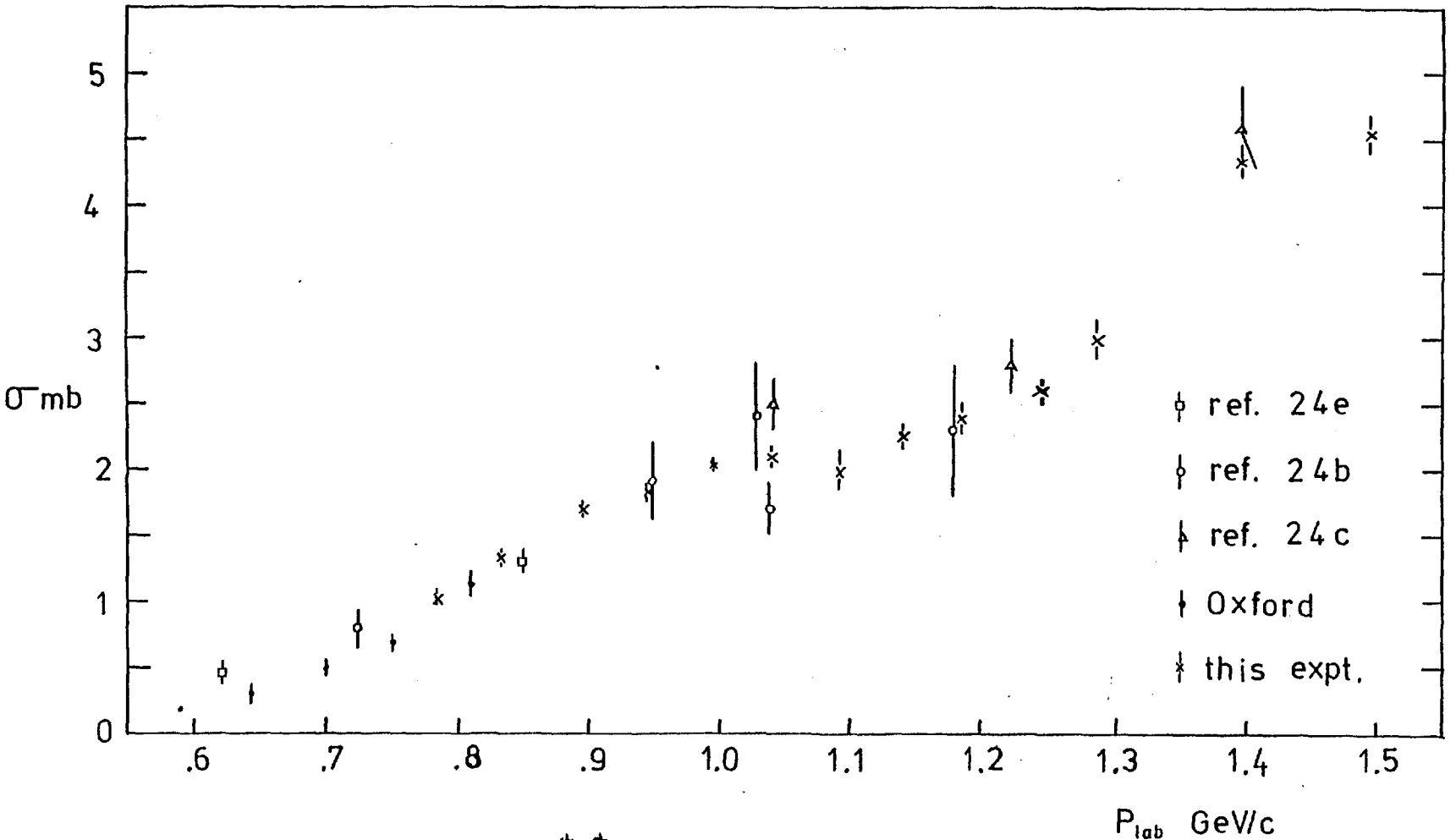

Figure III.5 $\pi^+\pi^+n$ cross-sections

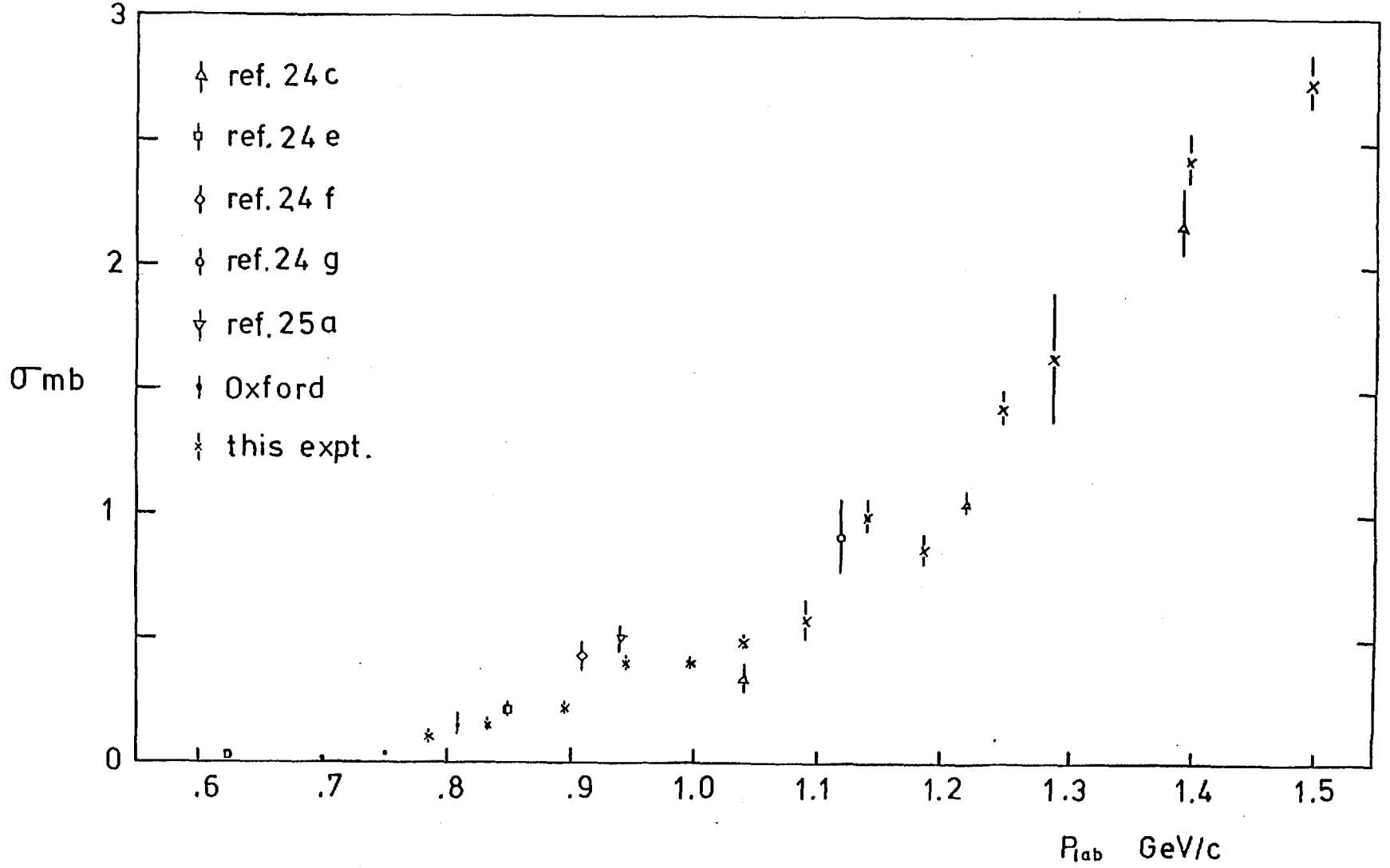

Figure III.6 $\pi^+\pi^+\pi^-p$ cross-sections

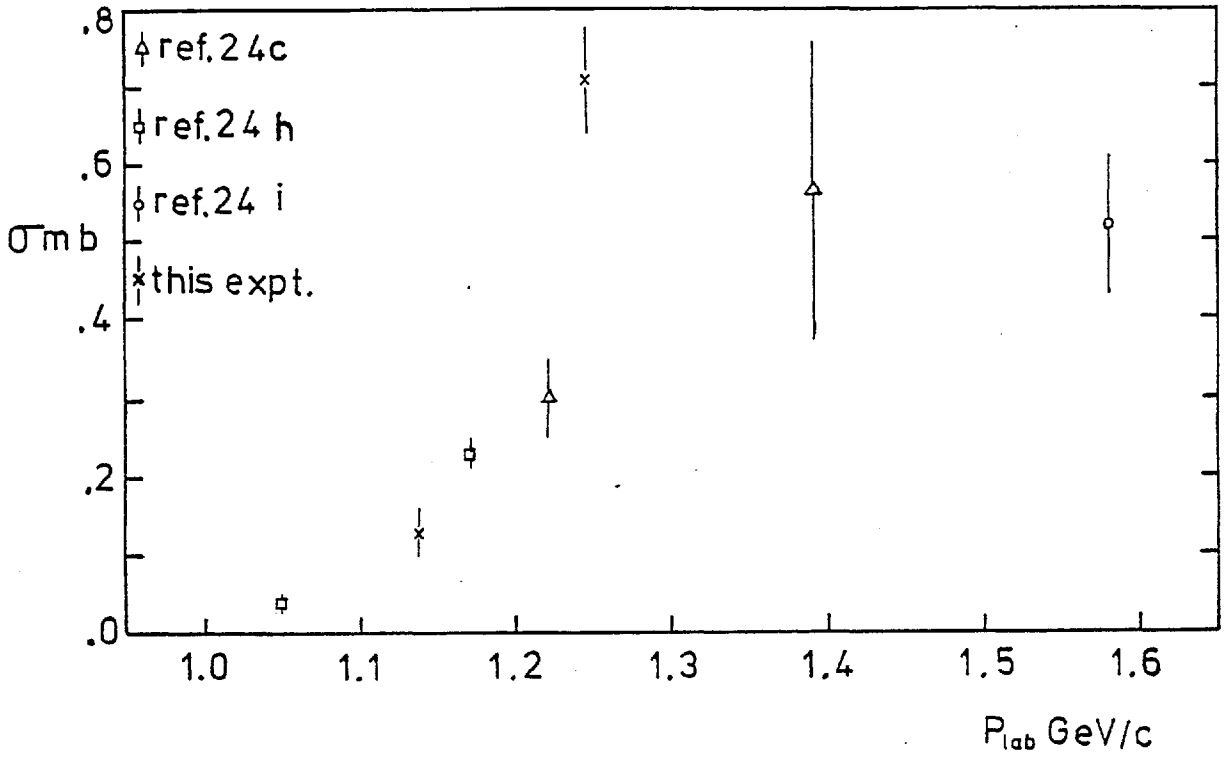

Figure III.7 $\pi^+ pn$ cross-sections

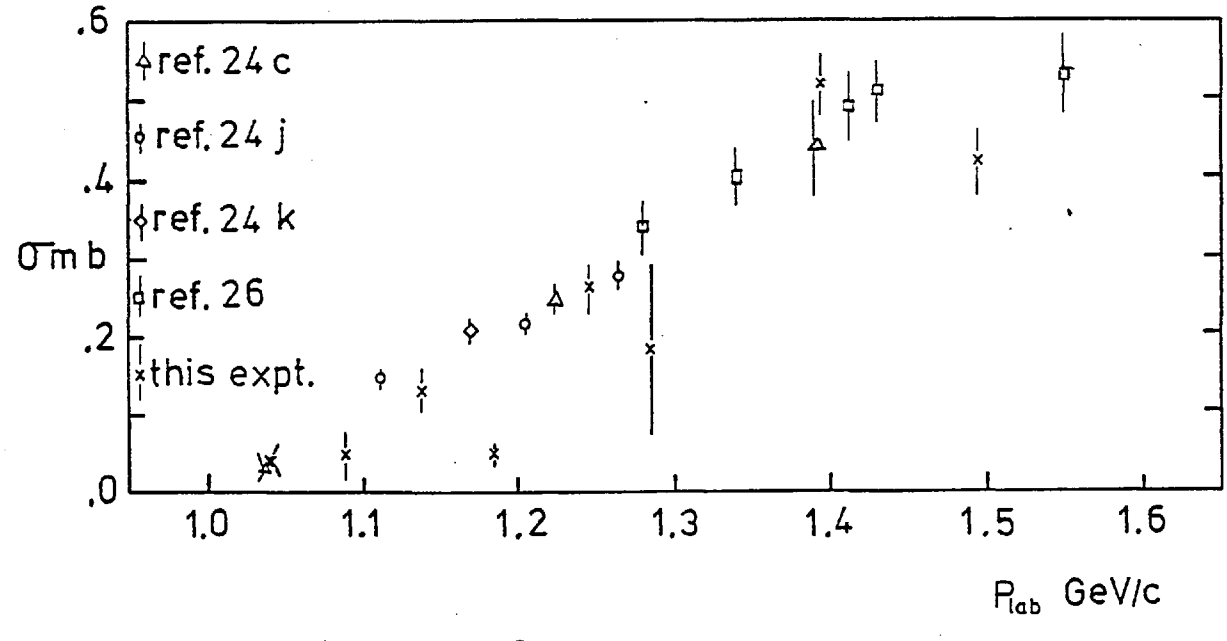

Figure III.8 ΣK cross-sections

III.4 Elastic Analysis

III.4.1 Elastic corrections

The elastic interactions can be described by two angles; the polar angle θ which is the deflection of the scattered pion from the incident pion direction, and the azimuthal angle ϕ, the orientation of the scattering plane relative to a fixed plane. Figure III.9 shows the distributions of these quantities for elastic events at 850 MeV/c. As in all bubble chamber experiments of this sort, there is a depletion of events in two regions. Events with $\cos\theta$ close to 1.0 are those where the pion scatters through a small angle. Such events are difficult to see and measure, since the pion direction changes only slightly, and the proton track is short. There is therefore a marked loss of events in this region.

In an experiment such as ours, with an unpolarised beam and target, the distribution in ϕ should be flat. Reactions whose scattering plane is approximately perpendicular to the plane of the bubble chamber cameras are however sometimes missed and are difficult to measure, because the outgoing tracks are overlaid, and the deflection of the beam track is again difficult to see. This is clearly seen on the ϕ plot. The plot has been folded so that all ϕ values lie between 0 and $\frac{\pi}{2}$, so only one depletion region is seen (the scale is marked in fractions of π from 0 to 0.5).

The standard procedure for correcting for these losses was applied at all four energies. The data was divided into

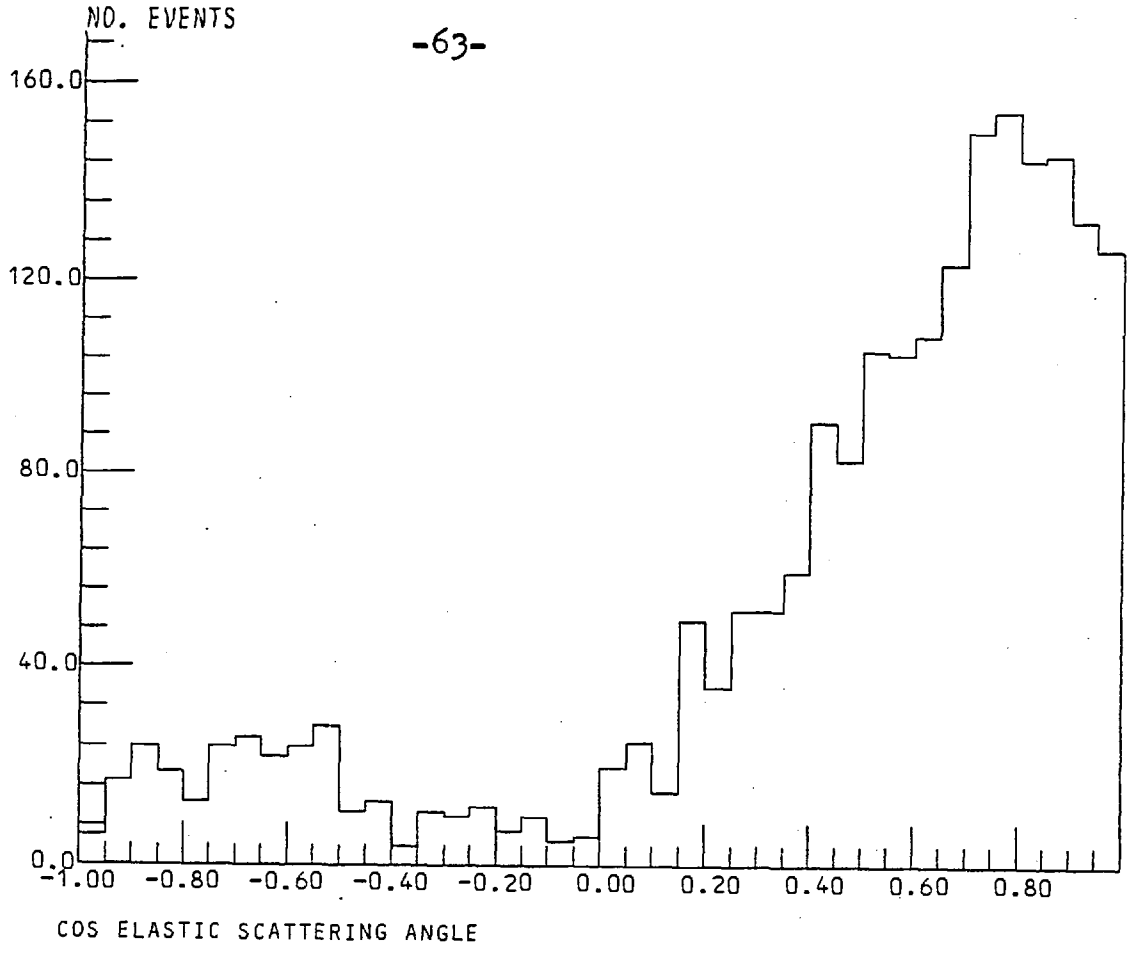

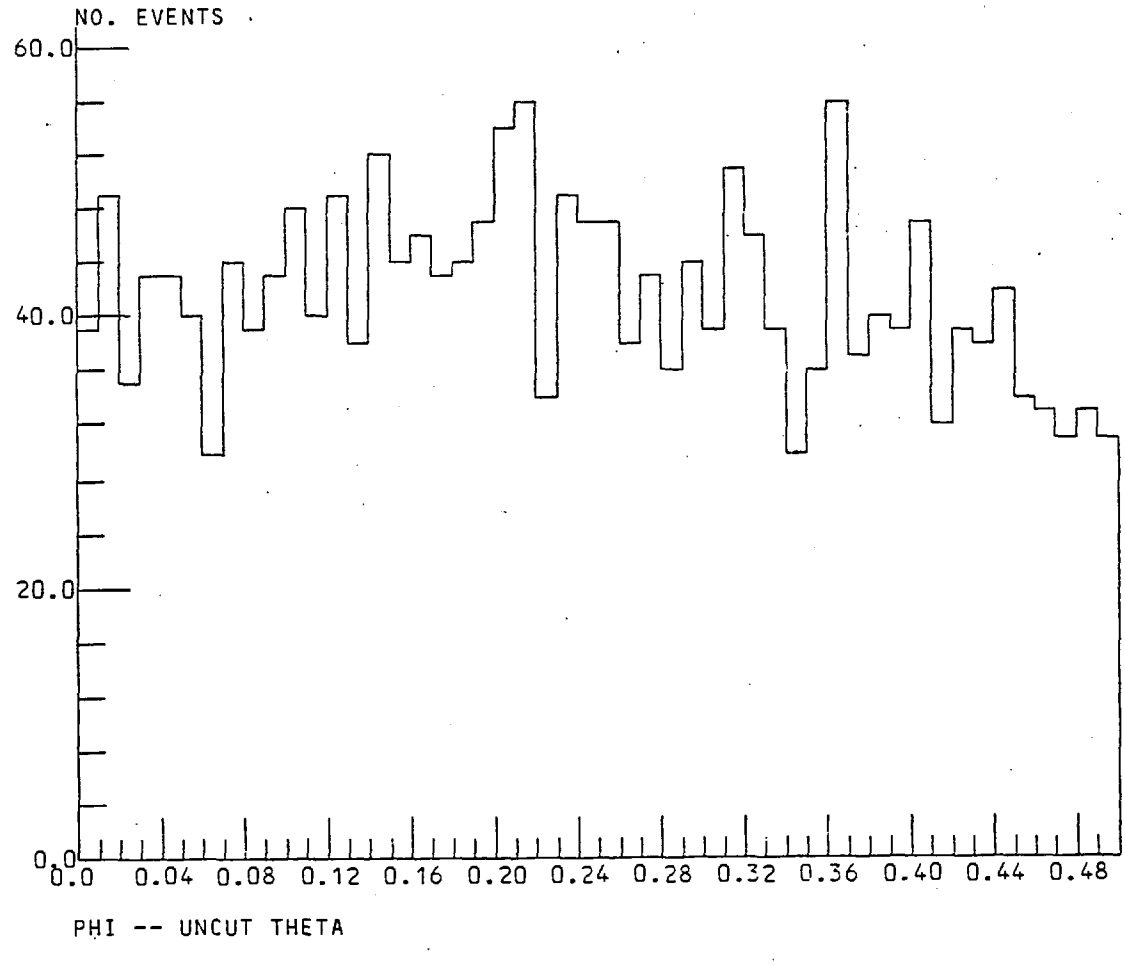

Figure III.9 Elastic θ and ϕ distributions

40 cosθ bins, and fitted by a Legendre polynomial series of the form -

$$\sum_{n=0}^{N_{max}} B_n P_n(\cos\theta) \qquad 3.5$$

by minimising the chi-squared

$$\chi^2 = \sum_{i=1}^{\text{no. of bins}} \left(\frac{N_f^i - N_e^i}{\Delta N_e^i} \right)^2$$

where N_e^i = experimental number of events in bin i

N_f^i = number of events in bin i predicted by fit

ΔN_e^i = error on N_e^i . Poisson statistics are assumed giving $\Delta N_e^i = \sqrt{N_e^i}$

The number of bins fitted was not 40; the purpose of the fit was to correct for forward losses, so the bins affected by the losses were not used in the fit. Cuts on ϕ were also imposed, Table III.2 gives the values of the cuts on the folded ϕ and on $\cos\theta$. The order of fit was chosen such that the Fischer ratio

$$F = \frac{\chi_n^2 - \chi_{n-1}^2}{\chi_n^2/\text{N.D.F.}}$$

became small, and the chi-squared per number of degrees of freedom (χ^2/N.D.F.) did not become smaller when the order n was increased by 1. The fit order used at each energy is also given in Table III.2 together with the χ^2 and N.D.F. The number of terms used in the Legendre series is one greater than the order because the first term is the zero order term.

The fitted series was then integrated over the whole $\cos\theta$ range to correct for the forward losses, and scaled up to the whole ϕ range to give a corrected total number of

Momentum (MeV/c)	785	833	1140	1246
Cos θ range used	-1. to .85	-1. to .80	-1. to .95	-1. to .95
ϕ range used	0. to .42π	0. to .44π	0. to .42π	0. to .42π
χ^2	33.9	55.8	38.1	34.0
N.D.F.	30	29	32	32
Order of fit	5	6	6	6

Table III.2

Cuts and elastic fit parameters

elastic events. The corrected numbers are given in Table III.1.

III.4.2 Elastic results

The fitted series 3.5 was used to provide plots and tables of differential cross-sections. Figures III.10.a to III.10.d show the fitted differential cross-sections at the four momenta, together with the data points used. Table III.3 gives the experimental differential cross-section values used at the four momenta, and the extrapolated forward and backward values. $\sqrt{N}$ errors are also given.

The Legendre polynomial series 3.5 can also be rewritten

$$\frac{d\sigma}{d\Omega} = \frac{1}{q^2} \sum_{n=0}^{N_{max}} A_n P_n (\cos\theta) \qquad 3.6$$

where q is the incident pion momentum in the centre of mass system. The Legendre coefficients A_i, and A_i/A_o are given in Table III.4. A_i/A_o are plotted in Figure III.11, which is Figure 3.5 of reference 9 with the new points added. Plots and tables of the differential cross-sections and Legendre coefficients at the other energies of this experiment can be found in the previous theses (refs. 1, 9, 11), some have also been published (refs. 3 and 11).

Tripp (ref. 28) gives coefficients for the partial waves contributing to each Legendre coefficient. As several waves contribute to each coefficient, a full partial wave analysis is needed to analyse them properly, but a few general observations can be made, particularly on the higher coefficients which contain no contributions from the lowest

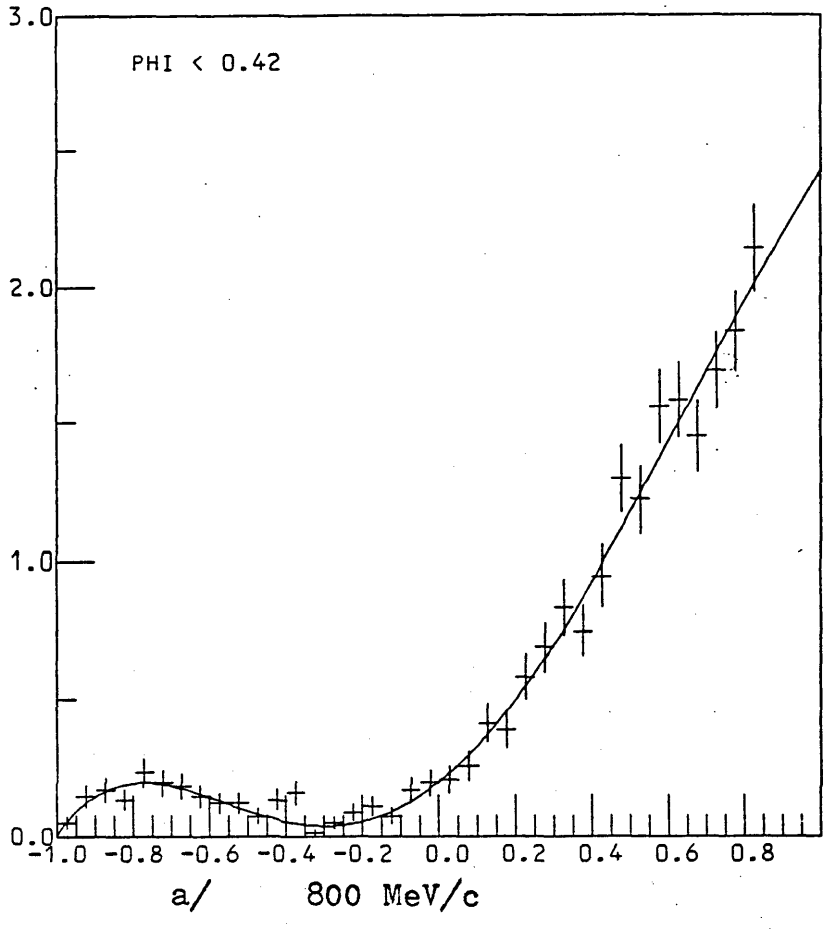

a/ 800 MeV/c

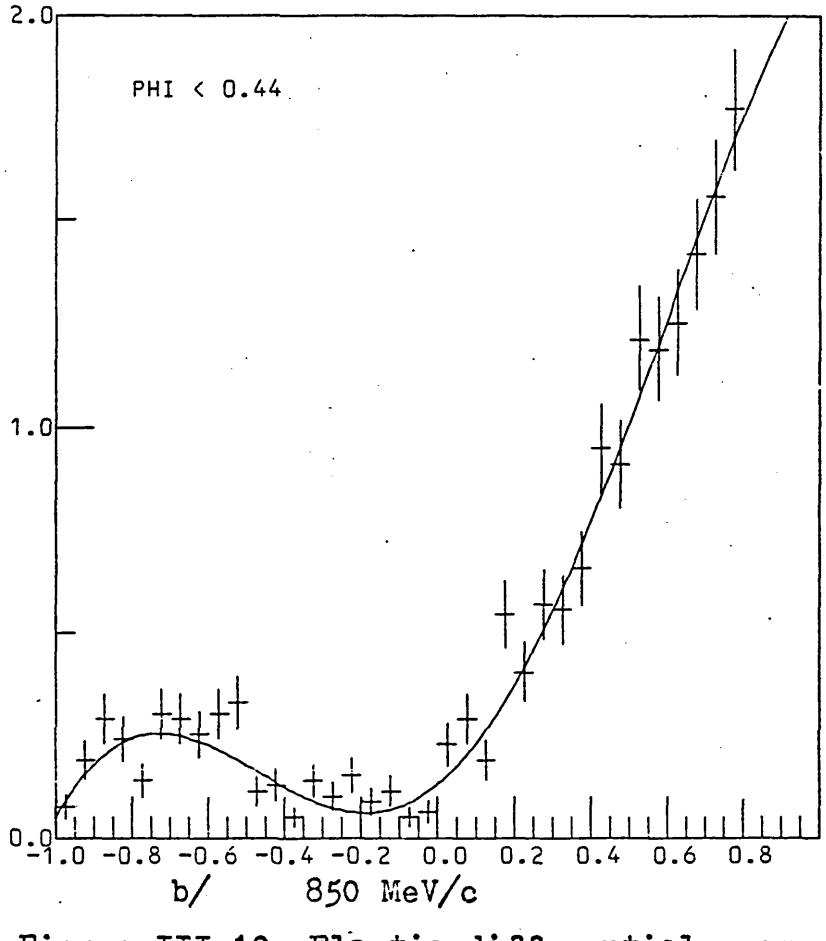

b/ 850 MeV/c

Figure III.10 Elastic differential cross-sections

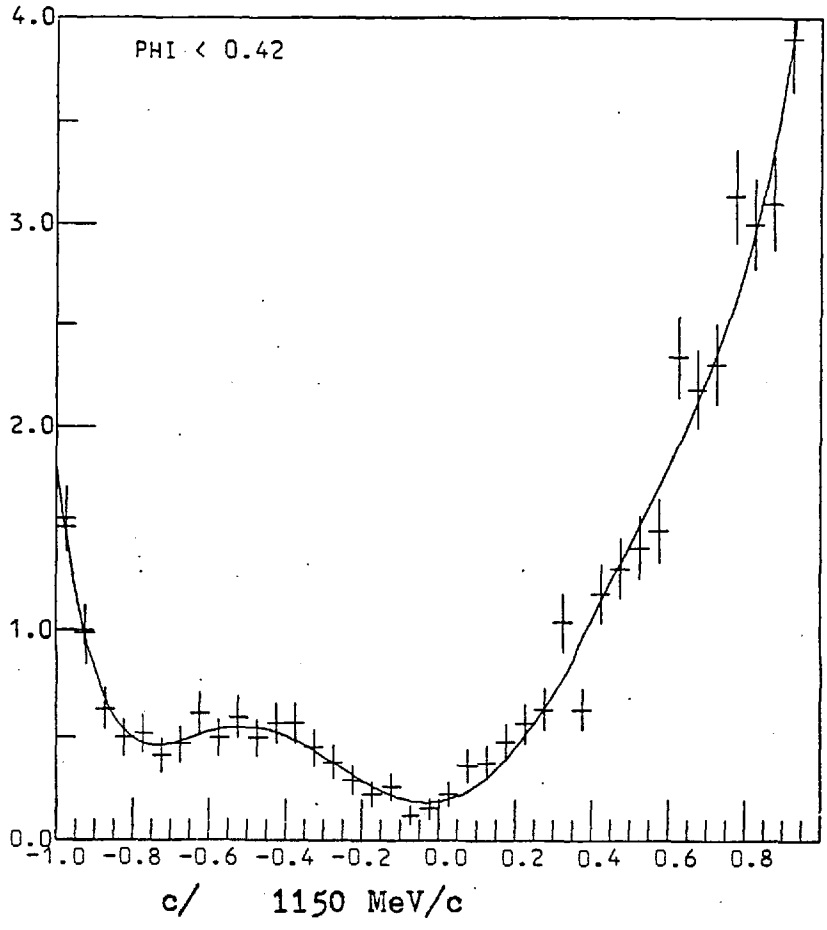

c/ 1150 MeV/c

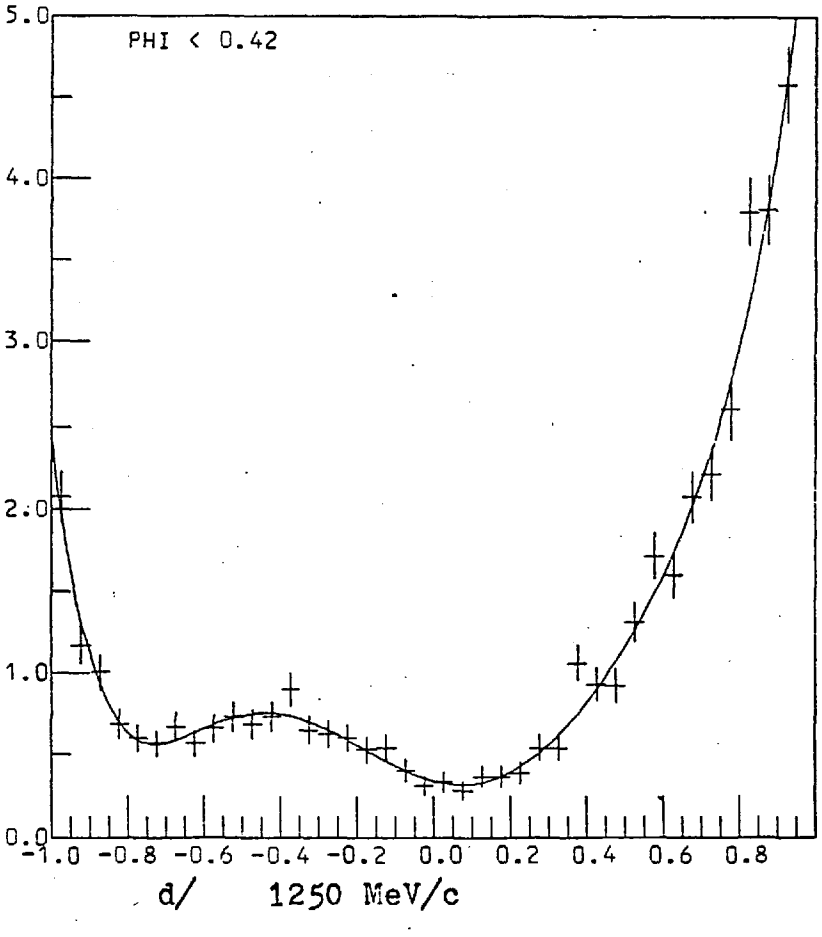

d/ 1250 MeV/c

Figure III.10 contd.

cos θ	785	833	1140	1246
-1.0	0.006±.009*	0.049±.025*	1.803±.177*	2.422±.169*
-.975	0.051±.025	0.076±.031	1.542±.163	2.073±.157
-.925	0.139±.042	0.190±.049	0.988±.131	1.173±.118
-.875	0.177±.047	0.291±.061	0.641±.105	1.007±.109
-.825	0.139±.042	0.240±.055	0.503±.093	0.687±.090
-.775	0.241±.055	0.139±.042	0.520±.095	0.604±.085
-.725	0.190±.049	0.303±.062	0.416±.085	0.569±.082
-.675	0.190±.049	0.291±.061	0.468±.090	0.675±.089
-.625	0.139±.042	0.253±.057	0.624±.104	0.569±.082
-.575	0.114±.038	0.303±.062	0.503±.093	0.663±.089
-.525	0.127±.040	0.329±.064	0.606±.103	0.735±.093
-.475	0.063±.028	0.114±.038	0.503±.093	0.687±.090
-.425	0.127±.040	0.126±.040	0.572±.100	0.735±.093
-.375	0.165±.046	0.051±.025	0.572±.100	0.900±.103
-.325	0.013±.013	0.139±.042	0.451±.088	0.652±.088
-.275	0.051±.025	0.101±.036	0.381±.081	0.628±.086
-.225	0.089±.034	0.152±.044	0.295±.071	0.604±.085
-.175	0.101±.036	0.089±.033	0.225±.062	0.533±.079
-.125	0.076±.031	0.114±.038	0.200±.067	0.545±.080
-.075	0.165±.046	0.051±.025	0.121±.046	0.403±.069
-.025	0.203±.051	0.063±.028	0.156±.052	0.308±.060
.025	0.190±.049	0.228±.054	0.225±.062	0.332±.063
.075	0.266±.058	0.291±.061	0.364±.079	0.284±.058
.125	0.418±.073	0.190±.049	0.381±.081	0.367±.066
.175	0.393±.071	0.544±.083	0.485±.092	0.367±.066
.225	0.570±.085	0.405±.072	0.572±.100	0.391±.068
.275	0.697±.094	0.569±.085	0.641±.105	0.545±.080
.325	0.836±.103	0.556±.084	1.040±.134	0.545±.080
.375	0.747±.097	0.658±.091	0.641±.105	1.066±.112
.425	0.887±.106	0.948±.110	1.178±.142	0.936±.105
.475	1.241±.125	0.910±.107	1.300±.150	0.924±.105
.525	1.241±.125	1.214±.124	1.404±.156	1.315±.125
.575	1.507±.138	1.189±.123	1.490±.161	1.718±.142
.625	1.558±.140	1.252±.126	2.339±.201	1.599±.138
.675	1.419±.134	1.416±.134	2.183±.195	2.073±.157
.725	1.723±.148	1.555±.140	2.305±.200	2.215±.162
.775	1.824±.152	1.770±.150	3.136±.233	2.595±.175
.825	2.141±.165	1.815±.151*	2.998±.228	3.803±.212
.875	2.174±.166*	1.923±.156*	3.102±.232	3.815±.213
.925	2.320±.171*	2.023±.160*	3.899±.260	4.585±.233
.975	2.471±.177*	2.115±.164*	4.617±.283*	5.645±.259*
1.0	2.547±.180*	2.158±.165*	5.047±.296*	6.229±.272*

* Extrapolated from polynomial fit

Table III.3 Differential cross-sections in the c.m.s.

Beam momentum MeV/c	785	833	1140	1246
Coefficient				
A_o	0.669±.025	0.607±.071	1.101±.027	1.239±.022
A_1	1.121±.065	0.938±.196	1.311±.062	1.268±.052
A_1/A_o	1.674±.097	1.546±.322	1.191±.056	1.023±.042
A_2	0.768±.094	0.740±.278	1.670±.085	1.983±.074
A_2/A_o	1.148±.141	1.219±.458	1.516±.078	1.600±.060
A_3	0.044±.103	0.111±.312	0.466±.105	0.898±.088
A_3/A_o	0.066±.154	0.183±.513	0.423±.095	0.725±.071
A_4	-0.220±.087	-0.262±.277	0.186±.119	0.633±.097
A_4/A_o	-0.329±.130	-0.432±.456	0.169±.108	0.511±.078
A_5	0.048±.052	0.005±.200	-0.156±.106	-0.262±.086
A_5/A_o	0.071±.078	0.009±.330	-0.142±.096	-0.212±.069
A_6		0.019±.108	0.468±.097	0.471±.083
A_6/A_o		0.031±.179	0.425±.088	0.380±.067

Table III.4

Elastic fit Legendre coefficients

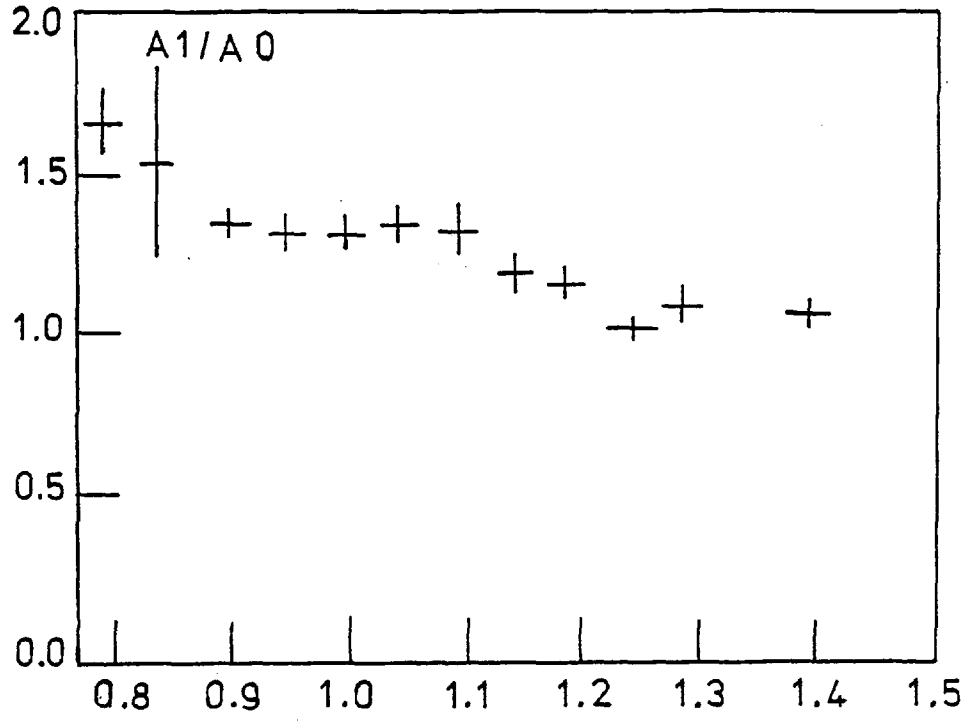

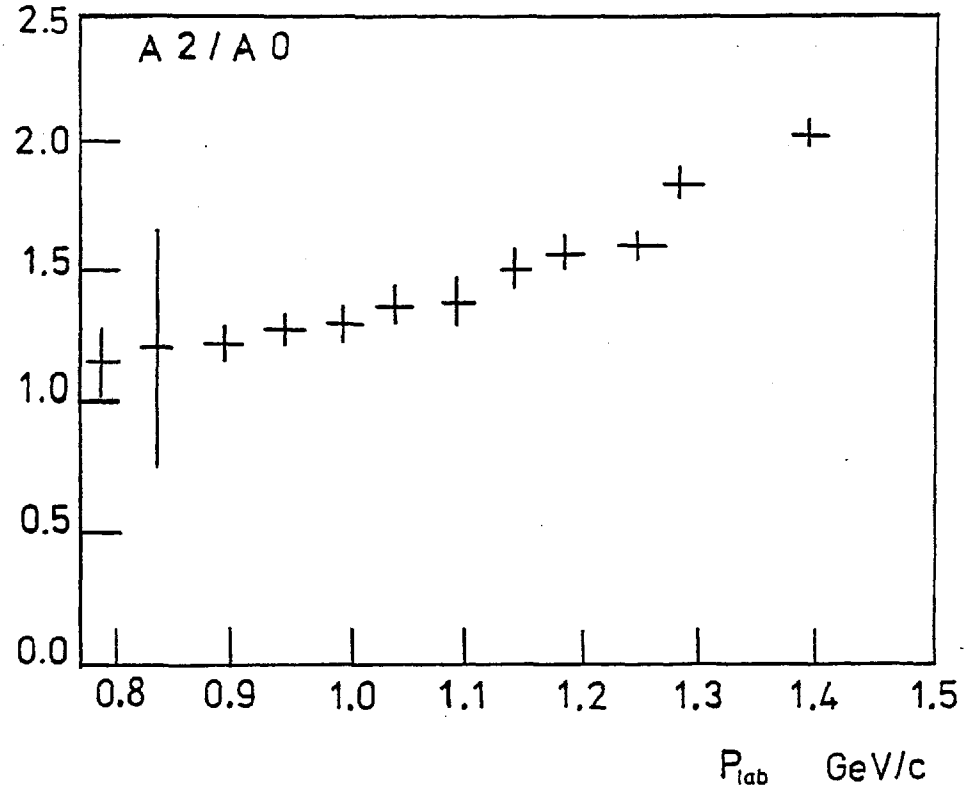

Figure III.11 Elastic fit Legendre coefficients

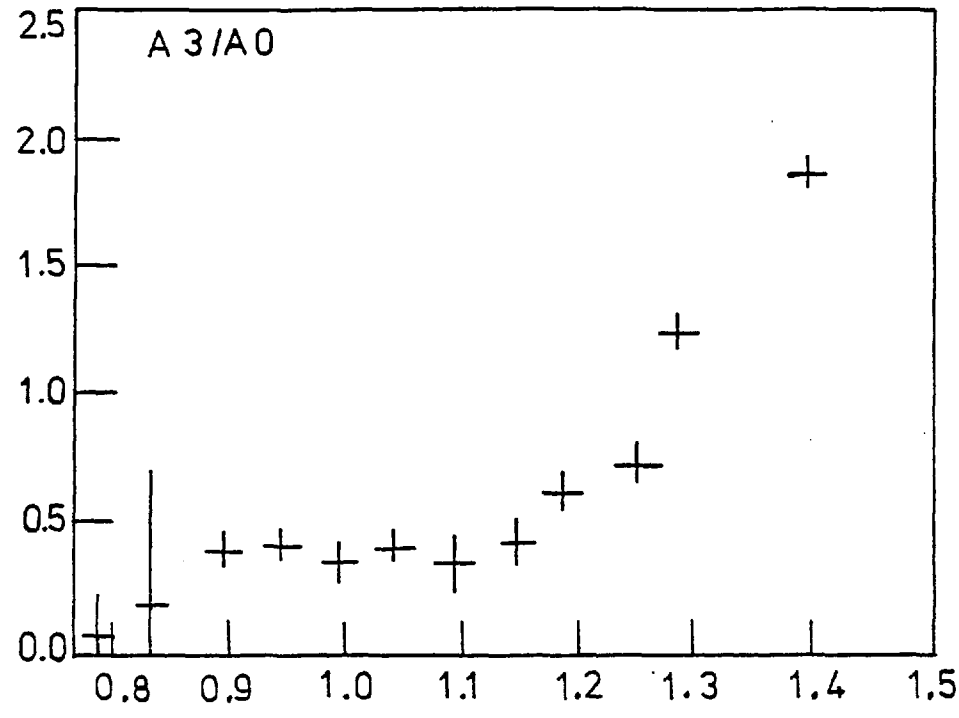

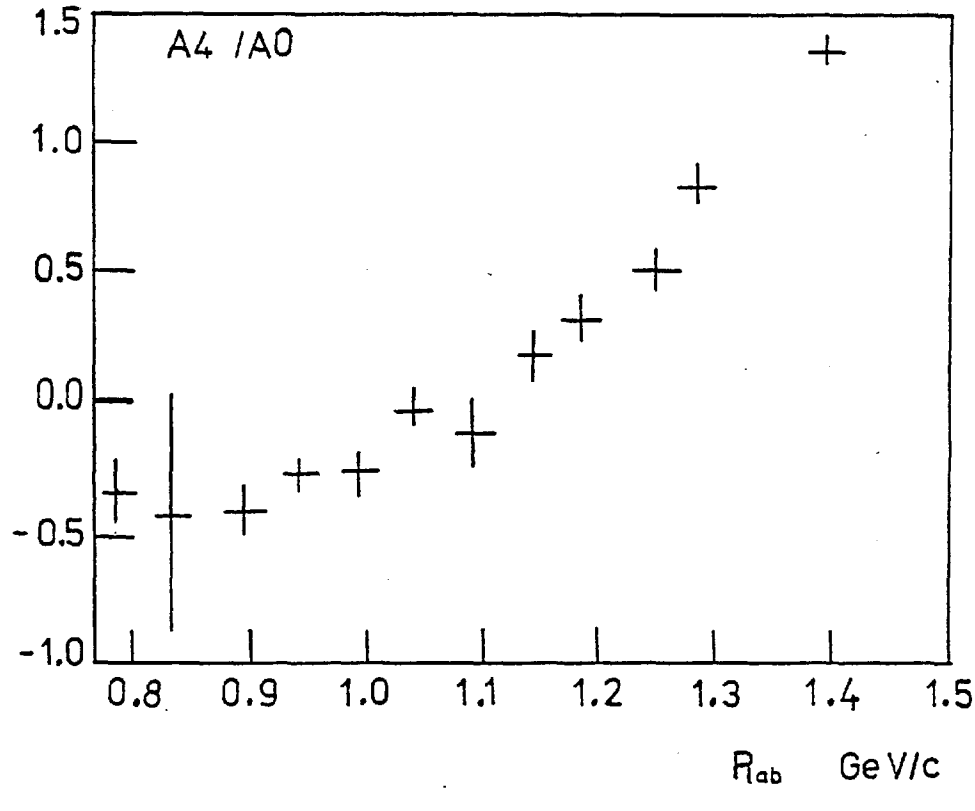

Figure III.11 contd.

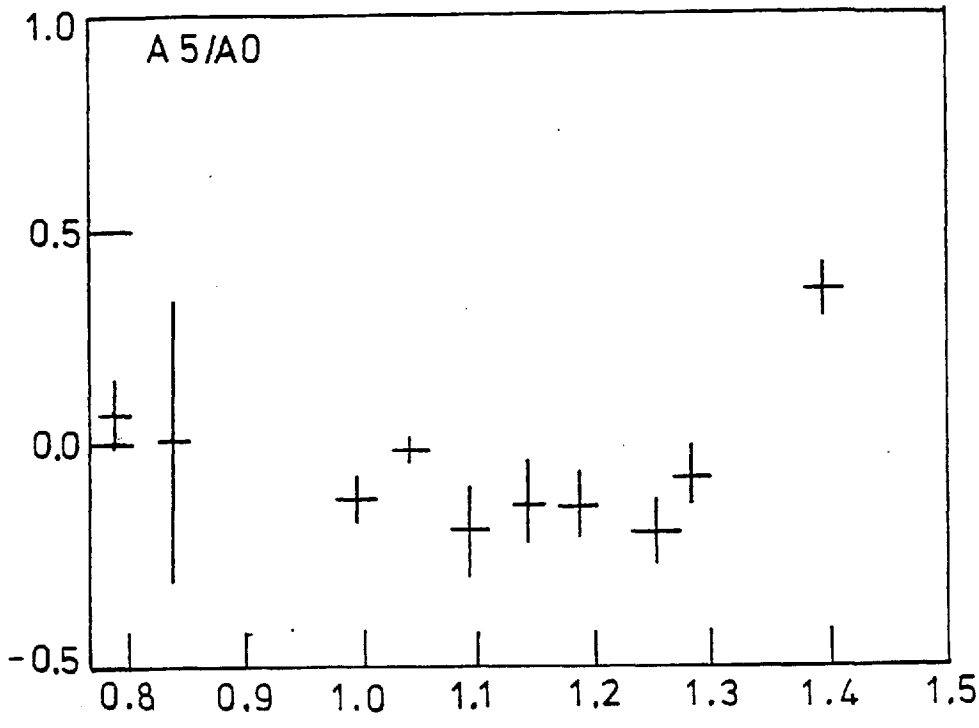

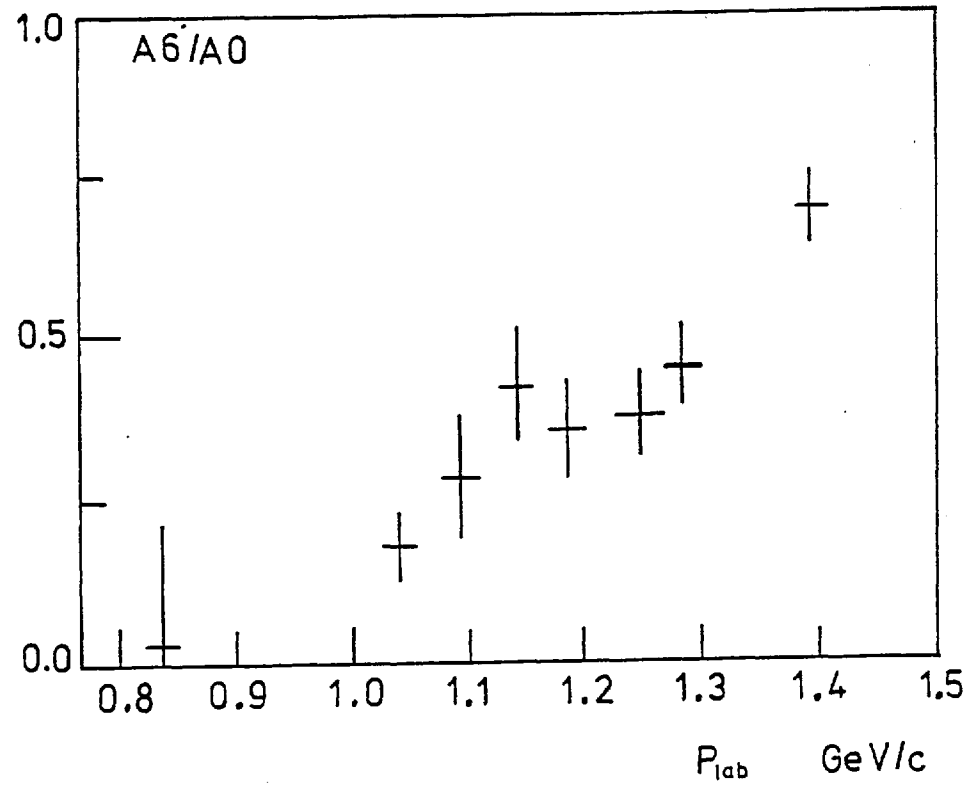

Figure III.11 contd.

waves. In the first place, the coefficients at the four new momenta are compatible with those previously determined. More coefficients were required at 800 and 850 MeV/c than at 895 and 945 MeV/c - this is somewhat surprising, there is no obvious explanation but it may be connected with the film problems or the worse statistics at the lower momenta. The larger errors on the 850 MeV/c coefficients support this suggestion.

As the highest order coefficients are the simplest, we consider them in decreasing order. The fact that A_7 and higher coefficients are unnecessary implies the absence of waves higher than $L_{2J} = F_7$. The rise in A_6 is then presumably due to the increasing importance of F_7, corresponding to the four-star ΔF37(1950) resonance; the F_5F_7 interference will also be rising at the upper momenta, approaching the ΔF35(1890) resonance. The negative values of A_5 at the lower momenta would come from the D_5F_5 interference term, and the change in sign at the highest momentum is most likely due to increasing D_3F_7 and D_5F_7 terms. The rise in A_4 at the upper momenta is most likely due to the increasing F_5 contribution, and the significantly negative A_4 values near 900 MeV/c are most likely due to a D_3D_5 contribution. A_3 starts off near zero, and the plateau between 900 and 1100 MeV/c can contain significant contributions from P_3D_5, D_3F_5, P_3D_3, S_1F_5 and P_1D_5 terms. These terms can only be unravelled by a partial wave analysis, but it is interesting to note that several terms involving D_5 are important near 900 MeV/c. 900 MeV/c corresponds to rather a low energy for the D_5 wave, but it will be shown in the inelastic analysis that this wave

contributes singificantly at 895 MeV/c and 945 MeV/c; these elastic A_3, A_4 and A_5 results give independent support to that claim. The rapid rise in A_3 at the higher momenta can again be attributed to the interferences of other waves with increasing F_5 and F_7 contributions. A_2, A_1 and A_0 are singnificantly non-zero throughout the momentum range - one can say without examining all their contributions that this means several waves and their interferences are important. This discussion of the Legendre coefficients has been rather sketchy, but it is emphasised that only a partial wave analysis could extract reliable numerical results from the coefficients.

III.4.3 Backward elastic cross-sections

Figure III.12 shows a plot of the backward elastic differential cross-sections determined by this experiment, and the Oxford experiment (ref. 6). Our results, and those of other bubble chamber experiments have tended to disagree seriously with counter experiment results, as for example Rothschild et al (ref. 27) whose results are given in Figure III.12, particularly at lower momenta. The latest accurate counter experiment, that of the Bristol/RHEL/Southampton group showed figures with their preliminary results at the Oxford Conference (ref. 13). The backward results read off from the figures given in reference 13 are included in Figure III.12. These are not very accurate, because they are preliminary results, and because it was difficult to read them off from the figure (impossible between 700 and 800 MeV/c), but they are in better agreement with our results at the lower

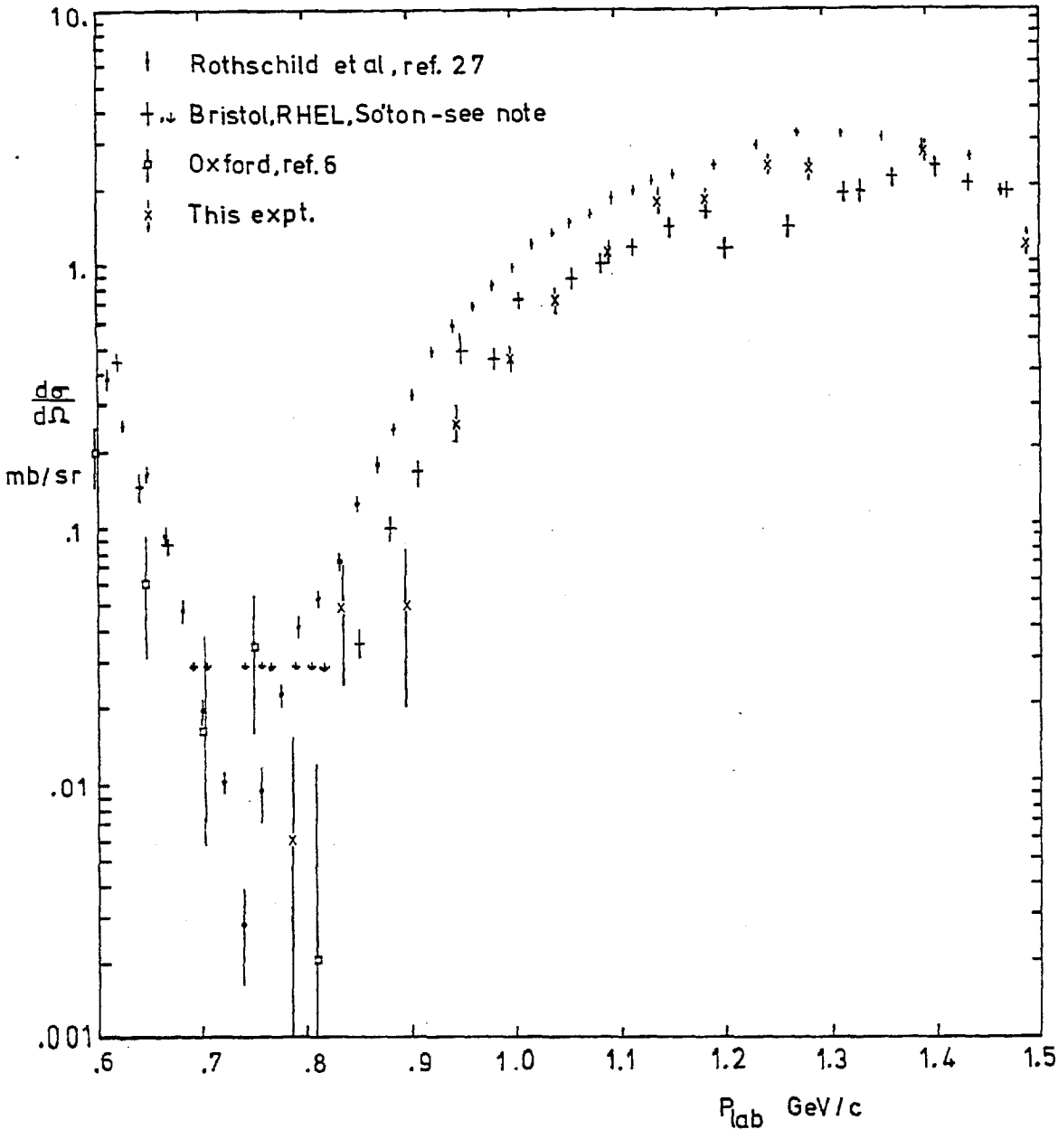

Note: the Bristol, RHEL, Southampton results shown here are preliminary values, taken from a figure published in the Oxford Conference Proceedings (ref. 13). As that figure did not show values below .03, these are indicated only by a downward arrow at .03.

Figure III.12

Backward elastic differential cross-sections

momenta, up to 1100 MeV/c. Unfortunately, the Bristol/RHEL/Southampton results above 1100 MeV/c are far lower than the Rothschild et al results. Our results at these momenta lie between those of the two counter experiments. It may of course be that the Bristol/RHEL/Southampton results above 1100 MeV/c will be revised upwards in their final publication.

Earlier work in our experiment showed no sign of losses in backward elastic events (ref. 1), and we continue to believe our results because serious differences between different counter experiments still exist unexplained.

III.5 Dalitz Plots

Figures III.13 to III.20 show Dalitz plots for $\pi^+p\pi^0$ and $\pi^+\pi^+n$ at our four momenta, together with their projections. Mass-squared of π^+p or π^+n is plotted along the x-axes, mass-squared of $\pi^+\pi^0$ or $\pi^+\pi^+$ is plotted along the y-axes. The phase-space area available increases rapidly with momentum. The $\Delta(1230)$ is seen on all x-axis projections, and its reflection is also seen, particularly on the π^+n projections, at the two higher momenta. The ρ meson is seen on the y-axis projections of the $\pi^+p\pi^0$ plots at the two higher momenta.

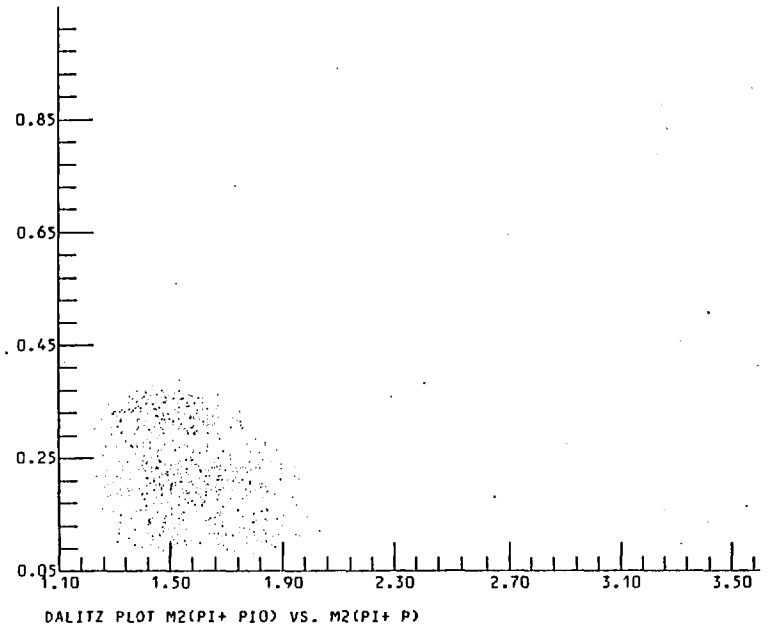

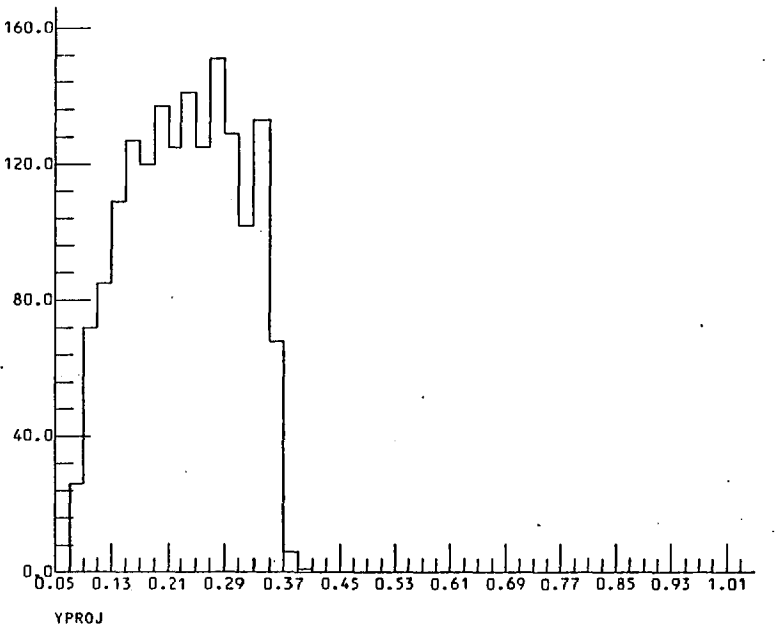

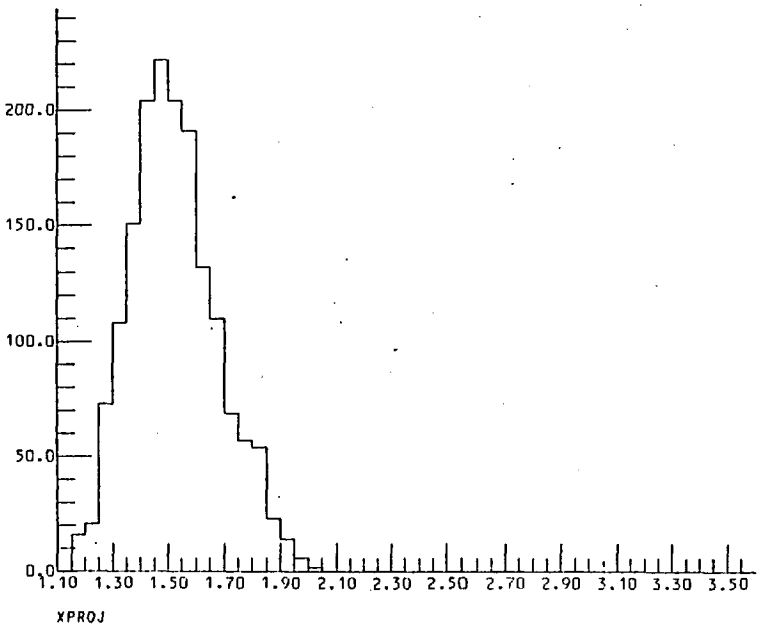

Figure III.13 $\pi^+ p \pi^o$ Dalitz plot and projections at 800 MeV/c

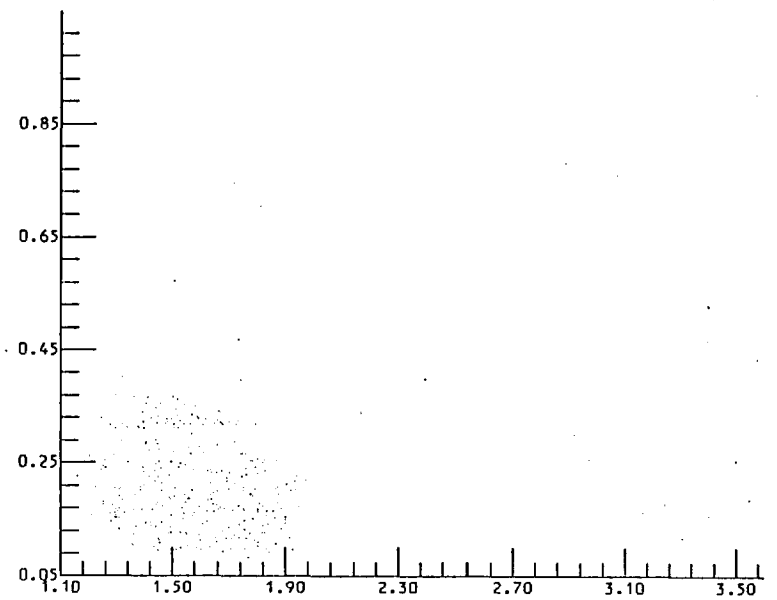

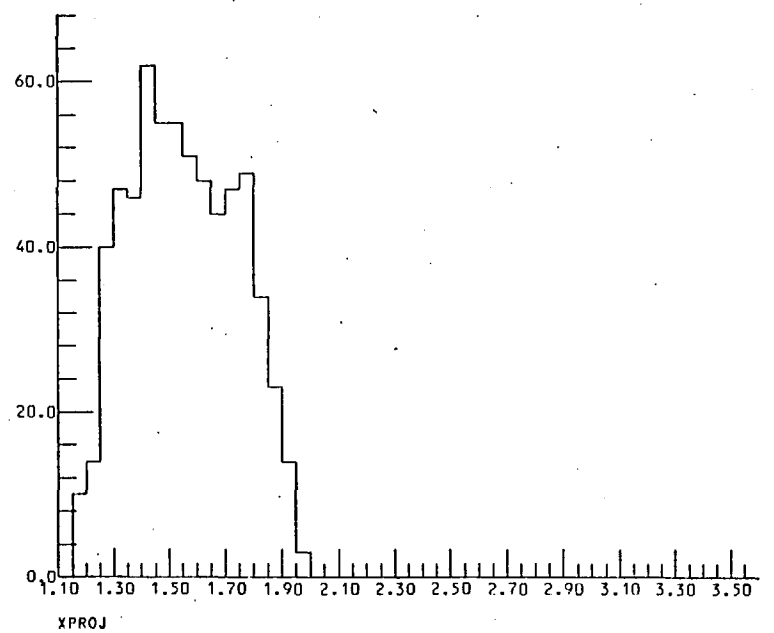

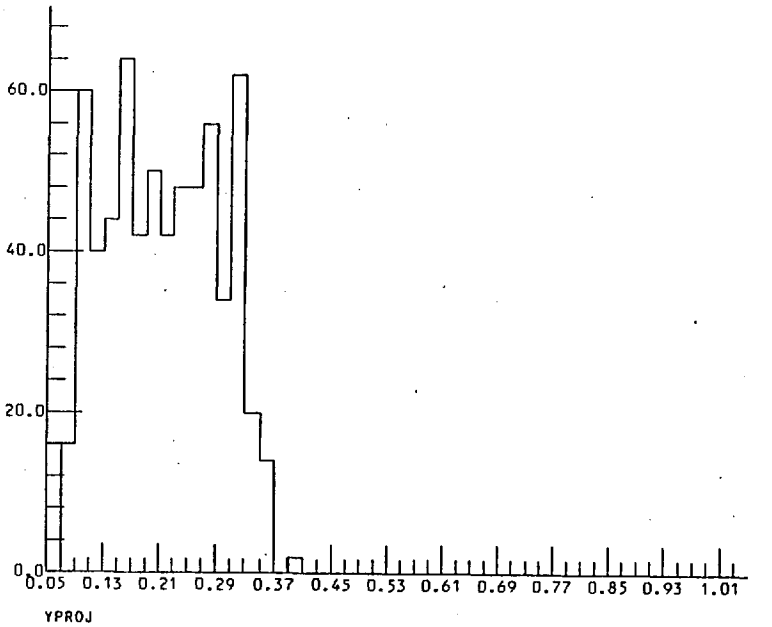

Figure III.14 $\pi^+\pi^+n$ Dalitz plot and projections at 800 MeV/c

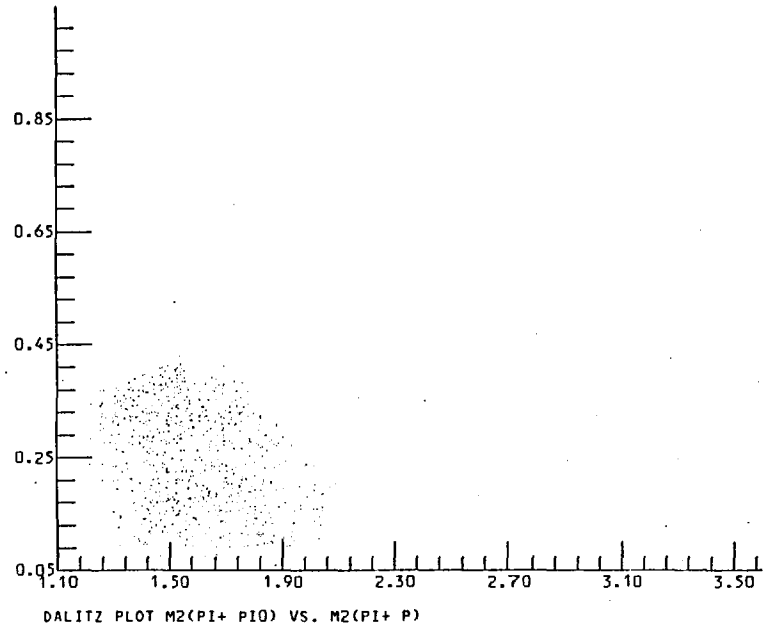

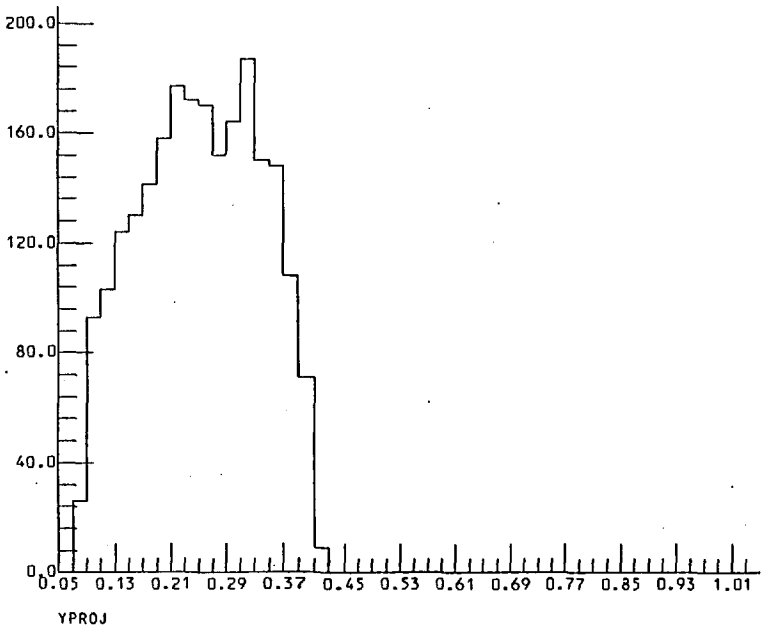

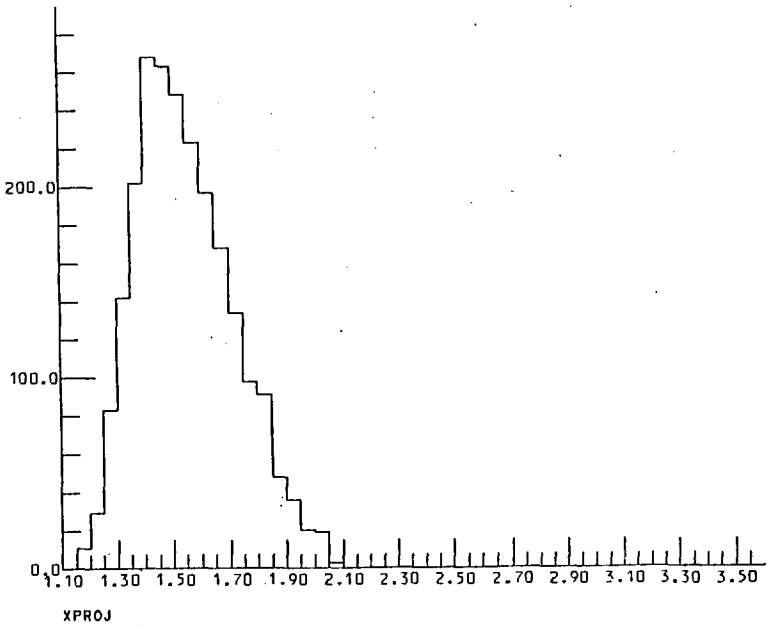

Figure III.15 $\pi^+ p \pi^o$ Dalitz plot and projections at 850 MeV/c

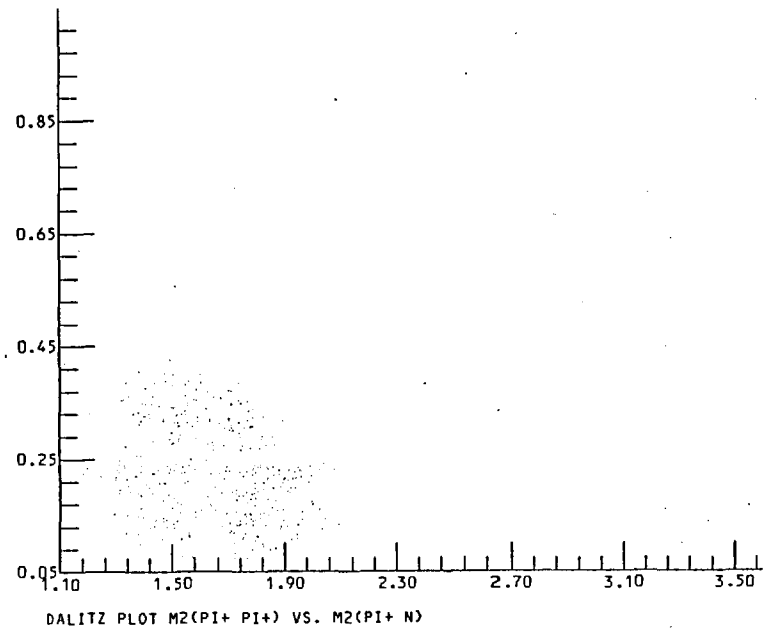

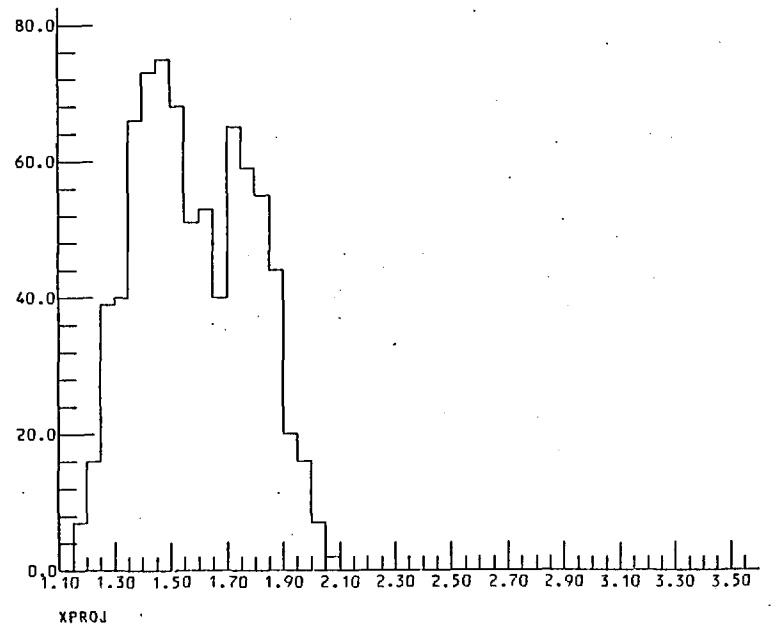

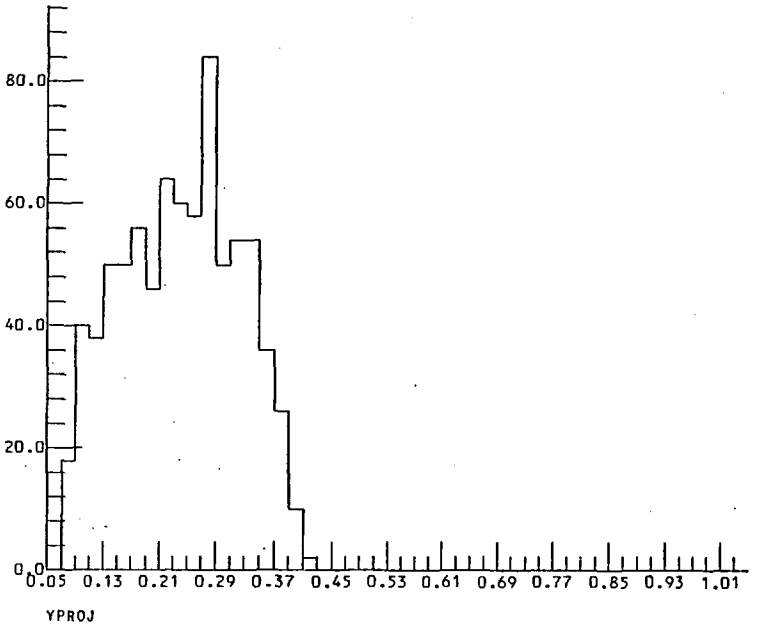

Figure III.16 $\pi^+\pi^+n$ Dalitz plot and projections at 850 MeV/c

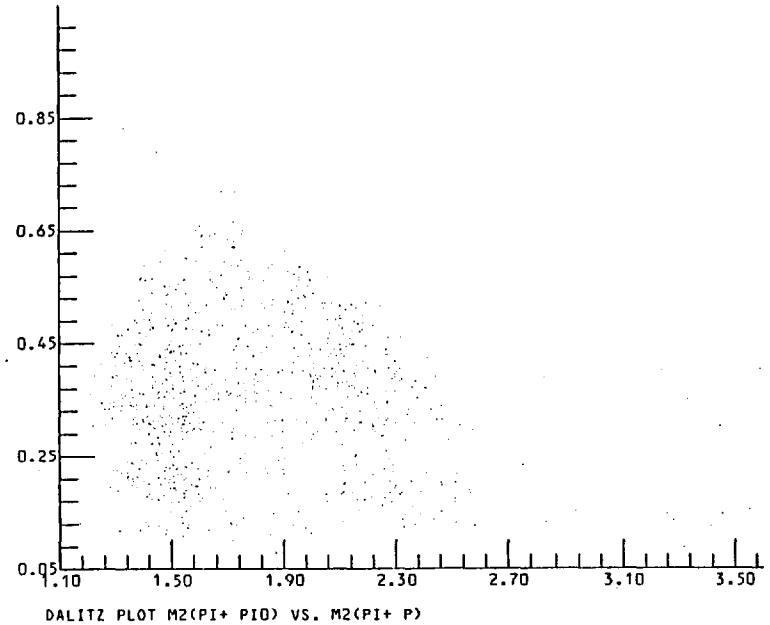

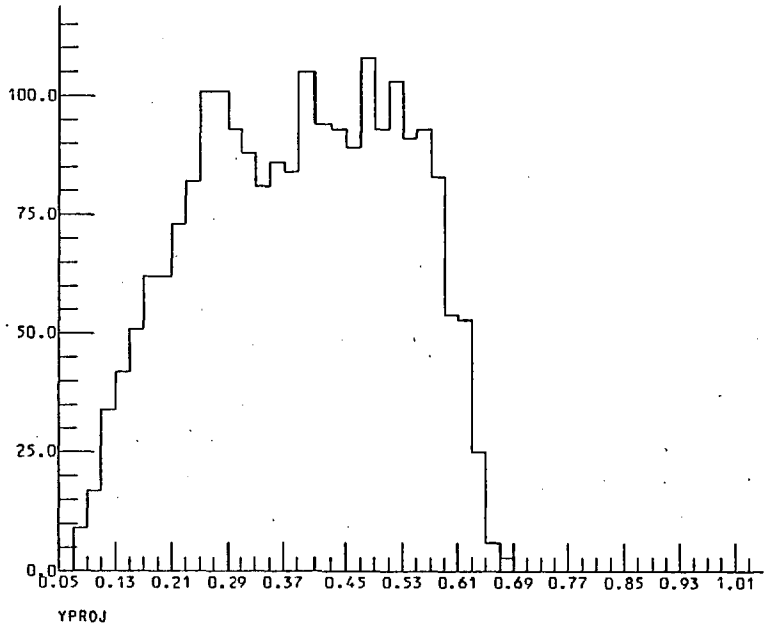

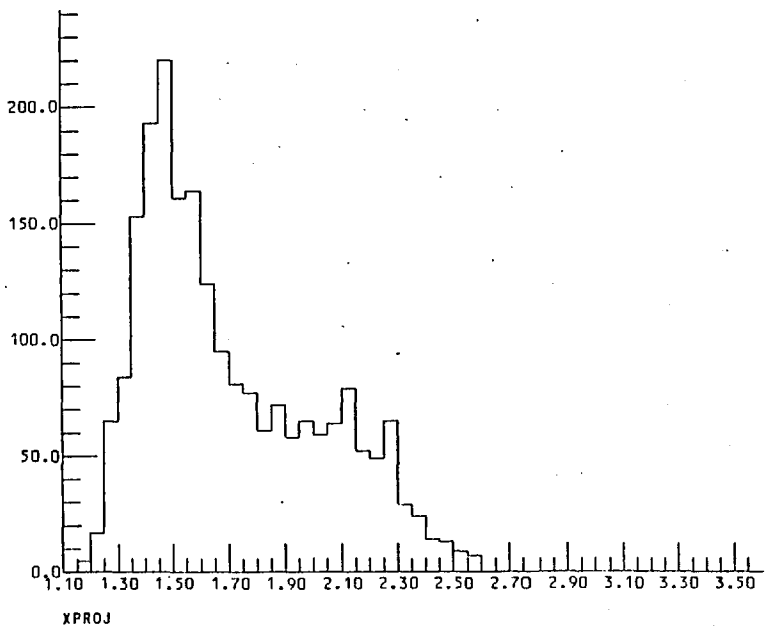

Figure III.17 $\pi^+ p \pi^0$ Dalitz plot and projections at 1150 MeV/c

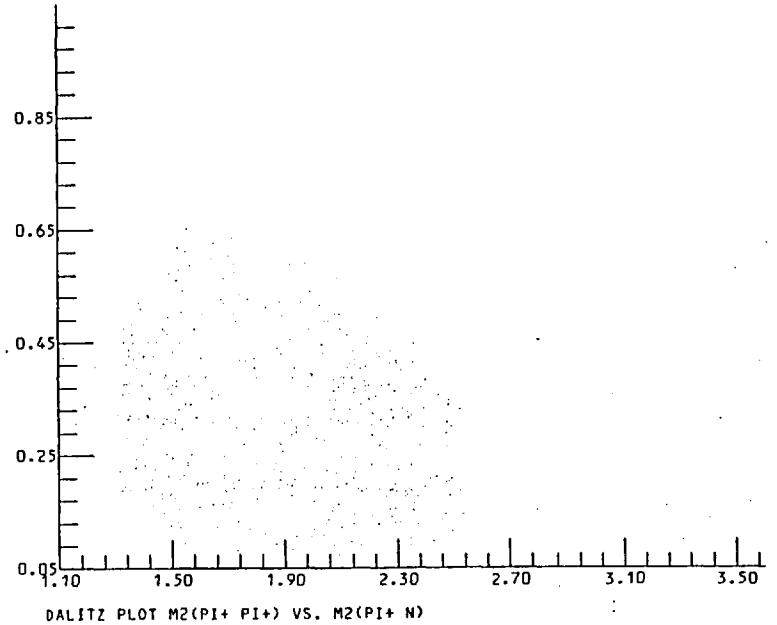

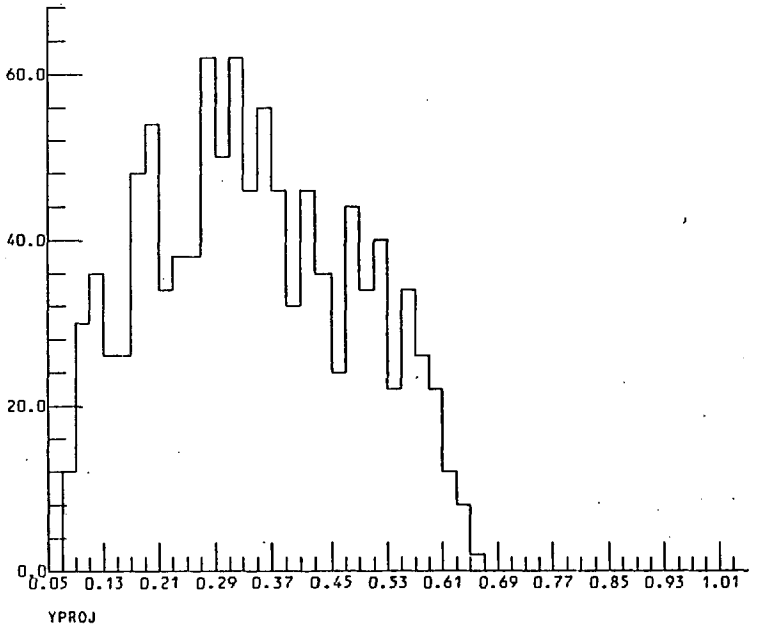

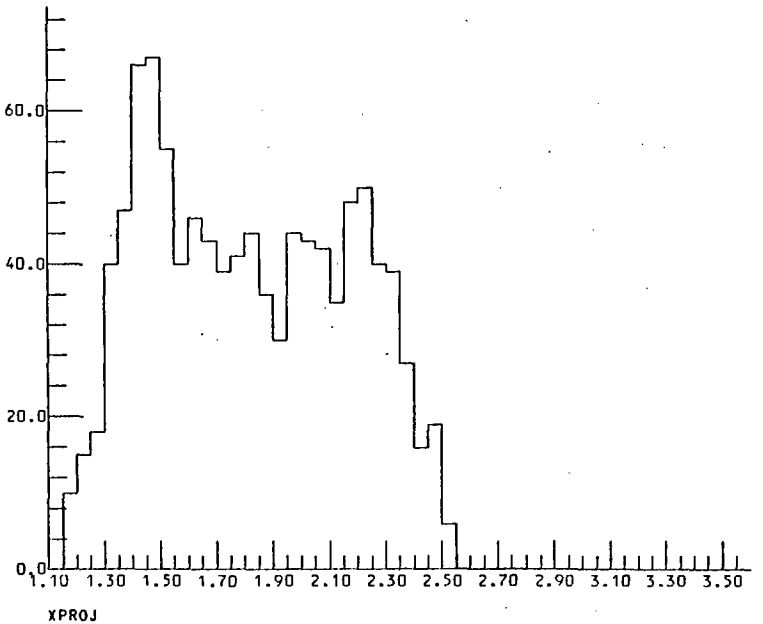

Figure III.18 $\pi^+\pi^+n$ Dalitz plot and projections at 1150 MeV/c

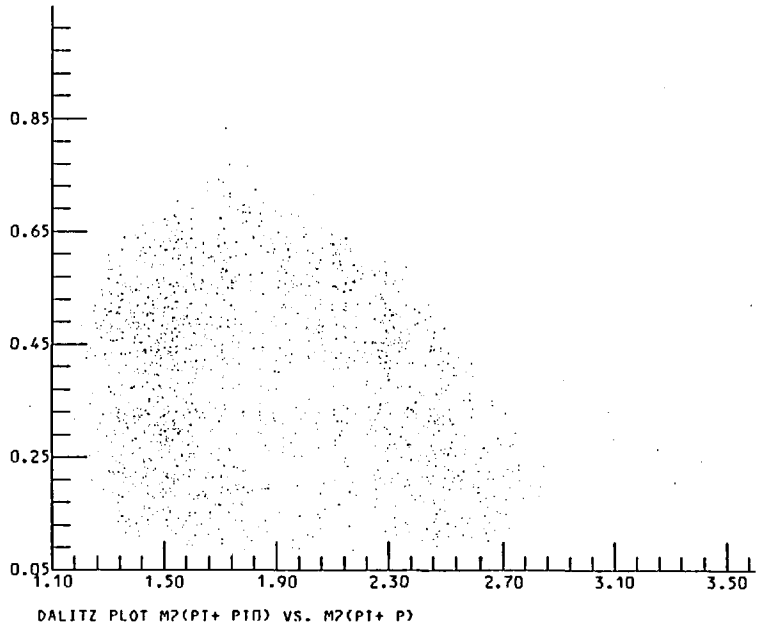

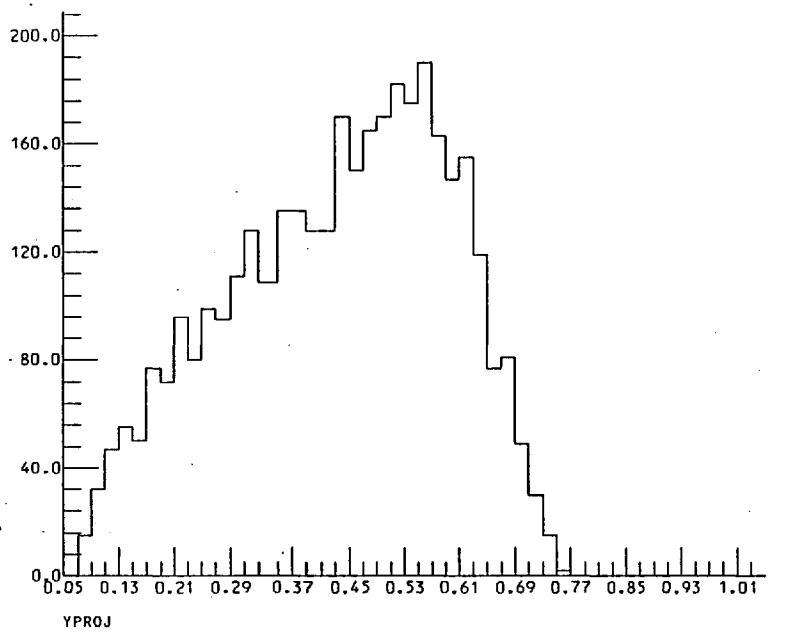

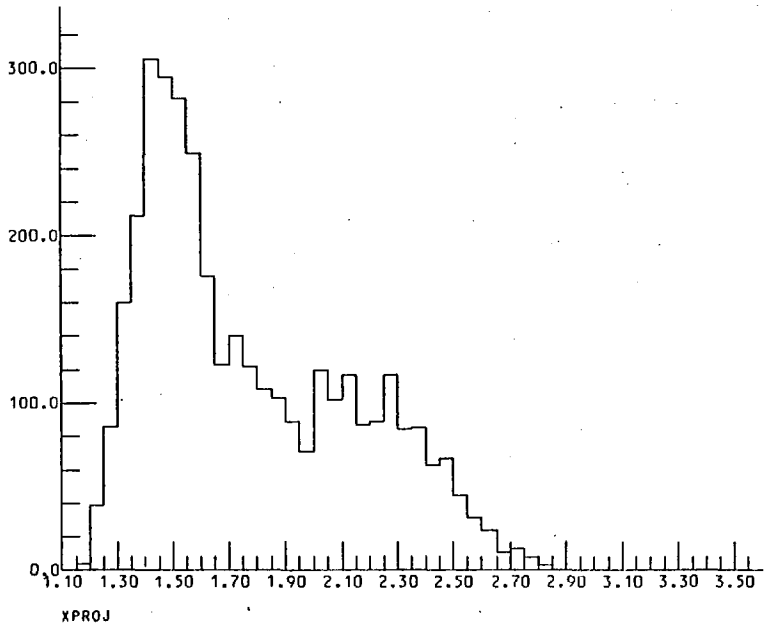

Figure III.19 $\pi^+ p \pi^0$ Dalitz plot and projections at 1250 MeV/c

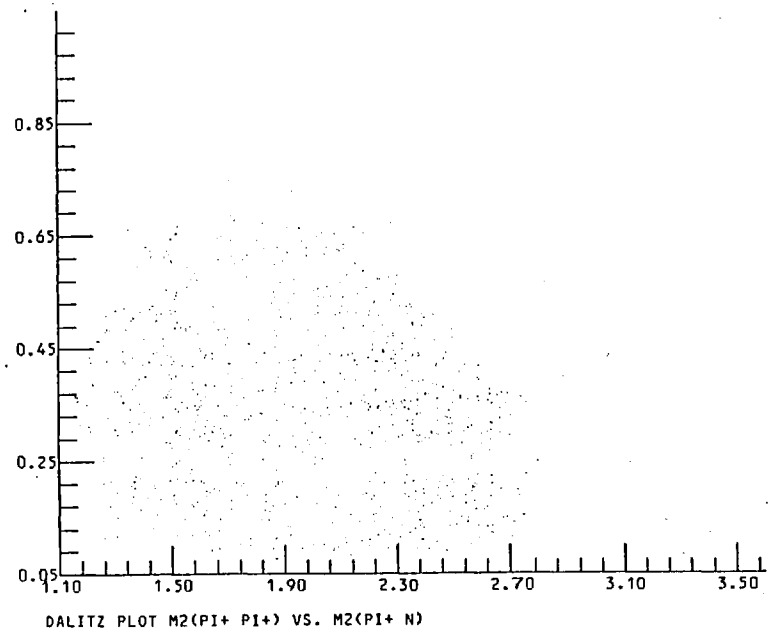

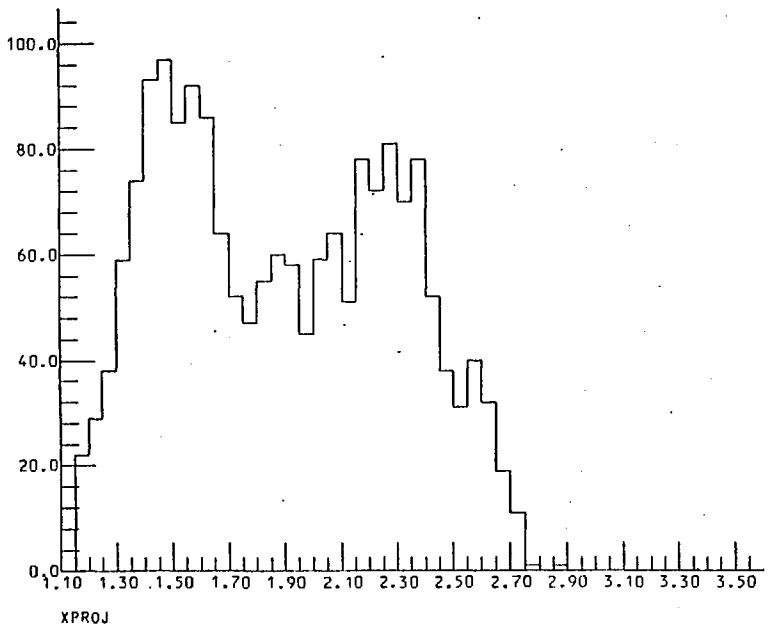

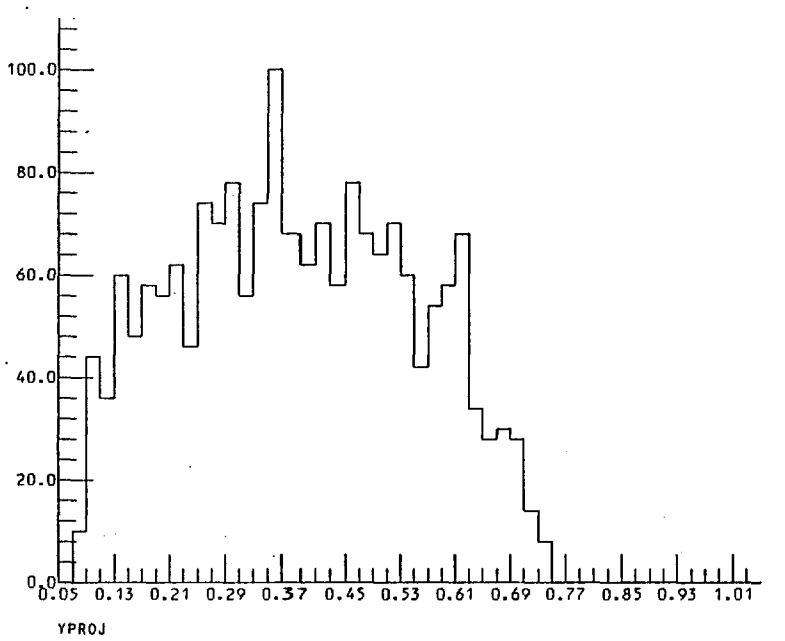

Figure III.20 $\pi^+\pi^+n$ Dalitz plot and projections at 1250 MeV/c

Chapter IV 4-Variable Fitting Formalism

IV.1 Introduction

We wish to use our $\pi^+ p \pi^0$ and $\pi^+\pi^+ n$ data to obtain T-matrix elements describing the transition from the initial $\pi^+ p$ state to these final states. Each event needs 6 kinematic variables to describe it. However when the target is unpolarised, and the data is split up into bins of approximately constant total energy, this is reduced to 4 variables per event.

Our 4-variable fitting program was written by Rob Stevens, and in his thesis (ref. 9) he described the formalism used. The author's contribution has been in rechecking that program, adding more waves to the fitting, extending the fits from 4 to 9 energies, and adding calculations of one-pion-exchange contributions to the fits. The O. P. E. work and its results are described in Chapter VII, the programs, their running, and the results without O. P. E. are described in Chapters V and VI. This chapter gives a recapitulation of the formalism more fully described by Rob Stevens, and contains an example of the formulae used: the FF7 wave which the author added to the analysis.

Further details, and comparisons between our formalism and others are given in Andy White's thesis, reference 10.

IV.2 $\pi\pi N$ Formalism

IV.2.1 The Isobar Model

The analysis of a 2-body to 3-body reaction:

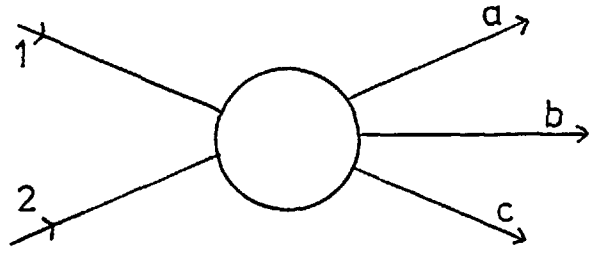

can be considerably simplified if 2 of the 3 final state particles are assumed to produce a resonance which subsequently decays:

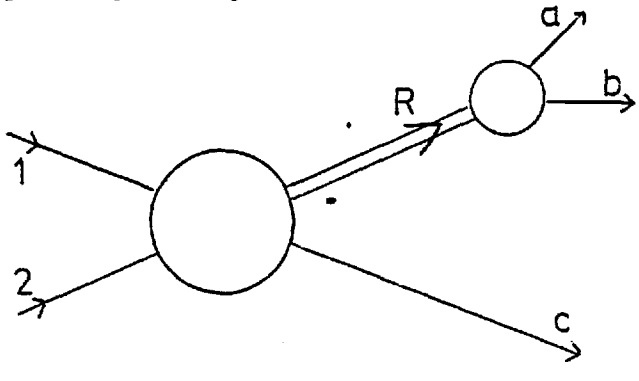

This was first proposed by Lindebaum and Sternheimer (ref. 29). It had been seen from Dalitz plots that final states with a diparticle mass close to that of the P33 N_{π}(1236 MeV) resonance were favoured, and they proposed that these reactions proceeded via production of this "isobar" and its subsequent decay. This only described one region of the Dalitz plot; present versions of the isobar model use several isobars, so that every event can be described in this way.

Symbolically:

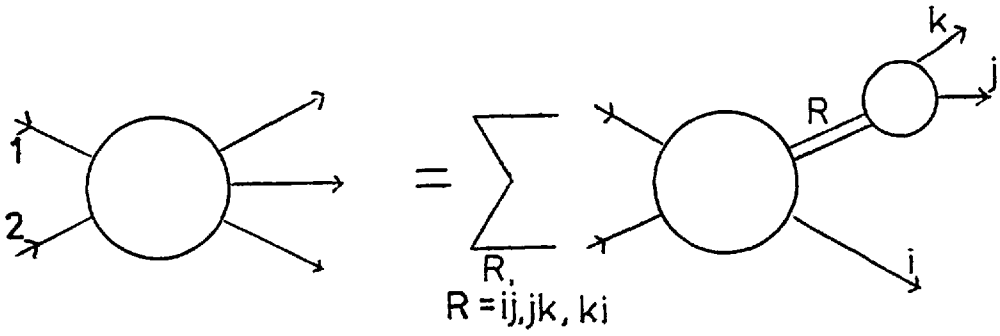

The model has a number of weaknesses. It assumes no direct 3-body decays, and no rescattering (such as a subsequent reaction between particles i and j above). The amplitudes constructed by the coherent sum over the three possible combinations do not exactly satisfy unitarity constraints. Various theoretical and practical improvements have been suggested, one is the addition of one-particle-exchange contributions described in Chapter VII here. Nevertheless the model appears to be phenomenologically justified, and gives reasonable results. Various tests of its validity have been made, one by our group is described in Chapter V, and so far they justify its use.

IV.2.2 Notation and Deler-Valladas Formalism

The transition from the initial $\pi^+ p$ state to the final $\pi_1 \pi_2 N$ state via a 2-body resonance R has to be parametrised in terms of 4 kinematic variables and the quantum numbers of the states involved. The Deler-Valladas formalism (ref. 30) chooses as its 4 independent variables 2 Dalitz plot masses w_1^2, w_2^2 and the polar angles of the incident pion Θ, Φ in a frame fixed with respect to the final state particles. All the angular dependence of the production and decay of the isobar is then taken out into functions

$f(w_1^2, w_2^2, \Theta, \Phi)$, whose form depends on the quantum numbers of the initial, intermediate, and final states, thus giving rise in a natural way to a partial wave series, each wave having different quantum numbers.

The symbols we use are described in Table IV.1 and Figure IV.1; a description of the notation we use for partial waves is also necessary. Each partial wave is labelled by its isobar, L and L′ (in spectroscopic notation - S, P, D, F etc.), 2I (twice its total I spin) and 2J (twice the total angular momentum). The isobars we consider and the parameters we use for them are:-

ΔP33	Mass = 1236, width = 120 MeV/c
N*P11	Mass = 1470, width = 195 MeV/c
ρ meson	Mass = 770, width = 146 MeV/c

The following restrictions to combinations of J, L, L′ apply:

In the initial state we have

$$J = L \pm \tfrac{1}{2}$$

in the intermediate state we have

$$J = L' \pm S$$

when $S = \frac{1}{2}$, angular momentum conservation and parity conservation allow only $L = L'$

when $S = 3/2$, $J = L+\frac{1}{2}$; $L = L'$, $L' + 2$ are allowed

when $S = 3/2$, $J = L-\frac{1}{2}$; $L = L'$, $L' - 2$ are allowed

Note also from Table IV.1 that

$$\hat{S} = \hat{j} + \hat{s}$$

means that $S = j$ for baryon resonances, but $S = 1 \pm \frac{1}{2}$ for the ρ meson.

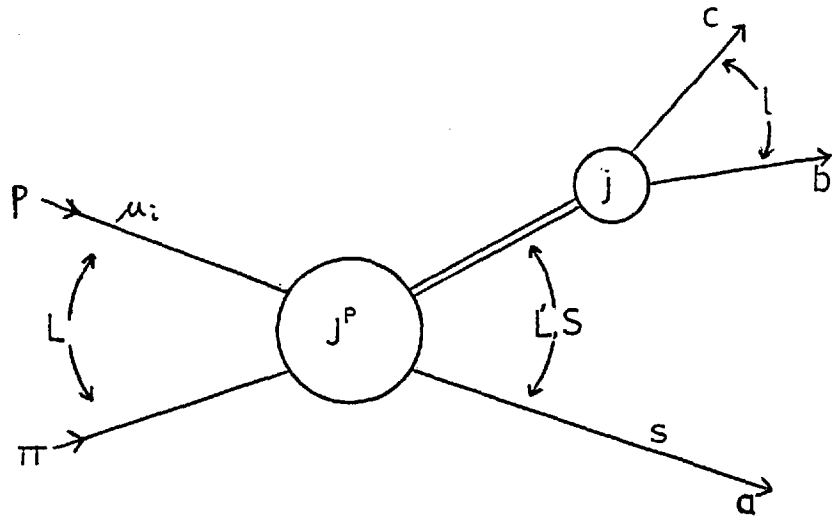

Figure IV.1

J	Total angular momentum
L	Orbital angular momentum between incident pion and target
L'	Orbital angular momentum between isobar and bachelor
j	Total invariant spin of isobar
l	Orbital angular momentum of isobar decay particles
s	Spin of bachelor
S	Total spin of isobar and bachelor $\hat{S} = \hat{j} + \hat{s}$
	note that for a pion bachelor s = 0 so S = j
M_f^*	Projection of nucleon spin on isobar direction in overall c.m.s.
λ	Helicity of isobar
ν	Projection of l on c.m.s. isobar direction
m	Projection of orbital angular momentum on z axis
μ_i, μ_f	Projection of initial and final nucleon spin on z axis

Table IV.1a - Quantum Numbers

W	Total c.m.s. energy
w_1^2, w_2^2	Invariant mass^2 of the N_2, N_1 systems
w_o	Nominal mass of the resonance
Γ, Γ_o	Full width and nominal width of the resonance
q_i	Relative c.m.s. momentum of incident state
q_k^*	Momentum of decay particle from isobar, in isobar rest frame (k = 1 to 3)
q_k	Momentum of decay pion from isobar, in c.m.s.
Q_k	c.m.s. momentum of recoil particle (bachelor)
q_o	Decay momentum of the isobar when its mass equals the nominal resonance mass.
Θ, Φ	Polar angles of beam particle in fixed frame
δ_1	Angle between $(\pi_2 N)$ and nucleon (+ve) in c.m.s.
δ_2	Angle between $(\pi_1 N)$ and nucleon (+ve) in c.m.s.
θ_1	Helicity decay angle to proton from $\pi_2 N$, i.e. the angle between the N direction in the $\pi_2 N$ rest frame, and the direction of the $(\pi_2 N)$ system in the overall c.m.s.
θ_2	Helicity decay angle to proton from $\pi_1 N$

Table IV.1b - Kinematics

Thus the ρ meson isobar case requires this extra quantum number to specify the state completely; 2S is subscripted to the symbol ρ for ρ waves.

The notation used for waves is thus :-

isobar L L′ 2I 2J

Since our experiment uses only $\pi^+ p$ interactions, the total I spin is always 3/2, so in discussing our results alone, we often drop the 2I label.

A choice of isobars must be made and maximum values for J, L, L′ must be decided when we consider possible waves for the analysis. We restrict ourselves to the three isobars described, and use a moments analysis to decide on a maximum value, for L and L′, of F. The reasons for choosing these isobars are given in Rob Stevens' thesis, and section V.4.1 describes the use of the moments analysis. The waves we use are then those described in Table IV.2. They include the FF7 waves, previously not allowed for, but shown to be significant, at 1040 MeV/c and above, by the moments analysis.

ΔSD1	N* SS1	ρ_1 SS1	ρ_3 SD1
ΔPP1	N* PP1	ρ_1 PP1	ρ_3 PP1
ΔPP3	N* PP3	ρ_1 PP3	ρ_3 PP3
ΔPF3	N* DD3	ρ_1 DD3	ρ_3 PF3
ΔDS3	N* DD5	ρ_1 DD5	ρ_3 DS3
ΔDD3	N* FF5	ρ_1 FF5	ρ_3 DD3
ΔDD5	N* FF7	ρ_1 FF7	ρ_3 DD5
ΔFP5			ρ_3 FP5
ΔFF5			ρ_3 FF5
ΔFF7			ρ_3 FF7

Table IV.2 List of Waves

We can now give the D-V expression for the transition:

$$\langle \pi_1 R|T_p|\pi^+_{inc} p\rangle\langle \pi_2 N|T_D|R\rangle = \sum_{\substack{JLL' \\ jl}} \frac{4W}{\pi}\sqrt{\frac{1}{q_i}}\sqrt{J+\tfrac{1}{2}}\; T_{JjLL'l}(W,w_1) f^{JLL'jl}_{\mu_i\mu_f}(\Theta_1,\delta_1,\Theta,\Phi) \tag{4.1}$$

$T_{JjLL'l}(W,w_1)$ contains the dynamics of the interaction ; it will be discussed in the next section.

The D-V expression for f, in our notation and with our choice of axes is :-

$$f^{JLL'j\ell}_{\mu_i\mu_f}(\theta_1,\delta_1,\Theta,\Phi) = (-1)\left[\frac{2J+1}{2L+1}\right]^{\frac{1}{2}} \sum_{\substack{M_f^*,m, \\ \mathcal{L},\lambda>0}} \{1+(-1)^{L+m+l}\}(-1)^{j+\frac{1}{2}}$$

$$\times\ (Jj-\lambda\lambda|L'0)(\ell\tfrac{1}{2}\nu M_f^*|j\lambda)(\tfrac{1}{2}J\mu_f(m-\mu_f)|\mathcal{L}m)$$

$$\times\ (\tfrac{1}{2}JM_f^*-\lambda|\mathcal{L}-\nu)(J\tfrac{1}{2}(m-\mu_f)\mu_i|L(m-\mu_f+\mu_i))$$

$$\times\ d^{\mathcal{L}}_{m,-\nu}(\tfrac{\pi}{2})P^{\nu}_{\ell}(\theta_1)\,(i)^{\nu}\,e^{im\delta_1}\,e^{i\mu_f\Omega_1}$$

$$\times\ Y_L^{m+\mu_i-\mu_f}(\Theta,\Phi) \tag{4.2}$$

Two additional symbols have been introduced; $\mathcal{L}$ is an index over $J+\frac{1}{2}$, $J-\frac{1}{2}$ for each J. Ω is the Stapp angle (ref. 31). At our energies it is close to zero, so the $e^{i\mu f\Omega}$ term will be ignored.

The definition of P_1^{ν} used here is:-

$$Y_1^{\nu}(\theta,\phi) = (-1)^{\nu} P_1^{\nu}(\theta)\, e^{i\nu\phi} / \sqrt{2\pi}$$

The assumption of the isobar model is that each event can be described by the sum of this term and other similar ones,

$$f^{JLL'\,jl}_{\mu_i\mu_f}(-\theta_2,-\delta_2,\Theta,\Phi)$$

for a $\pi_1 N$ isobar, and

$$f^{JLL'\,jl}_{\mu_i\mu_f}(\theta_3,\pi,\Theta,\Phi)$$

for a $\pi_1\pi_1$ isobar.

We can simplify the general expressions for $f^{JLL'\,jl}_{\mu_i\mu_f}$ to 6 special cases, and the expressions for individual waves can then be obtained from these. This is a tedious operation, and open to error, though the final expressions can be checked for various properties they must have. As a first step towards automating this process, the 6 special cases were programmed by Simon Orebi Gann into the algebraic manipulation program REDUCE (ref. 32). This was then used to check our programmed expressions, and showed up one error. The second step, programming the general expression into REDUCE, has also been performed. The results were helpful when we made comparisons between our expressions and those from Saclay, and from the formalism used by SLAC-Berkeley (ref. 33).

Andy White (ref. 10) has shown that the formalisms of Saclay and SLAC-Berkeley lead to the same signs for all waves. However some of our choices for definitions of angles differed from those made by Saclay. The appendix on the isobar model in J. Dolbeau's thesis (ref. 34) has been found very helpful, since he gives a detailed description of sign conventions. Re-definition of our angles to agree with these conventions, and correction of a sign error made in transcribing expressions for even L, S = 3/2 waves, give us expressions which agree with those of Saclay, and no longer have the sign problem in odd L N* and ρ_1 waves mentioned by Rob Stevens.

The FF7 waves were not originally included in Rob Stevens' programs; the author added them later, using the original "by hand" methods to evaluate the expressions. A summary of this is given here as an example of such evaluations.

The 6 special cases are

For S = 3/2 (Δ and ρ_3)

I $L' = L+2 = J+3/2$

$\therefore L = J-\frac{1}{2}$

II $L' = L = J+\frac{1}{2}$

III $L' = L = J-\frac{1}{2}$

IV $L' = L-2 = J-3/2$

$\therefore L = J+\frac{1}{2}$

For S = $\frac{1}{2}$ (N* and ρ_1)

I $L' = L = J-\frac{1}{2}$

II $L' = L = J+\frac{1}{2}$

For the 3/2Δ (and ρ_3) FF7 waves, case III, 3/2 applies.

For the $\frac{1}{2}$ N^*(and ς_1) FF7 waves, case I, $\frac{1}{2}$ applies; for convenience this wave is called NFF7 to distinguish it from the Δ FF7, or just FF7 wave.

In every case there are 4 possible combinations of μ_i and μ_f

$\mu_i = \mu_f = +\frac{1}{2}$, $\mu_i = \mu_f = -\frac{1}{2}$ are non-spin-flip terms (NSF)

$\mu_i = \frac{1}{2} = -\mu_f$, $\mu_i = -\frac{1}{2} = -\mu_f$ are spin-flip terms (SF)

The 2 NSF cases are similar, and so are the 2 SF cases, so expressions are evaluated for SF and NSF.

The 3/2 case III simplified expression for f is:-

$$\frac{1}{(2L+3)(L+1)} \cdot \frac{1}{\sqrt{2}} \cdot \frac{1}{\sqrt{L(L+1)(2L+1)}}$$

$$\cdot \sum_m (-1)^{m+1} P^m_{L+1}(0)\{L(L+1)\cos\theta + (-mL+(2L+3)(L+1-m)) i\sin\theta\} e^{im\delta}$$

$$\cdot \begin{cases} (-)\sqrt{\frac{(L-m+1)(L+m+1)}{(L+m)(L+m+1)}} \cdot Y^m_L(\Theta,\Phi) & \text{NSF} \\ \cdot\ Y^{m-1}_L(\Theta,\Phi) & \text{SF} \end{cases}$$

The sum over m is for all m values allowed for the given $J+\frac{1}{2}$, but several such terms contain at least one factor of zero. The non-zero terms are:

FF7 NSF

m = -2 $\quad -\frac{1}{8}\sqrt{\frac{5}{14}}\{5i\sin\theta + \cos\theta\} e^{-2i\delta} Y^{-2}_3$

$m = 0$ $\quad \frac{1}{8}\sqrt{\frac{3}{7}}\ \{\cos\theta + 3i\sin\theta\}\ Y_3^0$

$m = 2$ $\quad -\frac{1}{8}\sqrt{\frac{5}{14}}\ \{\cos\theta + i\sin\theta\}\ e^{2i\delta}\ Y_3^3$

FF7 SF

$m = -2$ $\quad \frac{1}{16}\sqrt{\frac{5}{21}}\ \{\cos\theta + 5i\sin\theta\}\ e^{-2i\delta}\ Y_3^{-3}$

$m = 0$ $\quad -\frac{3}{16}\sqrt{\frac{1}{7}}\ \{\cos\theta + 3i\sin\theta\}\ Y_3^{-1}$

$m = 2$ $\quad \frac{5}{16}\sqrt{\frac{1}{7}}\ \{\cos\theta + i\sin\theta\}\ e^{2i\delta}\ Y_3^1$

$m = 4$ $\quad -\frac{1}{16}\sqrt{\frac{35}{3}}\ \{\cos\theta - i\sin\theta\}\ e^{4i\delta}\ Y_3^3$

One property that the f's must satisfy is

$$\sum_{\mu_i \mu_f} \iiint \left| f^{JLL'j\nu}_{\mu_i \mu_f}(\theta, \delta, \Theta, \Phi) \right|^2 d\cos\theta \; d\cos\Theta \; d\Phi = 1$$

and this was used to check the correctness of the above expressions.

Expressions for NFF7 are similarly derived and checked, they are:

NFF7 NSF

$m = -2$ $\quad -\frac{1}{8}\sqrt{\frac{15}{14}}\ (\cos\theta - i\sin\theta)\ Y_3^{-2}\ e^{-2i\delta}$

$m = 0$ $\quad \frac{3}{8}\sqrt{\frac{1}{7}}\ (\cos\theta - i\sin\theta)\ Y_3^0$

$m = 2$ $\quad -\frac{3}{8}\sqrt{\frac{5}{42}}\ (\cos\theta - i\sin\theta)\ Y_3^2\ e^{2i\delta}$

NFF7 SF

$m = -2$ $\quad \frac{1}{16}\sqrt{\frac{5}{7}}\ (\cos\theta - i\sin\theta)\ Y_3^{-3}\ e^{-2i\delta}$

$m = 0$ $\quad -\frac{3}{16}\sqrt{\frac{3}{7}}\ (\cos\theta - i\sin\theta)\ Y_3^{-1}$

$$m = 2 \qquad \frac{5}{16}\sqrt{\frac{3}{7}} \quad (\cos\theta - i\sin\theta)\, Y_3^1 \quad e^{2i\delta}$$

$$m = 4 \qquad -\frac{7}{16}\sqrt{\frac{5}{7}} \quad (\cos\theta - i\sin\theta)\, Y_3^3 \quad e^{4i\delta}$$

These expressions are programmed into FORTRAN routines. θ,δ and the Y_L^M values for an event are passed to these routines and they return the real and imaginary parts of the spin-flip and non-spin-flip terms. This coding of the expressions is also susceptible to error, Andy White has written a program to compare the results of calculations in the SLAC-Berkeley formalism with the results of these subroutines. REDUCE has also been helpful, since it can produce FORTRAN code as its output: it was at this stage that an error in coding the NDD3 expressions was found.

IV.2.3 Other Parametrisations

Turning to the term $T_{JjLL'1}(W,w)$ in expression 4.1, we must choose a suitable parametrisation for this quantity to describe the dynamics of the interaction. We first separate it into 2 terms,

$$T_{JjlLL'}(W,w) = A_{JjlLL'}(W,w)\; B_{jl}(w) \qquad (4.3)$$

where A represents the amplitude for the production of the resonance, and B the dynamics of its decay. We then use a relativistic Breit-Wigner formulation from Jackson (ref. 35) for B

$$B_{jl}(w) = \left(\frac{w}{q}\right)^{\frac{1}{2}} \frac{\sqrt{w_o\Gamma}}{(w_o^2-w^2)-iw_o\Gamma} \quad (I_k I_k^z\, I_l I_l^z \,/\, II^z) \qquad (4.4)$$

The Clebsch-Gordan coefficient is for the combination of the I-spins of the isobar components (k,l) and allows comparison of different charge states of the same isobar. Γ is a mass-dependent width of the isobar.

$$\Gamma = \Gamma_o \left(\frac{q}{q_o}\right)^{2l+1} \frac{\phi(w)}{\phi(w_o)}$$

ϕ is a form factor, for baryon resonances we use the parametrisation of Rosenfeld and Glashow (ref. 36)

$$\phi(w) = w^{-1} (0.1225 + q^2)^{-1}$$

for the ρ meson we use

$$\phi(w) = w^{-1}$$

For A we write

$$A_{Jjl LL'}(W,w) = X_{Jjl LL'}(W)\ Y_L(q_i)\ Y_{L'}(Q_k)$$

The $X_{Jjl LL'}(W)$ are the (complex) transition amplitudes that we wish to obtain from the data; they depend only on the total c.m.s. energy. The Y's are centrifugal barrier terms. Various parametrisations are possible for these; after tests described in Rob Stevens' thesis, the simplest power dependence one was chosen.

$$A_{Jjl LL'}(W,w) = X^{I=3/2}_{Jjl LL'}(W)\ q_i^L\ Q_k^{L'}\ (II^z I_j I_j^z \,|\, 3/2\ 3/2) \qquad (4.5)$$

The Clebsch-Gordan coefficient is for the combination of the I-spins of isobar and bachelor, to make X charge independent.

This completes the brief description of our parametrisation, as stated earlier more details are given in Rob Stevens' thesis (ref. 9).

IV.2.4 Expressions for Cross-sections

Using the expression 4.1, we have for the differential cross-section with respect to the 4 Deler-Valladas variables:

$$\frac{d^4\sigma}{dw_i^2 dw_f^2 d\cos\Theta\, d\bar{\Phi}} = \frac{\pi}{32 q_{inc} W^3} \sum_{\mu_i \mu_f} \left| \sum_{JLL'j} \sum_{i} 4W \sqrt{\frac{1}{q_{inc}}} \sqrt{J+\tfrac{1}{2}}\, T^{(W,w_i)}_{JLL'j\ell} \int^{JLL'j\ell}_{\mu_i \mu_f} \right|^2 \tag{4.6}$$

The sum over i denotes a summation over the 4 isobars, and over the combinations $\pi_1 N, \pi_2 N$ where both contribute to an isobar. Expressions for the terms involved have already been given, and a simplified notation can now be introduced. Let the single index μ replace (μ_i, μ_f), and let the index n represent (JjlLL' Si). Our purpose is to find values for the partial wave amplitudes $X_n(W)$ in equation 4.5, so these will be written explicitly, but all remaining functional dependence and constants can be represented by the symbols F^n_μ. Equation 4.6 can now be written more simply as

$$\frac{d\sigma}{dw_i^2 dw_f^2 d\cos\Theta\, d\bar{\Phi}} = \sum_\mu \left\{ \sum_n X_n F^n_\mu \sum_m X^*_m F^{m*}_\mu \right\} \tag{4.7}$$

$$\left[F^n_\mu = \sqrt{\frac{\pi}{32 q_{inc} W^3}}\, 4W \sqrt{\frac{1}{q_{inc}}} \sqrt{(J+\tfrac{1}{2})} \int^{JLL'j\ell}_{\mu_i \mu_f} B_{j\ell}(w_i) q_i^\ell Q^{L'}_{Ik} \left(I\, I^2 I_j I_j^2 \middle| \tfrac{3}{2}\, \tfrac{3}{2} \right) \right.$$

by combining equations 4.3, 4.5 and 4.6]

We add another superscript, a, to the F^n_μ's to specify a particular channel ($\pi^+ p \pi^0$ or $\pi^+\pi^+ n$ in our experiment).

Integrating 4.7 over phase space, we obtain the total cross-section for channel a

$$\sigma^a = \sum_{nm} R^a_{nm} X_n X^*_m \qquad (4.8)$$

where

$$R^a_{nm} = \sum_\mu \int F^{na}_\mu F^{ma*}_\mu \, d(\text{phase space}) \qquad (4.9)$$

The R^a_{nm} are what we call normalisation integrals, though strictly speaking they are normalisation integrals when n = m, and overlap integrals when $n \neq m$.

Since X_n is a joint fit to several channels, equation 4.8 is not exact with finite statistics, but we can demand that it be exactly true for a sum over all channels being fitted.

$$\sigma^{tot} = \sum_a \sigma^a = \sum_a R^a_{nm} X_n X^*_m \qquad (4.10)$$

σ^{tot} is the total 3-body cross-section being fitted. Equation 4.10 is used to scale the X_n's correctly.

For a particular $J^j l L'$ S (or n) transition

$$\sigma^n = \left\{ \frac{\sum_a R^a_{nn} |X_n|^2}{\sum_{pq} R^a_{pq} X_p X^*_q} \right\} \sigma^{tot} \qquad (4.11)$$

Note that this is now independent of any scaling of X_n.

The T-matrix element for a transition is defined by

$$\sigma^n = 4\pi\lambda^2 (J+\tfrac{1}{2}) \left| T^n \right|^2 \qquad (4.12)$$

Taken on its own, this defines only the amplitude of T^n, the phase of T^n relative to other T's is that of the corresponding X_n. (Here λ is the wave number, $\lambda = 1/Q$).

With this definition, the T^n's lie on an argand plot inside a circle of radius $\frac{1}{2}$, centred at (0,0).

The total cross-section for a given J^P is

$$\sigma^{J^P} = \left\{ \frac{\sum_a \sum_{nm \epsilon J^P} R^a_{nm} X_n X^*_m}{\sum_a \sum_{pq} R^a_{pq} X_p X^*_q} \right\} \sigma^{tot} \qquad (4.13)$$

For any one event i, the differential cross-section predicted by its measurements $\underline{y}_i$, and by a given set of X's is:-

$$\frac{d\sigma_i}{dw_1^2 dw_2^2 d\cos\Theta d\underline{\phi}} = \left\{ \frac{\sum_\mu \sum_{nm} X_n X^*_m F^{na}_\mu i(\underline{y}_i) \left[F^{ma}_\mu i(\underline{y}_i) \right]^*}{\sum_{pq} X_p X^*_q R_{pq}} \right\} \sigma^{tot} \qquad (4.14)$$

Note that the summation over channels in the denominator has been performed implicitly so that $R_{pq} = \sum_a R^a_{pq}$. Note also that $F^{na}_\mu i\ (\underline{y}_i)$ denotes the set of F^n_μ's for event i in channel a_i, with measurements $(w_1^2, w_2^2, \Theta, \underline{\phi})$ denoted by the vector $\underline{y}_i$.

IV.3 Maximum Likelihood Formalism

We use the maximum likelihood method to obtain the partial wave amplitudes and relative phases X^n from our data.

If one assumes a function G that describes the probability distribution of measurements of a quantity y, that function will in general depend on a number of parameters θ. For example the function G may be a gaussian distribution, in which case the parameters will be the mean and standard deviation, and the measurement y will be a single measurement of the quantity whose distribution is being measured.

For a given set of parameters Θ_1, the predicted probability of a measurement y is

$$G_{\theta_1}(y)$$

and the predicted overall probability of N measurements is

$$\mathcal{L}_1 = \prod_{i=1}^{N} G_{\theta_1}(y_i)$$

Now take a different set of parameters for the theory, Θ_2. The predicted overall probability of the N measurements will now be

$$\mathcal{L}_2 = \prod_{i=1}^{N} G_{\theta_2}(y_i)$$

If $\mathcal{L}_2$ is higher than $\mathcal{L}_1$, then the set Θ_2 predicts the distribution of the measurements y_i better than does Θ_1, and is therefore a more likely description of the measurements. This then is the maximum likelihood method: look for a set Θ that predicts the highest overall probability for the set of measurements y_i.

The usual definition of probability is such that the total probability of all possible measurements y is equal to one.

$$\text{i.e.} \quad \int G_\Theta (y)\, dy = 1$$

In our case, the distribution of probabilities, G, is the differential cross-section 4.14 which describes the relative probability of a given event lying somewhere in the 4-variable space. The parameters Θ are the set of partial wave amplitudes X, and the measurements y_i are the set of variables $\underline{y}_i$ for each event.

We must therefore maximise the likelihood

$$\mathcal{L} = \prod_{i=1}^{N} \frac{d\sigma(\underline{X},\underline{y}_i)}{dw_1^2 dw_2^2 d\cos\Theta\, d\underline{\phi}} \qquad (4.15)$$

to obtain the set of X's that best describes our data.

With the expression 4.14, the integral of the relative probability distribution comes to the total cross-section rather than unity:

$$\int G_{\theta_T}(\underline{y})\, d\underline{y} = \int \frac{d\sigma}{dw_1^2 dw_2^2 d\cos\Theta\, d\tilde{\phi}}\, dw_1^2 dw_2^2 d\cos\Theta\, d\tilde{\phi} = \sigma^{Tot}$$

Alternatively, the σ^{Tot} term in 4.14 can be dropped, so that this integral does come to unity; this does not affect maximisation of the likelihood since σ^{Tot} is a constant.

The data to be fitted must be genuinely representative of the 4-parameter space, and there must be enough events to allow the construction of a meaningful likelihood, so a high statistics bubble chamber experiment which can detect all events with equal efficiency and provide a sufficient number of them is the best way to do this fitting. Apart from covering the 4-parameter space correctly, one must also correctly cover the channels being fitted; the numbers of events in different channels must be in the ratio of the channel cross-sections, as in our experiment, or normalisation expressions must be used to allow for different numbers of events per unit cross-section in different channels. The procedure for this is given in L. Miller's Ph.D. thesis (ref. 37). The likelihood expression quoted by Miller also contains a factor to force the X's to correctly predict the cross-section ratios in different channels. We do not do this; instead we compare the fitted ratio $\sigma_{\pi^+ p\pi^0} : \sigma_{\pi^+\pi^+ n}$ to the experimental ratio, and this gives us an additional check on the goodness of a fit.

Combining the expressions 4.14 and 4.15, dropping the σ^{Tot} factor as mentioned, we obtain the expression

$$\mathcal{L} = \prod_{i=1}^{N} \left\{ \frac{\sum_{\mu} \sum_{nm} X_n X_m^* F_{\mu}^{na} i(\underline{y}_i) \left[F_{\mu}^{ma} i(\underline{y}_i) \right]^*}{\sum_{pq} X_p X_q^* R_{pq}} \right\} \qquad (4.16)$$

This is a correctly formulated likelihood, it can be fitted as it is, but it can be multiplied by any constant, since this does not affect minimisation. We have chosen to fit the differential cross-section with respect to Lorentz invariant phase space : $\frac{d\sigma}{d\rho}$

The likelihood written in equation 4.15 becomes

$$\mathcal{L}_f = \prod_{i=1}^{N} \frac{d\sigma(\underline{x}, \underline{y}_i)}{d\rho} \Big/ \sigma_{Tot} \qquad (4.17)$$

and it has to be shown that this differs by only a constant from 4.15 (and hence 4.16), and what this constant is.

The Jacobian relating Deler-Valladas variables to the Lorentz invariant phase space element at a constant c.m.s. energy W is

$$\frac{\partial(\rho)}{\partial(w_1^2, w_2^2, \cos\Theta, \Phi, \alpha)} = \frac{1}{32W^2} \qquad (4.18)$$

α defines the rotation about the incident beam and can be integrated out in the case of an unpolarised beam.

4.17 can therefore be written

$$\mathcal{L}_f = \prod_{i=1}^{N} \frac{d\sigma}{d\rho} = \prod_{i=1}^{N} \frac{d\sigma}{dw_1^2 dw_2^2 d\cos\Theta d\Phi} \cdot \frac{2\pi}{32W^2} \cdot \frac{1}{\sigma_{\pi\pi}} \quad (4.19)$$

So the function used in fitting, $\mathcal{L}_f$ differs from 4.16 by a constant factor :

$$\mathcal{L}_f = \mathcal{L} \cdot \left(\frac{\pi}{16W^2} \right)^N \quad (4.20)$$

Chapter V Data Fitting and Results

V.1 Introduction

The formalism of Chapter IV has to be turned into computer programs. The F's and R's of equation 4.16 must be calculated, then the X's fitted. This chapter describes the programs that start at the data on the D.S.T.'s and lead to energy-independent solutions. These solutions are then presented. Figure V.1 shows the sequence of programs used.

Our top 4 energies had already been fitted but the results showed that a refit using more waves was needed, and we had not previously fitted the other 5 energies. We were therefore making a complete new set of fits, which gave us the chance to recheck the programs, and try some new techniques. The most significant difference from previous work was that we made many fits using all waves, up to some maximum, at each energy, and only then searched for a continuous 9-energy solution. Earlier workers started by fitting with many waves at each energy, then removed waves and refitted, searching for continuity, firstly at adjacent energies, finally coming to a continuous solution. This latter technique can lead to the removal of important waves, as happened with the SLAC-LBL solution A, and also with some of our earlier work.

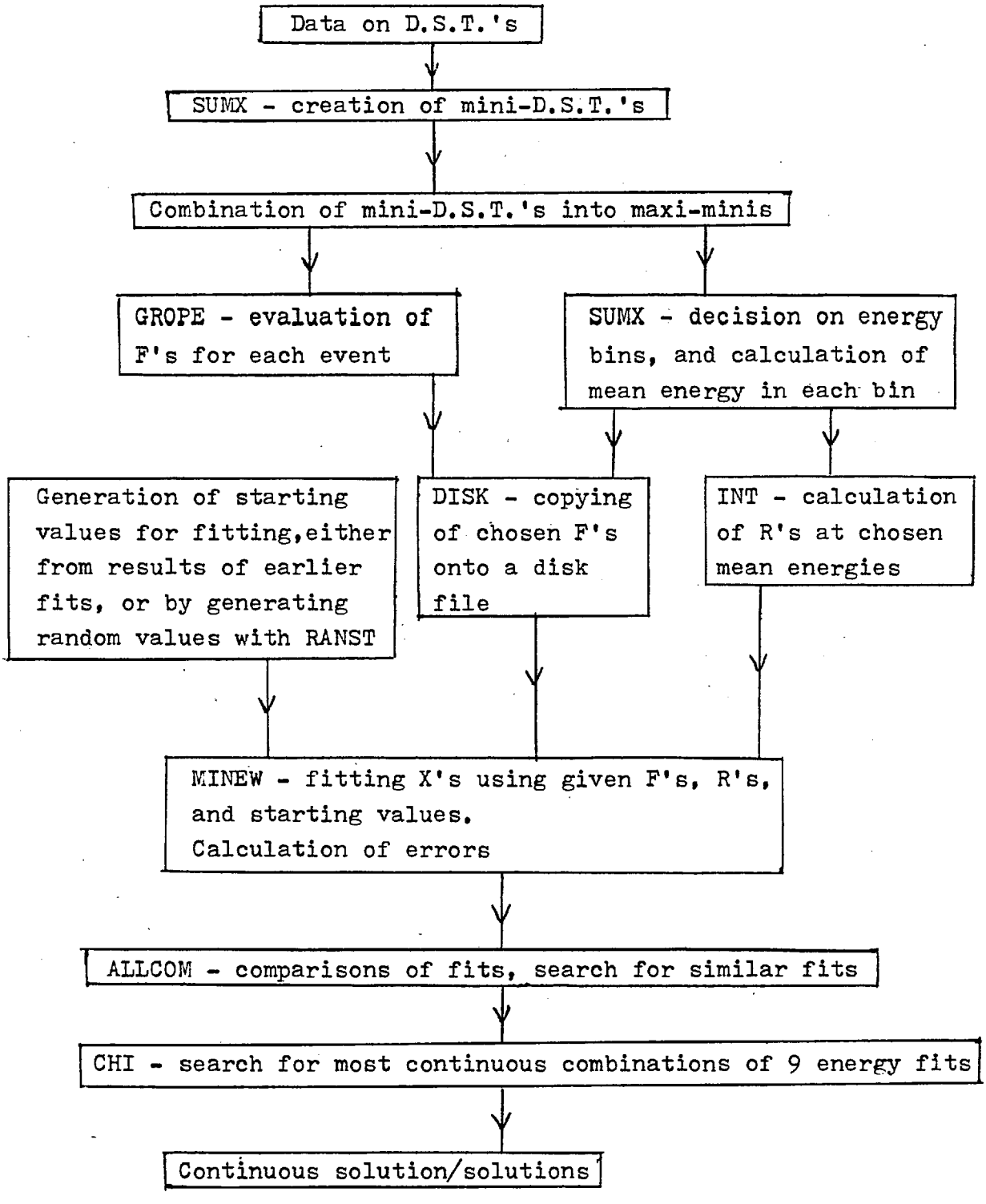

Figure V.1 The steps in finding a solution

V.2 Preparation of Data for Fitting

We first used SUMX (q.v.) to select $\pi^+p\pi^o$ and $\pi^+\pi^+n$ events from a D.S.T., within cuts on beam parameters. A special subroutine calculated the angles and effective masses needed for the evaluation of the Deler Valladas amplitudes for these events, another wrote them onto a mini D.S.T.

By imposing wide cuts on beam momenta, and then merging several mini D.S.T.'s into one "maxi-mini" D.S.T. we obtained better statistics than in our earlier work. An additional cut, rejecting events with a GRIND fit probability of less than 1% was made at this stage. Figure V.2 shows histograms of the c.m.s. energies of events on the two maxi-minis used in the present work. In both cases, statistics of the top bin were increased by the addition of events from our next higher energy. The data on the maxi-minis could then be divided into bins, each with a peak in the distribution and with a sufficient number of events to fit. The combining of the Oxford data with our data has led to more scatter about the peaks, but also to better statistics at the lower momenta, as can be seen from Table V.1 which summarises information on the bins chosen. The majority of events in the 800 and 850 MeV/c bins come from the author's work. Oxford data at 650 MeV/c was meagre; it was divided up between the 600 and 700 MeV/c bins.

For each event, the data from the maxi-mini is used to calculate the $F_\mu^{na}i$ values of equation 4.7. The channel

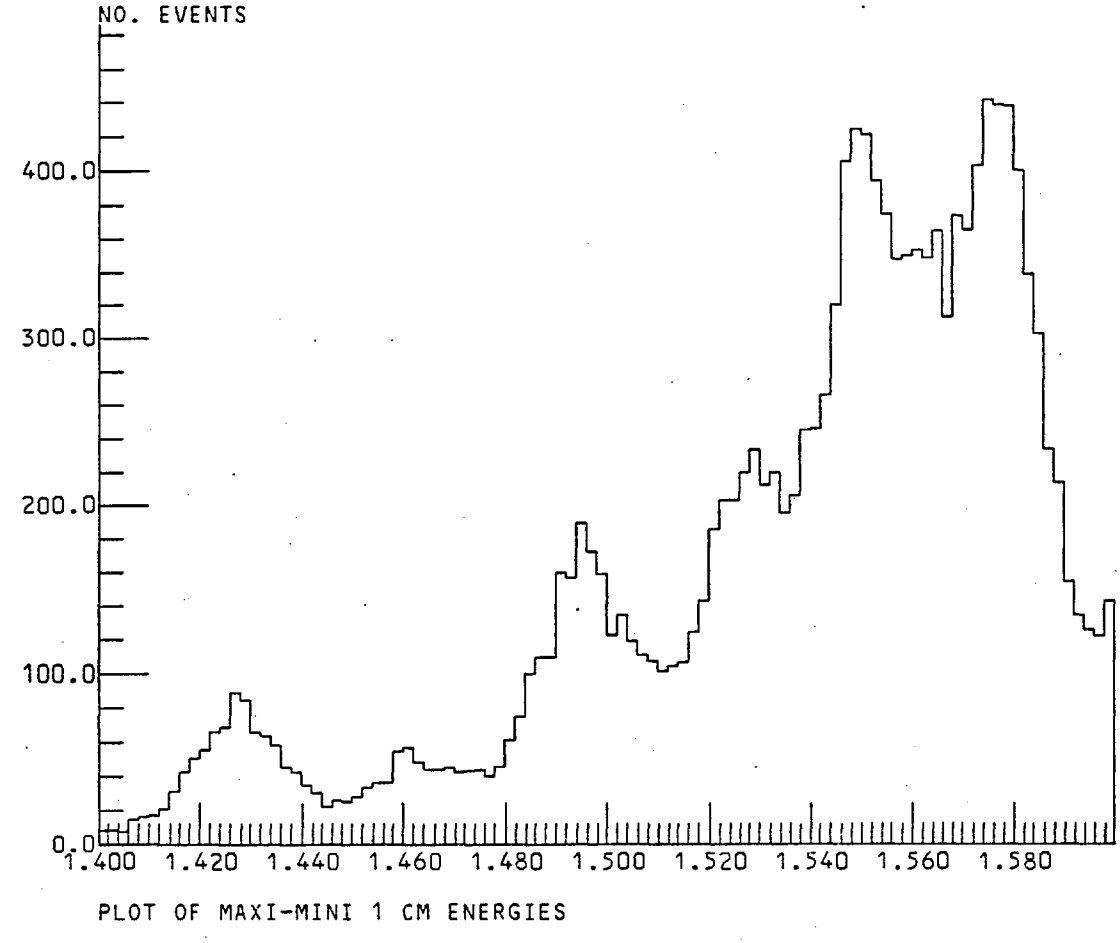
NO. EVENTS
400.0
300.0
200.0
100.0
0.0
1.400 1.420 1.440 1.460 1.480 1.500 1.520 1.540 1.560 1.580
PLOT OF MAXI-MINI 1 CM ENERGIES

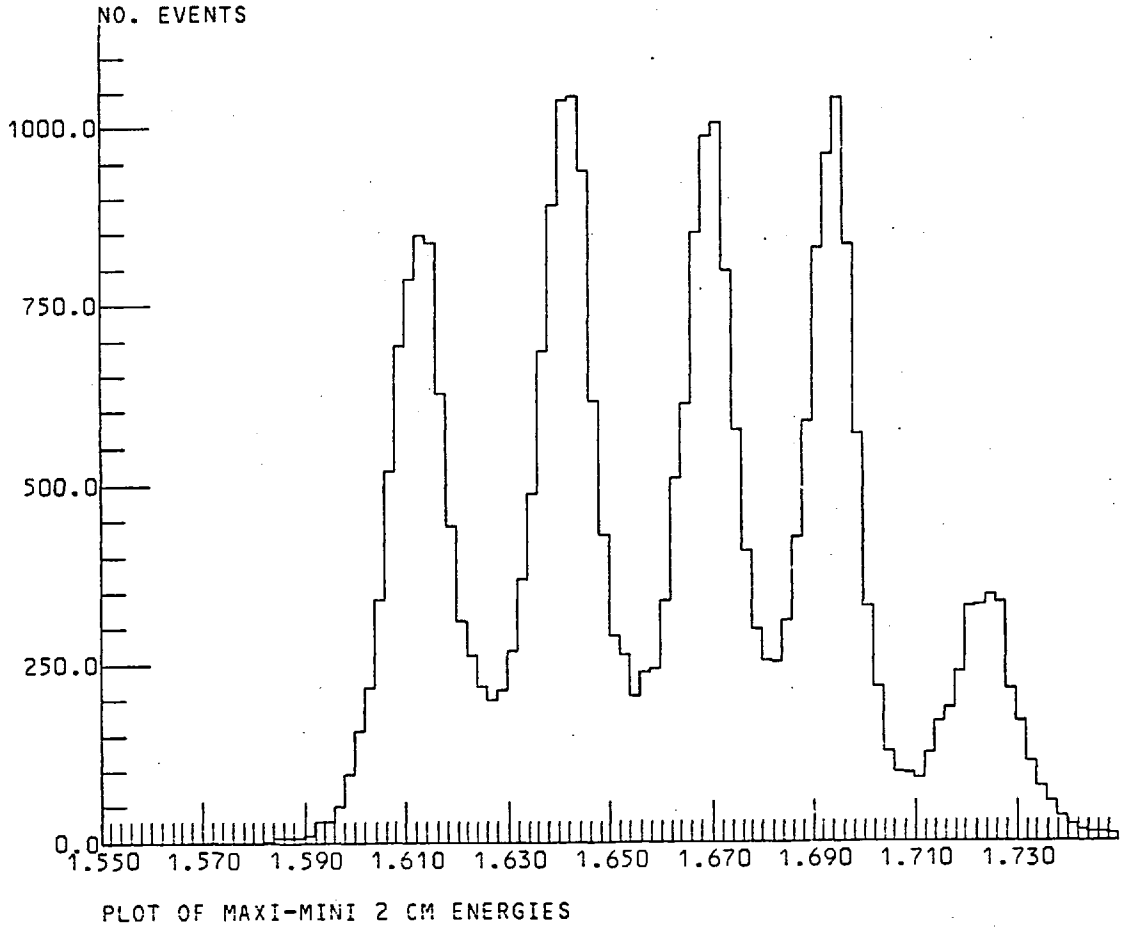
NO. EVENTS
1000.0
750.0
500.0
250.0
0.0
1.550 1.570 1.590 1.610 1.630 1.650 1.670 1.690 1.710 1.730
PLOT OF MAXI-MINI 2 CM ENERGIES

Figure V.2

Bin number	Nominal lab. Beam momentum (MeV/c)	Mean c.m. energy (GeV)	Lower energy cut	Upper energy cut	Number of Oxford events	Number of Oxford events	Number of C/IC/WC events	Number of C/IC/WC events	Maximum J value used in fits	$\pi^+p\pi^o$ cross-section	$\pi^+\pi^+n$ cross-section
1	600	1.439	1.400	1.473	1206	270	1	0	$\frac{3}{2}$ *	.86±.05	.19±.02
2	700	1.495	1.473	1.512	1730	384	15	7	$\frac{3}{2}$ *	2.06±.09	.49±.05
3	750	1.526	1.512	1.537	1669	284	256	53	$\frac{3}{2}$ *	3.70±.15	.70±.07
4	800	1.550	1.537	1.564	1477	269	2388	459	$\frac{3}{2}$ *	5.14±.16	.99±.06
5	850	1.577	1.564	1.598	937	149	3473	606	$\frac{3}{2}$ *	7.38±.20	1.29±.07
6	895	1.612	1.598	1.627	0	0	5547	915	$\frac{5}{2}$	10.22±.17	1.70±.06
7	945	1.640	1.627	1.656	0	0	6693	1169	$\frac{5}{2}$	10.66±.16	1.83±.06
8	995	1.668	1.656	1.682	0	0	5973	1158	$\frac{7}{2}$	10.60±.17	2.03±.06
9	1040	1.692	1.682	1.708	0	0	5506	1095	$\frac{7}{2}$	10.50±.18	2.10±.07

* one $\frac{5}{2}$ wave - the DD35 was used at these energies

Table V.1

Energy bins used in fitting

a_i determines which isobars will be used; on each maxi-mini all waves $\{n\}$ up to the chosen maximum combination of J, L, L′ are used, and for each wave eight numbers - the real and imaginary parts of the four $\mu_i \mu_f$ combinations - are calculated. These calculations are performed by the program GROPE which contains subroutines to calculate the D-V f functions, the other components of F, and to combine these. GROPE writes a tape carrying the maxi-mini quantities, and the F's, for each event.

The calculation of a likelihood requires the F's for all events in the given energy bin. Unfortunately, they cannot all be held in core simultaneously (e.g. 5,000 events, with 30 waves, each needing 8 numbers would take 9.6×10^6 bytes storage, whereas the computer we use has a total memory of 2 Mbytes). We therefore store the numbers on a disk, which can be read more rapidly than a tape, and does not need to be rewound after each calculation of a likelihood. To avoid reading of unnecessary data, F's are copied to disk for only those waves that are to be fitted. The program DISK is given a list of the required isobar-wave combinations, together with upper and lower c.m.s. energies. It reads a GROPE tape, selects events within the energy range, and copies the required F's and a channel flag for each event to a disk file.

V.3 Calculation of Normalisation Integrals

In principle, the best method of obtaining the normalisation and overlap integrals is to perform the integral 4.9 analytically. One would then be able to calculate the integrals at any c.m.s. energy by substituting that energy into the analytic expression and evaluating it. Unfortunately, the expressions are too complicated to permit this direct approach, and numerical integration must be used. Numerical integration over the four variables, using Simpson's rule integration on a computer, took impossibly long; an accuracy of 1% was never achieved. Since analytic integration over Θ and Φ is relatively easy, this was performed, simplifying the problem to that of numerical integration over 2 variables. The integrals we originally used were obtained by Simpson integration on a computer over the other two variables. . The program used for this assumed that the integrals had converged when the fractional difference between the results of two successive steps was smaller than the required accuracy. The integrals were evaluated at the mean c.m.s. energy of each energy bin, and separate runs had to be made at each energy.

Since orthogonality of the Y_L^M functions means that waves of different JL (or equivalently J^P) do not interfere, the program is written to calculate normalisations for different J values in different runs. For each J, the normalisations and overlaps for every L are programmed by coding the products of the D-V f functions, with the Y_L^M terms dropped as they are orthonormal. Expressions for the

remaining terms are coded separately, then the products are formed, and the program integrates over them. When the FF7 waves were added to the analysis, the author also wrote the J=7/2 L=3 expressions into the integration program.

An alternative technique for integration is provided by the Monte-Carlo method. Events are generated randomly with equal probability throughout phase space, each is analysed into F_{μ}^{na} terms by the same program as is used for the real events (GROPE), and the integral 4.9 is obtained by a summation over a large number of events. We used the CERN program FOWL (ref. 20); integration with a few ten thousand events was insufficient for accurate calculation of overlaps, but was considered sufficient for a check of the numerical integration program. The FF7 integrations by the two methods were indeed the same to within a few percent, but some other terms differed by factors of up to 2. A check of the numerical integration program revealed no errors, and a rerun of FOWL with 200,000 events did not improve the situation. It was here that REDUCE was used to check the D-V expressions and showed an error in the NDD3 subroutine (see section IV.2.2). With this corrected, the worst discrepancy went away, but others remained. In attempts to improve accuracy, the numerical integrator was run with 4,000,000 steps (2,000 in each direction), and the Monte-Carlo with up to 700,000 events (this is in 4 directions, but the accuracy of an integration with N Monte-Carlo events is similar to that of a Simpson integration with N^2 steps). These runs succeeded in using between 60 and 90 minutes

c.p. time each on the 360/195 computer, but the worst discrepancy was still about 60%.

The disagreements were all in the overlap integrals $R_{nm}(n \neq m)$, and in different ones at different energies. We concluded that the Monte-Carlo program had shown that the expressions in GROPE and in the numerical integrator were consistent, but that a more accurate integration method was needed for small off-diagonal terms. We therefore tried the Harwell integrating routine QB01A. Details of its use are given in reference 23; we used it to provide a Chebyshev polynomial integration instead of the Simpson integration. QB01A gave us integrals with a nominal accuracy of .01% and took 90 seconds instead of 90 minutes. As with the Simpson integration, this is not an exact value of the accuracy: in both methods a further step may give a larger change than the previous one at which the integration stopped. However, Chebyshev polynomials have been studied in detail and shown to have excellent convergence properties (see for example ref. 41), so we believe that this is far less likely to occur with QB01A than with the Simpson integration, and we believe the integrals to be correct to .1%. The results obtained were closer to those of the Simpson method than those from FOWL, but neither was sufficiently accurate.

In a recent paper (ref. 38) Y. Goradia presents a method, based on the SLAC-LBL formalism, for using overlap functions to simplify both the analytic integration over

two angles and the numerical integration. The checks described here confirm that a better integration method was required, but we are satisfied with our QB01A integrals and have not tried the overlap function method.

V.4 Data Fitting

V.4.1 Choice of Waves

The partial wave series of equation 4.1 must be truncated after a finite number of terms. Too low a cutoff results in bad fits, but fitting with too many waves wastes time and can cause overparametrisation problems. The 14 wave set used earlier gave acceptable results, but some waves exceeded the cross-sections predicted by elastic analyses, so a refit with more waves was undertaken, and a decision was needed as to the waves to be used in analysing the lower energies. Two questions arise - which should be the highest JL waves to use, and which waves in the range up to this combination should be fitted?

A moments analysis was used to answer the first question. The use of the method of moments in our experiment has been described in references 1, 2 and 9 - a very brief description will be given here.

The Δ^{++} isobar production cross-section is expanded:-

$$\frac{d^3\sigma}{d\cos\theta\, d\phi^*\, d\cos\theta^*} = \frac{\pi}{q^2}\sum_n \frac{2}{\sqrt{4\pi}}\left(c^n_{\frac{1}{2}\frac{1}{2}} + c^n_{\frac{1}{2}\frac{1}{2}}\right)P^0_n(\cos\theta)\,Y^0_0(\theta^*,\phi^*)$$

$$- \frac{1}{\sqrt{5\pi}}\left(c^n_{\frac{1}{2}\frac{1}{2}} - c^n_{\frac{1}{2}\frac{1}{2}}\right)P^0_n(\cos\theta)\,Y^0_2(\theta^*,\phi^*)$$

$$+ \sqrt{\frac{8}{5\pi}}\,\frac{\mathrm{Re}\; c^n_{\frac{1}{2}\frac{1}{2}}\; P^1_n(\cos\theta)\,\mathrm{Re}\,Y^1_2(\theta^*,\phi^*)}{\sqrt{n(n+1)}}$$

$$- \sqrt{\frac{8}{5\pi}}\,\frac{\mathrm{Re}\; c^n_{\frac{1}{2}-\frac{1}{2}}\; P^2_n(\cos\theta)\,\mathrm{Re}\,Y^2_2(\theta^*,\phi^*)}{\sqrt{n(n+1)(n-1)(n+2)}}$$

where Θ is the c.m.s. scattering angle

θ^*,ϕ^*, measured in any Δ rest frame with the z-axis in the production plane, describe the decay

q is the incident momentum in the overall c.m.s.

n labels the Legendre coefficient order

$$c^n_{MM'} = \sum_{\substack{JLL^* \\ J'L'L'^*}} R^{JLL^*,J'L'L'^*}_{n,MM'}\; T^{JLL^*}(W)\; T^{J'L'L'^*}(W)$$

The notation here is similar to that of Chapter IV, but the production angular momentum is denoted by L^*. The coefficient R is given by a combination of C-G coefficients, see ref. 9, or the paper by Roberts, ref. 42. As n increases the lowest wave contributing to R_n increases in J and L. Analysis of low terms is thus complicated, but few waves contribute to the highest non-zero terms, allowing one to decide which are the highest significant waves. This information is obtained from the data as follows.

The average value of any function f can be written

$$\langle f \rangle = \frac{\int f d^4\sigma}{\int d^4\sigma} = \frac{\int f d^4\sigma}{\frac{4\pi}{q^2}\left\{c^0_{\frac{1}{2}\frac{1}{2}} + c^0_{\frac{1}{2}\frac{1}{2}}\right\}}$$

so that expressions for moments can be written

$$\langle P^0_n(\cos\theta) Y^0_0(\theta^*, \phi^*)\rangle = \frac{1}{(2n+1)} \frac{1}{\sqrt{4\pi}} \frac{\left\{c^n_{\frac{1}{2}\frac{1}{2}} + c^n_{\frac{1}{2}\frac{1}{2}}\right\}}{\left\{c^0_{\frac{1}{2}\frac{1}{2}} + c^0_{\frac{1}{2}\frac{1}{2}}\right\}}$$

and similarly for $\langle P^0_n Y^0_2\rangle$, $\langle P^1_n Y^1_2\rangle$, $\langle P^2_n Y^2_2\rangle$.

SUMX is used to select Δ^{++} events with cuts on $M^2(p\pi^+)$ and $\cos\theta^* < 0$, and to calculate the mean and error on the above moments. Figure V.3 shows the higher moments. (The $\cos\theta^*$ cut removes events in the region of interference between Δ^{++} and Δ^+ or ρ^+, ref. 43)

Use of a different highest wave at each energy would have made continuity checks difficult, so the energy range was split into just three parts, each with a different highest wave. Moments with n=4 and above are compatible with zero up to 850 MeV/c. Examination of the R coefficients shows that DD5 and higher waves can therefore be neglected. DD3 waves would be the highest ones up to this energy, but ΔDD5, the largest 5/2 wave in Rob Stevens' analysis was also kept as a test of the validity of the technique. At 1040 MeV/c n=6 is the highest significant term; this means that incident G waves and above are negligible. The R_6 coefficients show that only incident F7 and above waves

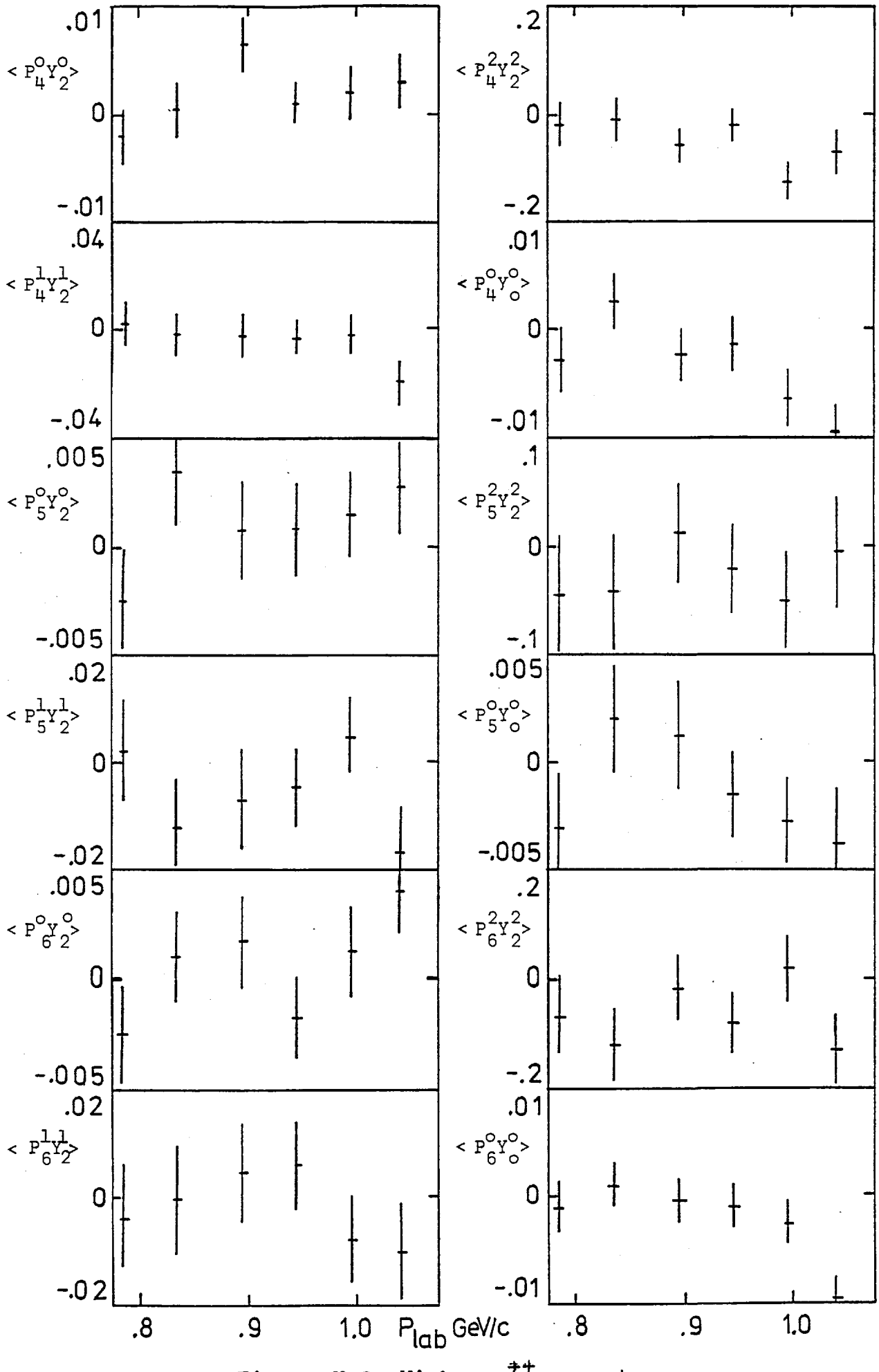

Figure V.3 Higher Δ^{++} moments

contribute to n=6, and that the direct contributions of FF7 and FH7 are in the ratio -4.404 to 1.616, so the highest wave included at 1040 MeV/c was the FF7. This was also the highest wave at 995, again as a check. At 895 and 945 MeV/c, J=5/2 was taken as the limit, giving FF5 as the highest wave, since incident (and hence outgoing) G waves were considered negligible.

The second question, that of deciding which waves to keep was approached in a new manner. The usual technique is to make many trial fits, using their results to decide which waves should be rejected, and finally to come to a set of waves for use in the final fits. Much computer time is used to reject supposedly insignificant waves, yet if they are insignificant then leaving them in the fit should not affect it much, and the computer time can be used to make more fits with the full set of waves. This can fail, particularly if there are few events, if the small waves parametrise statistical fluctuations. In such a case, many solutions may be found, or solutions at adjacent energies may be very different. Test runs showed that neither of these happened, so the full refitting was done using all waves up to the maximum in each set. We therefore had a 21-wave set up to 850 MeV/c, a 30-wave set at 895 and 945, and a 34-wave set at 995 and 1040 MeV/c.

For comparisons with the results of Saclay (ref. 16) we used an 8 wave set:-

Δ SD1, PP1, PP3, DS3, DD3

ρ_1 SS1, PP1

ρ_3 DS3

These were the only $J=\frac{1}{2}$ and $J=3/2\ \pi^+p$ waves in the SLAC-LBL solution B (ref. 15) Saclay used them in comparisons with SLAC-LBL $\pi^+p\pi^o$ results, we also found them sufficient for comparisons of our $\pi^+p\pi^o$ results with Saclay at c.m.e. 1.585 GeV.

V.4.2 Likelihood calculation and fitting routines

Given a list of waves together with a set of X's, with a file containing F's and a table of R's, one can calculate the likelihood $\mathcal{L}$. The programmed function that does this is the heart of the whole system of programs. It is used by a fitting routine which searches for a best value of $\mathcal{L}$ by trying various values of the X's. Some details of the likelihood calculating function must therefore depend on the nature of the fitting routines used.

We use the VA series of minimising routines from the Harwell subroutine library (ref. 23); some of these operate on knowledge of the function value alone, others also require gradients, or gradients and second differentials. Our function was written to provide either a value of $\mathcal{L}$ alone, or $\mathcal{L}$ and its gradients with respect to amplitudes and phases of the X's. Rob Stevens used VA01AD and VA06AD; the results given in his thesis (ref. 9) were obtained by VA06AD. We at first avoided the use of VA09AD; in a report on its performance (ref. 39) its author wrote that it was in many ways better than VA01AD and VA06AD, but that it could not always be guaranteed to find a minimum. It was however easier to calculate errors on parameters with VA09AD so after VA06AD had found a given minimum, a refit with VA09AD was used to obtain errors.

Further runs with the 14 wave set showed that VA09AD did find the same minima as VA06AD. Reference 39 also showed that as the number of parameters being fitted is increased, VA09AD becomes much superior to VA06AD. When we began to refit our data with all waves, we again compared the two. Four fits to the 750 MeV/c data set with 21 waves were made, each starting at a random set of parameters, using VA06AD with a loose convergence criterion. The results were compared with those of 24 similar runs using VA09AD with standard convergence criteria. Of the VA06AD runs, three took about 2800 function calls to minimise, and came to essentially the same minimum, with parameters differing by about 10%. Three of the VA09AD runs came to this same minimum - they took about 350 function calls each, and their fitted parameters differed by less than .01%. The fourth VA06AD run took 2550 calls to come to a different minimum, similar in some waves to a minimum found by two VA09AD runs, though owing to the loose convergence criterion it was not possible to determine if this was exactly the same minimum.

It became evident that for more waves we would have to use VA09AD. It has the further advantages of requiring less core storage than VA06AD, and of being very similar in use to VA10AD which calculates gradients numerically instead of taking analytic ones from the likelihood calculating function. This meant that a short run of VA10AD could easily be made to check the analytic expressions for gradients.

To simplify calculations and avoid the use of numbers too large for the computer to handle, we worked with the logarithm of $\mathcal{L}$. We used minimising routines to find maxima of $\mathcal{L}$, so we chose to minimise minus the log likelihood. We therefore rewrite equation 4.16:

$$L = -\ln \mathcal{L}$$

$$= -\sum_{i=1}^{N} \ln \left\{ \sum_{\mu} \sum_{nm} X_n X_m^* F_{\mu}^{na} i(\underline{y}_i) \left[F_{\mu}^{ma} i(\underline{y}_i) \right]^* \right\}$$

$$+ N \ln \left\{ \sum_{pq} X_p X_q^* R_{pq} \right\} \qquad (5\text{-}1)$$

Our results are presented as the amplitudes and phases of T-matrix elements, so the programs used amplitudes and phases of the X's as fitting parameters. A maximum likelihood solution is independent of the choice of physical parameters, so real and imaginary parts could also have been used. In order to test if this made minimising easier, particularly in the case of poorly determined phases, the author wrote a new version of the likelihood and gradient calculating function in terms of real and imaginary parts. Test runs showed that this gave the same minima as the amplitude and phase version but actually took longer to minimise, so we returned to the amplitude and phase version.

The considerable effort required to write this new version was not wasted though; it checked out the original version, and highlighted the importance of using double precision arithmetic.

FORTRAN Real variables on IBM System 360 computers are stored in 32 bits of memory. This is sufficiently accurate if relatively few operations are performed on some number, as in calculations of angles and masses for D-V analysis. Calculations involving many operations can however suffer serious loss in accuracy, so calculations of likelihoods and their gradients, which depend on many operations for each of up to 8,000 events, have to use double precision (64 bit) Real variables. If single precision is used, a minimiser may spend many iterations fruitlessly trying to improve on a minimum as a result of rounding errors. Double precision arithmetic on 360 computers is exactly the same as single precision arithmetic, so there is no loss of speed, only more memory is required. Complex double precision arithmetic does require subroutine calls and is therefore slower. Thus the real and imaginary parts version, which used complex double precision arithmetic, was slowed down relative to the amplitude and phase version, and any gains due to easier minimisation were lost.

While comparisons were being made between the two versions, it was noticed that some sines and cosines in the amplitude and phase version were being stored as single precision numbers. When these were changed to double precision VA09AD was found to minimise in some 20 iterations fewer than previously.

A recent addition to the CERN minimising program MINUIT (ref. 20) allows the user to plot contours of the function being fitted with respect to changes in two fitting parameters, and we wanted to try this. As the contour

plotting facility was available only with a single precision version of MINUIT, we used a single precision likelihood. MINUIT was completely unable to find a minimum, because single precision work makes minimising difficult as mentioned above, and because its minimising algorithms are too simple-minded. To obtain contours, MINUIT uses subroutine MIGRAD to calculate an estimated covariance matrix, but MIGRAD was unable to obtain a positive definite covariance matrix. A brief description of VA09AD which uses a similar, but more sophisticated minimising algorithm will help to explain the problem.

VA09AD uses a quasi-Newton minimising algorithm. The parameters at iteration number (k+1) are derived from those at iteration number k by:-

$$\underline{X}_{k+1} = \underline{X}_k - \alpha H_k \underline{g}_k$$

where $\underline{X}_k$ is the vector of parameters X at step k

$\underline{g}_k$ is the vector of gradients $\frac{\partial L}{\partial X}$ at step k, in the function L

α is a scalar, chosen by VA09AD, such that the reduction in L at step (k+1) should be about the same as the reduction at step k

H_k is the estimated covariance matrix at step k,

$$H_k = G_k^{-1},$$

G being the matrix of second derivatives $\frac{\partial^2 L}{\partial X_i \partial X_j}$

VA09AD represents G by

$$G \doteq L D L^T$$

where L is a lower triangular matrix and D is a diagonal matrix.

The approximation to G can then be kept positive definite by ensuring that d_{ii}, the elements of D, are all positive. This then avoids the problem encountered by MIGRAD. VA09AD starts with the assumption that G is a unit diagonal matrix, then updates its estimate of G during minimisation. The value of α at the first step is obtained from an estimate of the likely reduction in L, supplied by the user. Minimisation stops when it satisfies the convergence criterion:-

$$X^n_{k+1} - X^n_k < \varepsilon_n \text{ for all } n,$$

ε_n being the accuracy required by the user on the parameter X_n. Reference 39 gives full details of VA09AD, and reference 40 gives useful maximum likelihood formalism details.

Minimisations involving all waves and about 8,000 events spend up to 10 hours in the computer, and it is very wasteful to lose the results of a minimisation job that fails during execution because of computer troubles. In addition to checking and changing the likelihood calculating function, the author therefore rewrote VA09AD to store the vector $\underline{X}$ and the matrix H. The program could then be restarted with little trouble after any failure, and the final H could be kept for use in error calculations.

V.4.3 Performing the fits

Starting from a given set of parameters $\underline{X}$, VA09AD will search for a minimum of L corresponding to a new set $\underline{X}$ which describes the data better than does the starting set. If an approximate solution is known, it can be used to provide starting values. Such an approximate solution

is available in the case of a refit with a few waves changed, or if a solution at one energy is used as a starting point at another energy - a continuation fit. If no a priori knowledge is assumed, or if a very different solution is expected, random values are used for $\underline{X}$ - a random start. In the work described here random starts and continuity runs were both made.

The most convenient situation would be if all fitting runs at one energy found the same minimum, which should be a physically meaningful description of the interaction, and similar to solutions at neighbouring energies. It is more usual though to find several minima at each energy, and a suitable strategy for dealing with this must be adopted.

We can first note that a global minimum is wanted - one that is a minimum in relation to the whole parameter space, and whose presence can be detected in other regions of parameter space. Local minima are not useful, their existence can only be detected locally, they are found only if the minimiser happens to come close to them, so they are unlikely to be found by another fit starting from a different set of X's. Secondly, minima very different from the physically required one may be found, either because the minimiser has not "seen" enough of the parameter space to find the global minimum, or because there are not enough events in the data sample to distinguish the correct minimum clearly from the others. These minima can be rejected on the basis of continuity checks. Thirdly the required minimum may itself be ill-defined, and consist

of a number of minimum points lying close together in the parameter space.

What sort of runs should be made to identify these minima, and how many? We had the advantage of knowing what other workers had done, and with what results. The strategy usually adopted had been that of generating many random sets of values for the X's, and using all of them, or a selected subset as starting points for full fitting runs. SLAC-LBL generated 2000 sets at each energy, calculated the likelihood for each set (using only 600 events), and kept 10-20 sets that gave the best likelihood at each energy. They then used these for their initial fits.. Saclay performed 10-20 fits from unselected random starts at their highest energies, but scaled any amplitude that violated unitarity, and they claim that this makes their method equivalent to an enormous number of starting values. In our earlier work, Rob Stevens generated about 150 random starts at 895 and 945 MeV/c, and used the dozen or so with the best likelihoods as starting points for full minimisations. At 995 MeV/c, 50 random sets were generated, and the best 3 were used. The results of Rob Stevens' fits gave unique minima at the three energies, and continuity was used to obtain a 1040 MeV/c solution. SLAC-LBL and Saclay obtained more than one minimum, then removed or added waves and refitted until they obtained unique and continuous solutions.

As already mentioned, we decided not to remove small waves; instead of this we made random starts at all energies,

and followed these up with a few continuation runs. The idea of starting from those random starts that had the lowest minus log likelihoods did not appear to be worth pursuing, indeed if one starts too close to a minimum, the minimiser will have trouble in examining the parameter space and finding exactly where the minimum is. A case can even be made for starting at the random sets with the worst likelihoods, as these are bound to be far from minima, getting a good view of the parameter space, and having a better chance of finding global minima. We eventually decided to generate random starts with amplitudes linearly distributed between 0. and 100. and phases between 0. and 2π, using them without any prior checks or scaling. The first steps made by a minimiser are essentially random, so in effect the minimiser makes a random search for us, starting at the arbitrary point given to it, and deciding on a point from which to minimise properly. Given that the first 50 steps are nearly random, 20 random start jobs are equivalent to 1,000 individually tested random sets, but the information thus gained is used in further minimisation.

A random start job can take up to 60 minutes computer c.p. time, and stay in the computer for up to 10 hours. We wished to perform enough random fits to examine the probability distribution of minima at each energy without wasting computer time. Local minima and those with a small probability of being found could then be rejected, and the others kept for use in a continuity search. We decided to perform at least 20 random start runs at each energy. If a

minimum is found only once in 20 runs and if $\sqrt{N}$ errors are used on the probability distributions of minima, then that minimum has a probability of 5%±5%. Minima found by only one run were rejected because of this low probability, and also because they had been found only once and could have been local minima.

To check this technique, we made additional random starts at 750 MeV/c, bringing the total to 60 random starts. The numbers of minima found, and the relative probability of finding them, as the total number of runs increases, are shown in Table V.2. It can be seen that the assumption of $\sqrt{N}$ errors is justified, and also that 10 runs do not suffice to find all acceptable minima, whereas beyond 20 runs we are only improving statistics, unnecessary once we know which minima to retain.

Table V.3 summarises the runs made at each energy; random starts and continuation runs. 20 or 21 random starts were made at each energy except at 750 MeV/c, where the number was extended to 60 for the above test, and at 1040 MeV/c where a larger number of low probability minima was found. At this energy 35 random starts were made, and all minima found 2 or more times were kept - this represents an upper probability, within errors, of 9.75%, close to the 10% (within errors) limit imposed at the other energies.

The question of which minima were the same had to be examined in some detail. To begin with, our likelihood function,

Solution	Random starts which found this solution	%probability of finding given solution as predicted by the first n runs					
		n=10	n=20	n=30	n=40	n=50	n=60
1	1,2,4,5,8,9, 11,12,15,16, 18,29,30,39, 41,46,48,50, 51,52,53,54, 55,58	60±25	55±17	43±12	35±9	36±8	40±8
2	3,10,20,22,23, 24,31,32,36, 37,38,40,42, 43,44,47,49, 56,57,60	20±14	15±9	20±8	30±9	34±8	33±7
3	6,14,19,26,34, 35,45,59	10±10	15±9	13±7	15±6	14±5	13±5
4	7,33	10±10	5±5	3±3	5±4	4±2	3±2
5	13,17,27,28	-	10±7	13±7	10±5	8±4	6±3
6	21	-	-	3±3	3±3	2±2	2±2
7	25	-	-	3±3	3±3	2±2	2±2

Table V.2 Probabilities of finding different minima at 750 MeV/c

Mean c.m. energy (GeV)	Number of random starts	Number of continuation runs	Number of solutions found by 2 or more runs
1.439	20	1	2
1.495	20	3	2
1.526	21	3	5
1.526*	60	3	6
1.550	20	1	4
1.577	20	2	5
1.612	21	0	3
1.640	20	2	5
1.668	20	2	4
1.692	35	2	8

* Two lines are given for 1.526, the second gives the result of the increased number of runs, made to check statistics.

Table V.3

Summary of fitting runs

equation 4.16, is scale-independent; if all the amplitudes of the X's are multiplied by the same scale factor A, the value of 4.16 is unchanged. Similarly, if all phases are changed by the same angle ϕ, the likelihood is again unchanged. There are therefore two redundant parameters which could be removed by the fixing of the amplitude and phase of one wave. This method was not used though, because it leads to slower minimisation. The VA minimisers can cope with this redundant parametrisation, and do find minima, but with this arbitrary scale and phase. To simplify comparisons, the parameters were so scaled and rotated at the end of each fitting run as to make the amplitude and phase of the ΔSD1 wave equal to 1.0 and 0.0.

The program ALLCOM was then used to compare the minima found by all fitting runs at a given energy. Two levels of similarity between minima were observed. Some sets of minima were the same to 1 part in 10^3 in all parameters; these are the ones identified as being the same in tables V.2 and V.3. Groups of minima similar at the 20% level in the larger waves were also found, but they are identified as separate minima in the tables, and further discussion of them is left to Chapter VI.

V.4.4 Error Calculations

Once a minimum has been found, errors on the parameters can be calculated. The minimising technique of VA09AD helps in this, because it provides an approximate second derivative matrix, as described in V.4.2.

Given a maximum with parameters X_i^{max}, X_j^{max}, X_k^{max}.... and covariance matrix H, it can be shown (see for instance ref. 40) that :-

$$\langle (X_i - X_i^{max})(X_j - X_j^{max}) \rangle = H_{ij}$$

This is only true for a properly constructed log likelihood function. If terms that penalise undesirable results are included in the function to be maximised, then the equation is no longer true. Our likelihood function is not constrained, so no such problems are encountered.

From the definition of the standard deviation on a parameter X_i:

$$\Delta X_i = \sqrt{\langle (X_i - X_i^{max})^2 \rangle} \quad , \text{ we have}$$

$$\Delta X_i = \sqrt{H_{ii}}$$

VA09AD estimates the second derivative matrix

$$G = \frac{\partial^2 L}{\partial X_i \partial X_j} = H^{-1}$$

The exact second derivative matrix would be impossible to invert, because of the two redundant parameters (see end of V.4.3). Fortunately the approximate value of G saved by VA09AD at the end of a fitting run can be inverted, giving an approximate H, and hence approximate values for the standard deviations which we quote as the errors on the parameters. Errors obtained from values of G calculated by different random

starts that came to the same minimum varied by up to 20%. A number of fitting runs were also made with different waves fixed, and errors were calculated on the free waves. This is the correct technique as the matrix G thus obtained is no longer singular, but it was not found to make much difference; the errors were seen to lie within the 20% range of the approximate method. The method of calculating approximate errors is therefore satisfactory, and gives error estimates within 20% of the correct values.

Errors on T-matrix elements are obtained directly from the errors on the fitting parameters, since the fractional errors on the X amplitudes and the T amplitudes are the same, and the absolute errors on the X phases and the T phases are the same.

Other errors, in particular those on σ^{J^P}, the inelastic cross-section in a given J^P state, were also calculated from the covariance matrix. Given a function Y of the fitting parameters, the best estimate of Y is

$$Y^B = Y(X^{max})$$

To first order in $(X_i - X_i^{max})$

$$Y - Y^B = \sum_i \frac{\partial Y}{\partial X_i} (X_i - X_i^{max})$$

so that

$$\langle (Y - Y^B)^2 \rangle = \sum_i \sum_j \frac{\partial Y}{\partial X_i} \frac{\partial Y}{\partial X_j} \langle (X_i - X_i^{max})(X_j - X_j^{max}) \rangle$$

giving the error formula

$$\Delta Y = \sqrt{\sum_i \sum_j \frac{\partial Y}{\partial X_i} \frac{\partial Y}{\partial X_j} H_{ij}}$$

The redundant parametrisation must again be given consideration; the expression 4.13 for σ^{J^P} contains the scaling condition 4.10, necessary because of the scale invariance. In the same way as we calculate approximate errors on the fitting parameters, we ignore the effects of this scaling and calculate errors on 4.13 unscaled:

$$\sigma^{J^P} = \sum_a \sum_{nm \epsilon J^P} R^a_{nm} X_n X^*_m$$

The error formula is applied to this, then σ^{J^P} and $\Delta \sigma^{J^P}$ are scaled down. Comparisons of results from different random starts again show a variation of about 20% in the errors.

V.5 Results

V.5.1 Ability to reproduce Monte Carlo data.

Before turning to the real data, we describe a test of the programs using Monte Carlo data. The test was a relatively simple one, designed to check if the chain of fitting programs was working. 6 sets of Monte Carlo events were generated according to the old 14 wave solution at 895 MeV/c. The statistics were comparable to the original data, each set contained 6000 $\pi^+ p \pi^0$ events and 1007 $\pi^+ \pi^+ n$ events. These were passed through the GROPE and DISK programs, then fitted starting at the original 14 wave solution. Figure V.4 is an

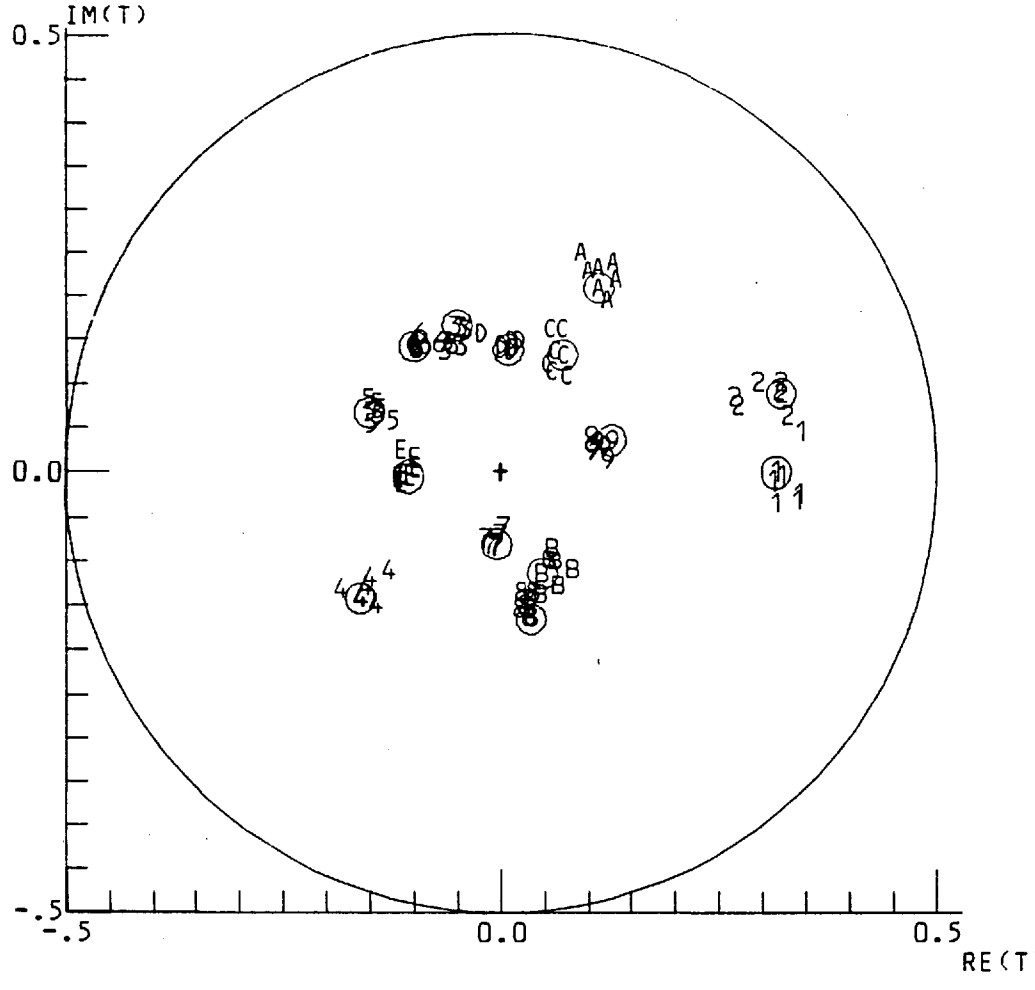

FIG V.4

Parameters used to generate 6 sets of Monte Carlo data (in rings), and results of fits to the 6 data sets.

Argand diagram showing T-matrix elements for the original 14 waves and the results of the fits. It is clear that the programs pass this test, as the solutions obtained do reproduce the original parameters within acceptable errors.

V.5.2 Reproduction of the experimental data

Figures V.5.a to V.5.i show histogrammed projections of the data at each energy together with a curve showing the results of the fit to that data. The fit results were obtained by generating about 100,000 Monte Carlo events at each energy in each channel, binning the required kinematic quantities, then drawing a smooth curve through the results. 6 projections in each channel at each energy were calculated. In the $\pi^+p\pi^0$ channel these are the squared masses of the $\pi^+\pi^0$, π^+p, π^0p combinations, the cosine of the Deler-Valladas Θ angle, the Deler-Valladas Φ angle, and $|t|$, the positive value of the 4-momentum squared transfer from the incident proton to the outgoing proton. In the $\pi^+\pi^+n$ channel the corresponding quantities are the squared masses of $\pi^+\pi^+$ and the two possible π^+n combinations, cosineΘ, Φ/π, and $|t|$ from the incident proton to the outgoing neutron. As the two pions in this channel are indistinguishable, it is a common practice to combine the two possible π^+n mass combinations in one plot, and to enter each event twice in the angle plots making these symmetrical about 0. We have followed this practice, so there is only one π^+n mass squared plot at each energy.

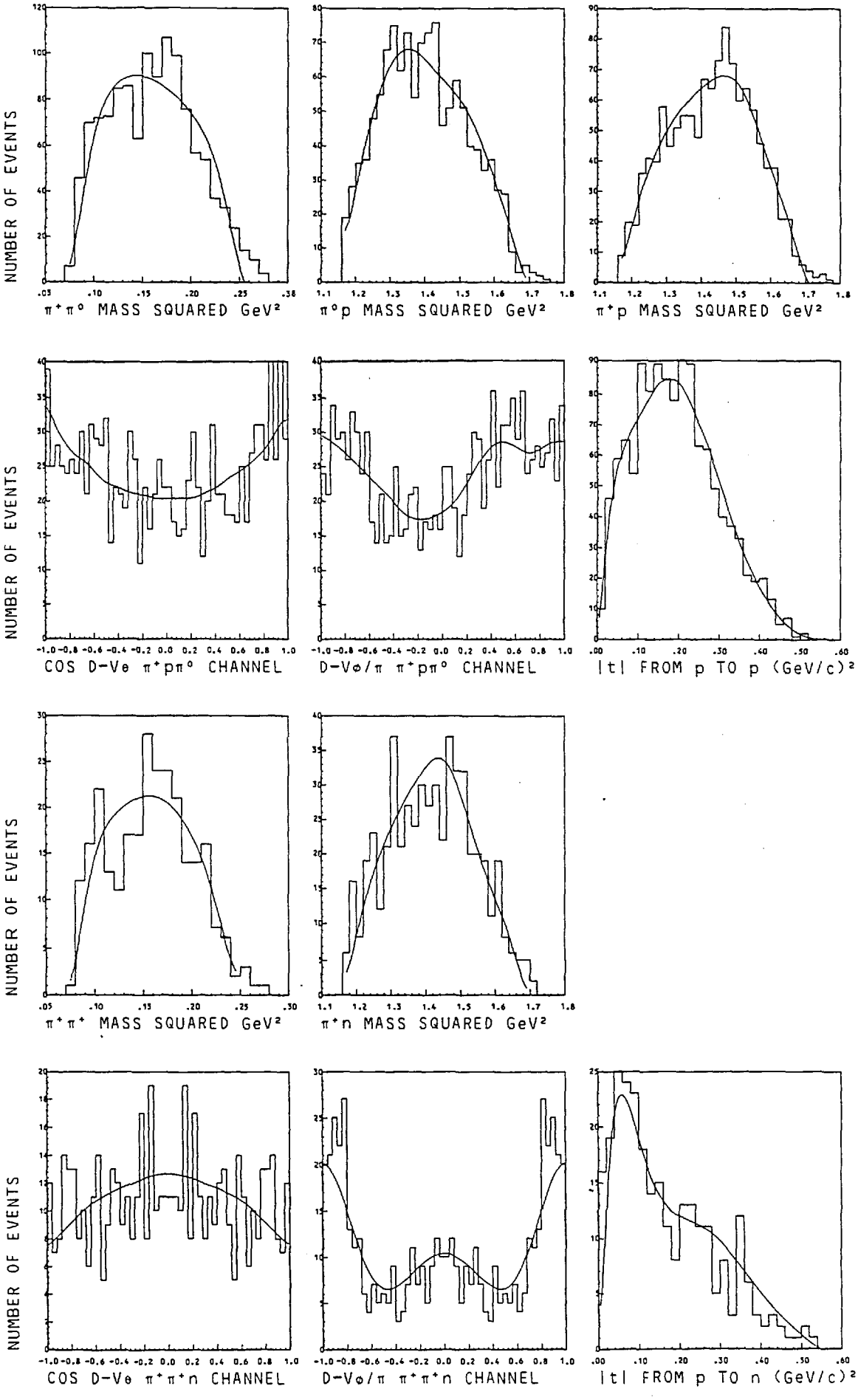

FIG V.5.a 600 MeV/c PROJECTIONS

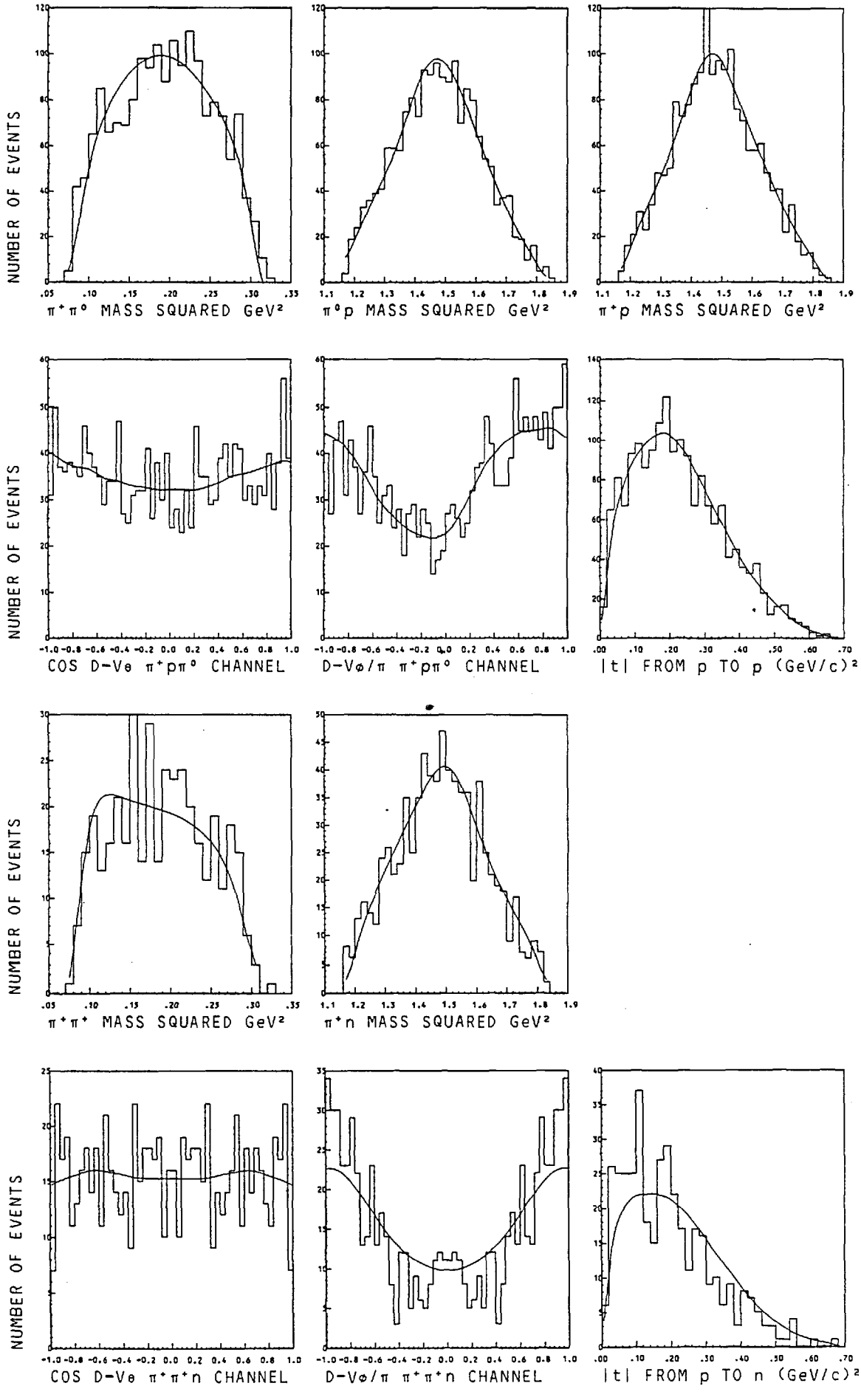

FIG V.5.b 700 MeV/c PROJECTIONS

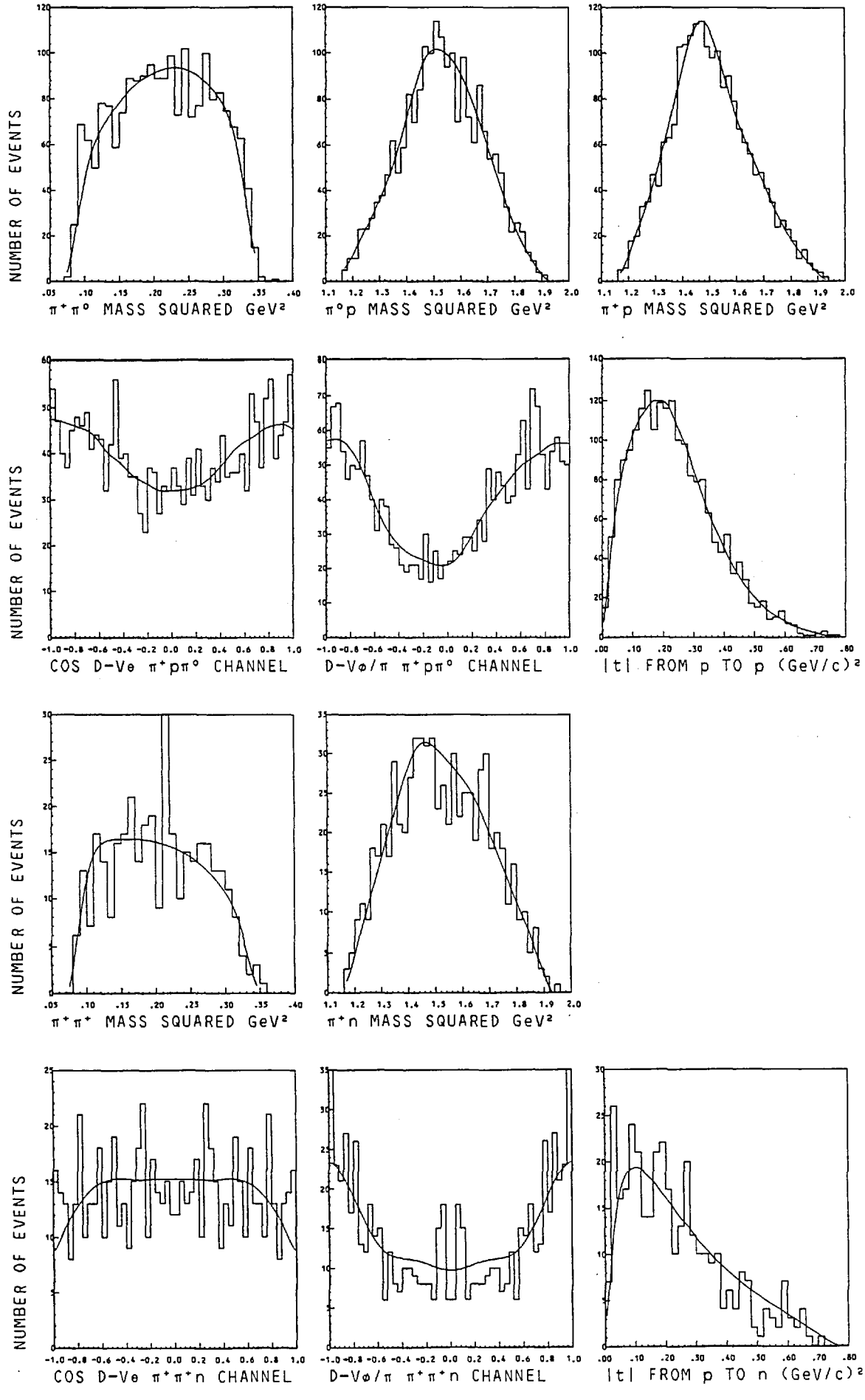

FIG V.5.c 750 MeV/c PROJECTIONS

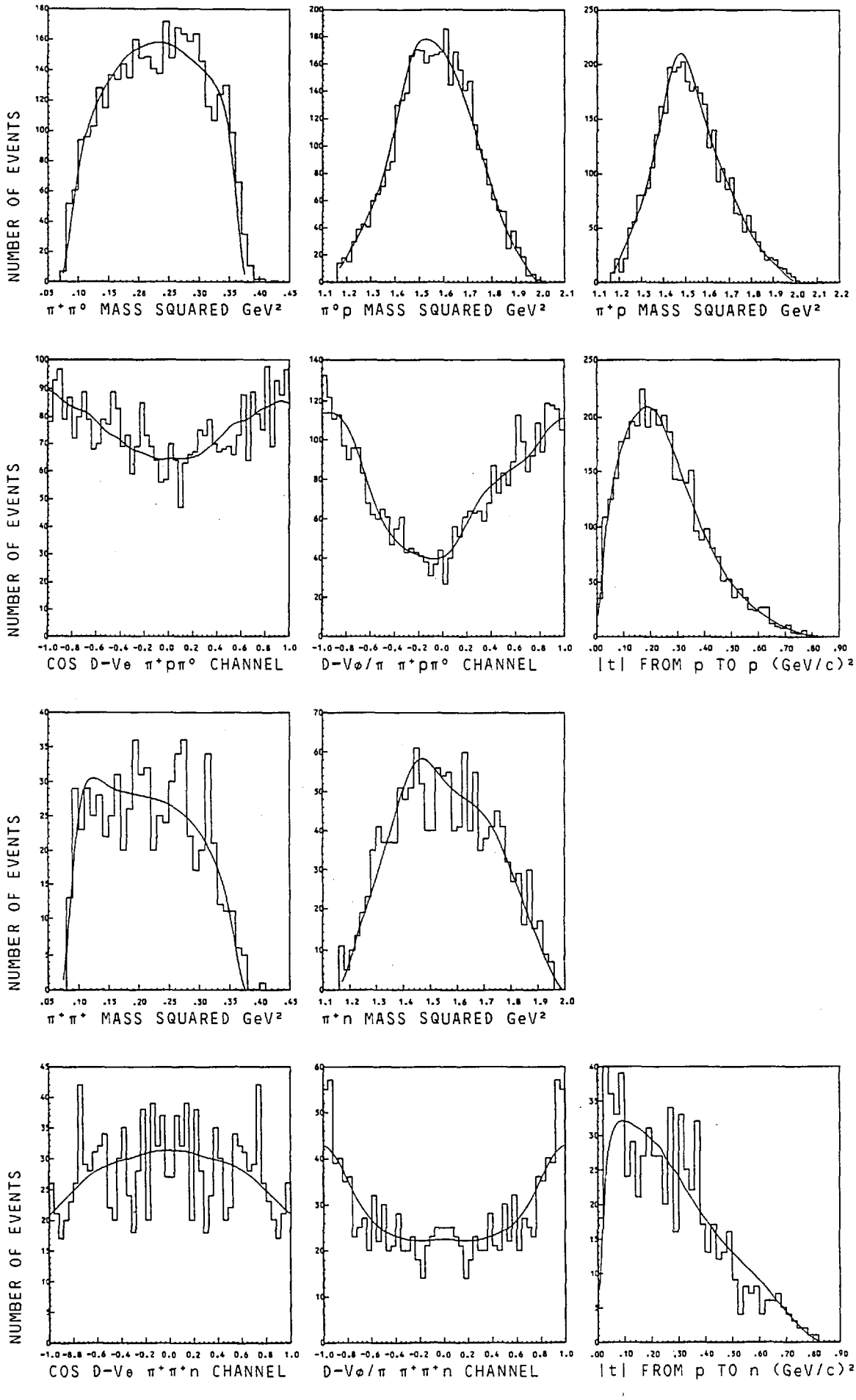

FIG V.5.d 800 MeV/c PROJECTIONS

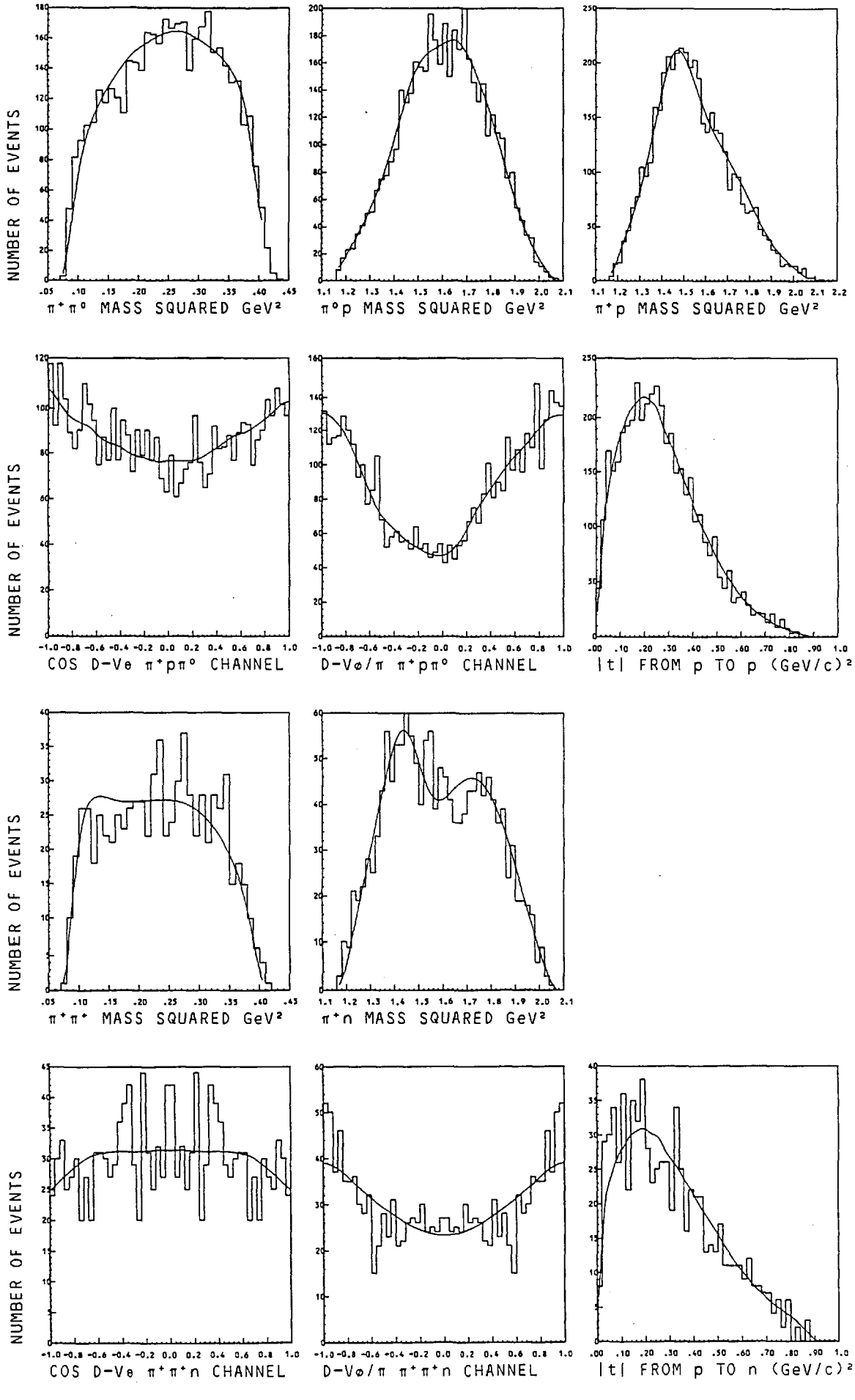

FIG V.5.e 850 MeV/c PROJECTIONS

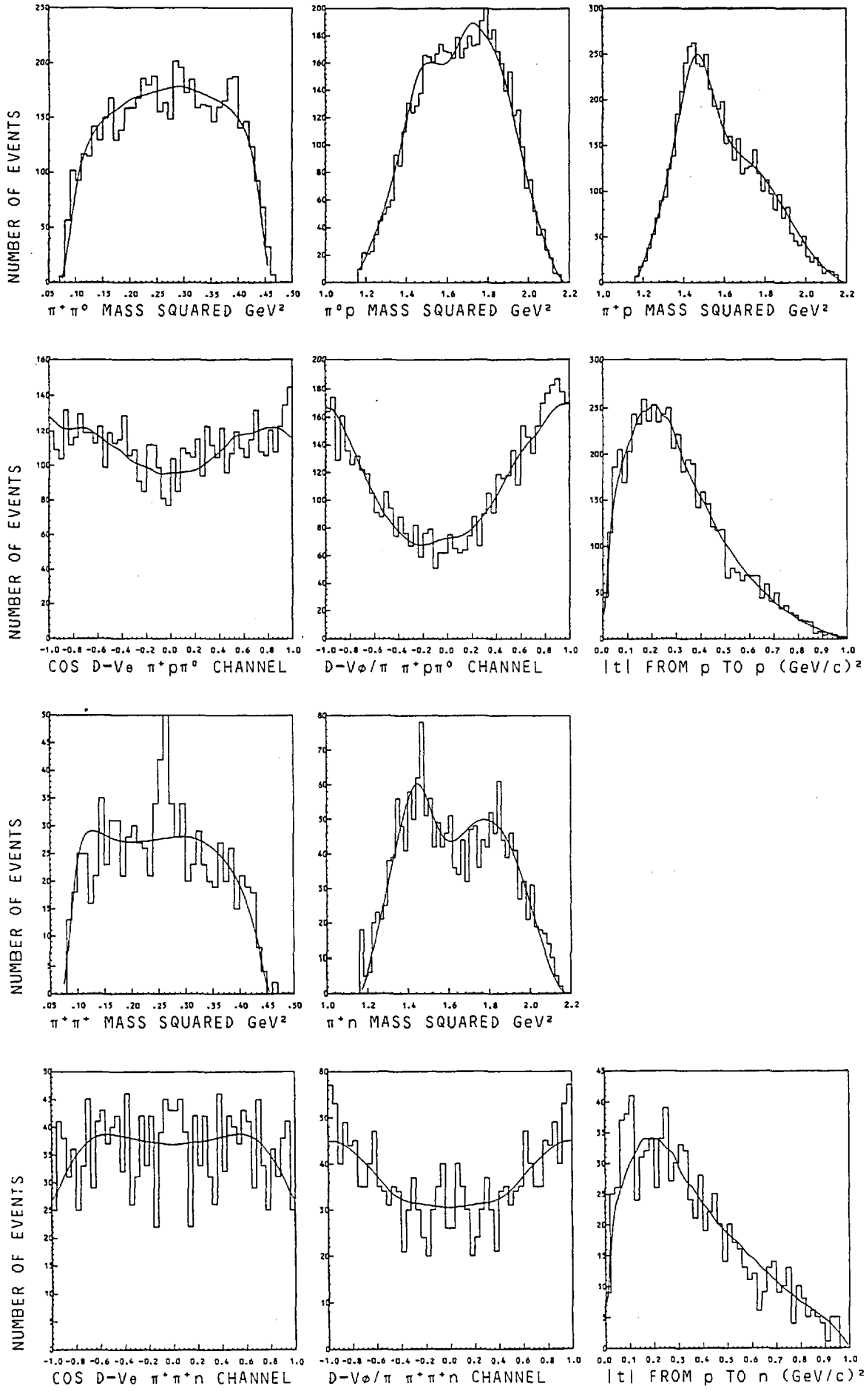

FIG V.5.f 895 MeV/c PROJECTIONS

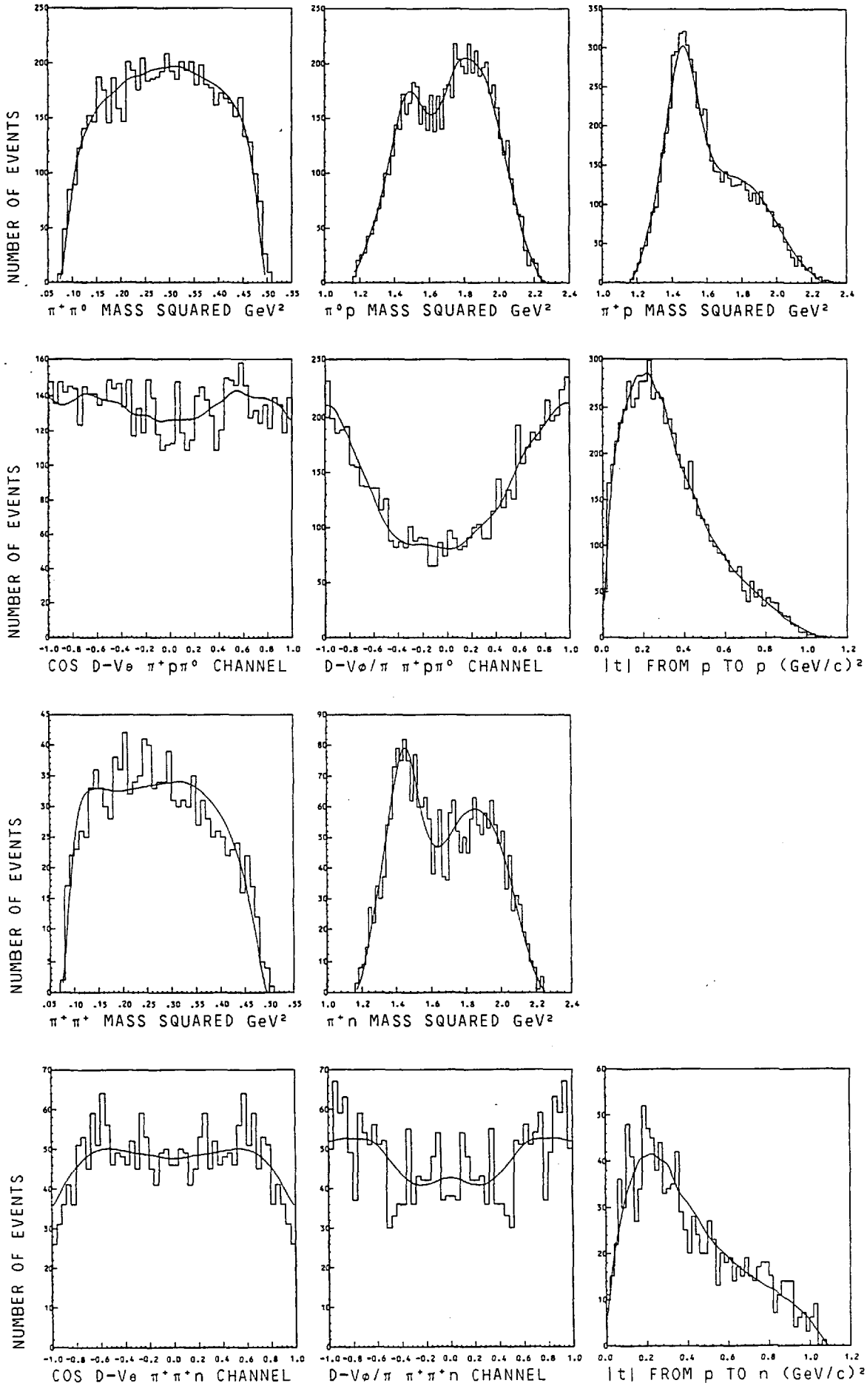

FIG V.5.g 945 MeV/c PROJECTIONS

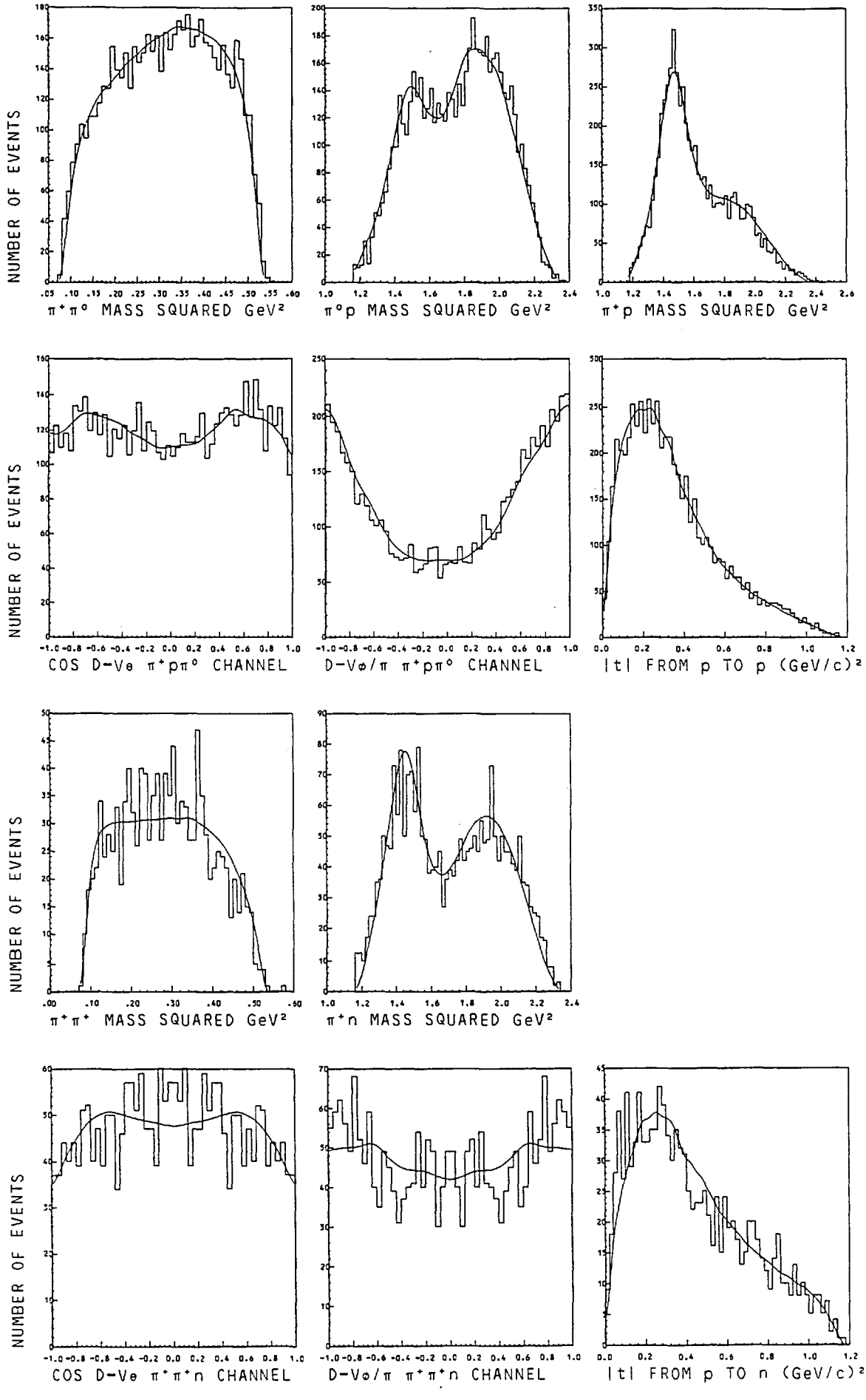

FIG V.5.h 995 MeV/c PROJECTIONS

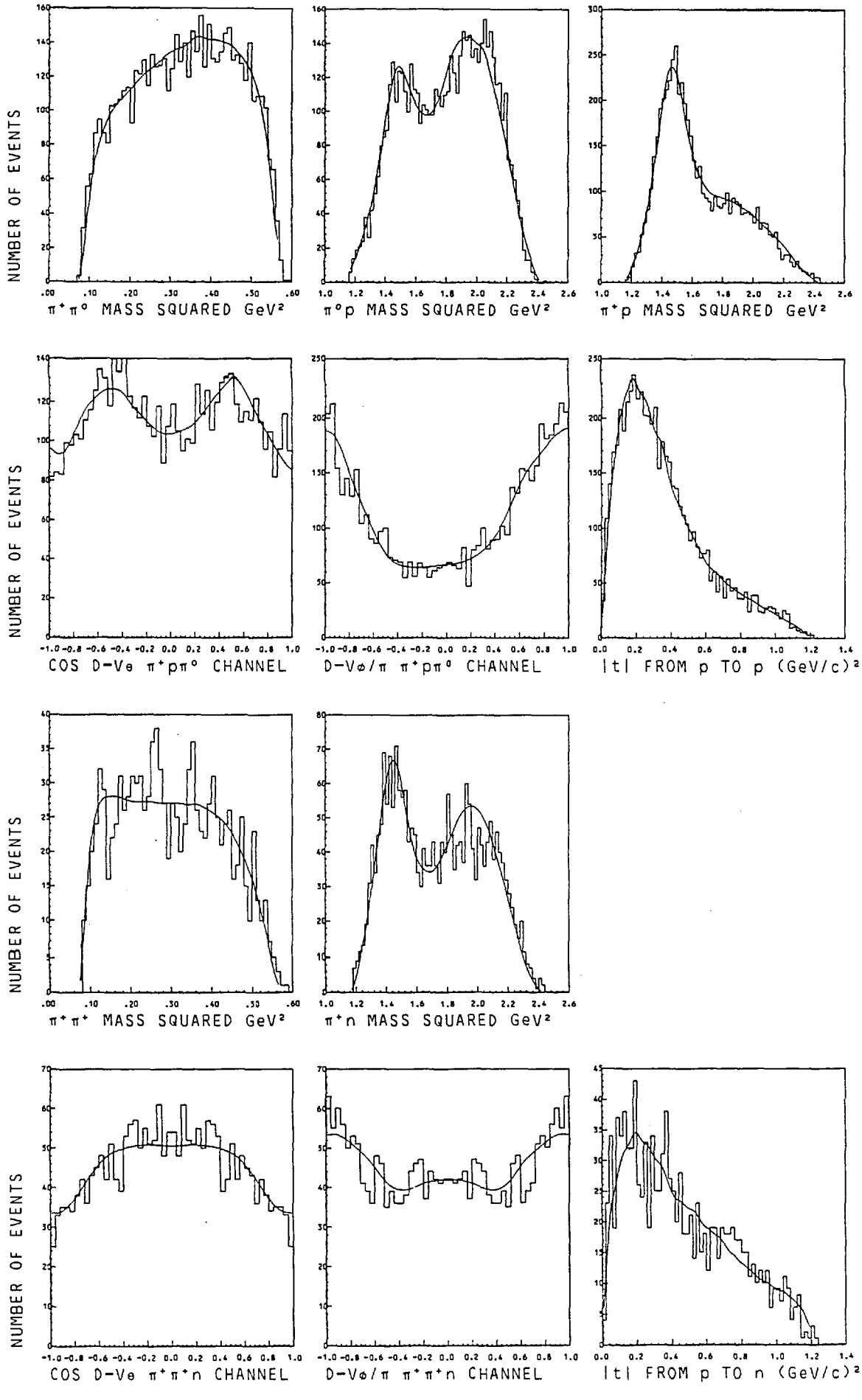

FIG V.5.i 1040 MeV/c PROJECTIONS

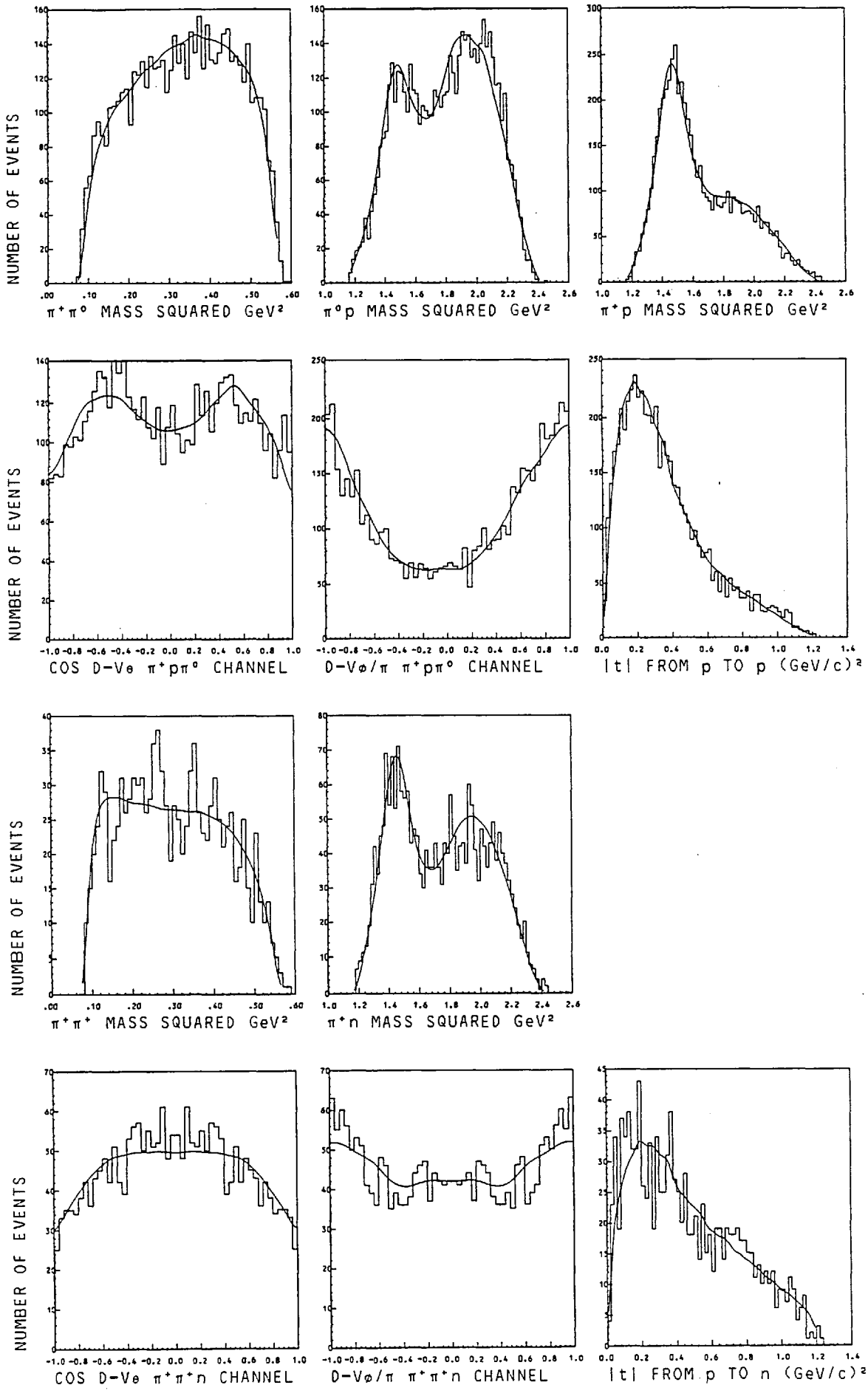

FIG V.5.j 1040 MeV/c PROJECTIONS, FROM ANOTHER SOLUTION

The next chapter describes how one solution was chosen at each energy, the fitted values shown here were obtained from the solutions thus chosen, but to show that the other solutions also represented the data well, figure V.5.j shows plots made using a different 1040 solution, they are all but identical to the first 1040 figure.

Looking at the plots in detail, and taking the $\pi^+ p\pi^o$ channel first, one sees that all the projections are well fitted. Both Δ^+ and Δ^{++} peaks are clearly represented, as are details such as the shoulder at around $\Phi = \pi/3$, particularly clear at the lower energies. The $\pi^+\pi^+ n$ channel is not reproduced quite so well. This can be partly explained by the much smaller numbers of $\pi^+\pi^+ n$ events but deserves careful examination. Comparison of the data at adjacent energies shows that some details in the plots are due to statistical fluctuations which one does not expect to be fitted. Any structure that can only be fitted at the expense of a deterioration in the $\pi^+ p\pi^o$ channel fits will remain unfitted because the $\pi^+ p\pi^o$ channel has a much higher weight. Taking the plots in turn, one first sees that the $\pi^+\pi^+$ mass squared plots show a good fit at some energies, but at other energies they exhibit an enhancement at low mass squared, followed by a dip, neither of which exist in the data. The $\pi^+ n$ mass squared plots are well reproduced at all energies, with the Δ^+ reflection also fitted at the higher energies where it is seen. Cos Θ is generally well represented, though a little too flat, but Φ is worse, with the rise at low and high values very poorly followed at some energies. These angular distribution problems occur when peripheral events are not

fitted, since:-

$$\cos\Phi \sin\Theta = \cos\theta^*$$

where $\cos\theta^*$ is the outgoing nucleon production angle in the c.m.s. system and is small in peripheral interactions. The effect can be shown clearly by plotting t, the invariant 4-momentum squared transfer from the incident proton to the outgoing nucleon, since this is small in peripheral interactions. Plots of $|t|$ (t is always negative in $\pi\pi$N reactions) do indeed show a general failure to fit such peripheral interactions in the $\pi^+\pi^+$n channel. Chapter VII describes a refit with OPE effects allowed for to give a better description of the $\pi^+\pi^+$n peripheral events and of the $\pi^+\pi^+$ mass distributions. This effect is not very serious, and overall the plots show that the data was well fitted.

Figure V.6.a shows the total fitted $\pi\pi$N cross-section in each J^p state, calculated from equation 4.15. The crosses with error bars are our fitted values, error bars are omitted if they are smaller that the crosses. Unitarity limits calculated from elastic partial wave analyses are also shown in the figure. Our values are again those from the fits chosen on the basis of continuity. The numerical values and errors are also presented in table V.4.

Let it be stressed again that the fits were in no way constrained to be similar to the elastic predictions, as was the case with the SLAC-LBL and Saclay analyses. Our results do generally follow the elastic predictions, and because they are obtained independently, this gives mutual credibility to the two sorts of analysis. As is discussed in the next chapter,

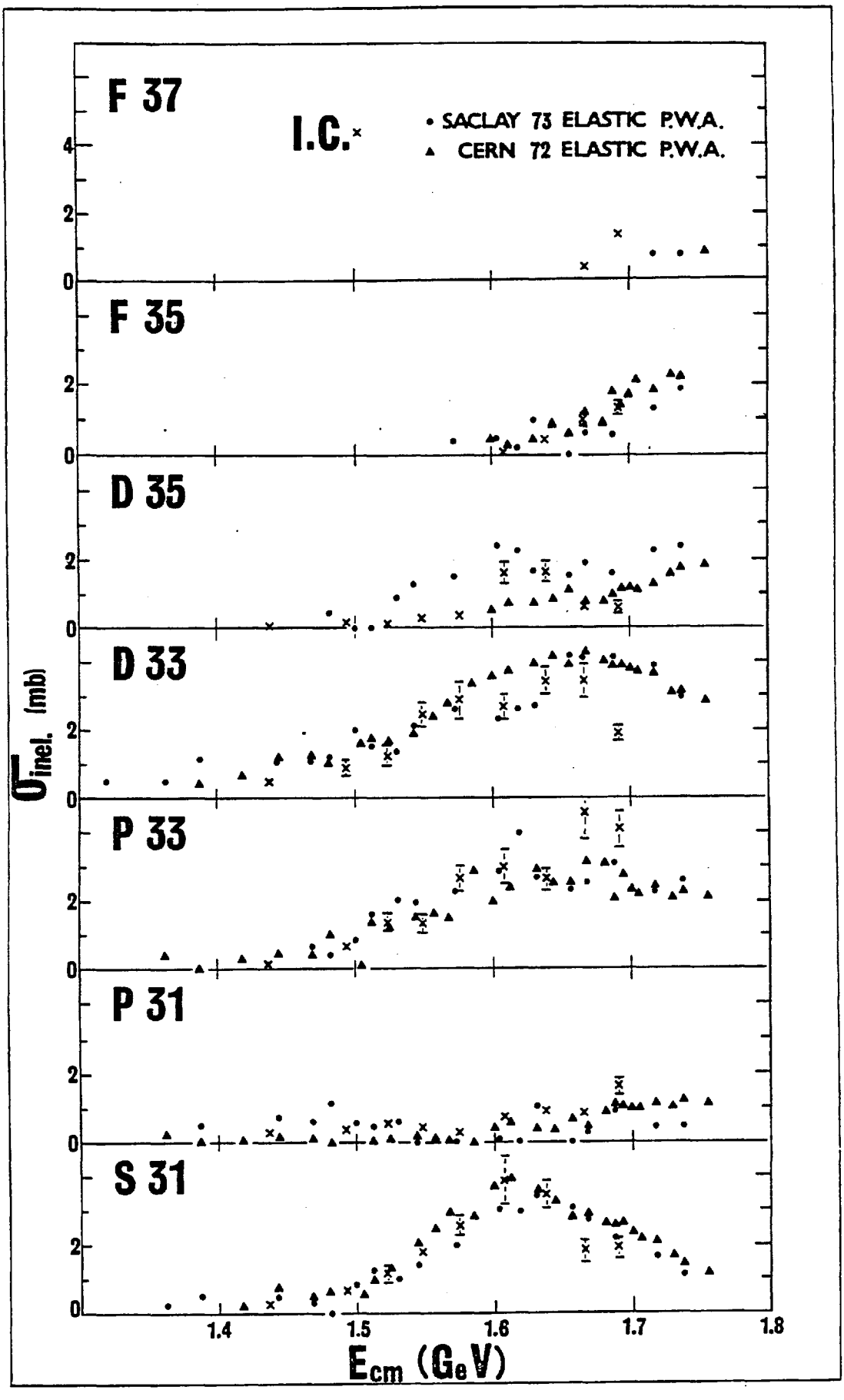

Figure V,6,a σ^{JP} values

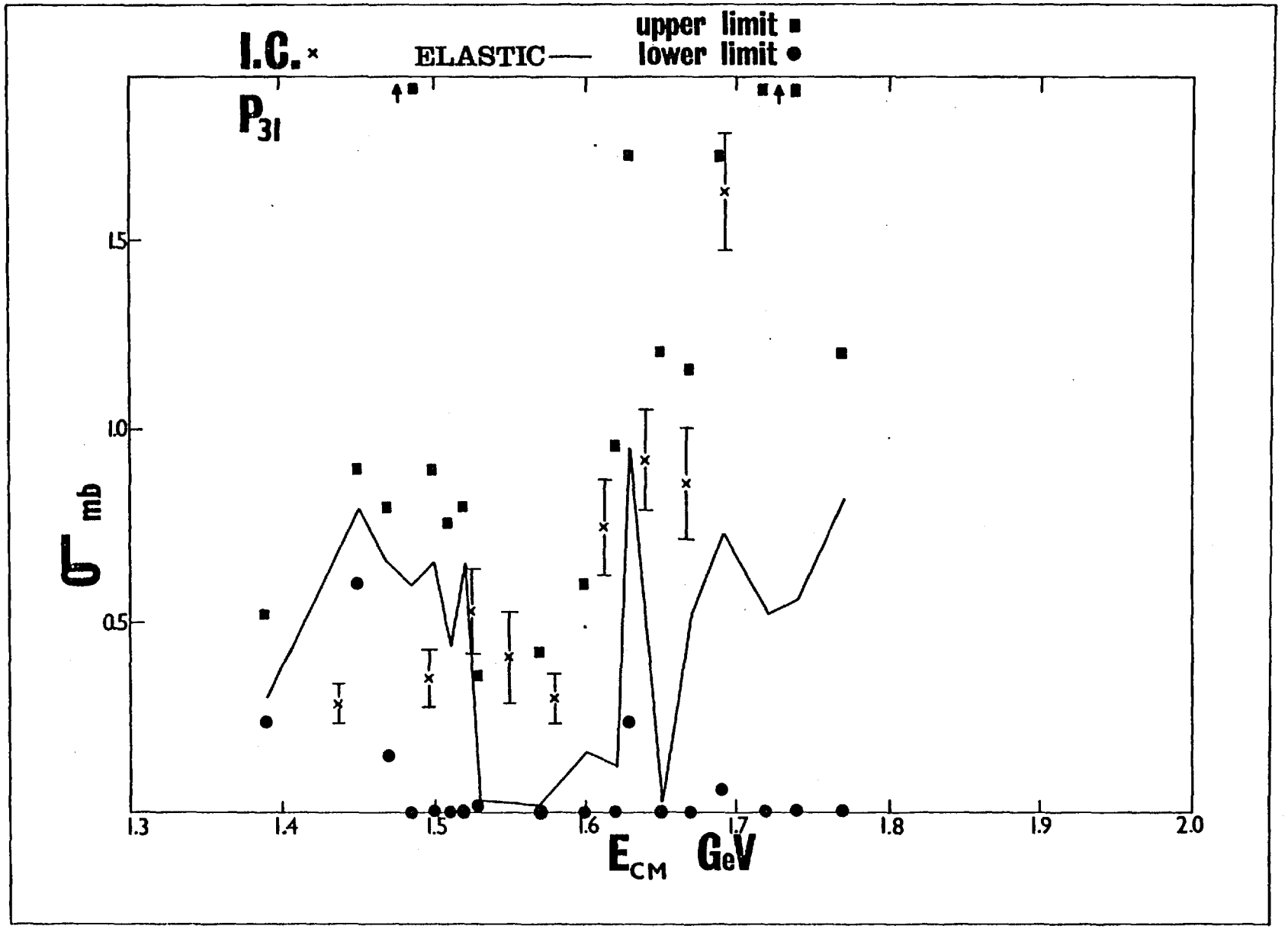

Figure V.6.b Enlarged P31 cross-sections

P_{lab} MeV/c	S31	P31	P33	D33	D35	F35	F37
600	0.270 ±.056	0.276 ±.053	0.093 ±.061	0.403 ±.098	0.008 ±.004		
700	0.681 ±.130	0.342 ±.083	0.627 ±.098	0.865 ±.183	0.036 ±.017		
750	1.188 ±.216	0.521 ±.112	1.355 ±.259	1.183 ±.275	0.153 ±.047		
800	1.788 ±.152	0.401 ±.122	1.310 ±.289	2.402 ±.358	0.231 ±.054		
850	2.560 ±.259	0.292 ±.067	2.655 ±.474	2.853 ±.563	0.311 ±.096		
895	3.897 ±.699	0.739 ±.125	2.998 ±.506	2.643 ±.464	1.578 ±.304	0.065 ±.023	
945	3.494 ±.452	0.918 ±.132	2.622 ±.379	3.417 ±.415	1.585 ±.279	0.454 ±.045	
995	1.882 ±.338	0.859 ±.131	4.549 ±.882	3.442 ±.597	0.577 ±.128	0.981 ±.162	0.340 ±.060
1040	1.911 ±.313	1.619 ±.241	4.104 ±.528	1.891 ±.186	0.534 ±.116	1.240 ±.149	1.300 ±.119

Table V.4

ππN cross-sections in different waves

our top energy is the most difficult to tie in with the rest - this would really require analysis of our higher momenta. The S31(1650) and D33(1670) peaks are clearly seen, as is the tail of the F35(1890).

The P31 wave shows interesting structure, it is shown on an enlarged scale in figure V.6.b. There is a clear bump around 1.53, seen also by the Saclay analysis at a slightly higher energy. Another structure is visible at around 1.65, but this is rather discontinuous at the top energy. This will be discussed again in the next chapter, and in chapter VII in relation to the OPE results.

The P33 shows a strong rise around 1.68 GeV, exceeding the elastic prediction limits as did the SLAC-LBL analysis; these results strongly support the P33(1690). The structure at lower energies in P33 is interesting, but insufficient to give definite support to the PP3(1560) proposed by Saclay (ref. 34). In D33 there is again some interesting but inconclusive detail at the lower energies. The sudden jump in D35 cross-section at the sixth energy is partly due to the fact that only the Δ D35 wave was fitted at the lower energies; the moments analysis did not suggest any need for more, but the plot here suggests that N* D35 and ρ D35 waves may be non-trivial at the lower energies. Even so, there is undeniably a bump in D35 around 1.63 GeV. The F37 wave was fitted only at the two highest momenta, so no firm conclusions can be drawn. The individual waves will be discussed again when the Argand diagrams are presented in the next chapter.

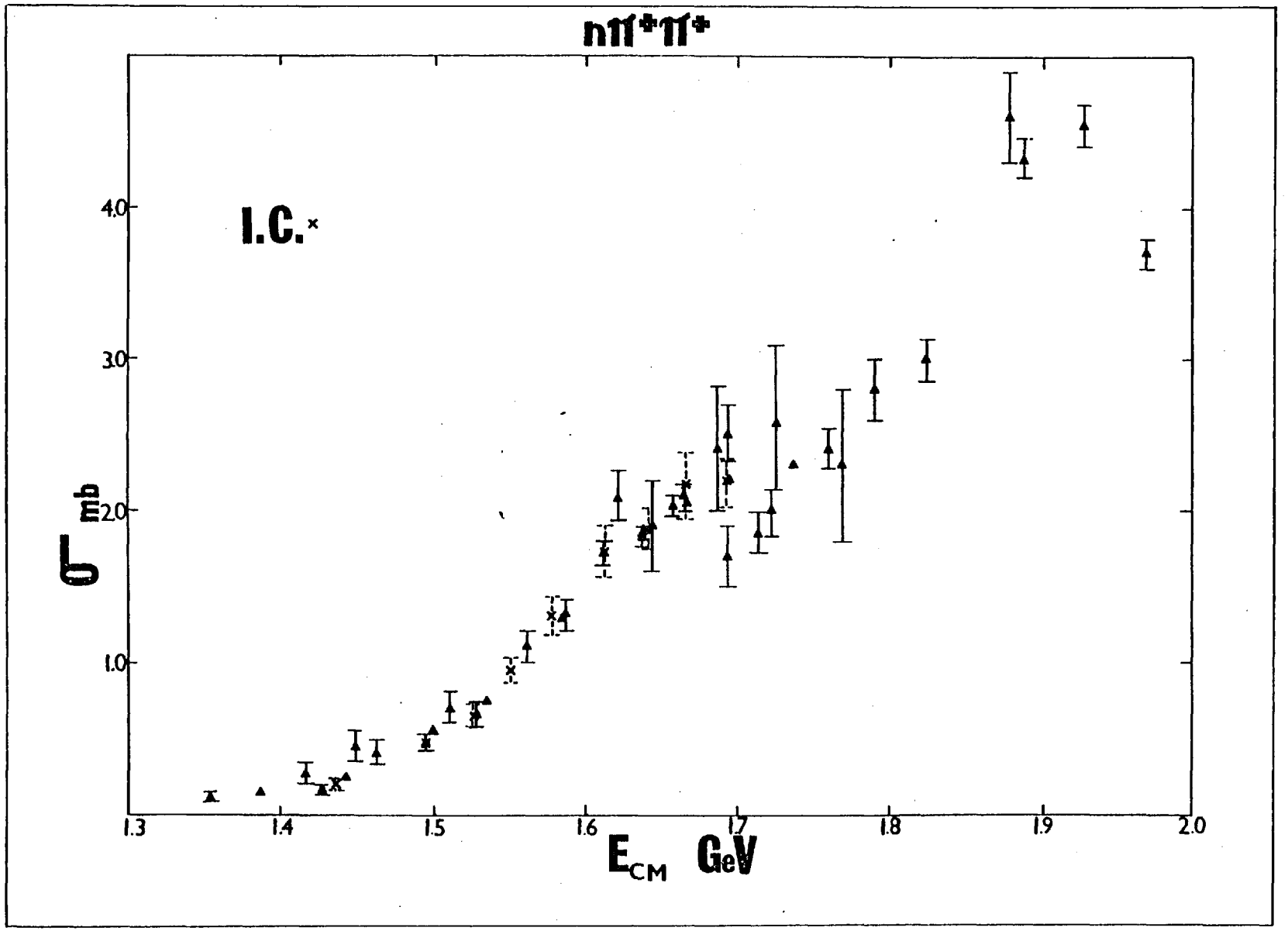

Figure V.7 Fitted $\pi^+\pi^+$n cross-sections

Figure V.7 shows our fitted $\pi^+\pi^+n$ cross-sections. It is a major point of this analysis that in fitting the I=3/2 waves alone, we do fit the $\pi^+\pi^+n$ channel and expect our results to be far closer to the data than the other two major analyses which only predict values for this channel. The results of our fit, marked as crosses with broken error bars do indeed follow measured values accurately. This too has been achieved without constraining the fits in any way.

V.6 Validity of the Isobar Model

Is the isobar model valid? An experiment can only answer such a question by showing whether or not its results are consistent with the original assumptions. If there are inconsistencies then their extent must be examined, and interpreted as being within experimental error, or as demanding refinements of the model, or major changes to it, or even its rejection. Whether or not a model or theory is true is a different question; science advances by improving or disproving theories rather than proving them, and discussion of the question lies outside the scope of this thesis.

The explication of the results of this work has reached a point when this specific question of isobar model self-consistency can be conveniently discussed. The projections and cross-sections just presented provide the material for this discussion; details of a search for continuity, not an isobar model question in itself can be left till later. Figure V.6 shows that all the J=1/2 and 3/2 waves start from low

cross-sections at 1.4 GeV and rise simultaneously. This indicates that the rise in total $\pi^+p \rightarrow \pi\pi N$ cross-section in this region is due to some effect in all the waves, rather than to additional waves opening and providing more cross-section. The isobar model is consistent with this: if $\pi\pi N$ production proceeds via an intermediate isobar, it can only occur at energies at which an isobar can be produced and can exist for long enough to travel away from the bachelor particle and decay independently. In the π^+p case, this can begin to occur with the production of the $\Delta P33(1236)$ isobar which together with a pion requires a centre of mass energy 1370 MeV, although this is only approximate because of the width of the isobar, and because of the need for kinetic energy to allow it to travel away from the bachelor. This isobar behaviour would affect all waves as is indeed seen in figure V.6. It is worth noting that the threshold for direct one pion production is 1213 MeV, but that as figure I.1 shows, the actual threshold is a little below 1400 MeV.

Another way to check the consistency of the isobar model, adopted by Keith Barnham, was first described at the 1976 Oxford Conference (ref. 13). The parametrisation described in IV.2.3 assumes that the complex transition amplitudes X are a function only of total c.m.s. energy; this cannot be exactly true as it leads to violation of unitarity constraints in the isobar subenergies (refs. 44 and 45). As there is considerable theoretical doubt as to the size of correction required (ref. 46), a fit in different regions of the Dalitz plot can be used to determine experimentally how much the X's vary. Figure V.8.a shows

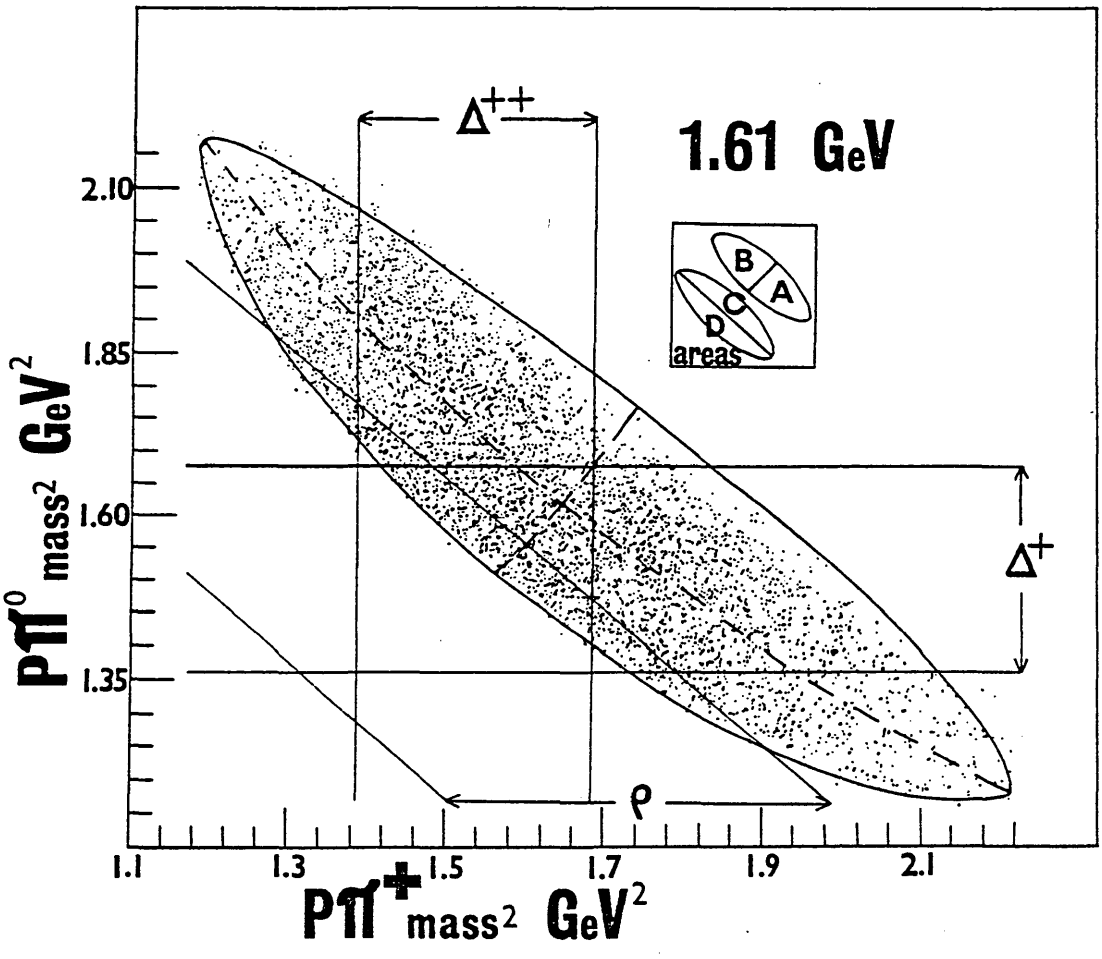

Figure V.8.a 895 MeV/c Dalitz plot - regions fitted

Symbol	Isobar	Partial Wave
1	Δπ	SD_{31}
2	Δπ	PP_{31}
3	Δπ	PP_{33}
5	Δπ	DS_{35}
6	Δπ	DD_{33}
7	Δπ	DD_{35}
9	Δπ	FF_{35}
A	$P_{11}(1470)\pi$	SS_{31}
B	$P_{11}(1470)\pi$	PP_{31}
C	$P_{11}(1470)\pi$	PP_{33}
G	ρ_1 N	SS_{31}
H	ρ_1 N	PP_{31}
I	ρ_1 N	PP_{33}
J	ρ_1 N	DD_{33}
M	ρ_3 N	SD_{31}
N	ρ_3 N	PP_{31}
O	ρ_3 N	PP_{33}
Q	ρ_3 N	DS_{33}
R	ρ_3 N	DD_{33}

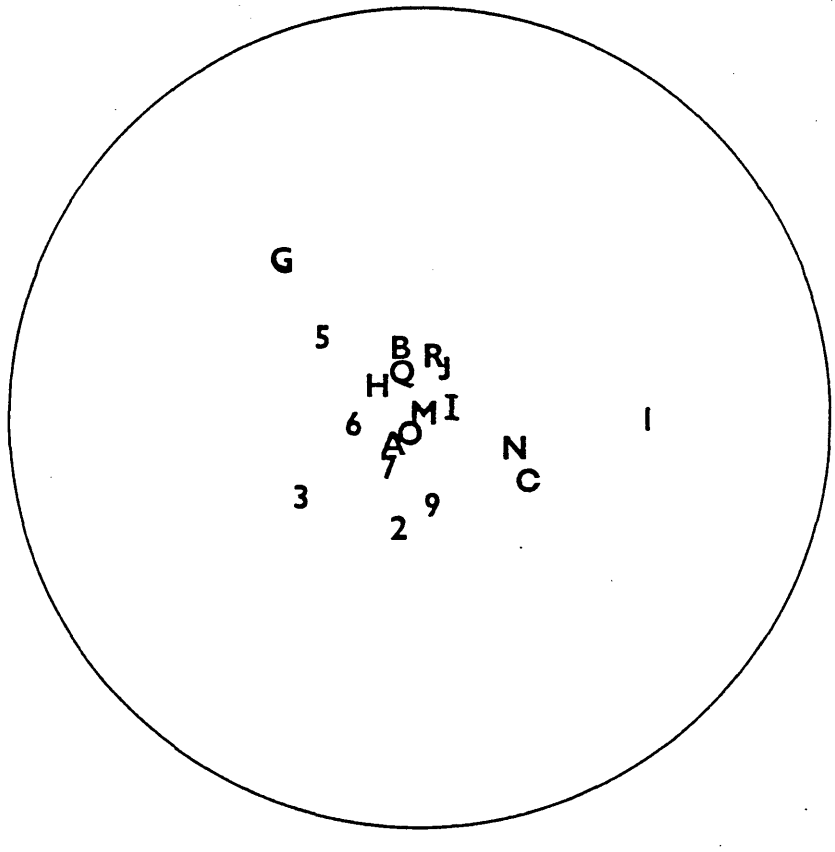

Figure V.8.b 19 wave fit to whole Dalitz plot data

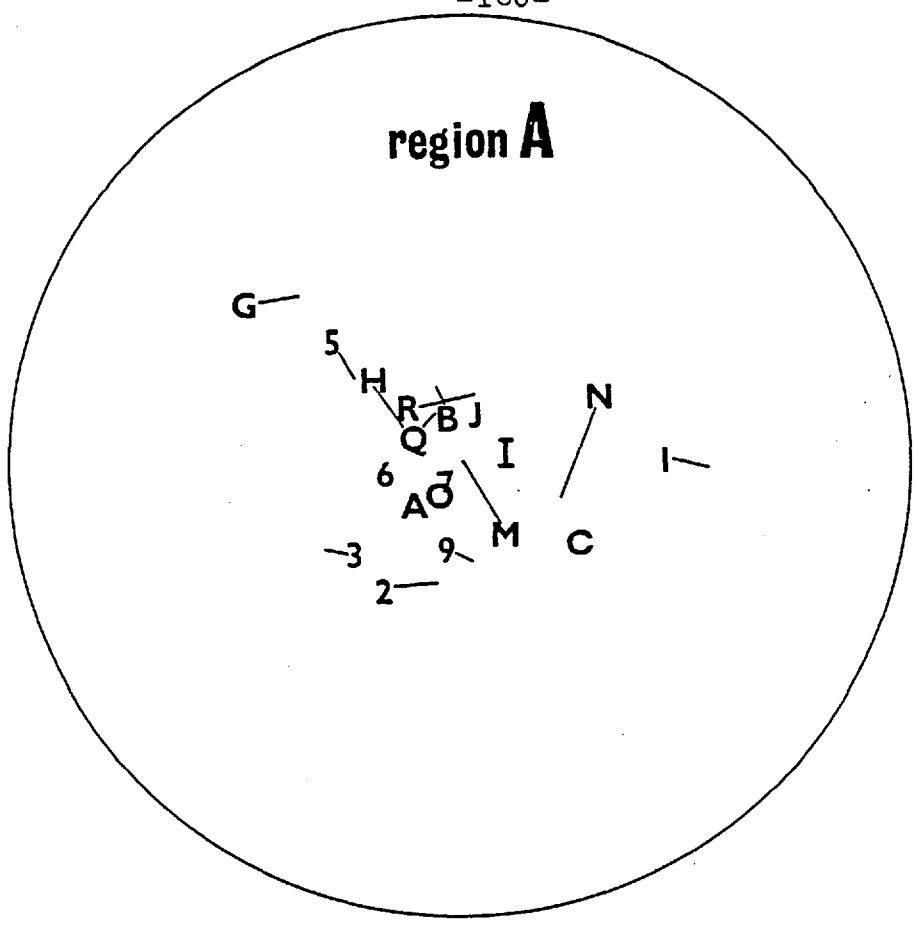

Figure V.8.c 19 wave fit to region A events

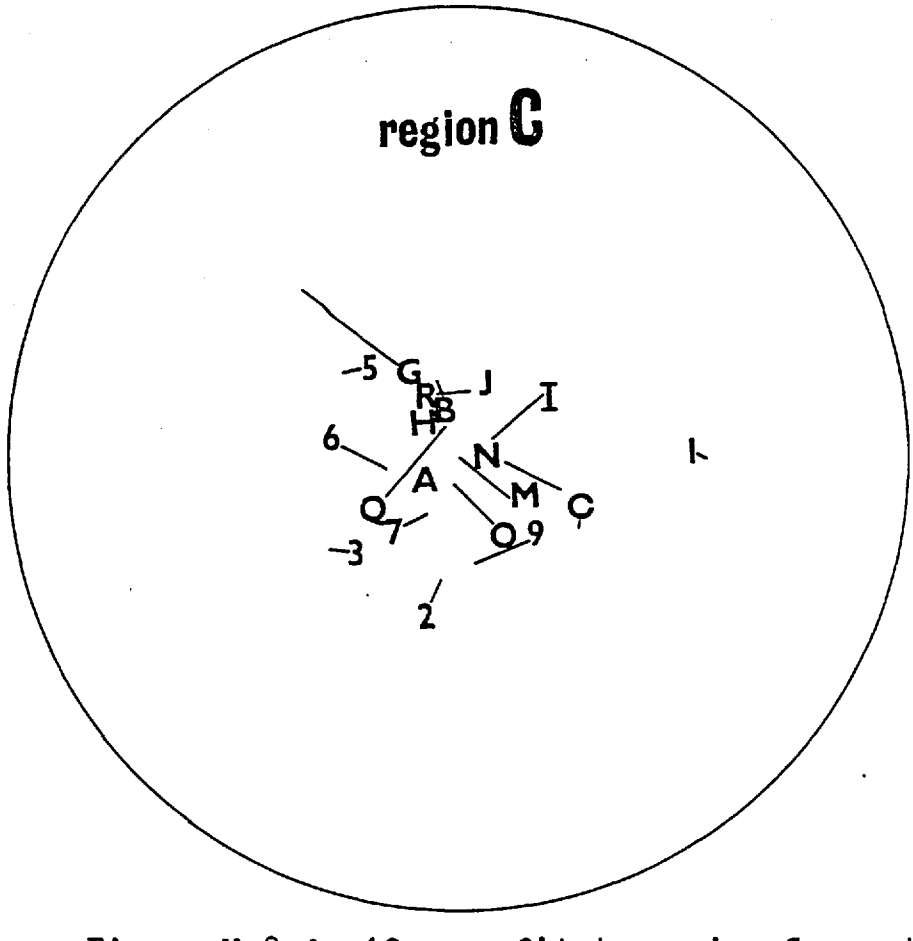

Figure V.8.d 19 wave fit to region C events

the regions fitted on the Dalitz plot, figure V.8.b shows, on an Argand plot, a fit to all the data at 895 MeV/c, using the 19 largest waves. Figures V.8.c and V.8.d show fits in regions A and C, with bars to show how far each wave has moved from the whole plot fit. Most of the shifts are of a size similar to the errors (see Chapter VI), the results were discussed in detail in ref. 13, and the following conclusions were drawn. Firstly, as the isobar model relates halves A and B by isospin Clebsch Gordan coefficients, they will differ from the overall fit because of direct 3-body production and statistical fluctuations; the fit shows that neither effect is serious. Secondly, C does not contain the regions of interference between the isobars, which provide most information on relative phases, and should show the largest changes in X. In fact, the changes are not much greater than those in region A, with the ρ waves moving most. This test shows that the assumption of X values being constant over the Dalitz plot is a good approximation.

The projections in figure V.5 have also shown that the model is capable of providing a good description of the data. Solutions at adjacent energies are similar, as one expects from a meaningful physical model, but not from fits with a technique that is purely an attempt to describe data numerically.

We have therefore shown that the isobar model is valid, and sufficient with present statistics. Improvements are worth making, both by including 3-body unitarity calculations, and OPE effects, but they will not radically change our results.

CHAPTER VI

Obtaining a 9-Energy Solution

VI.1 Introduction

When isobar analyses of $\pi\pi N$ final states were started, one of the hopes for them was that they would overcome the problem of ambiguous solutions encountered in elastic partial wave analyses. Theoretical work on continuum ambiguities and practical experience have shown that this was a forlorn hope. Some ambiguity may perhaps be blamed on insufficient statistics, but attempts to obtain a unique solution separately at each energy can lead to the removal of significant waves. We therefore pursued our aim of making at least 20 random starts at each energy without removing waves, and now show how we chose between the various solutions listed in table V.3.

VI.2 Comparing different solutions at one energy

A decision to retain only those solutions found by more than one run had already been made, but this still left 192,000 possible 9-energy combinations of solutions. An attempt was therefore made to reject more solutions at each energy. No constraints had been imposed on the ratio of cross-sections in the two channels, so solutions with unacceptable values could be rejected. The χ^2 value

$$\chi^2 = \frac{(\text{fitted ratio - experimental ratio})^2}{(\text{error on fitted ratio - experimental ratio})^2}$$

was calculated for every solution. All of the 31 solutions found below 945 MeV/c had χ^2 values below 1.0, and of 38 solutions at the top 3 energies, there were 9 with χ^2 values over 1.0, the largest being 1.8. No solution was rejected on this basis; as Figure V.7 showed, the fitted $\pi^+\pi^+n$ cross-sections were consistent with the experimental values, so this test only showed that the minimiser worked well, and that we had included sufficient waves to give a good parametrisation of the $\pi^+\pi^+n$ channel.

Another possible reason for rejecting a solution would be an unacceptably low likelihood value. A range of reasonable likelihood values should be established, and fits lying below this could be rejected. This can be simplified if likelihoods at different energies are converted to some number which can be compared at different energies and whose acceptable range can be determined by a Monte Carlo test.

Looking at the negative log likelihood function used in minimisation

$$L = -\ln \mathcal{L}_f = \sum_{i=\text{events}}^{N} -\ln \left(\frac{d\sigma_i}{d\rho} \Big/ \sigma_{tot} \right) \qquad \text{(VI.1)}$$

one can see that at a minimum this allows one to obtain the mean (geometric mean) likelihood per event

$$\mathcal{L}_m = \exp\frac{-L}{N} = \frac{d\sigma_{mean}}{d\rho} \Big/ \sigma_{tot} \qquad \text{(VI.2)}$$

N is the number of events at the given energy, σ_{tot} is the total $\pi\pi$N cross-section at that energy, and ρ is the Lorentz invariant phase space.

Now in the case of Gaussian statistics and a uniform distribution of events over phase space one would have:-

$$\frac{d\sigma}{d(\text{phase space})}_{\text{mean}} = \frac{\sigma_{tot}}{\text{phase space volume}}$$

$$\therefore \mathcal{L}_m = \frac{\sigma_{tot}}{\text{phase space volume}} \Big/ \sigma_{tot} = \frac{1}{\text{phase space volume}} \qquad \text{(VI.3)}$$

and one would have

$$\mathcal{L}_m \cdot (\text{phase space volume}) = 1 \qquad \text{(VI.4)}$$

The phase space volume ρ_W at a given energy W can be obtained by integrating equation 4.18

$$\rho_W = \int \frac{1}{32W^2}\, dw_1^2 dw_2^2 d\cos\Theta\, d\Phi\, d\alpha$$

$$= \frac{8\pi^2}{32W^2}\left[(W-m_\pi)^2-(m_\pi+m_N)^2\right]\left[(W-m_N)^2-4m_\pi^2\right] \qquad \text{(VI.5)}$$

Using VI.3 one can calculate a reduced mean likelihood $\mathcal{L}_r$

$$\mathcal{L}_r = \mathcal{L}_m \cdot \rho_W \qquad \text{(VI.6)}$$

where $\mathcal{L}_m$ and ρ_w are given by VI.2 and VI.5 respectively. As stated above, this would be exactly equal to unity only under special circumstances. In our case, statistics are not Gaussian, in particular the number of events at each energy does not have a Gaussian distribution with momentum. This would tend to lower the value of $\mathcal{L}_r$, particularly at 600 and 700 MeV/c where we have added the 650 MeV/c events. On the other hand, the distribution of events in phase space is also non-uniform, and this would tend to increase $\mathcal{L}_r$.

Figure VI.1 shows the range of values of $\mathcal{L}_r$ at each energy. The range of values obtained by fitting the 6 Monte Carlo data sets mentioned in V.5.1 is also shown. These 6 data sets are merely statistically distinct event samples generated from the same hypothesis, and the spread in their values gives an indication of the spread of acceptable likelihood values expected from statistics alone. The mean value of $\mathcal{L}_r$ does vary from energy to energy, in particular it is low at 600 and 700 MeV/c for the reason given above. All the values are close to 1, which means that the use of the reduced mean likelihood is a useful tool, and also that our likelihood function has been correctly formulated and programmed. The spread of values at each energy is very small, in fact the spread of the Monte Carlo values is larger than the spread in any of the real data values, so no solution can be rejected on this basis.

These tests show that the minimiser worked admirably, and did not provide any poor solutions. The number of solutions could also have been reduced by combining those solutions at each energy which were similar in the larger waves (see end

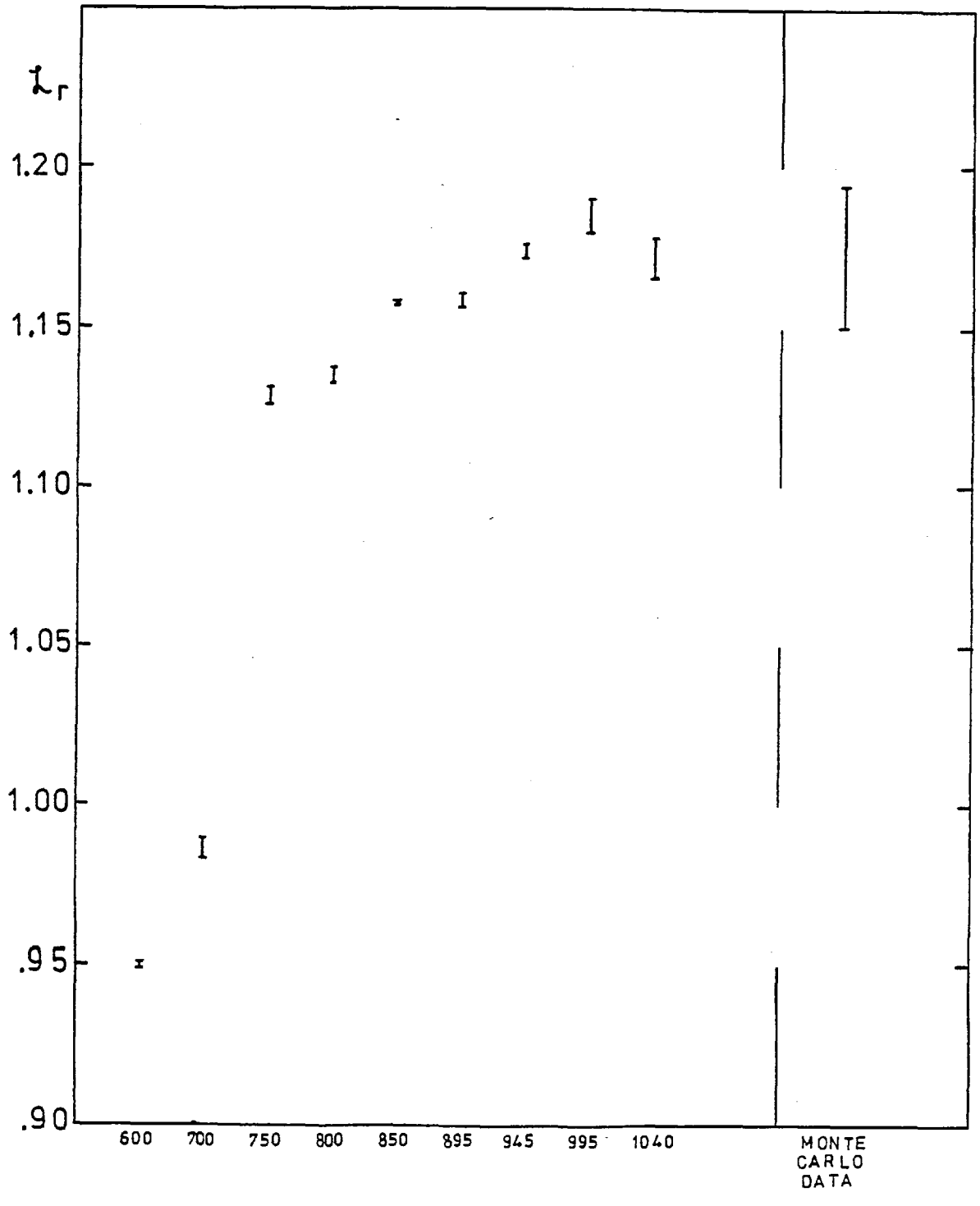

Figure VI.1 Range of reduced likelihoods, $\mathcal{L}_r$, at each momentum

of V.4.3), but the question of which solution to choose, or how to average them, was so awkward that all were kept to allow a continuity search to choose between them.

VI.3 Ambiguities and Continuity

VI.3.1 Discrete ambiguities and the continuum ambiguity

It was shown in the previous section that at every energy there exist several solutions which describe the data equally well. We first repeat those reasons for finding ambiguous solutions that were mentioned in Chapter V. The first and easiest to deal with were local minima which were removed by rejecting solutions found only once. Secondly some ambiguous solutions may be due to the minimiser never having reached a correct region of parameter space, though it is likely that such solutions would have been identified by the tests just described. Thirdly there are cases where a minimum splits into several minima because of poor statistics; these are not easily distinguished from continuum ambiguities, which will be described next, and can be treated like them.

Apart from these ambiguities connected with the practical details of minimisation, there exists the continuum ambiguity. Theoretical examination of an ideal model-independent, energy-independent partial wave analysis has shown that there must exist a continuum of solutions that all describe the data at one energy equally well, if that

energy is above the inelastic threshold (references 47, 48). A very good recent examination of the continuum ambiguity in the case of elastic π^+p phase shift analysis is given by the work of Atkinson et al in reference 49. They take the results of a partial wave analysis and generate an "ambiguity patch" in the Argand diagram around every T-matrix element. These ambiguity patches show how far the T-matrix elements can change while still describing the experimental observables as well as the original solution does.

A cutoff in the partial wave series reduces the continuum ambiguity to a number of discrete ambiguities, and if the number of partial waves is decreased, the number of discrete solutions also falls. Unfortunately the solutions are still distributed over the ambiguity patch, and a unique solution obtained by cutting down the number of waves may lie to one side of a patch and be different from solutions at adjacent energies. Analyses which attempt to obtain a unique solution at each energy in this manner may therefore give discontinuous behaviour in their Argand diagrams.

The same theoretical work has also revealed the existence of discrete ambiguities. These are however either trivial (a rotation by π of all waves), or else they lead to very discontinuous behaviour from energy to energy. They can therefore be rejected on the basis of continuity requirements. We use a continuity test to do this and indeed to choose just one solution at each energy.

VI,3,2 Continuity

We have so far used two models - the isobar model, and the assumption that a cutoff after a finite number of waves can be made. The theory and justification of both have been discussed. Some further assumption about the behaviour of the solutions must be made to permit a unique choice of solution at each energy. The model used in this analysis is that of continuity. A fairly smooth background behaviour, with Breit-Wigner resonances in some waves, is assumed. This is compatible with the isobar model, it is required by duality, and is in agreeement with theoretical interpretation of partial wave analysis results. We therefore searched for that combination of solutions at 9 energies which would give the best continuity.

This is certainly a justifiable way to reject truly discrete ambiguities, and those solutions that may be due to a failure by the minimiser to find the right part of the parameter space; indeed the two sorts of ambiguity may really be the same. Its use to choose between different solutions in the same ambiguity patch needs some discussion here. A three point scale, similar to that of reference 48 can be used to relate the possible results of using continuity to the extent of the continuum ambiguity.

a/ The ambiguities are small, so resonance structure is stable.

b/ The ambiguities are big enough to affect resonance parameters to some extent.

c/ The ambiguities are large and resonances may be lost.

The work of Atkinson et al in reference 49 shows that in $\pi^+ p \to \pi^+ p$ large resonances are not seriously affected; they lie somewhere between a/ and b/. Smaller resonances behave like b/, and two resonances with masses near 2000MeV fall under c/. No such analysis has been performed on $\pi p \to \pi\pi N$ results, but the practical results of our work could be used to give some idea of the extent of continuum ambiguities, and the work of reference 49 can provide us with guidelines. Their continuum patches were small at some energies, and indeed they found no continuum ambiguity at one energy. They used continuity arguments to claim that this reduced the acceptable extent of ambiguity at adjacent energies. We also find that the extent of ambiguity varies from energy to energy, so that some energies constrain the range of acceptable solutions at adjacent anergies.

Since the extent of ambiguities varies from energy to energy, it will also vary over the range of energies included in one energy bin during fitting. This means that a fit to experimental data in an energy bin should find solutions only in that ambiguity patch which is common to all energies in the bin. We therefore claim that theoretical calculations of the extent of ambiguities are likely to be overestimated, since they calculate the ambiguity only at the nominal energy of a bin, and take no account of variations with energy. This will be offset to some extent by the errors on a T-matrix element, which increase as the width of the energy bin increases. It may well be worth investigating what the optimum width of an energy bin should be to give

the best balance between the size of errors and the extent of the continuum ambiguity. In this analysis we use normalisation constants calculated at the mean c.m. energy of each bin, so we do not fully exploit the spread in energies. Nevertheless, the events used in each bin do cover a range of energies. The effect due to a spread in energies can be neglected only in those cases where the size and shape of the ambiguity patch are very slowly varying functions of energy, or where the spread in energy is very small.

Returning to the three point scale, we concluded that large resonances are safe, that smaller ones may have ill-defined parameters or may even not be seen, though the extent of continuum ambiguities may be overestimated. Small resonances may be lost because of the size of errors even if the continuum ambiguity is small. It is therefore important to analyse as many channels as possible, since a small resonance may be more clearly seen in one channel than in others: inelastic analyses in general are therefore important, ours for example provides new detailed information on resonances seen in the $\pi^+ p \to \pi N^*(1470)P11$ channel.

In view of the nature of the continuum ambiguity, the use of continuity to choose one solution at each energy is justifiable; it rejects discrete ambiguities, and the most continuous path through the ambiguity patches is as good as any other. It is also safer to fit with more than the minimum

required number of waves, and then to use continuity to select one solution at each energy, than to force uniqueness at each energy by cutting down the number of waves during fitting, as was done in previous analyses of our data and in other analyses.

VI.4 Using Continuity to choose a 9-energy Solution

VI.4.1 The continuity search formalism

To check the relative continuity of each possible combination, we first needed to define a method for tying together the solutions at different energies. The solution at any one energy gives the relative phases of the different waves at that energy, but not the overall phase. This overall phase from one energy to the next is usually taken from elastic analyses. Phases can be tied directly to those of an elastic analysis, but this relies totally on the success of the elastic analysis. Phases can also be related to the elastic phases via a K matrix analysis, but this is a lengthy process, useful if one solution has been chosen at each energy, but not suitable for continuity comparisons between many different solutions. We have preferred to tie to a Breit-Wigner using well-established resonances. This reduces our dependence on any one elastic analysis, but increases our dependence on the knowledge of resonance parameters, so we tried more then one resonance, and various values for their masses and widths.

Writing a relativistic Breit-Wigner expression -

$$T = \frac{\sqrt{x_e x_r}\, M\Gamma}{M^2-E^2 - iM\Gamma} = \frac{\sqrt{x_e x_r}\left(\frac{M^2-E^2}{M\Gamma}\right)}{1 + \left(\frac{M^2-E^2}{M\Gamma}\right)^2} + i \frac{\sqrt{x_e x_r}}{1 + \left(\frac{M^2-E^2}{M\Gamma}\right)^2}$$

one sees that T has the phase

$$\phi = \tan^{-1} \frac{M\Gamma}{M^2-E^2}$$

In the above x_e = elastic partial width

x_r = inelastic partial width in channel r

M = resonance mass

Γ = resonance width

E = c.m.s. energy of the system

Given M and Γ, the phase of the chosen wave can be calculated at energy E. The B-W formula holds good to about 2 widths from resonance mass, which is sufficient for our energy range. We fix the overall phase of each solution by rotating that solution so that the phase of the chosen wave is that predicted by the B-W at the energy of that solution.

The 9 separate solutions comprising each combination can thus be tied together for the purposes of continuity comparisons. To perform these we construct a chi-squared function. Taking the Argand diagram for one wave, as shown in Figure VI.2

$$\chi^2_{wave} = \sum_{(i,j)=1,2}^{(8,9)} \left(\frac{l_{ij}}{\delta l_{ij}} \right)^2 \qquad \text{VI.7}$$

where l_{ij} are distances between successive pairs of points, and δl_{ij} are the errors on these distances.

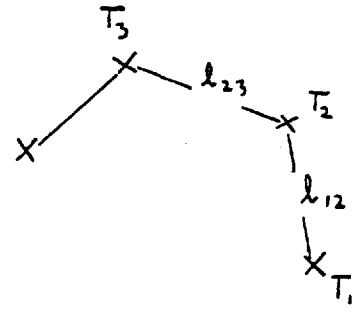

Figure VI.2

T_1, T_2, T_3... represent T-matrix elements at energies 1, 2, 3...

l_{12}, l_{23}... represent distances between successive pairs of points

An overall χ^2 can then be calculated by summing χ^2_{wave} for all significant waves

$$\chi^2_{combination} = \sum_{waves} \chi^2_{wave} \qquad \text{VI.8}$$

The use of straight lines for the distances between points on the Argand diagram is unrealistic; the B-W predicts a circle, so some curved line would be a better approximation, particularly for points that lie far apart. The number of path length elements to be calculated is nearly 31 million: 192,000(combinations) x 20 (waves) x 8 (pairs of points). The program is to be run many times, so a path whose chi-squared can be calculated quickly is required. An approximately spiral path, whose chi-squared calculation needs no subroutine calls is suitable.

Given points T_1 and T_2 defined by amplitudes and phases (A_1,θ_1) and (A_2,θ_2), the length of a spiral path between them is approximately

$$l_{12} = \tfrac{1}{2}(A_1+A_2)(\theta_2-\theta_1) \qquad \text{VI.9}$$

Some care is needed in the evaluation of $\theta_2 - \theta_1$ it should be the smallest angle between T_1 and T_2, for example a value of 350^o must be replaced by 10^o.

The error on l_{12}, in terms of errors on amplitudes and phases is given by

$$\left(\frac{\delta l_{12}}{l_{12}}\right)^2 = \frac{\delta A_1^2+\delta A_2^2}{(A_1+A_2)^2} + \frac{\delta\theta_1^2+\delta\theta_2^2}{(\theta_1-\theta_2)^2} \qquad \text{VI.10}$$

so the chi-squared contribution from one pair of points in one wave is

$$\chi^2_{wave,12} = \left(\frac{\delta A_1^2+\delta A_2^2}{(A_1+A_2)^2} + \frac{\delta\theta_1^2+\delta\theta_2^2}{(\theta_1-\theta_2)^2}\right)^{-1} \qquad \text{VI.11}$$

and by substituting VI.11 in VI.7 and hence VI.8 we calculate a χ^2 for every 9-energy combination. This provides us with a χ^2 distribution, with a minimum value provided by the preferred combination of solutions. The waves used in calculating this χ^2 were those 21 waves that we fitted at all 9 energies, with the exception of the N*DD3 which was compatible with zero at most energies. This gives 20 waves, with 8 path segments in each wave, and an amplitude and phase part to each segment - 320 degrees of freedom in the χ^2. As we use 20 waves, the dependence on any one wave is not very

large. In particular, there will not be any marked tendency to smooth out resonance effects in any one wave as would happen if only a few waves were used. There is still a bias against narrow resonances, but our spacing of 30-50 MeV between c.m.s. energies makes it difficult to see such detailed structure.

We also calculate the confidence level CL corresponding to the χ^2 values. This is the probability of χ^2 exceeding its observed value if the values were distributed according to the χ^2 distribution function

$$CL = \int_{\chi^2_{observed}}^{\infty} d\chi^2 \, P_{ND}(\chi^2)$$

where P_{ND} is the χ^2 probability distribution function for ND degrees of freedom.

VI.4.2 Performing the continuity search

The above formalism was turned into the program CHI. This read the solutions at each energy, and the mass and width of a resonance in a given wave, then calculated a χ^2 for every 9-energy combination, and printed a list of the 100 best combinations. To provide a means of identifying the different solutions at each energy, they were numbered in the order in which they were read, and these numbers are used in Tables VI.1, VI.4 and VI.5.

Table VI.1 shows the results of the first CHI run, tied to the ΔDS33 wave with a mass of 1.67 GeV and width

0.2 GeV, which are the nominal parameters given by the Particle Data Group tables (ref. 50). The first 20 combinations are shown. The spread in χ^2 was rather small; this could have been due to some solutions at certain energies being similar, or to CHI being insensitive to differences between solutions at a given energy. We felt that this should be checked before more CHI runs were made. In order to make this test independent of CHI and the calculated errors we used a separate program RANCOM.

At each energy RANCOM compared all solutions checking each wave in turn to determine whether T-matrix amplitudes and phases were the same within specified limits. Waves with an amplitude smaller than the amplitude limit were not checked at all. The limits used at each energy are given in Table VI.2; they were wide both in amplitude so that small waves were ignored, and in phase because some of the waves were known to have large phase errors. Solutions that were the same within these limits were considered to be sufficiently similar for it not to matter which was picked by CHI. As RANCOM was used merely as a double-check on CHI, and not to examine the continuum ambiguity, no great importance should be attached to these limits.

The results in Table VI.1 were reexamined in the light of these comparisons. Solutions 1, 2 and 3 at 945 MeV/c were similar according to RANCOM, but solution 1 at 1040MeV/c was not the same as solution 8. This alternative solution was larger in the ΔSD1, ΔDS3 and ρ_3SD1 amplitudes, and

Momentum (MeV/c)	600	700	750	800	850	895	945	995	1040	χ^2	C.L.%
Combination number											
1	1	2	2	3	3	1	3	1	8	312.7	60.4
2	1	2	2	3	3	1	3	1	1*	315.7	55.8
3	1	2	2	3	3	1	1	1	8	316.1	55.0
4	1	2	2	3	3	1	1	1	1*	319.1	50.4
5	1	2	2	3	3	1	2	1	8	322.0	45.8
6	1	2	2	3	3	1	2	1	1*	324.9	41.3
7	3	2	2	3	3	1	3	1	8	326.2	39.3
8	1	2	2	3	3	1	3	1	7	326.5	39.0
9	3	2	2	3	3	1	3	1	1*	329.2	35.0
10	3	2	2	3	3	1	1	1	8	329.7	34.3
11	1	2	2	3	3	1	1	1	7	329.9	34.0
12	1	2	3*	3	3	1	3	1	8	332.6	30.3
13	3	2	2	3	3	1	1	1	1*	332.6	30.2
14	1	2	2	3	1	3	3	1	8	333.9	28.6
15	1	2	2	3	1	1	4*	1	8	334.0	28.4
16	1	1*	3*	3	3	1	3	1	8	334.9	27.2
17	1	2	3*	3	3	1	3	1	1*	335.5	26.5
18	3	2	2	3	3	1	2	1	8	335.5	26.4
19	1	2	2	3	3	1	2	1	7	335.7	26.2
20	1	2	3*	3	3	1	1	1	8	336.0	25.9

The columns show the 9 momenta, and the solutions picked in each combination at each momentum. (The numbers identify different solutions at each energy as described in the text. Any solution that differs from the first one at that energy according to RANCOM is marked with an asterisk.)

Table VI.1

The 20 best combinations found by CHI when tied to ΔDS33 with Mass=1.67 GeV, Width=0.20 GeV.

Momentum bin (MeV/c)	Amplitude limit	Phase limit (radians)
600	0.05	1.2
700	0.05	1.2
750	0.06	1.2
800	0.08	1.2
850	0.08	1.2
895	0.1	1.2
945	0.1	1.2
995	0.1	1.2
1040	0.1	1.2

Table VI.2 Limits allowed on T-matrix element amplitudes and phases in program RANCOM

smaller in several others. It is not surprising that such a problem should arise at 1040 MeV/c since it is tied only from the lower energy side, and therefore less constrained; solutions at higher energies should help to resolve this problem. Fortunately the difference is not great, and disappears after the O.P.E. refits described in the next chapter. We also examined Table VI.1 looking for the first combination that differed significantly from the best one at two energies. This was found to be the sixteenth combination, with a χ^2 of 334.9, corresponding to a confidence level of 27%; it differed from the best solutions at 700 and 750 MeV/c.

The best CHI combination could have been best merely because it contained solutions with the largest errors. In such a case the next best combinations would have been those containing solutions with the next largest errors rather than those most similar to the best combination. As RANCOM was independent of the calculated errors, it showed that the size of the errors was not an overriding factor in CHI, and a check of the errors on various solutions confirmed this: errors on different solutions at the same energy were not very different.

RANCOM also found three cases where several solutions, each found only once and therefore excluded from the first CHI runs, were similar within the defined limits. These could have been cases of poor statistics splitting up a minimum, and not local minima, so they were added to the

set of minima used by CHI. At the same time solutions found only once but by starting from another energy solution (continuation runs) were also added to the CHI input. These solutions could not be treated on a par with random starts, and were unlikely to be local minima. This increased the number of combinations in CHI to 691,200; as none of the solutions added at this stage were chosen by later runs of CHI it seems to have been an unnecessary precaution.

These tests showed that CHI did behave as required, and further runs were than made. Table VI.3 shows the χ^2 for the best combination obtained by tying to ΔSD31 and ΔDS33 resonances with a range of masses and widths. These two resonances were chosen because they are large, well-established, and cover our range of energies. The same combination comes out with the best χ^2 over the whole range tested for both waves. χ^2 values tend to improve with increasing mass and width because both effects bring the different energies closer together on the Argand diagram thus decreasing the path lengths. Table VI.4 shows the results of tying to a variety of known or suspected resonances. In each case the best and second best combinations are shown and for Δ waves the first combination that differed from the best at 2 energies is included. For each combination the table gives the χ^2, confidence level and the position of the combination in the list of best combinations for that run of CHI. Solutions that are outside the RANCOM limits when compared to the corresponding energy solution in combination 1-2-2-3-3-1-3-1-8 are marked with an asterisk.

It is particularly interesting to note that tying to suspected PP1 and PP3 resonances in $\Delta\pi$ gives the same best answer as ΔDS3 and ΔSD1. This gives support to belief in resonances in these waves. Tying to resonances in N*, $\rho_{\frac{1}{2}}$ and $\rho_{3/2}$ gives some differences from the best answer, probably because there is more background in these channels. Table VI.5 shows the results of running CHI using more or fewer than the standard 20 waves in computing the χ^2. The results here are also similar or identical to the best combination, showing that the choice of waves here was not critical.

The results of these tests, as shown in Tables VI.1, VI.3, VI.4 and VI.5 show that combination 122331318 is the preferred one. It is chosen by all parameter combinations in Table VI.3, and all the Δ waves in Table VI.4. In Table VI.5, the combinations are the same as it, or differ at only one energy. The first combinations differing at two energies, shown for the Δ waves in Table VI.4, lie some way down the CHI table. This 9-energy solution is the end result of the whole partial wave analysis, of the preceding data analysis, and of the subsequent continuity analysis. It provides new information on N*PP11(1470)$_\pi$ waves, and additional information on other π^+p induced final states. The single energy solutions in it were used to generate the Monte Carlo projections and the cross-section plots of Chapter V. (The alternative 1040 MeV/c solution was used to generate the additional 1040 MeV/c Monte Carlo plots in Figure V.5.j. These differ little from Figure V.5.i, showing that the two solutions describe the data equally well).

Width \ Mass	1.50	1.58	1.65	1.72	1.80
0.03	315.24	320.71	333.51	310.97	310.50
0.08	312.48	315.46	319.05	311.73	310.56
0.14	311.69	313.42	314.42	311.71	310.65
0.20	311.40	312.43	312.73	311.49	310.71
0.35	311.05	311.35	311.35	311.04	310.73
0.45	310.91	311.05	311.03	310.83	310.69

Best χ^2 tying to ΔSD1 with various masses and widths

Width \ Mass	1.52	1.60	1.67	1.74	1.82
0.05	319.40	342.83	350.20 *	307.27	304.22
0.13	308.81	318.45	319.61	309.04	304.93
0.20	307.22	312.32	312.72	308.32	305.26
0.27	306.47	309.37	309.53	307.40	305.35
0.35	305.91	307.53	307.65	306.55	305.26
0.45	305.43	306.26	306.33	305.80	305.06

Best χ^2 tying to ΔDS3 with various masses and widths
* = normal second best path is no longer second best

Table VI.3

Wave tied to & parameters, mass & width (GeV)	Solutions picked at each energy. Numbers and asterisks used as in Table VI.1	Position in CHI table	χ^2	C.L.%
ΔDS3	122331318	1	312.7	60.4
1.67, 0.2	122331311*	2	315.7	55.8
	11*3*331318	16	334.9	27.2
ΔSD1	122331318	1	314.4	57.8
1.65, 0.14	122331311*	2	315.6	56.0
	11*3*331318	4	317.0	53.7
ΔPP1	122331318	1	350.1	11.9
1.65, 0.09	122331118	2	351.9	10.6
	11*3*331318	6	355.6	8.4
ΔPP3	122331318	1	304.2	73.5
1.69, 0.25	122331118	2	305.1	71.7
	11*3*331318	18	328.5	36.0
N*SS1	11*4*332*118	1	424.5	0.0
1.65, 0.14	11*4*332*111*	2	424.7	0.0
N*PP1	123*331318	1	432.9	0.0
1.65, 0.09	123*331311*	2	434.1	0.0
N*PP3	11*4*331311*	1	281.2	94.2
1.69, 0.25	122331311*	2	281.8	93.9
ρ_1SS1	31*1*331318	1	291.1	87.6
1.65, 0.14	11*1*331318	2	292.9	85.9
ρ_3DS3	11*2331111*	1	340.2	21.0
1.67, 0.20	23*2331111*	2	345.5	15.7

Table VI.4

Results of CHI tied to various waves

Waves used in computing χ^2	Solutions picked at each energy. Numbers and asterisks used as in Table VI.1	Position in CHI table	χ^2	C.L.(%)
<u>20 waves</u>				
(21 wave set	122331318	1	312.7	60.4
except N*DD3)	122331311*	2	315.7	55.8
<u>14 waves</u>				
(21 wave set	122331311*	1	193.4	93.2
except ΔPF3,	322331311*	2	194.3	92.5
N*DD3, ρ_1PP3,				
ρ_1DD3, ρ_3SD1,				
ρ_3PP3, ρ_3PF3)				
<u>15 waves</u>				
(21 wave set	122331311*	1	194.3	98.6
except ΔPF3,	122331111*	2	195.0	98.5
N*SS1, ρ_1PP3,				
ρ_3SD1, ρ_3PP1,				
ρ_3PF3)				
<u>16 waves</u>				
(21 wave set	122331318	1	229.2	88.5
except ΔPF3,	122331118	2	230.4	87.4
N*SS1, N*DD3,				
ρ_3SS1, ρ_3PF3)				
<u>21 waves</u>				
(complete 21	121*321317	1	314.6	79.3
wave set)	121*311317	2	316.0	77.7

<u>Table VI.5</u>

<u>Results of running CHI tied to ΔDS3, using various numbers of waves</u>

We now turn to Argand plots of this 9-energy solution.

VI.5 Results, Argand Diagrams and discussion

Figure VI.3.a shows Argand plots of the Δ SD31 and Δ DS33 T-matrix elements for the 9-energy solution, tied to a Breit-Wigner in Δ SD31, using the resonance parameters of Table VI.4. Points are marked by the symbols 1 to 9 for the nine energy bins starting at the lowest. Errors on amplitudes and phases are shown unless they are as small as the symbol. Figure VI.3.b shows the same waves, after tying to a resonance in Δ DS33, using the resonance parameters of Table VI.4. Overall behaviour in the two pairs of plots is similar, except for the lowest energies, and there is a relative rotation of 50° between the VI.3.a and VI.3.b plots. The DS33 resonance is wider than the SD31, so it gives a better coverage of our energy range and we have chosen to tie to it in producing our Argand plots for the other waves. Tying to the Δ DS33 makes it lie at $+90^{\circ}$ at 1670 MeV, and moves the Δ SD31 resonance position 50° off -90° at its nominal mass. These are the two best-established resonances in our energy range, but their masses are not well-determined, so we have rotated all our final Argand plots by -25°, so that the two waves lie equally far from $\pm 90^{\circ}$ at their nominal resonance masses.

Table VI.6 gives T-matrix element amplitudes and phases, with errors, with the phases fixed according to the above prescription. Figure VI.4 shows corresponding Argand diagrams for waves with T-matrix elements greater than or

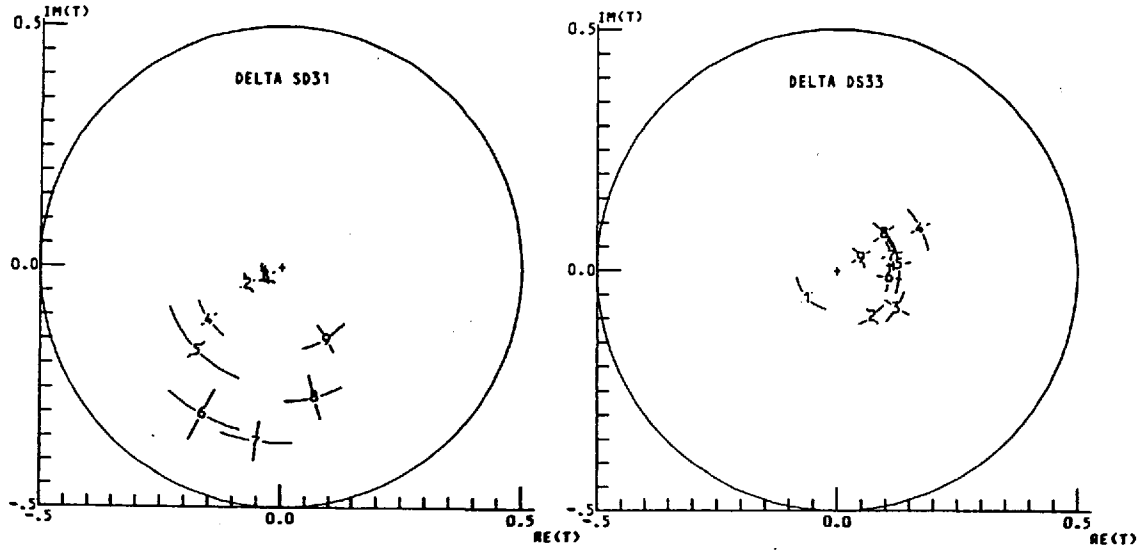

Figure VI.3.a

ΔSD31 and ΔDS33 waves tied to a ΔSD31 resonance with M=1650 MeV, Γ=140 MeV

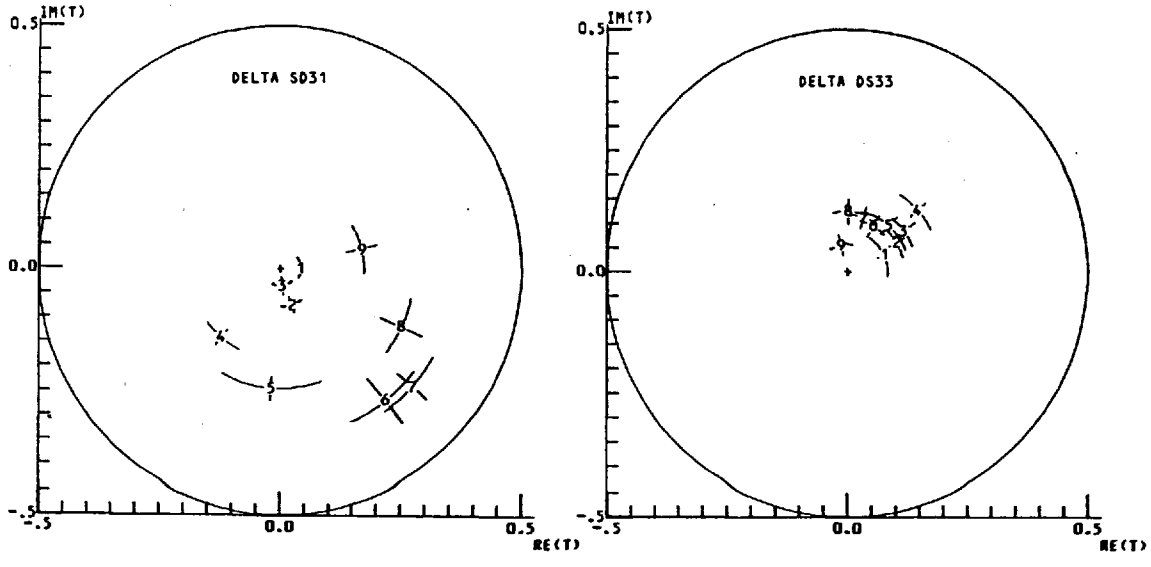

Figure VI.3.b

ΔSD31 and ΔDS33 waves tied to a ΔDS33 resonance with M=1670 MeV, Γ=200 MeV

close to 0.1. Errors are informative, but can be confusing, so they have been omitted from these plots: Argand diagrams, with error bars, for all waves are shown in Appendix A. Our signs are those of the "baryon first" convention, with other definitions as used by Saclay. Details of these conventions are given by Dolbeau in his thesis (ref. 34), and in other Saclay papers (ref. 16). These conventions agree with those of SLAC-LBL; we have checked them against the SLAC-LBL report (ref. 33) and against our own programs, as described in Andy White's thesis (ref. 10). However to make comparisons with theory easier, we have additionally rotated all waves through 180° to agree with the convention of Hey et al (ref. 51).

A careful examination of these Argand diagrams will provide information on resonance parameters and signs. The best method of obtaining this information is to perform a K-matrix analysis; SLAC-LBL and Saclay have described how they did this (references 15, 16) after performing their partial wave analyses. Our Imperial College/Westfield College collaboration has an independent K-matrix analysis program written by Steve Glickman but this has not yet been used. In the meantime, a search by eye for circles on the Argand diagrams and for corresponding bumps on the σ^{JP} plots can provide the same information. The results of such a search are described here, but the search is repeated in greater detail after the refit with One Pion Exchange, described in the next chapter.

Taking the waves in order of J^P, and starting with the S31 wave, one immediately sees the well-known $\Delta(1650)$

resonance. This shows up as a very clear bump in the σ^{JP} plot, and as a large clear resonant loop in ΔSD31. It is obviously a good wave for tying to in CHI. Clear resonance structure is also seen in ρ_1SS31. though it is not as smooth as the Δ wave. Signs are unambiguous in both cases, the Δ resonates in the lower half of the Argand circle and ρ_1 in the upper half; this is the first clear determination of the ρ_1SS31 sign. The mass of the resonance is not at 90^o (see earlier note about rotating the Argand diagrams), and does not agree exactly between the Argand diagrams and the σ^{JP} plot. These are common problems, and are reasons for using K-matrix analyses. N*SS31 and ρ_3SD31 show smaller amplitudes, there are indications of an anti-clockwise loop in N*SS31 but a sign cannot be determined. The P31 wave has small cross-section, and is difficult to interpret. It will be discussed in detail in the next chapter, but it is worth noting that the confused behaviour at our energies could be due either to the presence of more than one resonance, or to rapidly moving backgrounds. The enlarged cross-section plot for this wave, Figure V.6.b, showed bumps at energies 3 and 7, and all four PP31 Argand plots show interesting behaviour at these energies.

The P33 wave is large, particularly at the top two energies where its cross-section exceeds the predictions of elastic analyses. ΔPP33 and N*PP33 show clearly resonant behaviour, ρ_1PP33 and ρ_3PP33 are much smaller, but show anti-clockwise motion. We clearly confirm the Δ P33(1690) resonance given only one star in the 1976 Particle Data Group Tables (ref. 50), its sign is positive in both ΔPP33

and N*PP33; ours is the first analysis to show the latter wave and its sign. There is considerable structure at the lower energies in the cross-section plot and in the ΔPP33 Argand diagram; a lot of background variation would be needed to explain this, so it could be due to further resonant behaviour at these lower energies. The PF33 waves are small.

Of the D33 waves, ΔDS33 shows a clearly resonant loop, but as it was used to tie the phases of all the Argand plots, only its amplitude needs to be considered. The amplitude at energy 4 is larger than at the adjacent energies, but consideration of the errors shows that there is no discrepancy. The ρ_3DS33 wave is also large, but less continuous. The DD33 waves are all smaller than the DS33 waves - they are confused, but show an overall tendency to anti-clockwise motion.

In D35, only the ΔDD35 wave merits showing here; it exhibits a clear counter-clockwise rotation, with points 6 and 7 larger and somewhat displaced. The same energies are also larger in the σ^{JP} plot, but it is difficult to draw any conclusions from this behaviour.

Finally, the F waves - these are small and are not shown here, but only in Appendix A. More energies must be analysed before any conclusions can be drawn from the behaviour of these waves.

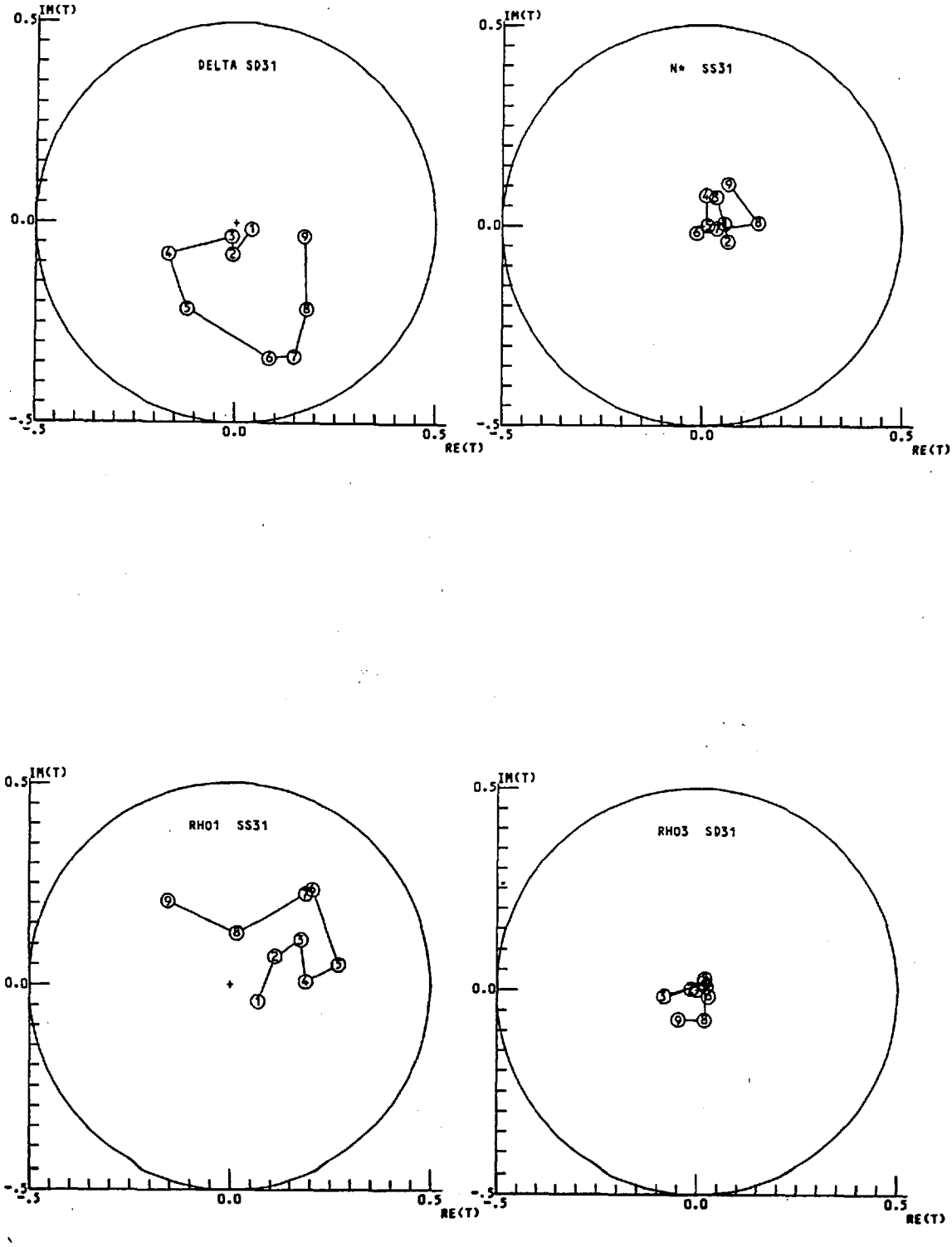

Figure VI.4.a

(details at foot of Fig.VI.4.e)

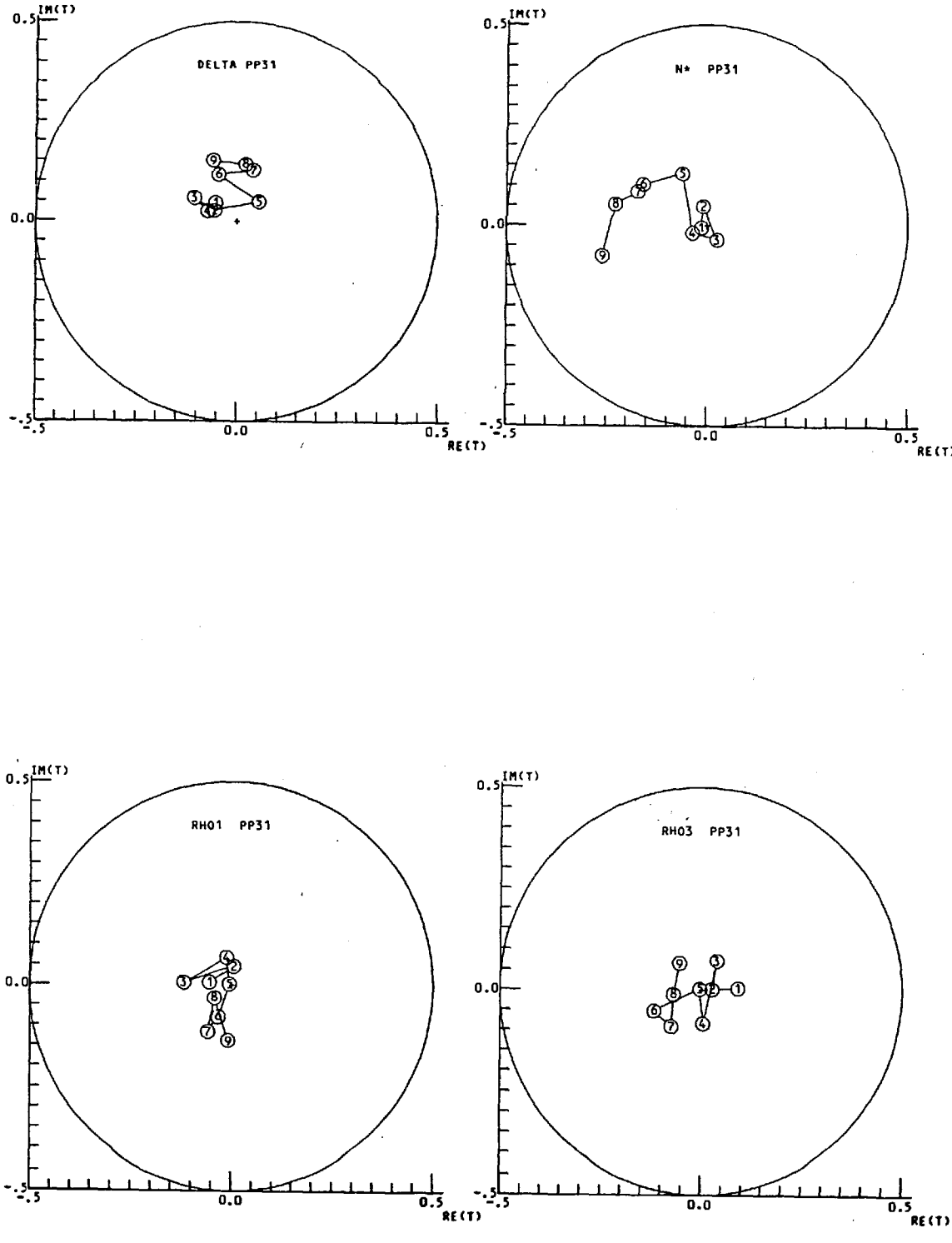

Figure VI.4.b

(details at foot of Fig.VI.4.e)

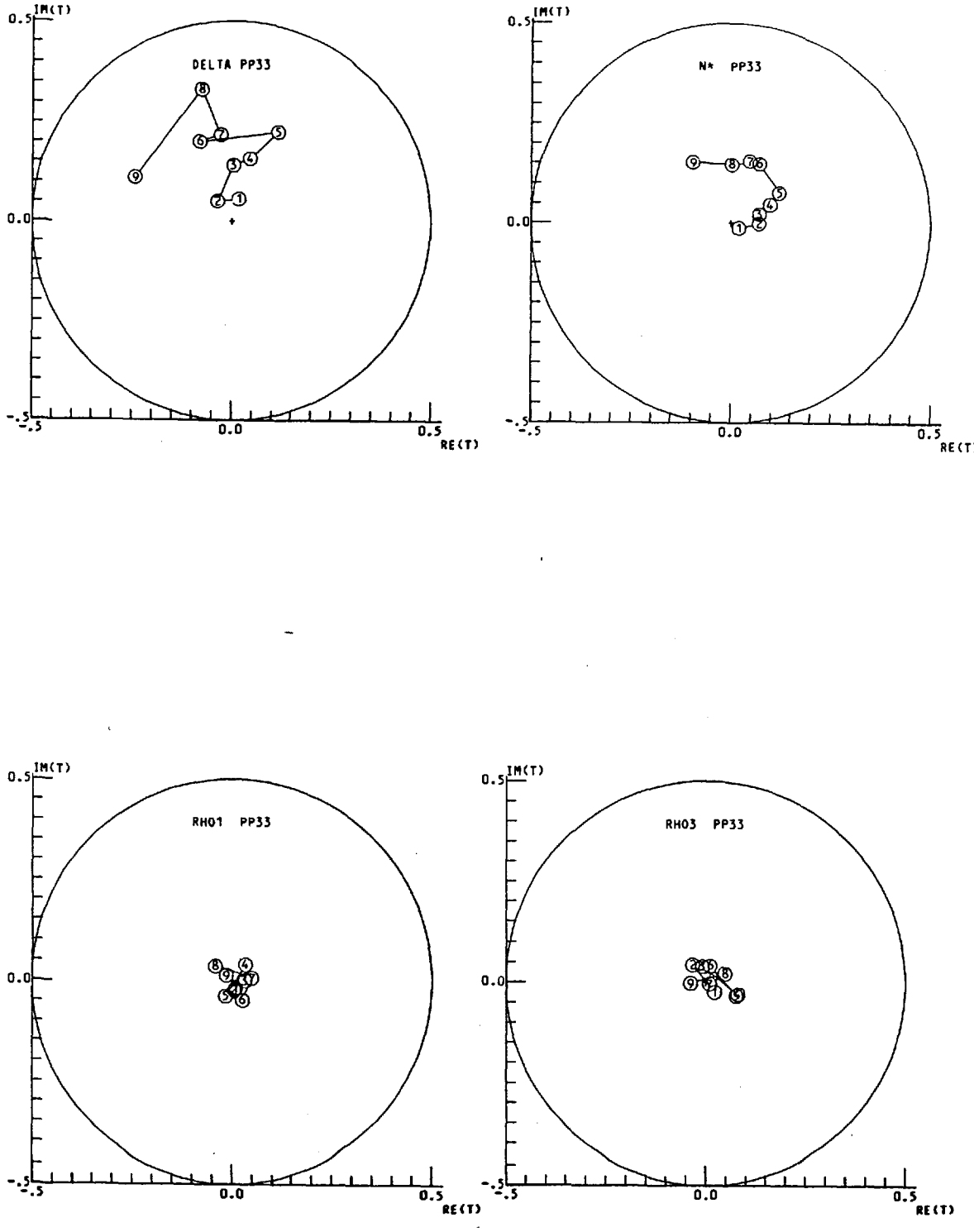

Figure VI.4.c

(details at foot of Fig.VI.4.e)

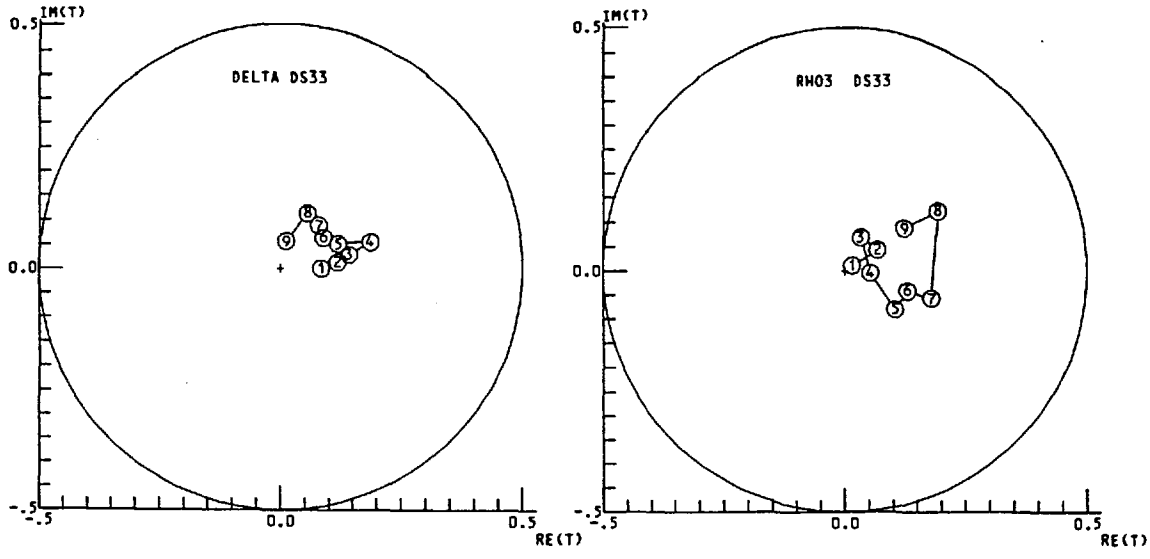

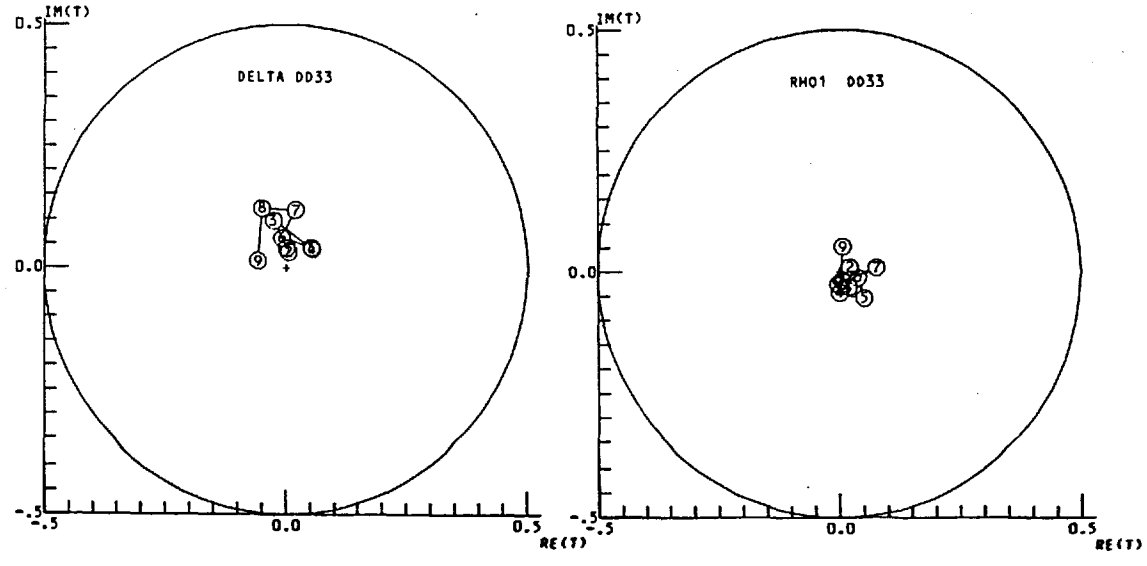

Figure VI.4.d

(details at foot of Fig.VI.4.e)

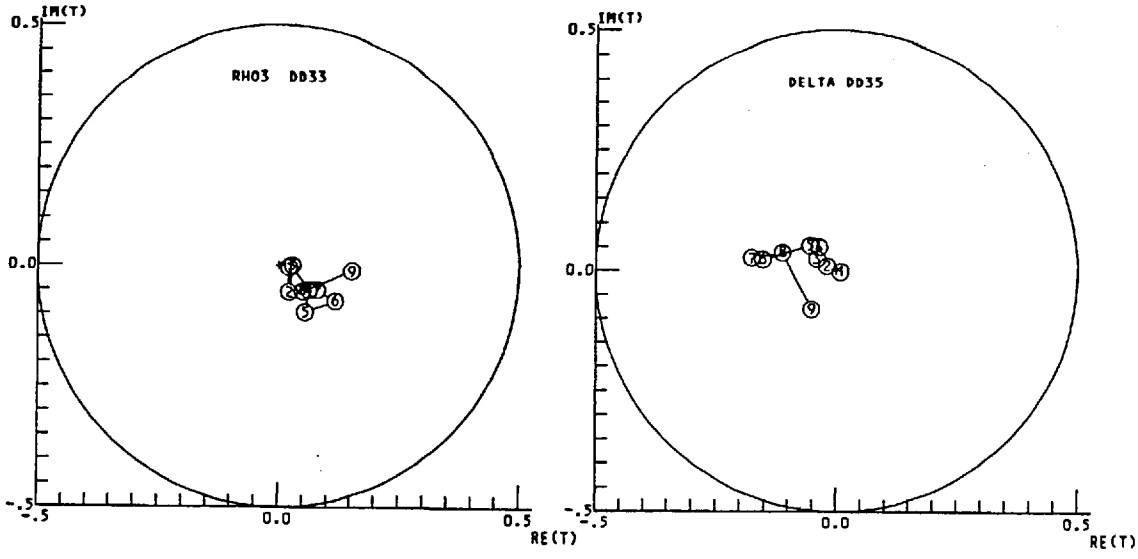

Figure VI.4.e

Argand diagrams for most continuous solution, tied to Δ DS33 with M=1670 MeV, Γ=200 MeV, rotated by 135° (see text)

Points 1-9 denote solutions at the following energies (in GeV)

1 - 1.439

2 - 1.495

3 - 1.526

4 - 1.551

5 - 1.577

6 - 1.612

7 - 1.640

8 - 1.668

9 - 1.693

Amplitudes and phases of T-matrix elements

Waves	Energies in GeV 1.439	1.495	1.526	1.551	1.577	1.612	1.640	1.668	1.693
DELTA SD31									
AMPLITUDE	0.042	0.079	0.035	0.186	0.246	0.347	0.364	0.278	0.174
& ERROR	0.012	0.019	0.020	0.021	0.025	0.059	0.042	0.048	0.034
PHASE	-0.39	-1.68	-1.87	-2.71	-2.08	-1.32	-1.15	-0.88	-0.19
& ERROR	0.54	0.28	0.61	0.24	0.44	0.24	0.21	0.23	0.30
DELTA PP31									
AMPLITUDE	0.070	0.061	0.120	0.077	0.072	0.125	0.134	0.144	0.163
& ERROR	0.013	0.017	0.032	0.029	0.027	0.030	0.027	0.028	0.039
PHASE	2.43	-3.58	-3.64	-3.48	0.73	-4.34	1.27	1.42	1.94
& ERROR	0.55	0.42	0.28	0.30	0.61	0.37	0.27	0.32	0.32
DELTA PP33									
AMPLITUDE	0.059	0.062	0.141	0.165	0.253	0.216	0.220	0.340	0.267
& ERROR	-.017	0.018	0.033	0.019	0.028	0.035	0.033	0.069	0.030
PHASE	1.25	-4.11	-4.75	-5.00	-5.19	-4.33	1.70	1.79	2.71
& ERROR	0.59	0.40	0.25	0.26	0.42	0.29	0.23	0.20	0.21
DELTA PF33									
AMPLITUDE	0.016	0.013	0.026	0.020	0.072	0.066	0.050	0.017	0.092
& ERROR	0.005	0.008	0.012	0.006	0.011	0.016	0.015	0.015	0.019
PHASE	0.08	-1.26	-0.12	-2.68	-0.89	-0.22	-0.05	-0.87	0.01
& ERROR	0.62	0.63	0.54	0.58	0.43	0.37	0.35	0.80	0.27
DELTA DS33									
AMPLITUDE	0.085	0.119	0.145	0.194	0.129	0.109	0.118	0.125	0.057
& ERROR	0.016	0.020	0.029	0.022	0.025	0.026	0.024	0.027	0.023
PHASE	-0.00	0.11	0.19	0.28	0.40	0.62	0.85	1.11	1.36
& ERROR	0.57	0.29	0.26	0.26	0.48	0.29	0.27	0.27	0.43
DELTA DD33									
AMPLITUDE	0.041	0.034	0.100	0.067	0.067	0.062	0.121	0.132	0.060
& ERROR	0.012	0.013	0.024	0.012	0.020	0.023	0.020	0.034	0.034
PHASE	1.53	1.40	-4.47	-5.65	0.67	1.70	1.41	1.95	2.88
& ERROR	0.55	0.37	0.28	0.34	0.48	0.38	0.25	0.28	0.56

Table VI.6

	1.439	1.495	1.526	1.551	1.577	1.612	1.640	1.668	1.693
DELTA DD35									
AMPLITUDE	0.009	0.022	0.047	0.061	0.075	0.155	0.178	0.118	0.095
& ERROR	0.005	0.010	0.013	0.014	0.023	0.028	0.026	0.022	0.014
PHASE	-0.22	-3.60	-3.70	-4.09	-3.91	-3.29	-3.29	-3.47	-2.14
& ERROR	0.60	0.40	0.31	0.26	0.46	0.24	0.21	0.25	0.26
DELTA FP35									
AMPLITUDE	-	-	-	-	-	0.012	0.022	0.056	0.032
& ERROR	-	-	-	-	-	0.011	0.013	0.016	0.018
PHASE	-	-	-	-	-	-4.31	-3.49	-2.57	-0.76
& ERROR	-	-	-	-	-	0.75	0.44	0.30	0.44
DELTA FF35									
AMPLITUDE	-	-	-	-	-	0.024	0.030	0.050	0.141
& ERROR	-	-	-	-	-	0.013	0.012	0.025	0.020
PHASE	-	-	-	-	-	-2.98	-4.05	0.13	-3.16
& ERROR	-	-	-	-	-	0.57	0.44	0.40	0.22
DELTA FF37									
AMPLITUDE	-	-	-	-	-	-	-	0.072	0.119
& ERROR	-	-	-	-	-	-	-	0.014	0.018
PHASE	-	-	-	-	-	-	-	1.88	-2.49
& ERROR	-	-	-	-	-	-	-	0.29	0.26
N* SS31									
AMPLITUDE	0.057	0.075	0.080	0.077	0.015	0.021	0.039	0.142	0.124
& ERROR	0.012	0.013	0.018	0.012	0.013	0.016	0.021	0.027	0.032
PHASE	0.11	-0.53	1.10	-4.85	0.12	-2.20	-0.15	0.06	1.01
& ERROR	0.56	0.28	0.29	0.30	1.02	1.07	0.41	0.27	0.29
N* PP31									
AMPLITUDE	0.014	0.049	0.043	0.039	0.143	0.189	0.192	0.235	0.271
& ERROR	0.008	0.019	0.016	0.016	0.027	0.035	0.025	0.041	0.030
PHASE	3.53	1.77	-0.93	-2.67	2.01	2.57	2.69	2.92	3.42
& ERROR	0.87	0.38	0.44	0.42	0.47	0.25	0.21	0.22	0.22
N* PP33									
AMPLITUDE	0.024	0.071	0.075	0.108	0.142	0.164	0.162	0.146	0.178
& ERROR	0.006	0.011	0.015	0.012	0.014	0.028	0.021	0.027	0.024
PHASE	5.72	-0.03	0.29	0.43	0.55	1.11	1.27	1.55	2.13
& ERROR	0.58	0.27	0.27	0.25	0.44	0.25	0.21	0.21	0.21

	1.439	1.495	1.526	1.551	1.577	1.612	1.640	1.668	1.693
N* DD33									
AMPLITUDE	0.010	0.019	0.023	0.033	0.025	0.025	0.033	0.034	0.041
& ERROR	0.005	0.006	0.008	0.009	0.011	0.010	0.011	0.011	0.018
PHASE	-1.22	-3.67	-1.82	-0.88	-2.92	-1.92	-0.23	-0.06	0.97
& ERROR	0.74	0.46	0.44	0.35	0.63	0.49	0.35	0.48	0.41
N* DD35									
AMPLITUDE	-	-	-	-	-	0.018	0.013	0.013	0.009
& ERROR	-	-	-	-	-	0.008	0.008	0.009	0.018
PHASE	-	-	-	-	-	0.97	-1.47	-0.35	-1.09
& ERROR	-	-	-	-	-	0.55	0.78	0.82	1.30
N* FF35									
AMPLITUDE	-	-	-	-	-	0.011	0.027	0.008	0.032
& ERROR	-	-	-	-	-	0.007	0.011	0.012	0.016
PHASE	-	-	-	-	-	1.92	3.24	3.95	4.08
& ERROR	-	-	-	-	-	0.92	0.37	1.15	0.38
N* FF37									
AMPLITUDE	-	-	-	-	-	-	-	0.012	0.031
& ERROR	-	-	-	-	-	-	-	0.009	0.010
PHASE	-	-	-	-	-	-	-	1.82	3.43
& ERROR	-	-	-	-	-	-	-	0.75	0.44
RHO1 SS31									
AMPLITUDE	0.081	0.133	0.210	0.189	0.275	0.312	0.293	0.127	0.257
& ERROR	0.019	0.032	0.037	0.020	0.036	0.057	0.041	0.042	0.044
PHASE	-0.52	0.56	0.55	0.04	0.18	0.85	0.87	1.42	2.21
& ERROR	0.54	0.27	0.26	0.24	0.42	0.25	0.21	0.24	0.22
RHO1 PP31									
AMPLITUDE	0.054	0.047	0.117	0.069	0.006	0.085	0.128	0.052	0.136
& ERROR	0.013	0.018	0.028	0.036	0.024	0.032	0.028	0.032	0.031
PHASE	3.01	1.45	3.09	1.74	2.58	4.33	4.25	3.81	4.65
& ERROR	0.58	0.51	0.34	0.44	5.99	0.49	0.31	0.57	0.34
RHO1 PP33									
AMPLITUDE	0.022	0.025	0.033	0.052	0.041	0.055	0.049	0.054	0.019
& ERROR	0.011	0.013	0.015	0.021	0.016	0.017	0.015	0.021	0.016
PHASE	5.09	-1.33	-0.01	0.85	-1.96	-1.07	0.13	2.44	2.41
& ERROR	0.69	0.47	0.54	0.31	0.45	0.41	0.38	0.28	1.17

	1.439	1.495	1.526	1.551	1.577	1.612	1.640	1.668	1.693
RH01 DD33									
AMPLITUDE	0.018	0.024	0.038	0.044	0.075	0.041	0.078	0.025	0.053
& ERROR	0.008	0.010	0.012	0.011	0.014	0.017	0.015	0.016	0.019
PHASE	-1.22	0.42	-0.98	-1.52	-0.80	-0.30	0.12	-1.62	1.42
& ERROR	0.80	0.57	0.39	0.39	0.44	0.46	0.30	0.66	0.40
RH01 DD35									
AMPLITUDE	-	-	-	-	-	0.028	0.021	0.033	0.044
& ERROR	-	-	-	-	-	0.014	0.011	0.010	0.013
PHASE	-	-	-	-	-	0.37	0.08	-2.41	-2.79
& ERROR	-	-	-	-	-	0.47	0.59	0.42	0.43
RH01 FF35									
AMPLITUDE	-	-	-	-	-	0.004	0.036	0.029	0.023
& ERROR	-	-	-	-	-	0.011	0.007	0.013	0.013
PHASE	-	-	-	-	-	-0.01	3.97	5.04	1.20
& ERROR	-	-	-	-	-	2.30	0.35	0.57	0.56
RH01 FF37									
AMPLITUDE	-	-	-	-	-	-	-	0.016	0.036
& ERROR	-	-	-	-	-	-	-	0.009	0.014
PHASE	-	-	-	-	-	-	-	4.88	4.59
& ERROR	-	-	-	-	-	-	-	0.79	0.33
RH03 SD31									
AMPLITUDE	0.001	0.016	0.084	0.025	0.033	0.032	0.024	0.075	0.085
& ERROR	0.007	0.018	0.028	0.015	0.020	0.027	0.020	0.034	0.032
PHASE	1.96	-3.37	-2.96	-5.46	0.96	-0.51	0.36	-1.32	-2.15
& ERROR	9.71	0.71	0.32	0.76	0.81	0.82	0.93	0.46	0.37
RH03 PP31									
AMPLITUDE	0.091	0.027	0.083	0.083	0.004	0.128	0.116	0.070	0.086
& ERROR	0.018	0.015	0.030	0.028	0.027	0.040	0.025	0.031	0.025
PHASE	0.05	0.10	1.08	-1.51	-3.76	-2.72	-2.25	-2.99	2.25
& ERROR	0.56	0.84	0.37	0.39	5.74	0.30	0.28	0.37	0.43
RH03 PP33									
AMPLITUDE	0.033	0.054	0.040	0.086	0.083	0.042	0.010	0.053	0.038
& ERROR	0.015	0.017	0.018	0.022	0.021	0.022	0.020	0.026	0.019
PHASE	-0.80	-4.07	-4.52	-0.34	-0.40	1.30	-0.30	0.42	-3.10
& ERROR	0.73	0.39	0.48	0.33	0.57	0.55	1.89	0.44	0.51

	1.439	1.495	1.526	1.551	1.577	1.612	1.640	1.668	1.693
RHO3 PF33									
AMPLITUDE	0.010	0.023	0.027	0.040	0.017	0.053	0.032	0.035	0.087
& ERROR	0.006	0.005	0.010	0.012	0.012	0.011	0.013	0.016	0.020
PHASE	-1.90	0.05	-4.54	-3.40	-3.32	1.66	-4.25	2.13	2.73
& ERROR	0.71	0.50	0.47	0.31	1.00	0.32	0.43	0.40	0.24
RHO3 DS33									
AMPLITUDE	0.020	0.081	0.077	0.054	0.130	0.136	0.187	0.228	0.151
& ERROR	0.007	0.025	0.019	0.017	0.021	0.034	0.027	0.051	0.023
PHASE	0.64	0.58	1.12	-0.06	-0.65	-0.30	-0.30	0.57	0.63
& ERROR	0.72	0.30	0.28	0.41	0.49	0.24	0.21	0.21	0.23
RHO3 DD33									
AMPLITUDE	0.022	0.058	0.029	0.080	0.111	0.139	0.094	0.072	0.153
& ERROR	0.007	0.014	0.010	0.010	0.009	0.023	0.019	0.019	0.021
PHASE	-0.13	-1.19	0.03	-0.67	-1.05	-0.55	-0.56	-0.81	-0.06
& ERROR	0.69	0.33	0.60	0.32	0.54	0.27	0.24	0.31	0.22
RHO3 DD35									
AMPLITUDE	-	-	-	-	-	0.022	0.022	0.009	0.009
& ERROR	-	-	-	-	-	0.015	0.016	0.013	0.017
PHASE	-	-	-	-	-	-3.75	-2.09	-1.22	0.77
& ERROR	-	-	-	-	-	0.83	0.63	1.59	1.76
RHO3 FP35									
AMPLITUDE	-	-	-	-	-	0.016	0.059	0.104	0.079
& ERROR	-	-	-	-	-	0.010	0.014	0.019	0.016
PHASE	-	-	-	-	-	-1.72	-2.65	-2.38	-2.07
& ERROR	-	-	-	-	-	1.01	0.26	0.23	0.25
RHO3 FF35									
AMPLITUDE	-	-	-	-	-	0.009	0.036	0.017	0.009
& ERROR	-	-	-	-	-	0.011	0.008	0.015	0.014
PHASE	-	-	-	-	-	-2.95	-3.44	1.44	-3.31
& ERROR	-	-	-	-	-	1.50	0.37	0.86	1.34
RHO3 FF37									
AMPLITUDE	-	-	-	-	-	-	-	0.031	0.078
& ERROR	-	-	-	-	-	-	-	0.012	0.015
PHASE	-	-	-	-	-	-	-	-0.79	1.77
& ERROR	-	-	-	-	-	-	-	0.46	0.25

CHAPTER VII

ONE PION EXCHANGE EFFECTS AND FINAL RESULTS

VII.1 Introduction

A number of possible isobar model problems have been mentioned in previous chapters. The results of fitting our data with an isobar model alone, presented in chapters V and VI are satisfactory, particularly in that direct three body production is minimal and three body unitarity corrections are of the same size as our errors. It is nevertheless worth examining other effects not allowed for so far. Two such effects are well-known and were added to our isobar model analysis. The first is an S-wave I=2 $\pi\pi$ state (ref. 52). The Oxford analysis included this as an isobar (ref. 7) and Saclay used it as an additional isobar in analysing their $\pi^+\pi^+n$ data at their highest energy (ref.16). The other effect is that of peripheral processes, which generally become more important at higher energies, and can be allowed for either by the inclusion of higher partial waves, or by the addition of t-channel exchange effects to the analysis programs. The SLAC-LBL paper(ref.15a) points out that this may be needed and their data has been recently refitted by D.E. Novoseller (refs. 53,54) with an isobar model plus t-channel exchange.

The standard isobar model picture of a πp interaction, used at low energies, is the s-channel resonances plus background one presented in Chapter IV

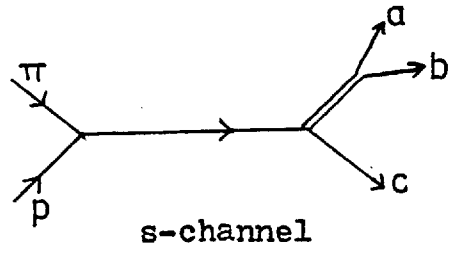

s-channel

An alternative picture, more commonly used at higher energies, typically 5 GeV/c incident momentum and above, is the t-channel exchange one

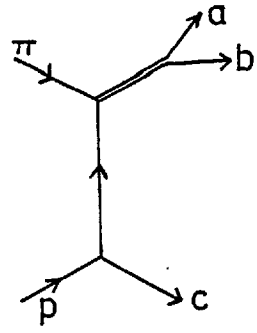

t-channel

According to duality, the two pictures are equivalent, so arbitrary combinations of the two in one fit can involve double counting, and care must be taken when using both. At our energies, only the $\pi^+\pi^+n$ channel shows a failure to fit peripheral events. Only those t-channel effects that lead to an I=2 $\pi\pi$ state, not allowed for in our isobar model, contribute to this channel, so no double counting problems arise. This chapter describes a re-analysis of our data with t-channel effects used to describe the I=2 final state, and to allow for peripheral processes. This is not primarily a $\pi\pi$ analysis of our data, as was the work of ref. 11, the main interest lies in improvements to the s-channel analysis; nevertheless the I=2 results are also interesting.

The formalism, analysis and results of the refit are described in the same order as was used to describe the main

analysis in Chapters IV, V, VI. A detailed discussion of the results follows, and the chapter ends with some concluding remarks on the whole analysis.

VII.2 Formalism of I=2 $\pi\pi$ effects

VII.2.1 Formalism of I=2 $\pi\pi$

The isobar model describes the reaction 1+2 → a+b+c, in terms of an (ab) isobar or resonance, such that a and b undergo a reaction unaffected by c. A summation is then performed over possible isobars.

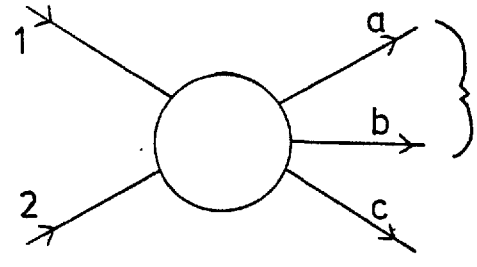

In the case where a and b are both pions, the (ab) system can have isospin 0, 1 or 2, and the results of $\pi\pi$ scattering analyses can be used to find suitable parametrisations for each case. The I=1 state is most amenable to isobar model analysis; it is dominated by the p-wave ρ meson , which SLAC-LBL, Saclay, and our own analysis treat as one of the isobars, The I=0 case is more difficult; the wide enhancement at about 640 MeV may or may not be a resonance - SLAC-LBL and Saclay treat it as such, we do not need to consider it as I=0 is not accessible in $\pi^+p \to \pi\pi N$. The I=2 case is the worst, it is an exotic state, $\pi\pi$ analyses

show that it is a repulsive interaction. A good recent analysis of this state, that of Hoogland et al, reference 55, shows clearly that there is no resonance at our energies. (There has however been recent interest in possible exotic meson resonances at higher energies.) Some allowance for the I=2 interaction should be made, particularly in analyses of the $\pi^+\pi^+n$ final state. SLAC-LBL and earlier isobar analyses of our data ignored I=2. Both the Oxford analysis (ref. 7) and Saclay's analysis of $\pi^+\pi^+n$ at their top energy included an s-wave I=2 $\pi\pi$ isobar. This is better than making no allowance at all, but is clearly not in the spirit of the isobar model; some other picture that allows a close encounter between the pions without requiring them to form an I=2 isobar is preferable. Two possibilities would be direct three body decay followed by an interaction between the pions, or a final state interaction between two pions after an isobar decay, but the isobar model assumes, apparently correctly, that direct three-body decay, and rescattering are negligible at our level of accuracy. The third kind favoured by us, describes the interaction in terms of one pion exchange (O.P.E.). This is the t-channel exchange model normally used in $\pi\pi$ analyses such as that of Hoogland et al., it is normally used at energies higher than ours. At energies close to ours, R.D. Baker analysed data from our collaboration at 1.4 and 1.5 GeV/c, using t-channel exchange (refs. 11a and 11b). D.E. Novoseller has also refitted the SLAC-LBL results using their isobar model with the addition of t-channel exchange effects (refs. 53 and 54).

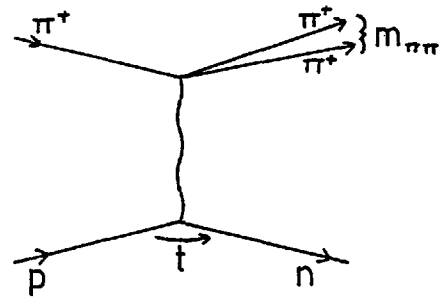

Figure VII.1 t-channel diagram

The reaction, as shown in Figure VII.1 is described by a product of two vertex functions, and a propagator. We use the Goebel Chew-Low formula (refs. 56, 57)

$$T_{\pi N\to\pi\pi N} = T_{NN\pi}\,\frac{G(t)}{(t-\mu^2)}\,T_{\pi\pi\to\pi\pi} \qquad 7.1$$

t is the 4 momentum squared transfer from the proton to the outgoing neutron (always negative)

μ is the pion mass

$\frac{1}{(t-\mu^2)}$ is the pion propagator, G(t) being a function to allow for corrections to it

$\pi\pi$ analyses attempt to isolate $T_{\pi\pi\to\pi\pi}$ and study it in detail. Ours is primarily an isobar model analysis, so an uncomplicated parametrisation of $T_{\pi\pi\to\pi\pi}$ is sufficient. We follow the parametrisation of Wolf (refs. 58 and 59).

As described in Chapter IV, the likelihood function is calculated in terms of $\frac{d\sigma}{d\rho}$ the differential cross-section with respect to invariant phase space ρ. The 5 variables commonly used in O.P.E. analyses are

$m^2_{\pi\pi}$ the squared mass of the dipion system in its centre of mass frame

t the 4-momentum squared transfer from incident to outgoing nucleon

$\cos\theta$, ϕ the polar and azimuthal angles defining the $\pi\pi$ system; in an s-wave $\pi\pi$ state, there is a uniform distribution of probability over $\cos\theta$ and ϕ, so they will be integrated out

α a rotation about the incident beam direction, which can also be integrated out in the case of an unpolarised beam and target

$\frac{d\sigma}{d\rho}$ will therefore be obtained in terms of these variables.

We can write

$$\frac{d\sigma}{d\rho} = \frac{d^5\sigma}{dm^2_{\pi\pi}\,dt\,d\cos\theta\,d\phi\,d\alpha} \cdot \frac{\partial(m^2_{\pi\pi},t,\cos\theta,\phi,\alpha)}{\partial(\rho)} \qquad 7.2$$

The Jacobian is given by

$$\frac{\partial(m^2_{\pi\pi},t,\cos\theta,\phi,\alpha)}{\partial(\rho)} = \frac{32\, m_p\, p_{lab}\, m_{\pi\pi}}{q_{\pi\pi}} \qquad 7.3$$

(For a derivation, see for instance reference 62, Page 119).

The new variables are

m_p = proton mass

p_{lab} = laboratory momentum of incident pion

$q_{\pi\pi}$ = momentum of one pion in the dipion centre of mass system

$q_{\pi\pi}$ can be calculated from $m_{\pi\pi}$. It will be useful to define the function that gives the squared momentum of a particle in the centre of mass system of 2 particles. If a system of total mass m_3 consists of 2 particles masses m_1, m_2, then the squared momentum of particles 1 or 2 is given by

$$P^2(m_1^2,m_2^2,m_3^2) = \left(\frac{m_1^4+m_2^4-m_3^4-2(m_1^2m_2^2+m_1^2m_3^2+m_2^2m_3^2)}{4m_3^2} \right) \qquad 7.4$$

$q_{\pi\pi}$ can now be written

$$q_{\pi\pi} = P(\mu^2, \mu^2, m^2_{\pi\pi}) \qquad 7.4a$$

Integrating over the angles in the differential cross-section one gets -

$$\frac{d^2\sigma}{dm^2_{\pi\pi}dt} = \int \frac{d^5\sigma}{dm^2_{\pi\pi}dt\, d\cos\theta d\phi d\alpha} \cdot d\cos\theta d\phi d\alpha$$

$$= \frac{d^5\sigma}{dm^2_{\pi\pi}dt\, d\cos\theta d\phi d\alpha} \int d\cos\theta d\phi d\alpha$$

(because the function is independent of $\cos\theta, \phi, \alpha$)

$$\therefore \quad \frac{1}{8\pi^2} \frac{d^2\sigma}{dm^2_{\pi\pi}dt} = \frac{d^5\sigma}{dm^2_{\pi\pi}dt\cos\theta d\phi d\alpha} \qquad 7.5$$

Combining 7.5, 7.2 and 7.3 gives

$$\frac{d\sigma}{d\rho} = \frac{4}{\pi^2} \cdot \frac{m_p p_{lab} m_{\pi\pi}}{q_{\pi\pi}} \cdot \frac{d^2\sigma}{dm^2_{\pi\pi}dt} \qquad 7.6$$

Using the expression 7.1, and including a flux factor, one gets

$$\frac{d^2\sigma}{dm^2_{\pi\pi}dt} = \frac{1}{4\pi^3 p^2_{lab} m^2_p} |T_{NN\pi}(t)|^2 \frac{G^2(t)}{(t-\mu^2)^2} |T_{\pi\pi,\pi\pi}(m^2_{\pi\pi},t)|^2 \qquad 7.7$$

This is the formula used by Wolf in reference 59, equation 21. We use the Dürr-Pilkuhn form factor (ref. 60) giving

$$|T_{NN\pi}(t)|^2 = -t \frac{1 + R_N^2 q_N^2}{1 + R_N^2 q_{Nt}^2} \pi^2 g^2_{NN\pi} \qquad 7.8$$

q_{Nt} is the off-mass-shell pion momentum, in the (pt) rest frame

q_N is the on-mass-shell pion momentum , in the ($p\pi$) rest frame

Equation 7.4 can be used for both these

$$q_{Nt} = P(t,m^2_p,m^2_n) \qquad 7.4b$$

$$q_N = P(\mu^2,m^2_p,m^2_n) \qquad 7.4c$$

Wolf obtained values for R_N and G(t) by fitting O.P.E. cross-sections to experimental data; he found G(t)=1 (i.e. no correction) and $R_N=2.86\pm.08 GeV^{-1}$.

$g^2_{NN\pi}$ is the $NN\pi$ coupling constant = 29.2 for π^+ and π^-, for π^o it is 14.6. In the rest of this derivation, we shall use expressions for $\pi^+\pi^+$, and introduce corrections for $\pi^+\pi^o$ at the end.

For the second vertex function we again follow Wolf and write

$$|T_{\pi\pi\to\pi\pi}(m^2_{\pi\pi},t)|^2 = m^2_{\pi\pi}\,\frac{u_1(q_{\pi t}R_{\pi\pi})}{u_1(q_{\pi\pi}R_{\pi\pi})}\; q_{\pi\pi}\sigma_{\pi^+\pi^+}(m_{\pi^+\pi^+}) \qquad 7.9$$

This is equation 16 of reference 59, written for $\pi^+\pi^+\to\pi^+\pi^+$ Wolf found $R_{\pi\pi}\simeq 0$, so the u_1 terms cancel.

The s-wave dominates in I=2 at our energies, so we write

$$\sigma_{\pi^+\pi^+}(m_{\pi^+\pi^+}) = \frac{4\pi}{k^2}\sin^2\delta_o^2 \qquad 7.10$$

k is the pion wave number ($=q_{\pi\pi}$), and δ_o^2 is the L=0, I=2 phase shift.

Continuing with simple parametrisations, we take an effective range expansion for δ_o^2 (see for example ref. 61)

$$k \cot \delta_o^2 = -\frac{1}{a} + \tfrac{1}{2} r_o k^2 \qquad 7.11$$

with a = scattering length, r_o = effective range; these are the parameters to be fitted in analysing the O.P.E. contribution to the final state. The Oxford analysis used the same expression, but fixed the values of a and r_o (ref. 7). For $\pi^+\pi^o$, a Clebsch-Gordan coefficient of $\frac{1}{2}$ is introduced : $\sigma_{\pi^+\pi^o} = \frac{1}{2}\sigma_{\pi^+\pi^+}$

Combining 7.10 and 7.11 gives

$$\sigma_{\pi^+\pi^+} = \frac{4\pi}{q_{\pi\pi}^2}(1 + \cot^2\delta)^{-1} = 4\pi(q^2_{\pi\pi} + (\tfrac{1}{2}r_o q^2_{\pi\pi} - \tfrac{1}{a})^2)^{-1} \qquad 7.12$$

All these expressions can now be combined to evaluate $\frac{d\sigma}{d\rho}$

$$\frac{d\sigma}{d\rho} = \frac{4}{\pi^2}\,\frac{m_p\, p_{lab}\, m_{\pi\pi}}{q_{\pi\pi}} \cdot \frac{-t}{4\pi^3\, p^2_{lab}\, m^2_p}\,\frac{1+8.18q^2_N}{1+8.18q^2_{Nt}} \cdot \frac{\pi^2 . 29.2 q_{\pi\pi}}{(t-\mu^2)^2}\, m^2_{\pi\pi}\sigma_{\pi\pi}(q_{\pi\pi})$$

$$= \frac{29.2 m^3_{\pi\pi}}{\pi^3\, p_{lab}\, m_p}\,\frac{(-t)}{(t-\mu^2)^2}\,\frac{1+8.18q^2_N}{1+8.18q^2_{Nt}}\;\sigma(q_{\pi\pi};r_o,a) \qquad 7.13a$$

$$= X(m_{\pi\pi},t)\;\sigma(q_{\pi\pi};r_o,a) \qquad 7.13b$$

For each event, X can be calculated before fitting; σ is a function of $q_{\pi\pi}$ which can also be calculated before fitting, and of r_o, a which are fitting parameters. If the mass differences between $\pi^+\pi^o$ and between p, n are ignored, then the same expressions hold for $\pi^+ p \pi^o$, except that X must be multiplied by 1/4, because of the factors of $\frac{1}{2}$ in $g^2_{NN\pi}$ and $\sigma_{\pi\pi}$.

The total I=2 O.P.E. contribution to the $\pi^+\pi^+ n$ cross-section is given by

$$\sigma_{I=2}(\pi^+\pi^+n) = \int_{t_{min}}^{t_{max}} \int_{(2\mu)^2}^{m^2_{max}} \frac{d^2\sigma}{dm^2_{\pi\pi}dt}\, dm^2_{\pi\pi}dt \qquad 7.14$$

This is just the integral over the Chew-Low plot. Again the $\pi^+ p \pi^0$ cross-section is a quarter of this.

VII.2.2 Inclusion in Likelihood Calculations

The likelihood function in Chapter IV was constructed from the s-channel cross-section expressions

$$\mathcal{L} = \prod_{\text{events}} \frac{d^4\sigma}{dw_1^2 dw_2^2 d\cos\Theta d\Phi} \qquad \text{(equation 4.15)}$$

This was normalised by dividing the likelihood for each event by the total cross-section. It was also expressed in terms of Lorentz invariant phase space ρ, so that the likelihood contribution from one event i is given by

$$\mathcal{L}_i = \frac{d^4\sigma(\underline{X},\underline{Y}_i)}{d\rho} \cdot \frac{1}{\sigma_{tot}(\underline{X})} \qquad 7.15$$

$\underline{Y}_i$ is the vector of measurements describing the event.

$\underline{X}$ is the vector of fitting parameters, describing the s-channel waves, so 7.15 can be written

$$\mathcal{L}_i = \frac{d^4\sigma(\text{waves})}{d\rho} \cdot \frac{1}{\sigma_{tot}(\text{waves})} \qquad 7.16a$$

Now that an O.P.E. contribution has been added, this must be written

$$\mathcal{L}_i = \frac{d^4\sigma(\text{waves and O.P.E.})}{d\rho} \cdot \frac{1}{\sigma_{tot}(\text{waves and O.P.E.})} \qquad 7.16b$$

Since the I=2 effect is small, we ignore overlaps, and use an incoherent sum of the two effects.

$$\mathcal{L}_i = \left[\frac{d^4\sigma(\text{waves})}{d\rho} + \frac{d^4\sigma(\text{O.P.E.})}{d\rho}\right] \cdot \frac{1}{\sigma_{tot}(\text{waves}) + \sigma_{tot}(\text{O.P.E.})} \qquad 7.17$$

The normalisation by $\frac{1}{\sigma_{tot}(\underline{X})}$ in 7.15 is required because a change of scale in the amplitudes of $\underline{X}$ caused a corresponding change in the differential (and hence also the total) cross-section. This scaling was permitted in the minimisation for the reasons given at the end of V.4.3, so in effect 7.16a should be written with a scaling factor taken out of both numerator and denominator.

$$\mathcal{L}_i = s.\frac{d^4\sigma(waves)'}{d\rho} \cdot \frac{1}{s.\sigma_{tot}(waves)'} \qquad 7.18$$

The primed values are the true ones, and the unprimed ones are the calculated ones so that

$$\sigma_{tot}(experimental) = \sigma_{tot}(waves)' = \frac{1}{s}\sigma_{tot}(waves)$$

$$\therefore \quad s = \frac{\sigma_{tot}(waves)}{\sigma_{tot}(experimental)} \qquad 7.19a$$

Now that the total cross-section is to include an O.P.E. component, the expression for s must be rewritten. The O.P.E. cross-section is obtained from equation 7.14 which has no such scale factor, so now

$$\sigma_{tot}(experimental) = \sigma_{tot}(waves)' + \sigma_{tot}(O.P.E.) = \frac{1}{s}\sigma_{tot}(waves) + \sigma_{tot}(O.P.E.)$$

$$\therefore \quad s = \frac{\sigma_{tot}(waves)}{\sigma_{tot}(experimental) - \sigma_{tot}(O.P.E.)} \qquad 7.19b$$

This scale factor must be allowed for in equation 7.17

$$\mathcal{L}_i = \left[\frac{d^4\sigma(waves)'}{d\rho} + \frac{d^4\sigma(O.P.E.)}{d\rho}\right] \frac{1}{\sigma_{tot}(waves)'+\sigma_{tot}(O.P.E.)}$$

The primes are to indicate that the true values, not the scaled ones should be used. As the likelihood function uses

the scaled values, we write

$$\mathcal{L}_i = \left[\frac{1}{s}\,\frac{d^4\sigma(\text{waves})}{d\rho} + \frac{d^4\sigma(\text{O.P.E.})}{d\rho}\right] \frac{1}{\frac{1}{s}\sigma_{tot}(\text{waves}) + \sigma_{tot}(\text{O.P.E.})}$$

$$\therefore \mathcal{L}_i = \left[\frac{d^4\sigma(\text{waves})}{d\rho} + s\,\frac{d^4\sigma(\text{O.P.E.})}{d\rho}\right] \frac{1}{\sigma_{tot}(\text{waves}) + s\sigma_{tot}(\text{O.P.E.})} \qquad 7.20$$

This then is the expression to be evaluated for each event. The "waves" terms are the same as those used for the non-O.P.E. analysis: they are the numerator and denominator of the original likelihood function 4.17. The O.P.E. terms are calculated from equations 7.13 and 7.14, the scale term from equation 7.19b.

VII.3 Performing the Fits

VII.3.1 Programming the likelihood function

The new version of the likelihood function had to be turned into a new Fortran function, and other changes in the fitting procedure were needed. Equation 7.20, written in more detail to show these requirements is -

$$\mathcal{L} = \prod_{i=\text{events}} \frac{\frac{d\sigma}{d\rho}(\text{waves})_i + s \times \sigma(q_{\pi\pi};a,r_o)_i}{\sigma_{tot}(\text{waves}) + s\,\sigma_{tot}(\text{O.P.E.})} \qquad 7.21$$

This form of the likelihood requires no changes at all to the s-channel expressions already programmed. The scope for possible errors is thus much reduced which is very important. Only the additional terms and the derivatives required changes to the programs. The following changes were made to the programs described in Chapter V.

i) X and $q_{\pi\pi}$ were calculated for each event by the program DISK and added to the set of numbers passed to the fitting program. $q_{\pi\pi}$ is given by equation 7.4a. X comprises the expression given by equation 7.13a; that part of $\frac{d\sigma}{d\rho}$(O.P.E.) which does not depend on the fitting parameters a, r_o. The same expression was used for $\pi^+\pi^+$n events and for $\pi^+p\pi^o$ events. For $\pi^+p\,\pi^o$ events it was then multiplied by $\frac{1}{4}$. This factor was first put in incorrectly as $\frac{1}{2}$ and many unsuccessful test runs were made before the error was discovered. The Jacobian (equation 7.3) was also omitted, and this was not corrected until after random starts had been made at the top 4 energies.

ii) a and r_o were 2 additional fitting parameters used by VA09AD. The calls to VA09AD were changed accordingly, and expressions for differentials with respect to these variables

had to be evaluated. Differentials with respect to all other variables also had to be rewritten to allow for the extra terms. The new expressions were checked by making comparisons with numerical gradients calculated by VA10AD; an obscure error was eventually traced to the use of a single precision variable where double precision was needed.

iii) The I=2 $\pi\pi$ cross-section $\sigma(q_{\pi\pi};a,r_o)$ was calculated for each event using the value of $q_{\pi\pi}$ for that event and values of a, r_o provided by the minimiser at that step.

iv) The integral $$\sigma_{tot}(\text{O.P.E.}) = \int \frac{d\sigma(a,r_o)}{dm^2_{\pi\pi}dt}\, dm^2_{\pi\pi}\, dt$$ had to be calculated at every minimisation step, using the values of a and r_o provided at that step. The differentials of σ_{tot}(O.P.E.) with respect to a and r_o were also needed in the gradient calculations. Two methods of calculating these integrals were considered. The integral, and its differentials, could be evaluated by a numerical integration at each minimisation step. Alternatively, the integral could be evaluated for a set of values of a and r_o, providing a grid of $\sigma(a,r_o)$ values. This grid could be evaluated separately from the fitting program, which could then read it in, obtaining σ values by interpolation, and approximating differentials by differences between adjacent grid points.

The use of a grid would need less computer time than exact calculations at each step, so this was tried first. Monte Carlo events were generated, and $\frac{d\sigma(a,r_o)}{dm^2_{\pi\pi}dt}$ was calculated for 50 (evenly spaced) a values and 50 r_o values for each event. The normalised sums over 50,000 events at each point provided a grid allowing r_o values between 0

and 40 fermis, and a values between -10 and 10 fermis. This was found to be inaccurate near the origin, even when the number of Monte Carlo events was increased to 300,000 so a second grid for use close to the origin was calculated, and then a third even finer one. Each grid had 50 x 50 steps, but even three grids were found to be inaccurate, and the use of more grids or larger grids would have required too much computer storage. The linear interpolation was replaced by the calculation of a paraboloid on five grid points around the required position, so that the integral and its differentials could be interpolated on the paraboloid. When this too was found to be insufficiently accurate, the grids were recalculated using a simple numerical integrator, but still without success.

The accuracy of the integrals was then questioned, and as in the case of the normalisation integrals (section V.3), QB01A was tried. This gave better results and took only between $\frac{1}{6}$ and $\frac{1}{3}$ second for each integral, so that it was possible to evaluate the integral, and its differentials, exactly at each minimisation step. The use of a grid was abandoned, and the integral, with its differentials, was calculated by 3 calls to QB01A at each step although this took more computing time.

As σ(O.P.E.) was being calculated using the $\pi^+\pi^+n$ expressions, it was multiplied by $\frac{5}{4}$ to allow for the additional $\pi^+p\pi^o$ cross-section, giving σ_{tot}(O.P.E.).

v) Once σ_{tot}(O.P.E.) had been calculated, the scale

$$s = \frac{\sigma_{tot}(\text{waves})}{\sigma_{tot}(\text{experimental}) - \sigma_{tot}(\text{O.P.E.})} \qquad \text{(equation 7.19b)}$$

could be evaluated. This could cause trouble if the minimiser tried large values of a and r_o, making σ_{tot}(O.P.E.) > σ_{tot}(experimental), as a negative scale would be meaningless. While a grid was being used to evaluate σ_{tot}(O.P.E.) it was also necessary to use only values within the grid limits, so attempts were made to limit the values of a and r_o by giving extremely steep gradients at the boundaries of the grid. We also tried to limit the range of a and r_o by minimising their arc tangents, normalised to the allowed range, so that the minimisation variables could tend to infinity without a and r_o exceeding their limits. The use of QB01A allowed us to dispense with limits on a and r_o. We instead set $s=1.0$ if it became negative. In cases where the minimiser tried this once and then went back to sensible values it did not matter, whereas if the minimiser stayed at large values of a and r_o, the fit "blew up" and was discarded, but this only happened in a few cases.

vi) Once all the additional terms were calculated, the new expression (7.21) for the likelihood was evaluated.

vii) At the end of a minimisation run, the O.P.E. parameters and cross-sections were printed out in addition to the s-channel cross-sections and parameters. a and r_o were measured in GeV^{-1} in the expression 7.12 (because $q_{\pi\pi}$ is measured in GeV/c), but were output in fermis.

VII.3.2 Data fitting and error calculations

The original programs, with the changes described above, and the original normalisation constants were used to refit our data. Twenty successful random starts had been

made at each of the top four energies before the missing Jacobian was noticed. Although these runs were not correct, the I=2 O.P.E. cross-section accounts for only about 3% of the total cross-section at these energies, so their qualitative results were of some use. They showed that minima came in groups as in the fits without O.P.E., that there were fewer different solutions, and that these solutions were distinctly similar to non-O.P.E. solutions. A further 10 random starts at 895 MeV/c and 5 at 945 MeV/c, with the Jacobian corrected, confirmed this. The remaining fits were therefore made by starting at every non-O.P.E. solution found by more than one run and refitting them with O.P.E. allowed for. A few refits starting from the incorrect O.P.E. runs were also made.

In the random starts, the waves were given the same random starting values as for the corresponding non-O.P.E. random starts. Although O.P.E. solutions were similar to non-O.P.E. solutions, it was not always the case that corresponding O.P.E. and non-O.P.E. random starts came to the same solutions. The parameters a and r_o were given random starting values in the ranges -1. to 1. and 0. to 10. fermis respectively. The runs starting from non-O.P.E. solutions were given starting values of a = 0.1fm, r_o = 2.0fm, as these were approximately the values found by the random starts.

At 895 MeV/c and 945 MeV/c, where correct random starts and continuation runs were made, the same minima were found by both types of run. This justified the use of

continuation runs alone at the other energies, which saved a lot of computer time. The total number of minima was smaller than in the non-O.P.E. case because different continuation runs sometimes came to the same solutions. This gave us confidence that the addition of the O.P.E. term was improving the quality of the fit.

All runs made at 600 MeV/c failed because they tried to fit with very large values of r_o, which caused them to "blow up" as described earlier. The projections shown in Figure V.5.a had shown no loss of peripheral events, so the I=2 O.P.E. contribution at this energy is small, and evidently too small to allow a determination of the parameters.

The error calculations also followed the methods used for the non-O.P.E. analysis. Errors on the wave parameters, and on σ^{JP} were calculated as before. Errors on a , r_o, and σ(O.P.E.) were calculated, using the error formula given in V.4.4, from the relevant terms in the inverted second derivative matrix. Some care with units was again needed.

VII.3.3 Reproduction of experimental data

Figures VII.2.a to VII.2.i show projections corresponding to those of V.5.a to V.5.i. The O.P.E. solutions chosen by CHI at each energy are used. At 600 MeV/c there was no O.P.E. solution, but CHI chose a different non-O.P.E. solution to that previously used, so its projections are included here (this solution was similar to the one previously chosen, within RANCOM limits). It is immediately obvious that the $\pi^+\pi^+$n channel is better fitted

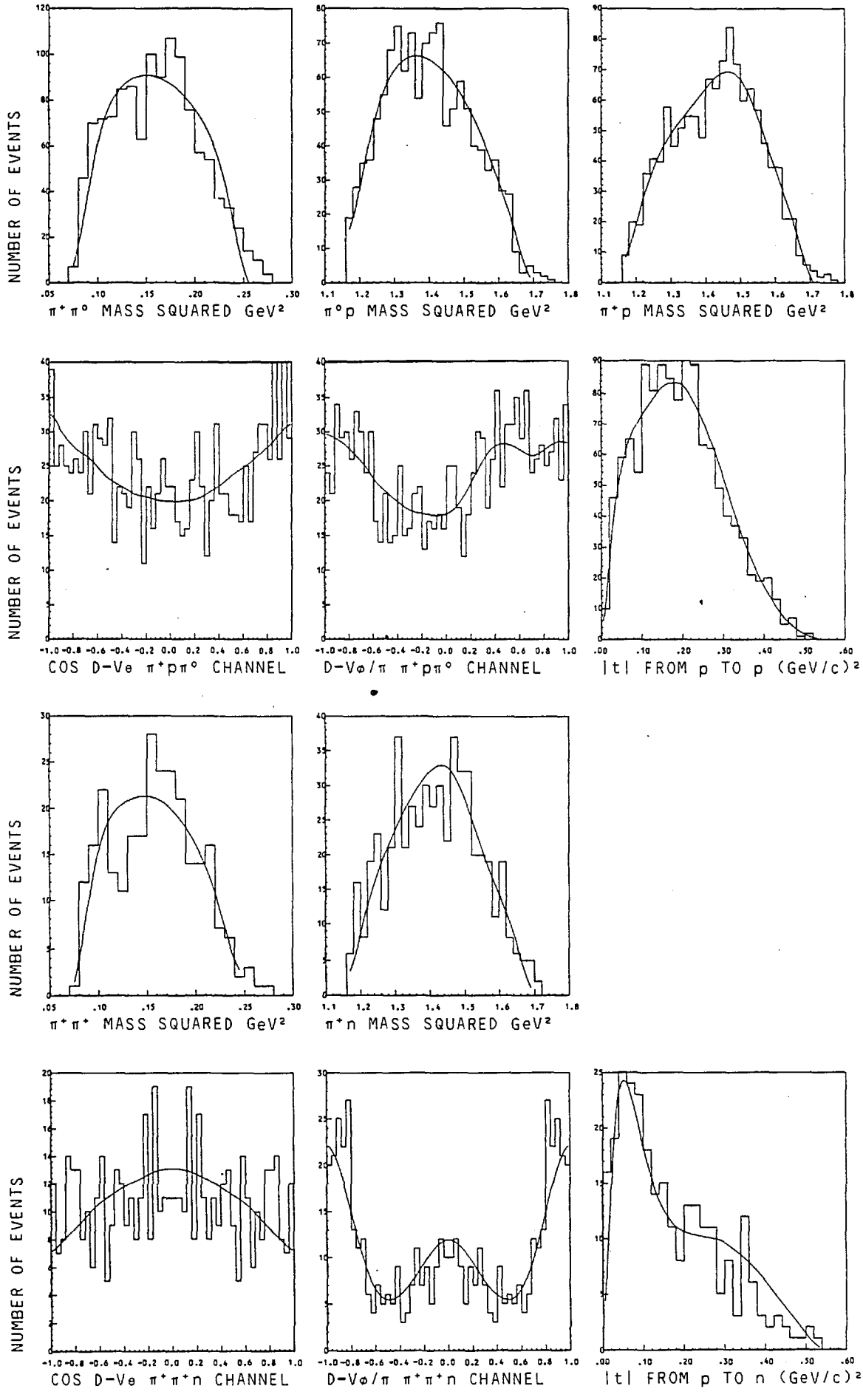

FIG VII.2.a 600 MeV/c PROJECTIONS AFTER OPE REFIT

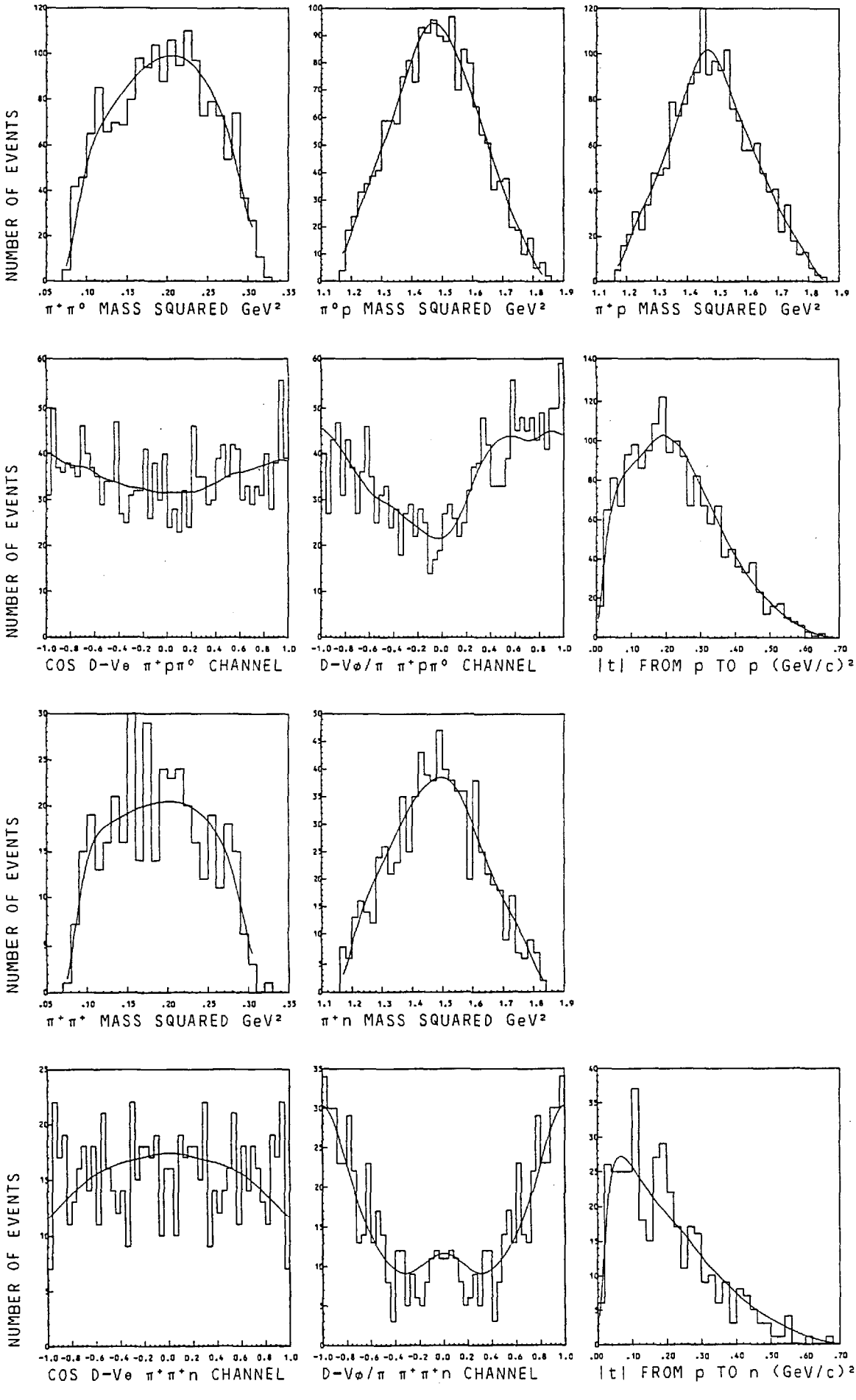

FIG VII.2.b 700 MeV/c PROJECTIONS AFTER OPE REFIT

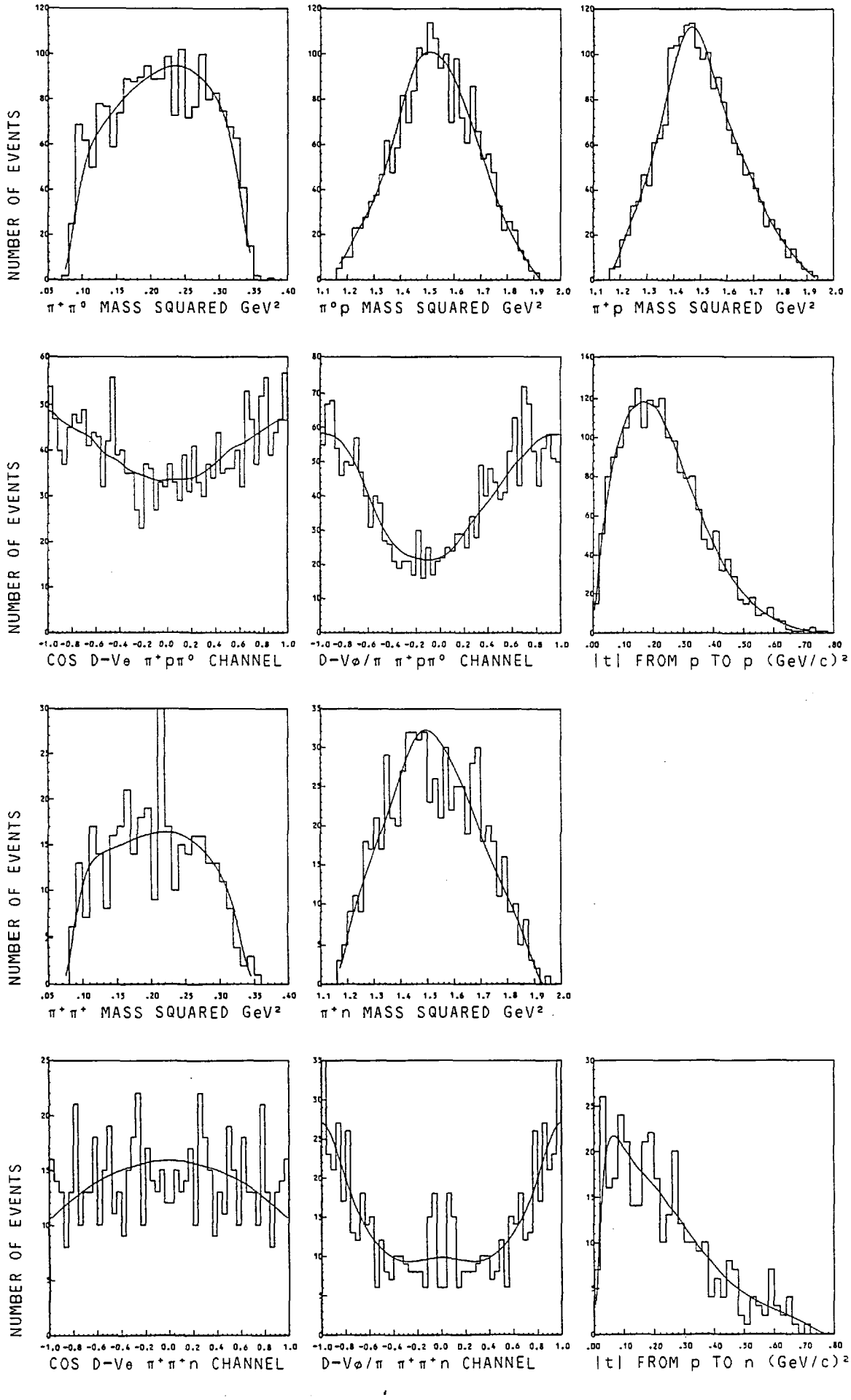

FIG VII.2.c 750 MeV/c PROJECTIONS AFTER OPE REFIT

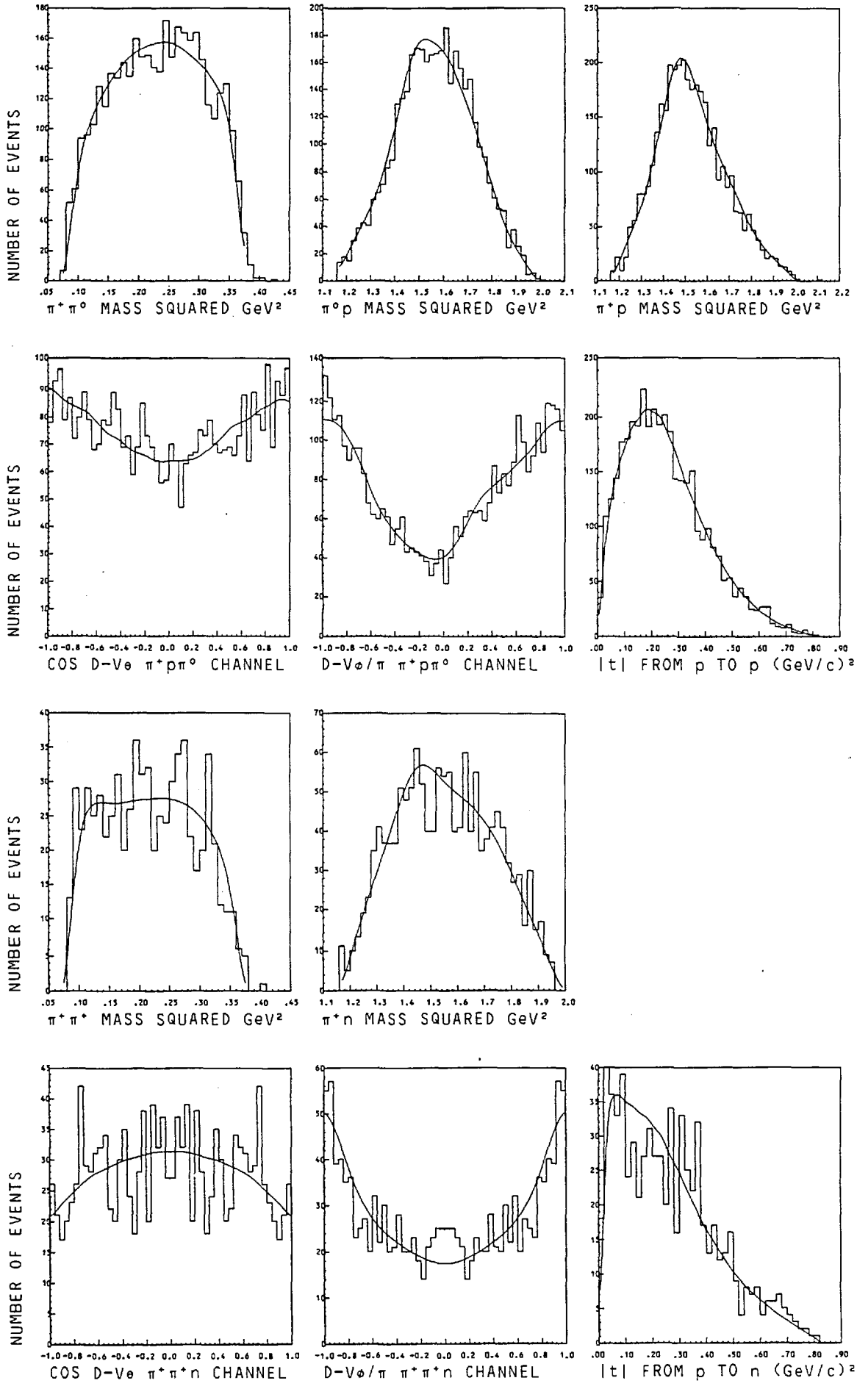

FIG VII.2.d 800 MeV/c PROJECTIONS AFTER OPE REFIT

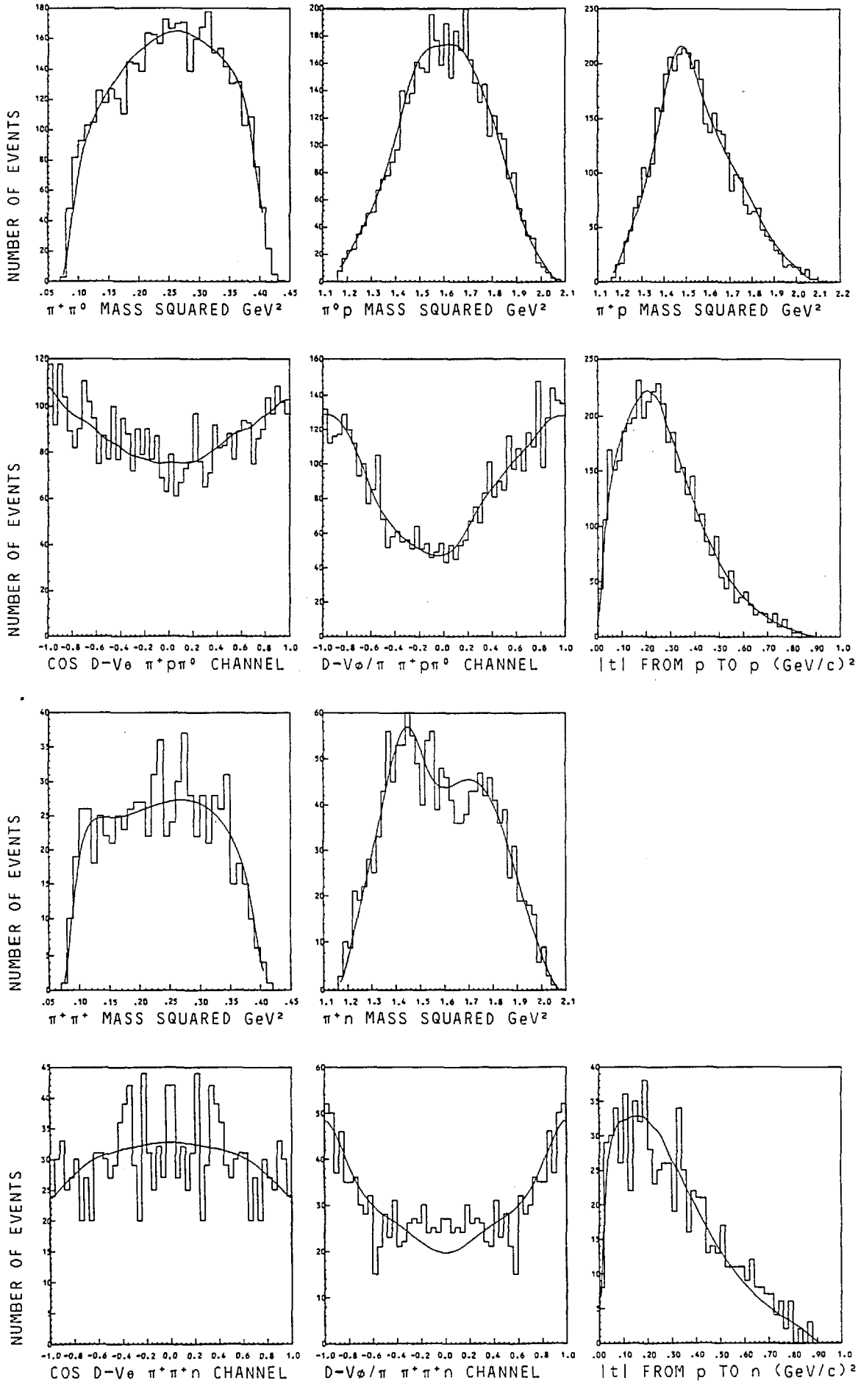

FIG VII.2.e 850 MeV/c PROJECTIONS AFTER OPE REFIT

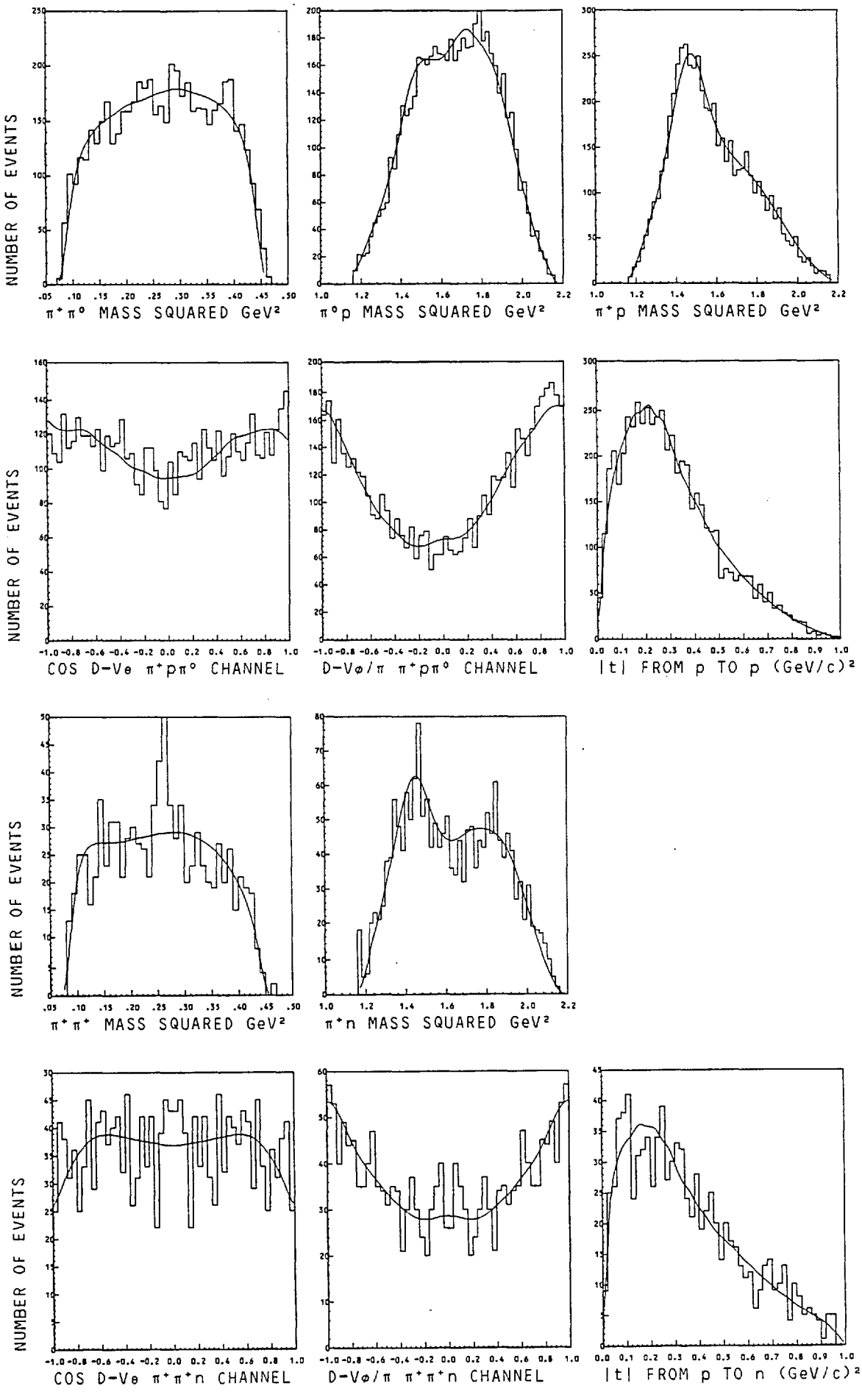

FIG VII.2.f 895 MeV/c PROJECTIONS AFTER OPE REFIT

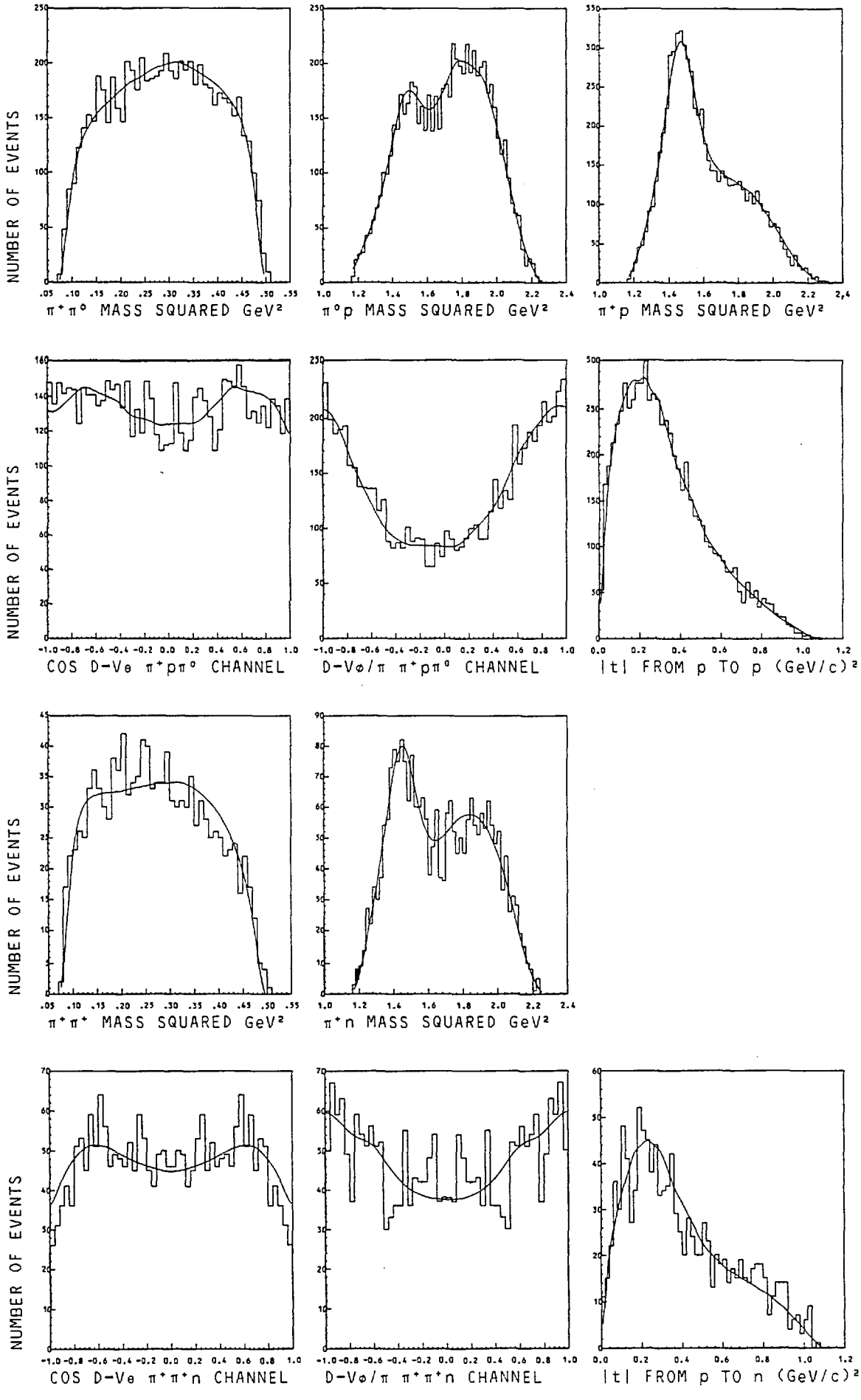

FIG VII.2.g 945 MeV/c PROJECTIONS AFTER OPE REFIT

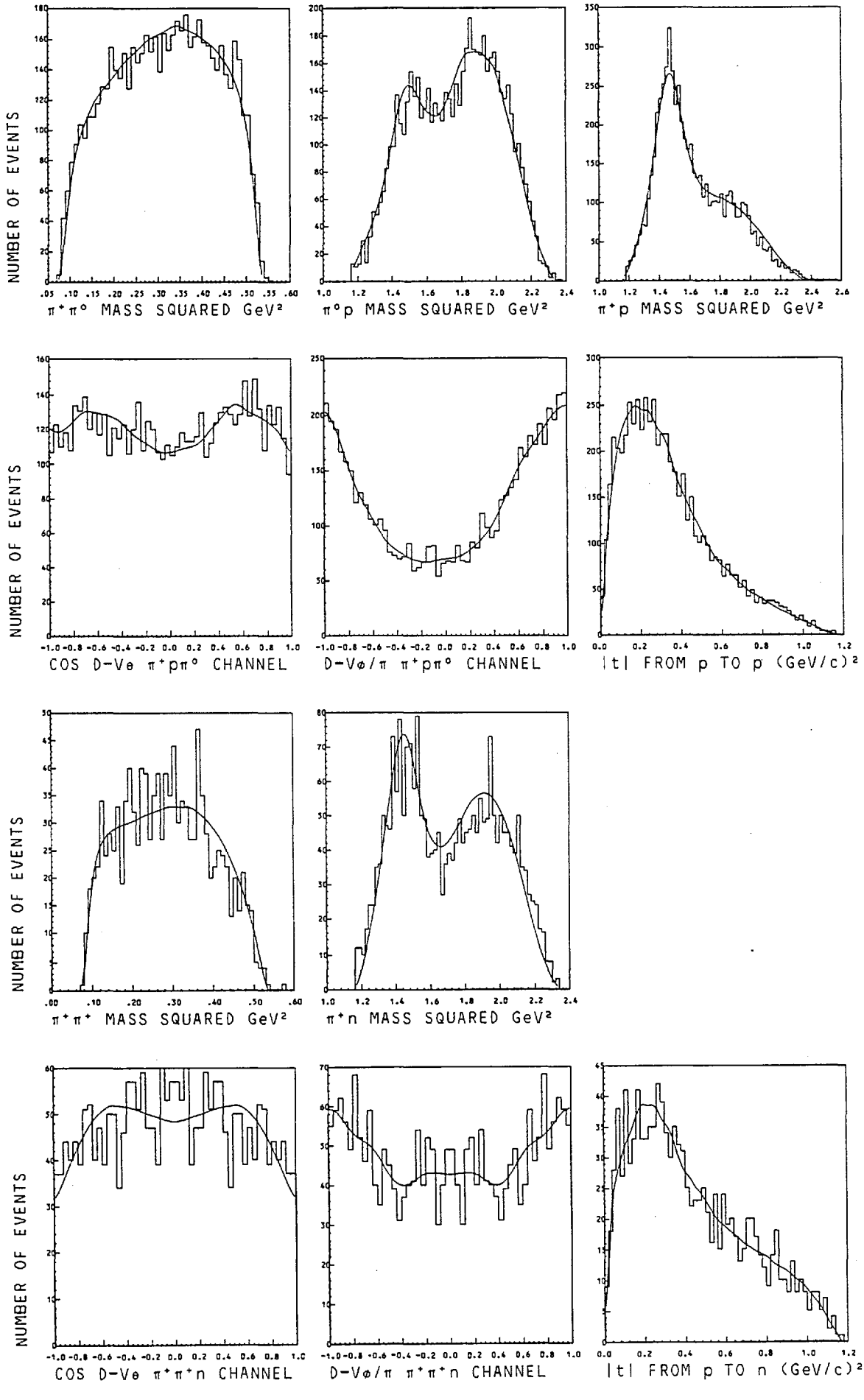

FIG VII.2.h 995 MeV/c PROJECTIONS AFTER OPE REFIT

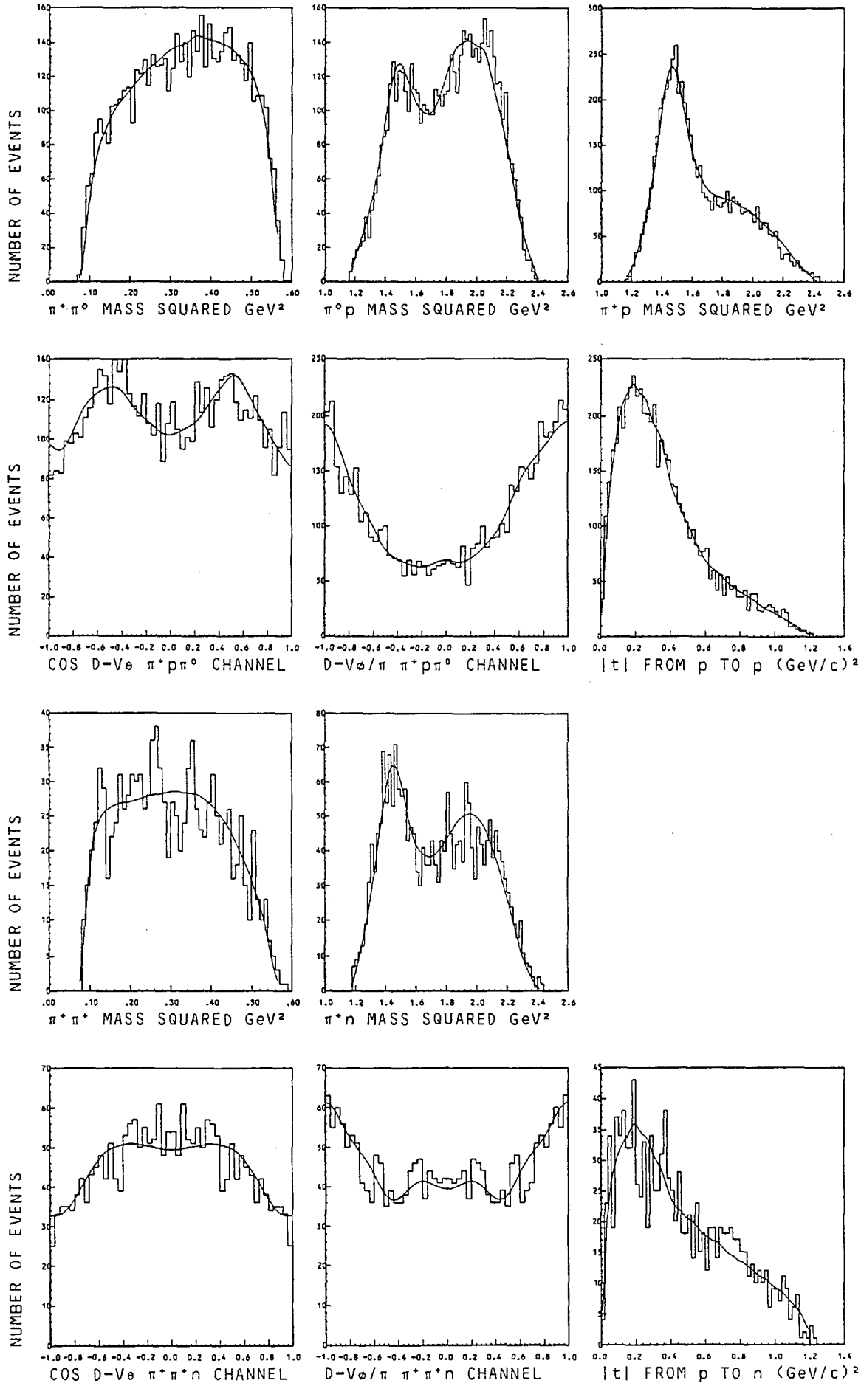

FIG VII.2.i 1040 MeV/c PROJECTIONS AFTER OPE REFIT

than before. The Deler-Vallades angles are in general better reproduced, and $|t|$ has the correct forward peak. The mass squared plots for $\pi^+\pi^+$ are also improved. The $\pi^+p\pi^o$ projections are very little different; there are slight improvements in a few places, such as in Φ at 1040 MeV/c.

The improved reproduction of the experimental data vindicates the use of the t-channel I=2 effect to describe peripheral effects, its other results are described later. The use of O.P.E. to describe ρ production was also investigated, and some fitting programs with it were run, but it was found to be unnecessary, as the projections show.

VII.4 Continuity search and results

VII.4.1 Continuity search and s-channel results

Compared to the non-O.P.E. analysis there were fewer solutions, log likelihoods were higher (typically by 20 units), and the $\pi^+\pi^+n$ cross-sections were equally good. No attempts were made to remove solutions before the continuity analysis which was again used to choose one solution at each energy. The same programs were used as in the non-O.P.E. case, O.P.E. parameters were not used, and at 600 MeV/c the non-O.P.E. solutions were used because there were no acceptable O.P.E. refits. RANCOM was used with the same limits as before to check which solutions were similar, then various runs of CHI were made. After some preliminary runs and a check of the plots and Argand diagrams, a preferred mass and width were chosen for the ΔD33 resonance. Details are given in VII.5.1, the values were M = 1650 MeV, Γ = 160 MeV.

Table VII.1 shows the results of a CHI run tied to ΔDS33 with these preferred parameters; the best 20 combinations are shown as before. The χ^2 values here are lower than in the non-O.P.E. analysis, which means that the best combinations are now more continuous. The first 7 combinations are all the same within RANCOM limits; there is no problem of a competing solution at 1040 MeV/c. The first combination to differ significantly from the best one is number 39 (shown in Table VII.3). Table VII.2 shows the results of CHI runs tied to various masses and widths in the ΔSD31 and ΔDS33 waves; combination 222111211, the best in Table VII.1, is best through the whole range. χ^2 changes only slowly with these parameters; as before χ^2 tends to fall with increasing mass or width.

In Chapter VI, the results of a few runs of CHI tied to waves other than ΔSD31 and ΔDS33 were shown. The CHI results were better after the refit with O.P.E., so a lot of runs tied to other waves were made. Table VII.3.a shows the results of tying to various $\Delta\pi$ waves, the best two combinations are shown together with the first one that differs at two energies according to RANCOM. Of 9 waves, 8 choose combination 222111211 as the best, and 5 give a confidence level above 80%. In 7 of the 9 waves, the first very different solution lies beyond position 30 in the CHI list. These results speak for themselves - the $\Delta\pi$ waves are continuous and show a strong preference for combination 222111211. Table VII.3.b shows the results of tying to six N*π waves, these generally show much poorer results than the $\Delta\pi$ waves, so the first different combination is not shown.

Combination number	600	700	750	800	850	895	945	995	1040	χ^2	C.L.%
1	2	2	2	1	1	1	2	1	1	278.2	95.6
2	2	2	2	1	1	1	2	1	8	279.6	95.0
3	2	2	2	1	1	2	2	1	1	283.1	93.2
4	2	2	2	1	1	2	2	1	8	284.6	92.3
5	2	2	2	1	2	1	2	1	1	286.2	91.3
6	2	2	2	1	2	1	2	1	8	287.7	90.2
7	1	2	2	1	1	1	2	1	1	291.1	87.6
8	1	1*	2	1	1	1	2	1	1	292.1	86.7
9	1	2	2	1	1	1	2	1	8	292.5	86.3
10	2	2	2	1	2	2	2	1	1	292.7	86.1
11	1	1*	2	1	1	1	2	1	8	293.5	85.3
12	2	2	2	1	2	2	2	1	8	294.2	84.7
13	1	2	2	1	1	2	2	1	1	296.0	82.8
14	1	1*	2	1	1	2	2	1	1	297.0	81.7
15	1	2	2	1	1	2	2	1	8	297.5	81.2
16	1	1*	2	1	1	2	2	1	8	298.5	80.1
17	1	2	2	1	2	1	2	1	1	299.1	79.3
18	1	1*	2	1	2	1	2	1	1	300.1	78.1
19	2	2	2	1	1	1	2	1	10*	300.5	77.7
20	1	2	2	1	2	1	2	1	8	300.6	77.6

The columns show the 9 momenta, and the solutions picked at each momentum. (The numbers identify different solutions at each energy as described in Chapter VI. Any solution that differs from the first one at that energy according to RANCOM is marked with an asterisk.)

Table VII.1

The 20 best combinations found by CHI tied to Δ DS33 with Mass=1.65 GeV, Width=0.20 GeV

Width \ Mass (GeV)	1.58	1.61	1.65	1.72
0.08	294.28	295.19	294.52	286.35
0.14	290.28	290.48	289.77	286.42
0.16	289.56	289.64	289.00	286.37
0.20	288.50	288.47	287.96	286.24

Best χ^2 tying to ΔSD1 with various masses and widths

Width \ Mass (GeV)	1.60	1.65	1.67	1.74
0.13	286.90	282.15	279.36	266.14
0.16	282.00	278.18	275.84	266.24
0.20	277.61	274.64	272.86	266.14
0.27	272.90	270.90	269.78	265.71

Best χ^2 tying to ΔDS3 with various masses and widths

Table VII.2

The N*PP3 wave is quite exceptional, with a mass of 1690 and a width of 250 MeV it gives a confidence level of 100% (to 3 significant figures). It has, admittedly, been noted that χ^2 tends to fall with rising mass and width, and the mass and width here are the highest of any tried. Even after allowing for this, the χ^2 is exceptionally low, as if the N*π decay of the ΔPP3 resonance were exceptionally clean, and this is discussed in Section VII.5.3. N*DD3 also gives an acceptable χ^2, it was not one of the 20 waves originally used in CHI, so a special run with it included was made. The other waves give much larger χ^2 values, because they are small, or have large backgrounds. Table VII.3.c shows the results of tying to ρN waves. Only ρ_1SS31 and ρ_1DD33 give good χ^2 values, the other waves give very poor values, though several choose combinations similar to 222111211. These poor χ^2 values, even when the preferred combination is found, suggest large backgrounds or other problems in ρN waves. All our energies lie below the ρ production threshold (1711 MeV) so problems could be expected. Finally Table VII.4 shows the results of using more or fewer than 20 waves in the calculation of χ^2, the best combinations are similar to the preferred one within RANCOM limits, or differ at only one energy.

Combination 222111211 was used to produce Argand diagrams and σ^{JP} plots, as in Chapter VI, except that the Argand diagrams were tied to a ΔDS33 of mass 1650 MeV, and width 160 MeV, and they were not rotated by -25°. Figure VII.3 shows Argand diagrams, without errors, for the larger

Wave tied, mass and width in GeV	Solutions picked at each energy. Numbers and asterisks as in Table VII.1	Position in CHI table	χ^2	C.L.%
ΔSD1	222111211	1	289.8	88.7
1.65, 0.14	222112211	2	291.7	87.0
	11*211121 10*	59	334.4	27.6
ΔPP1	222112211	1	324.3	42.1
1.525, 0.04	11*2112211	2	324.6	41.7
	11*211221 10*	31	356.3	7.9
ΔPP1	222111211	1	309.3	65.6
1.68, 0.08	222112211	2	309.9	64.6
	11*211121 10*	34	344.1	17.0
ΔPP3	222111211	1	298.2	80.4
1.60, 0.08	222112211	2	300.1	78.2
	11*211121 10*	38	332.0	31.0
ΔPP3	222111211	1	281.6	94.1
1.69, 0.25	222112211	2	284.2	92.6
	11*211121 10*	36	315.2	56.6
ΔPF3	222111211	1	348.3	13.2
1.69, 0.25	222121211	2	350.3	11.8
	221*111212*	45	393.4	0.3
ΔDS3	222111211	1	278.2	95.6
1.65, 0.16	222111218	2	279.6	95.0
	11*211121 10*	39	314.4	57.8
ΔDD3	11*2111218	1	271.9	97.6
1.65, 0.16	11*2112218	2	274.6	96.9
	222111211	15	297.1	81.6
	11*2111212*	19	302.0	75.8
ΔDD5	222111211	1	334.6	27.8
1.64, 0.04	222111218	2	335.6	26.6
	2221111*12*	24	368.0	3.3

Table VII.3.a

Results of CHI runs tied to various Δ waves

Wave tied, mass & width in GeV	Solutions picked at each energy. Numbers and asterisks as in Table VII.1	Position in CHI table	χ^2	C.L.%
N*SS1	2221253*2*2*	1	494.6	0.0
1.65, 0.14	2221254*2*2*	2	495.7	0.0
N*PP1	11*2112211	1	404.7	0.1
1.525, 0.04	11*2112218	2	406.4	0.1
N*PP1	12211222* 10*	1	390.3	0.4
1.68, 0.08	12211122* 10*	2	391.5	0.4
N*PP3	222111211	1	277.8	95.7
1.60, 0.08	222111218	2	283.4	93.1
N*PP3	222111211	1	234.7	100.
1.69, 0.25	222111218	2	240.4	100.
N*DD3	222126211	1	348.9	30.2
1.65, 0.16	222126218	2	353.4	24.6

Table VII.3.b

Results of CHI runs tied to various N* waves

Wave tied, mass & width in GeV	Solutions picked at each energy. Numbers and asterisks as in Table VII.1	Position in CHI table	χ^2	C.L.%
ρ_1SS1	222111211	1	278.1	95.6
1.65, 0.14	222111218	2	279.1	95.2
ρ_1PP1	222115211	1	366.8	3.6
1.525, 0.04	222112211	2	371.0	2.6
ρ_1PP1	222115218	1	428.0	0.0
1.68, 0.08	222112218	2	433.2	0.0
ρ_1PP3	221*2121*2*1	1	584.0	0.0
1.69, 0.25	121*2121*2*1	2	586.9	0.0
ρ_1DD3	222111211	1	305.5	71.1
1.65, 0.16	222111218	2	311.8	61.8
ρ_3SD1	1224*23*4*12*	1	598.2	0.0
1.65, 0.14	1224*23*4*1 10*	2	598.4	0.0
ρ_3PP1	2221154*2*7*	1	458.9	0.0
1.525, 0.04	221*1154*2*7*	2	467.1	0.0
ρ_3PP1	221*111211	1	445.6	0.0
1.68, 0.08	121*111211	2	454.2	0.0
ρ_3PP3	11*2115213*	1	592.7	0.0
1.69, 0.25	31*2115213*	2	602.0	0.0
ρ_3DS3	11*21213*2*7*	1	406.0	0.1
1.65, 0.16	11*21214*2*7*	2	408.2	0.1
ρ_3DD3	11*2111211	1	394.5	0.3
1.65, 0.16	11*2321211	2	396.9	0.2

Table VII.3.c

Results of CHI runs tied to various ρ waves

Waves used in computing χ^2	Solutions picked at each energy. Numbers and asterisks used as in Table VII.1	Position in CHI table	χ^2	C.L.%
14 waves (21 wave set except ΔPF3, N*DD3, ρ_1PP3, ρ_1DD3, ρ_3SD1, ρ_3PP3, ρ_3PF3)	11*2111211	1	187.5	96.4
	11*2112211	2	187.6	96.3
15 waves (21 wave set except ΔPF3, N*SS1, ρ_1PP3, ρ_3SD1, ρ_3PP1, ρ_3PF3)	11*2111218	1	192.0	99.0
	11*2112218	2	192.3	99.0
16 waves (21 wave set except ΔPF3, N*SS1, N*DD3, ρ_3SS1, ρ_3PF3)	11*2111211	1	215.1	97.0
	11*2111218	2	215.5	96.9
20 waves (21 wave set except N*DD3)	222111211	1	278.2	95.6
	222111218	2	279.6	95.0
21 waves (complete 21 wave set)	222111218	1	313.9	80.2
	2221111*18	2	314.9	79.0

Table VII.4

Results of running CHI tied to ΔDS3, using various numbers of waves

waves. Table VII.5 gives T-matrix element amplitudes and phases with errors for all waves; Argand diagrams for all waves, with errors, are shown in Appendix B. Figure VII.4 shows σ^{JP} plots, Figure VII.5 shows σ^{JP} for the P31 wave enlarged, with elastic predictions and upper and lower limits. The σ^{JP} values are given, with errors, in Table VII.6.

As in the non-O.P.E. analysis, the Argand diagrams show clear resonance structure in ΔSD31, ρ_1SS31, ΔPP33, N*PP33 and ΔDS33. These waves are, if anything, more continuous than in the non-O.P.E. analysis, and no other waves become as significant. In the S waves ρ_1SS31 in particular becomes more continuous, whereas N*SS31 and ρ_3SD31 become smaller. In P31, ΔPP31 remains confused, the higher energies move by almost $\pi/2$ relative to the non-O.P.E. Argand diagrams, and points 3 and 7 are rather discontinuous. N*PP31 becomes smaller, and shows an anticlockwise loop, with discontinuous behaviour at energies 3 and 7 again. ρ_1PP31 is larger, and shows approximately anticlockwise behaviour except for energy 2. ρ_3PP31 is a distorted version of the same motions as without O.P.E. All this structure is interesting, and would need very rapid background motion to explain it alone, but it is not in itself enough to locate any resonances. Of the P33 waves, ΔPP33 becomes more continuous, and N*PP33 changes little. ρ_1PP33 and ρ_3PP33 remain confused with a tendency to anticlockwise motion at the higher energies. In D33, ρ_3DS33 becomes smaller, but retains an anticlockwise motion, and the other waves become somewhat larger and more continuous. ΔDS33, the wave tied to,

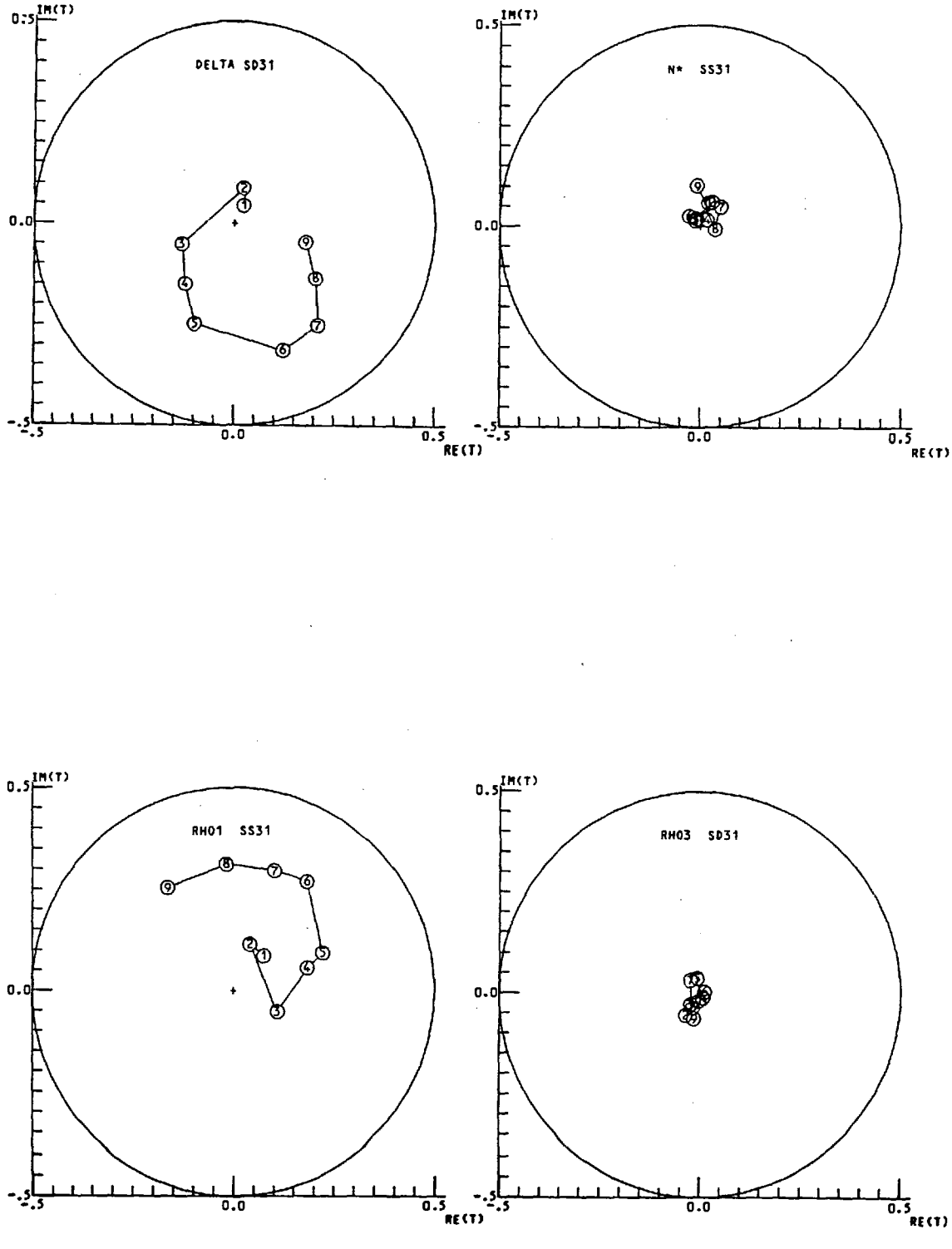

Figure VII.3.a

(details at foot of Fig.VII.3.e)

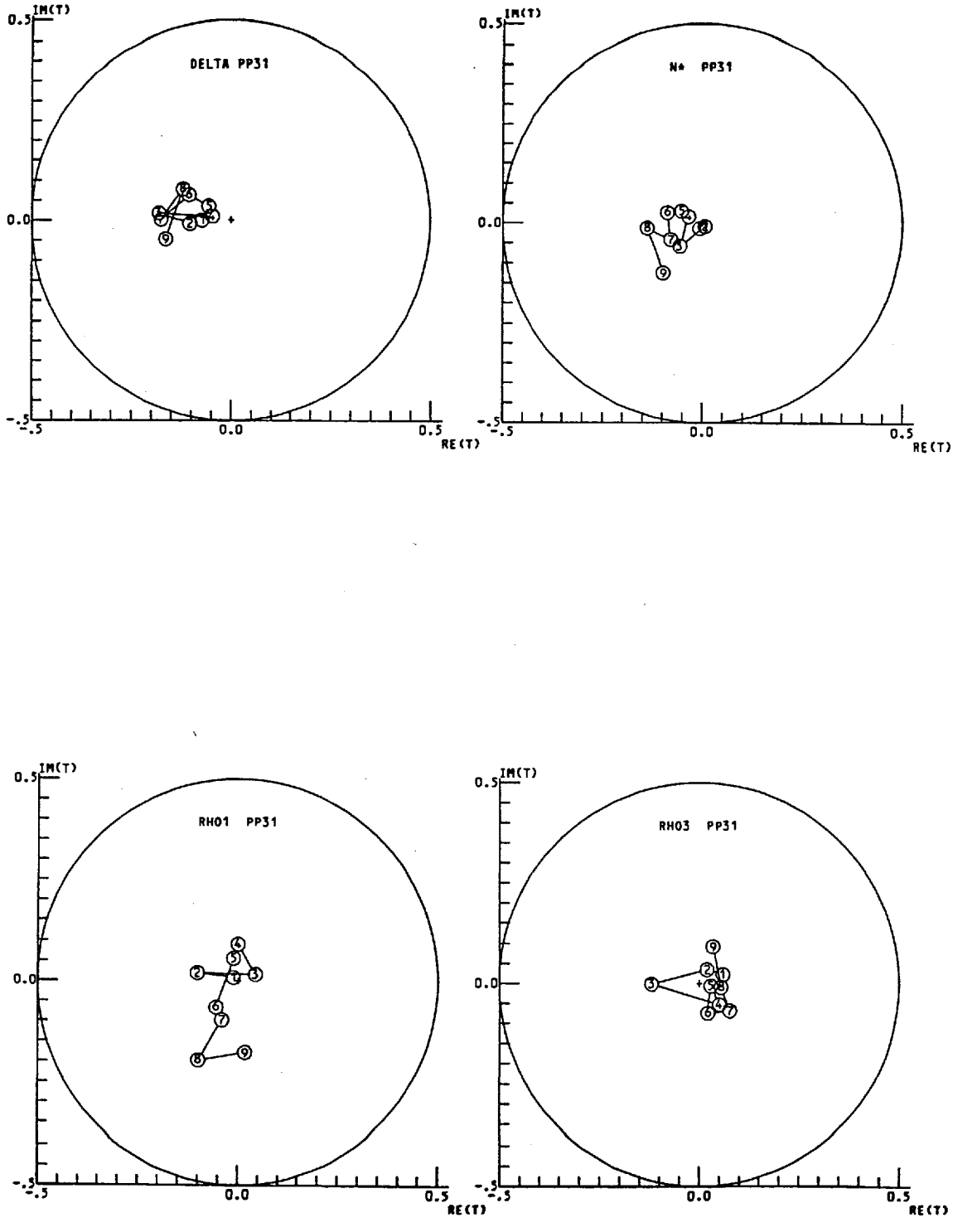

Figure VII.3.b

(details at foot of Fig.VII.3.e)

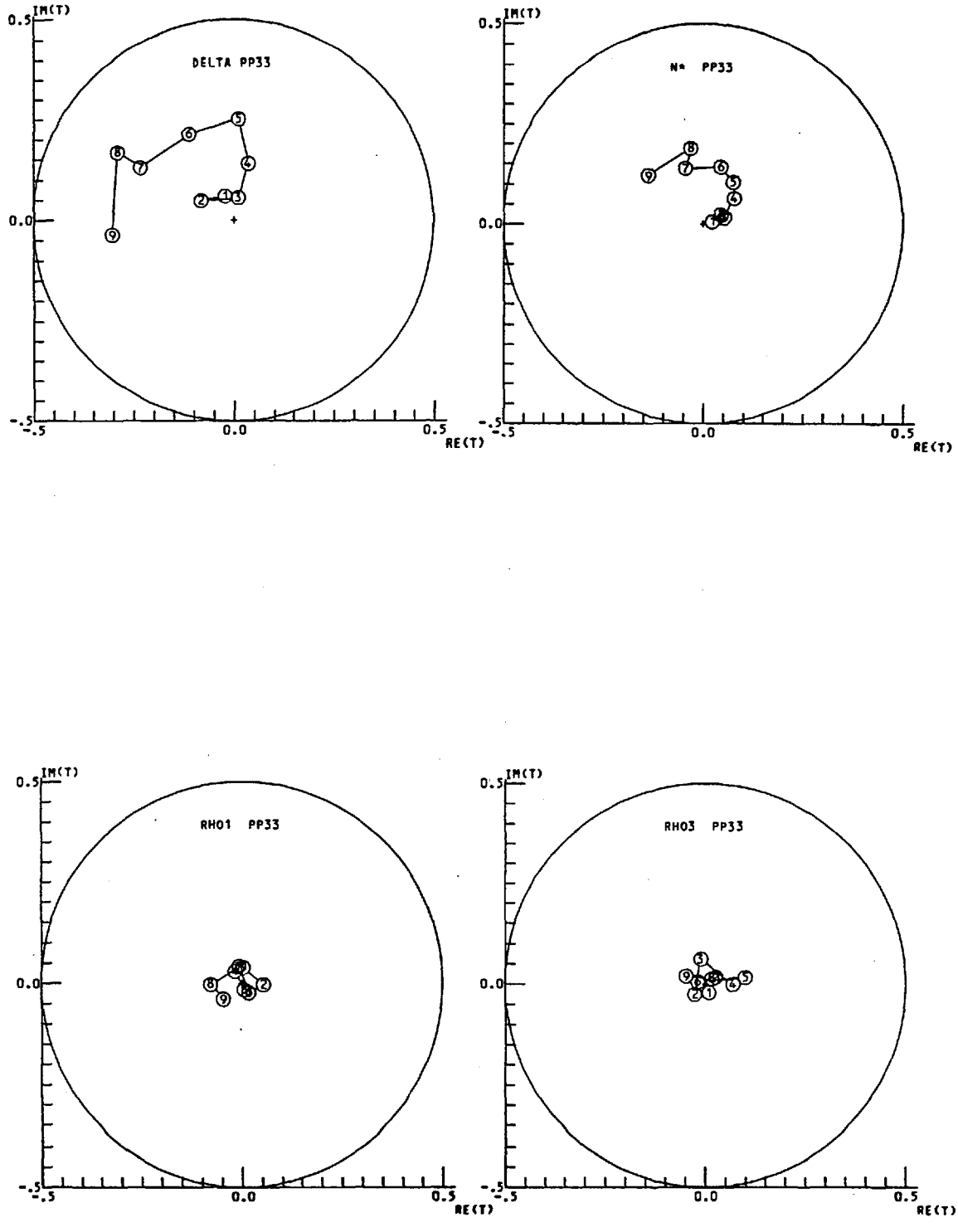

Figure VII.3.c

(details at foot of Fig.VII.3.e)

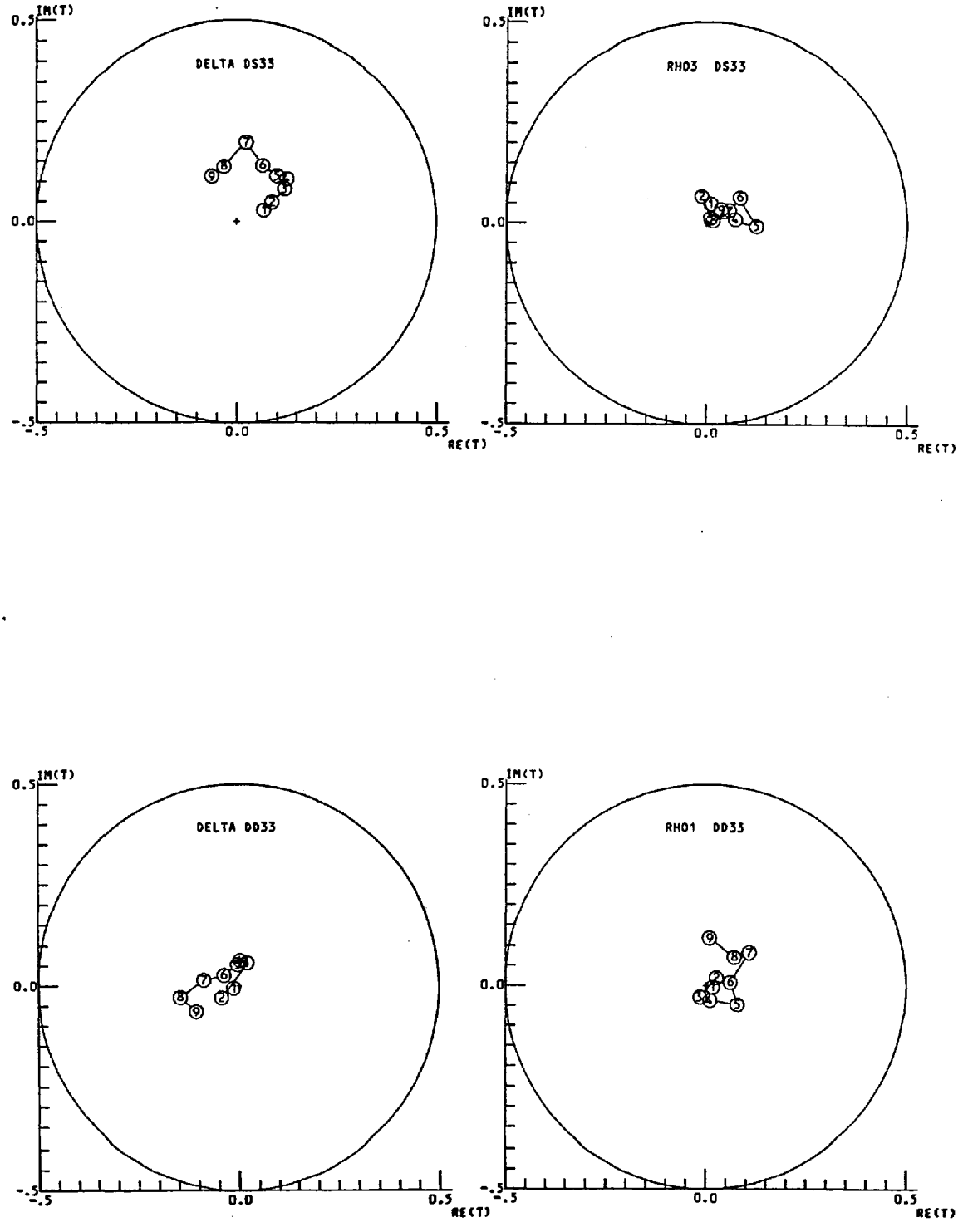

Figure VII.3.d

(details at foot of Fig.VII.3.e)

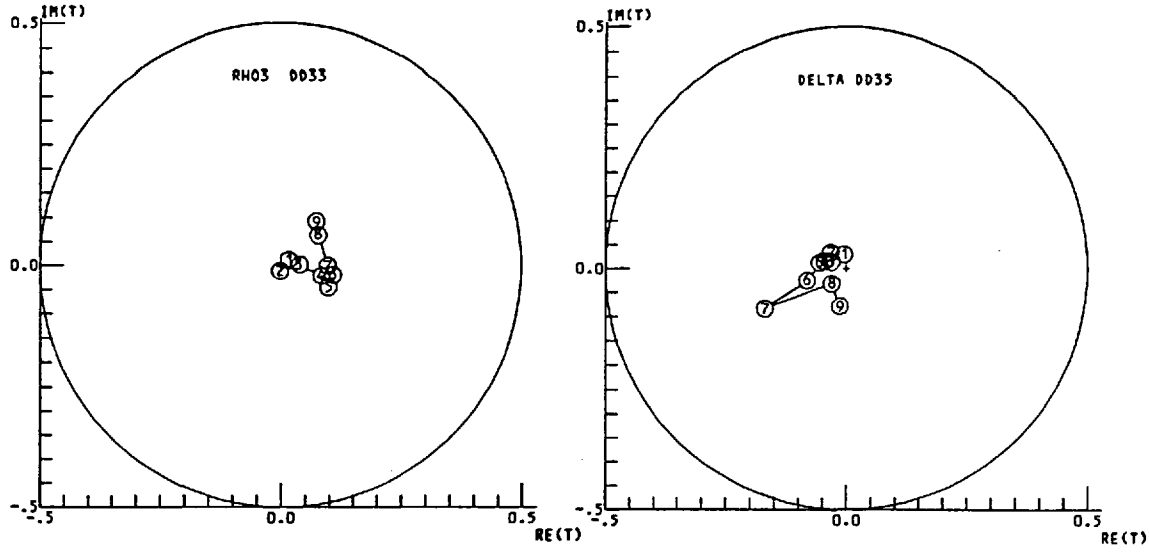

Figure VII.3.e

Argand diagrams for most continuous solution, tied to Δ DS33 with M=1650 MeV, Γ=160 MeV, rotated by 180° (see text)

Points 1-9 denote solutions at the following energies (in GeV)

1 - 1.439

2 - 1.495

3 - 1.526

4 - 1.551

5 - 1.577

6 - 1.612

7 - 1.640

8 - 1.668

9 - 1.693

Amplitudes and phases of T-matrix elements after O.P.E. refit

Waves	Energies in GeV 1.439	1.495	1.526	1.551	1.577	1.612	1.640	1.668	1.693
DELTA SD31									
AMPLITUDE	0.050	0.091	0.140	0.193	0.267	0.337	0.327	0.244	0.184
& ERROR	0.021	0.018	0.031	0.025	0.031	0.063	0.044	0.028	0.028
PHASE	1.11	1.32	3.52	-2.26	-1.95	-1.20	-0.87	-0.59	-0.25
& ERROR	0.29	0.29	0.27	0.26	0.25	0.23	0.20	0.22	0.31
DELTA PP31									
AMPLITUDE	0.072	0.103	0.181	0.047	0.065	0.122	0.175	0.142	0.170
& ERROR	0.028	0.022	0.037	0.026	0.026	0.055	0.031	0.028	0.040
PHASE	3.14	3.22	3.04	-3.35	-3.71	-3.69	-3.15	-3.72	-2.86
& ERROR	0.31	0.29	0.27	0.41	0.41	0.46	0.23	0.33	0.27
DELTA PP33									
AMPLITUDE	0.063	0.093	0.057	0.146	0.253	0.241	0.266	0.334	0.305
& ERROR	0.025	0.020	0.028	0.022	0.032	0.043	0.039	0.042	0.030
PHASE	1.89	2.60	1.34	-4.98	-4.77	-4.24	-3.65	-3.67	-3.02
& ERROR	0.33	0.31	0.42	0.25	0.24	0.31	0.21	0.20	0.20
DELTA PF33									
AMPLITUDE	0.008	0.019	0.023	0.020	0.048	0.041	0.050	0.063	0.071
& ERROR	0.005	0.009	0.015	0.008	0.012	0.019	0.015	0.016	0.018
PHASE	0.15	-0.20	1.63	-2.41	-0.88	-0.48	0.01	-0.20	0.31
& ERROR	0.74	0.48	0.66	0.68	0.29	0.45	0.35	0.30	0.33
DELTA DS33									
AMPLITUDE	0.074	0.101	0.146	0.165	0.152	0.154	0.200	0.141	0.128
& ERROR	0.025	0.019	0.027	0.030	0.026	0.037	0.031	0.025	0.023
PHASE	0.38	0.50	0.59	0.69	0.84	1.13	1.45	1.79	2.07
& ERROR	0.27	0.32	0.27	0.26	0.28	0.27	0.21	0.24	0.23
DELTA DD33									
AMPLITUDE	0.014	0.051	0.062	0.064	0.054	0.045	0.088	0.148	0.124
& ERROR	0.010	0.011	0.019	0.016	0.016	0.018	0.020	0.028	0.036
PHASE	3.48	3.73	1.22	-4.78	-4.67	-3.78	-3.30	-2.95	-2.60
& ERROR	0.61	0.34	0.35	0.35	0.44	0.62	0.26	0.22	0.24

Table VII.5

	1.439	1.495	1.526	1.551	1.577	1.612	1.640	1.668	1.693
DELTA DD35									
AMPLITUDE	0.030	0.046	0.033	0.048	0.056	0.085	0.188	0.043	0.079
& ERROR	0.011	0.012	0.012	0.013	0.017	0.033	0.028	0.020	0.017
PHASE	1.69	2.32	2.70	-3.49	-3.37	-2.85	-2.68	-2.34	-1.73
& ERROR	0.30	0.30	0.36	0.29	0.26	0.31	0.20	0.34	0.24
DELTA FP35									
AMPLITUDE	-	-	-	-	-	0.005	0.029	0.062	0.014
& ERROR	-	-	-	-	-	0.012	0.013	0.015	0.014
PHASE	-	-	-	-	-	-3.27	-2.39	-1.78	-0.55
& ERROR	-	-	-	-	-	2.00	0.41	0.28	1.06
DELTA FF35									
AMPLITUDE	-	-	-	-	-	0.111	0.081	0.108	0.118
& ERROR	-	-	-	-	-	0.025	0.016	0.018	0.028
PHASE	-	-	-	-	-	-2.82	-2.20	-2.48	-2.27
& ERROR	-	-	-	-	-	0.27	0.23	0.22	0.24
DELTA FF37									
AMPLITUDE	-	-	-	-	-	-	-	0.068	0.127
& ERROR	-	-	-	-	-	-	-	0.015	0.024
PHASE	-	-	-	-	-	-	-	-3.54	-2.23
& ERROR	-	-	-	-	-	-	-	0.28	0.25
N* SS31									
AMPLITUDE	0.062	0.068	0.021	0.025	0.019	0.036	0.072	0.038	0.102
& ERROR	0.023	0.015	0.015	0.014	0.017	0.017	0.018	0.027	0.022
PHASE	1.22	1.11	1.98	0.74	-4.02	-3.91	0.76	-0.17	1.64
& ERROR	0.28	0.31	0.71	0.59	0.61	0.50	0.27	0.67	0.31
N* PP31									
AMPLITUDE	0.015	0.012	0.081	0.037	0.060	0.090	0.089	0.139	0.158
& ERROR	0.010	0.013	0.024	0.012	0.020	0.021	0.020	0.031	0.028
PHASE	4.30	5.42	3.95	2.71	2.62	2.85	3.63	3.23	4.05
& ERROR	0.66	0.92	0.31	0.57	0.36	0.42	0.26	0.25	0.24
N* PP33									
AMPLITUDE	0.024	0.051	0.056	0.101	0.129	0.150	0.146	0.191	0.183
& ERROR	0.010	0.011	0.014	0.014	0.016	0.030	0.022	0.023	0.023
PHASE	6.53	6.77	6.57	0.68	0.94	1.27	1.87	1.73	2.42
& ERROR	0.34	0.28	0.28	0.26	0.25	0.25	0.20	0.20	0.21

	1.439	1.495	1.526	1.551	1.577	1.612	1.640	1.668	1.693
N* DD33									
AMPLITUDE	0.011	0.015	0.018	0.010	0.028	0.046	0.039	0.061	0.051
& ERROR	0.007	0.006	0.009	0.008	0.011	0.011	0.012	0.014	0.013
PHASE	-0.81	-1.31	4.03	-1.57	-2.25	-0.63	0.75	0.45	1.26
& ERROR	0.41	0.56	0.59	0.98	0.46	0.43	0.30	0.27	0.27
N* DD35									
AMPLITUDE	-	-	-	-	-	0.012	0.052	0.031	0.067
& ERROR	-	-	-	-	-	0.009	0.010	0.010	0.013
PHASE	-	-	-	-	-	-1.26	-0.78	-0.72	-0.51
& ERROR	-	-	-	-	-	0.94	0.26	0.40	0.24
N* FF35									
AMPLITUDE	-	-	-	-	-	0.027	0.011	0.022	0.007
& ERROR	-	-	-	-	-	0.009	0.010	0.008	0.008
PHASE	-	-	-	-	-	3.64	4.61	5.44	5.84
& ERROR	-	-	-	-	-	0.37	0.75	0.50	1.92
N* FF37									
AMPLITUDE	-	-	-	-	-	-	-	0.028	0.045
& ERROR	-	-	-	-	-	-	-	0.010	0.010
PHASE	-	-	-	-	-	-	-	1.72	2.62
& ERROR	-	-	-	-	-	-	-	0.42	0.38
RHO1 SS31									
AMPLITUDE	0.114	0.121	0.122	0.193	0.242	0.326	0.313	0.312	0.301
& ERROR	0.049	0.026	0.030	0.029	0.034	0.051	0.044	0.043	0.048
PHASE	0.84	1.22	5.84	0.29	0.39	0.97	1.24	1.62	2.14
& ERROR	0.28	0.29	0.34	0.31	0.24	0.24	0.20	0.20	0.21
RHO1 PP31									
AMPLITUDE	0.014	0.103	0.047	0.091	0.057	0.085	0.105	0.220	0.178
& ERROR	0.013	0.027	0.035	0.035	0.024	0.030	0.025	0.040	0.028
PHASE	2.50	2.95	6.65	1.57	1.77	4.02	4.32	4.24	4.81
& ERROR	0.80	0.29	0.55	0.44	0.40	0.41	0.29	0.21	0.24
RHO1 PP33									
AMPLITUDE	0.028	0.054	0.038	0.034	0.017	0.030	0.042	0.078	0.060
& ERROR	0.013	0.016	0.015	0.021	0.014	0.024	0.018	0.020	0.021
PHASE	5.35	6.22	7.79	2.09	-1.25	-0.96	1.76	3.19	3.84
& ERROR	0.38	0.33	0.47	0.69	0.78	0.67	0.33	0.29	0.35

	1.439	1.495	1.526	1.551	1.577	1.612	1.640	1.668	1.693
RHO1 DD33									
AMPLITUDE	0.018	0.033	0.032	0.039	0.092	0.062	0.137	0.101	0.119
& ERROR	0.007	0.006	0.013	0.012	0.013	0.018	0.019	0.017	0.017
PHASE	-0.18	0.63	4.26	-1.29	-0.54	0.13	0.66	0.78	1.49
& ERROR	0.47	0.37	0.47	0.53	0.28	0.33	0.22	0.26	0.28
RHO1 DD35									
AMPLITUDE	-	-	-	-	-	0.041	0.028	0.040	0.047
& ERROR	-	-	-	-	-	0.011	0.012	0.011	0.011
PHASE	-	-	-	-	-	-0.19	-1.07	-2.17	-1.89
& ERROR	-	-	-	-	-	0.39	0.40	0.36	0.31
RHO1 FF35									
AMPLITUDE	-	-	-	-	-	0.038	0.030	0.010	0.009
& ERROR	-	-	-	-	-	0.012	0.008	0.012	0.011
PHASE	-	-	-	-	-	1.87	5.03	2.91	4.98
& ERROR	-	-	-	-	-	0.32	0.37	1.02	1.20
RHO1 FF37									
AMPLITUDE	-	-	-	-	-	-	-	0.017	0.021
& ERROR	-	-	-	-	-	-	-	0.009	0.009
PHASE	-	-	-	-	-	-	-	5.06	5.18
& ERROR	-	-	-	-	-	-	-	0.65	0.55
RHO3 SD31									
AMPLITUDE	0.018	0.064	0.035	0.013	0.038	0.013	0.040	0.040	0.064
& ERROR	0.012	0.018	0.018	0.024	0.018	0.018	0.023	0.025	0.028
PHASE	-1.64	4.12	4.02	-0.93	-4.55	0.31	2.20	-2.04	-1.80
& ERROR	0.78	0.29	0.57	1.45	0.54	1.99	0.48	0.63	0.53
RHO3 PP31									
AMPLITUDE	0.064	0.041	0.119	0.072	0.030	0.077	0.102	0.056	0.099
& ERROR	0.019	0.016	0.034	0.027	0.019	0.035	0.024	0.024	0.026
PHASE	0.37	1.06	3.15	-0.80	-0.17	-1.28	-0.72	-0.15	1.21
& ERROR	0.30	0.52	0.29	0.48	0.70	0.46	0.28	0.42	0.37
RHO3 PP33									
AMPLITUDE	0.024	0.036	0.063	0.070	0.102	0.018	0.032	0.022	0.051
& ERROR	0.016	0.021	0.020	0.021	0.021	0.019	0.017	0.019	0.018
PHASE	-1.11	3.93	1.74	-0.01	0.16	-3.44	0.56	0.63	2.74
& ERROR	0.66	0.48	0.47	0.50	0.31	1.44	0.53	0.75	0.39

	1.439	1.495	1.526	1.551	1.577	1.612	1.640	1.668	1.693
RH03 PF33									
AMPLITUDE	0.008	0.004	0.031	0.031	0.036	0.035	0.031	0.054	0.100
& ERROR	0.006	0.010	0.008	0.012	0.015	0.013	0.015	0.016	0.014
PHASE	2.67	-0.56	1.01	-3.02	-2.41	-4.11	2.11	-3.66	-3.02
& ERROR	0.97	1.20	0.46	0.44	0.33	0.47	0.36	0.36	0.26
RH03 DS33									
AMPLITUDE	0.050	0.068	0.017	0.073	0.125	0.106	0.066	0.018	0.051
& ERROR	0.019	0.017	0.020	0.016	0.023	0.027	0.018	0.026	0.022
PHASE	1.35	1.74	0.90	0.13	-0.06	0.65	0.51	0.34	0.75
& ERROR	0.27	0.29	1.04	0.50	0.24	0.29	0.28	0.90	0.34
RH03 DD33									
AMPLITUDE	0.020	0.012	0.040	0.087	0.108	0.110	0.098	0.100	0.118
& ERROR	0.007	0.010	0.015	0.017	0.015	0.027	0.019	0.017	0.020
PHASE	0.57	-1.66	6.33	-0.25	-0.43	-0.18	-0.01	0.67	0.89
& ERROR	0.59	0.97	0.43	0.31	0.29	0.29	0.24	0.24	0.24
RH03 DD35									
AMPLITUDE	-	-	-	-	-	0.024	0.030	0.045	0.034
& ERROR	-	-	-	-	-	0.014	0.015	0.014	0.015
PHASE	-	-	-	-	-	-0.13	0.48	-0.55	-0.51
& ERROR	-	-	-	-	-	0.71	0.49	0.40	0.41
RH03 FP35									
AMPLITUDE	-	-	-	-	-	0.050	0.041	0.029	0.022
& ERROR	-	-	-	-	-	0.016	0.013	0.013	0.013
PHASE	-	-	-	-	-	-0.56	-0.21	-0.03	-0.58
& ERROR	-	-	-	-	-	0.34	0.34	0.40	0.56
RH03 FF35									
AMPLITUDE	-	-	-	-	-	0.024	0.026	0.019	0.038
& ERROR	-	-	-	-	-	0.014	0.006	0.013	0.021
PHASE	-	-	-	-	-	-0.61	-3.83	2.22	-2.84
& ERROR	-	-	-	-	-	0.51	0.51	0.53	0.39
RH03 FF37									
AMPLITUDE	-	-	-	-	-	-	-	0.023	0.033
& ERROR	-	-	-	-	-	-	-	0.012	0.018
PHASE	-	-	-	-	-	-	-	1.54	2.23
& ERROR	-	-	-	-	-	-	-	0.58	0.57

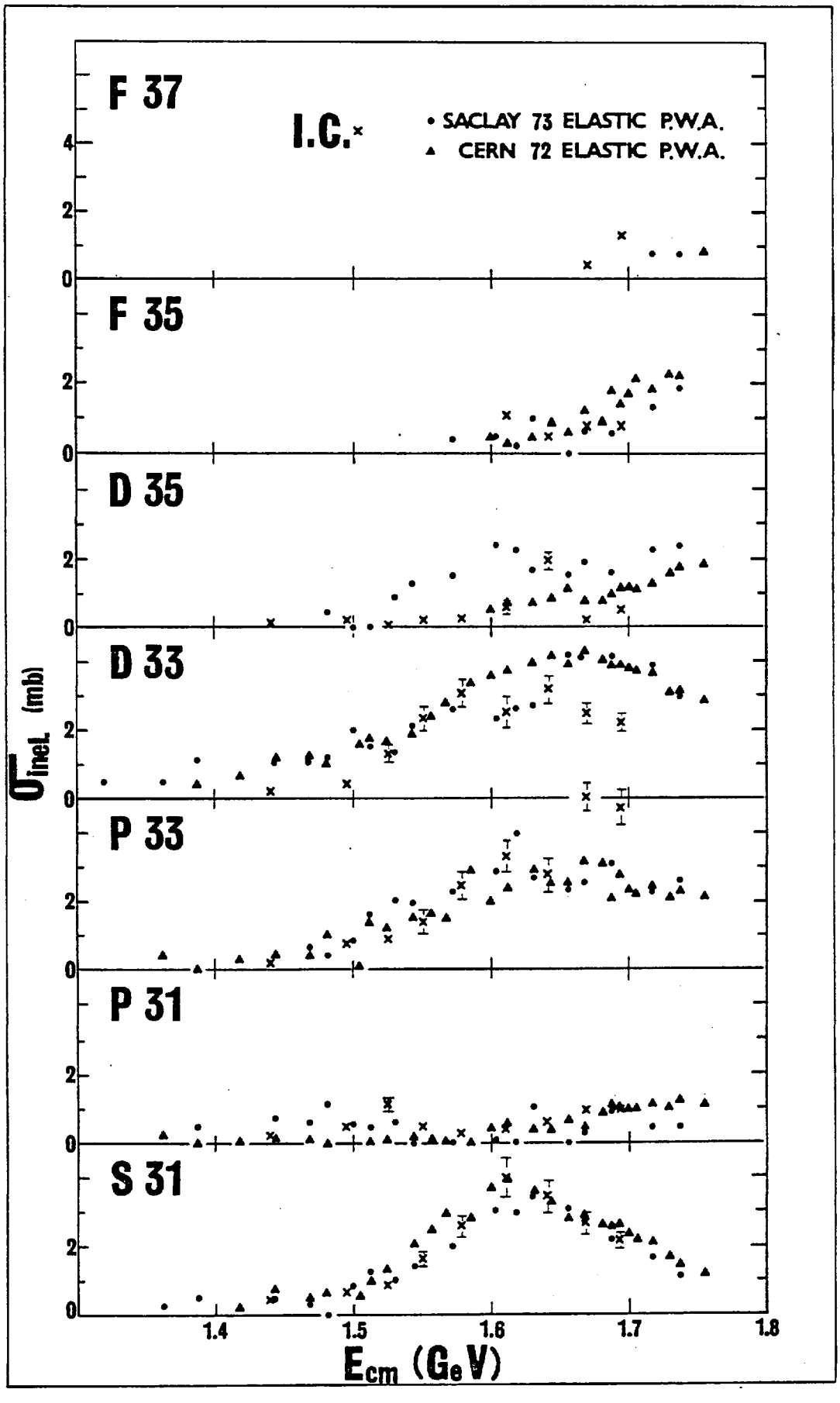

Figure VII.4 $\pi\pi$N cross-sections in different waves

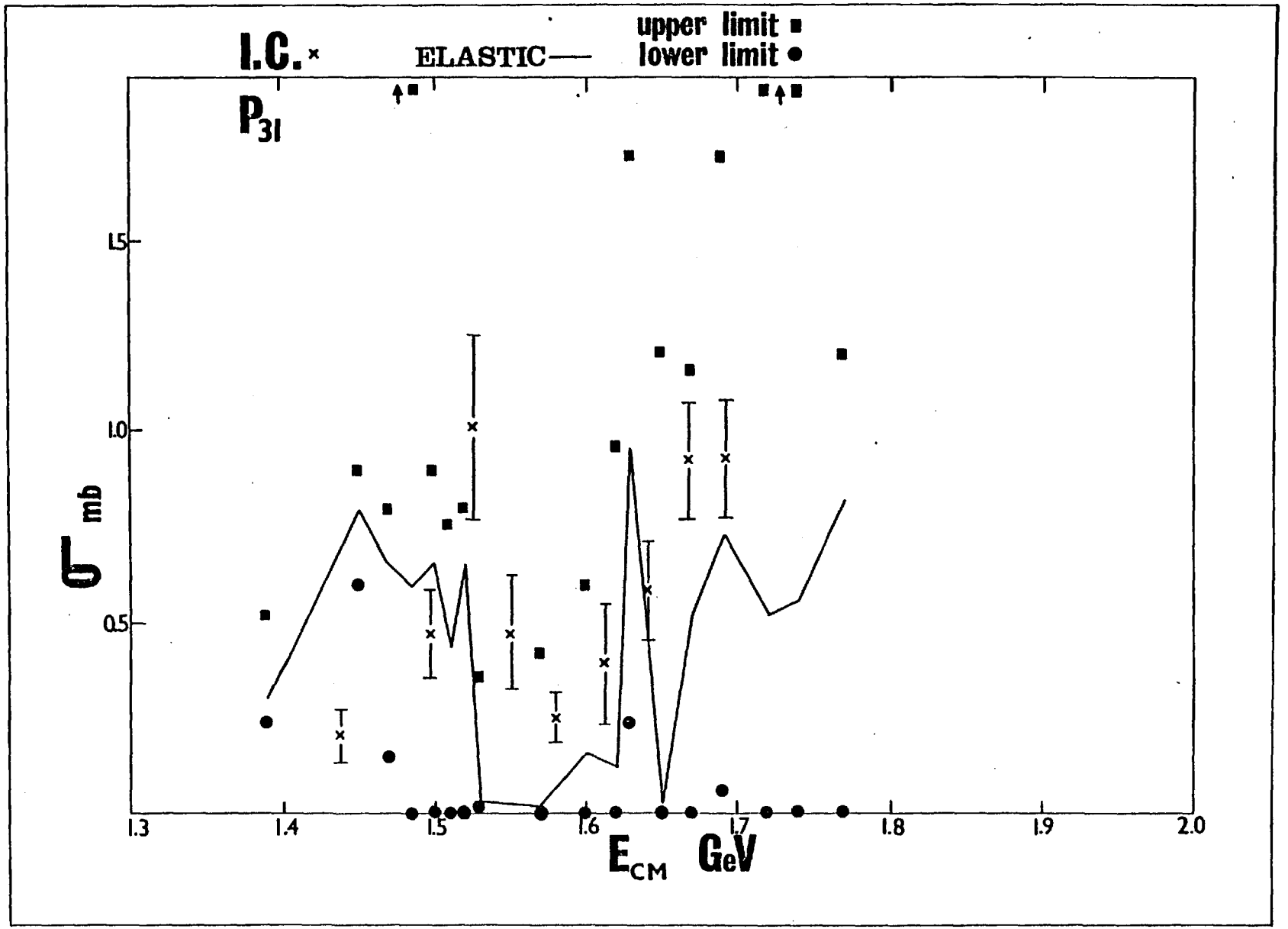

Figure VII.5 Enlarged P31 cross-sections

Waves / Energy	S31	P31	P33	D33	D35	F35	F37	I=2
1.439	0.464 ±.185	0.203 ±.068	0.139 ±.052	0.161 ±.068	0.083 ±.030	-	-	-
1.495	0.662 ±.122	0.470 ±.117	0.701 ±.162	0.391 ±.086	0.164 ±.043	-	-	0.161 ±.035
1.526	0.841 ±.164	1.097 ±.242	0.848 ±.187	1.241 ±.234	0.076 ±.027	-	-	0.297 ±.040
1.551	1.619 ±.223	0.471 ±.144	1.368 ±.391	2.240 ±.360	0.145 ±.038	-	-	0.289 ±.039
1.577	2.553 ±.307	0.250 ±.065	2.384 ±.440	3.018 ±.417	0.174 ±.048	-	-	0.293 ±.048
1.612	3.979 ±.651	0.394 ±.157	3.238 ±.520	2.423 ±.572	0.520 ±.201	1.023 ±.152	-	0.342 ±.044
1.640	3.434 ±.483	0.587 ±.124	2.757 ±.440	3.142 ±.467	1.849 ±.324	0.462 ±.078	-	0.258 ±.044
1.668	2.634 ±.326	0.924 ±.146	5.041 ±.674	2.415 ±.294	0.181 ±.047	0.738 ±.111	0.410 ±.057	0.287 ±.047
1.693	2.149 ±.237	0.931 ±.153	4.675 ±.516	2.152 ±.279	0.423 ±.085	0.724 ±.151	1.224 ±.168	0.323 ±.057

Table VII.6

σ^{JP} values after O.P.E. refit

shows a very clear resonance structure, and ΔDD33, ρ_1DD33, ρ_3DD33 show a clearer anticlockwise movement. Δ DD35 becomes smaller, but still shows a large amplitude near 1640 MeV though now only in one energy. None of the other waves show any noteworthy changes.

The CHI results, the projections, and the Argand diagrams have all improved with the O.P.E. refit. Improvements in the results after the refit can be attributed to the allowance for O.P.E., but some differences between the two sets of Argands can be explained in terms of the continuum ambiguity. The fact that these differences are mostly small suggests that the continuum ambiguity is not a serious problem. These improvements inspire confidence in the value of the anlaysis with O.P.E., but before the waves are discussed in detail in conjunction with the plots, the O.P.E. results should be examined to check if they too make sense.

VII.4.2 I=2 $\pi\pi$ results

Table VII.6 and Figure VII.6 show the fitted values of the cross-section contribution from I=2 O.P.E. to the $\pi^+p \to \pi\pi N$ cross-section. The values used are those from the fit chosen by CHI at each energy. No meaningful O.P.E. fits were obtained at 600 MeV/c, apparently because the O.P.E. cross-section is close to zero. The cross-section at 700 MeV/c is half that at the higher energies, where the cross-section is constant within the errors. The total $\pi^+p \to \pi\pi N$ cross-section is rising in our energy range, so the I=2 O.P.E.

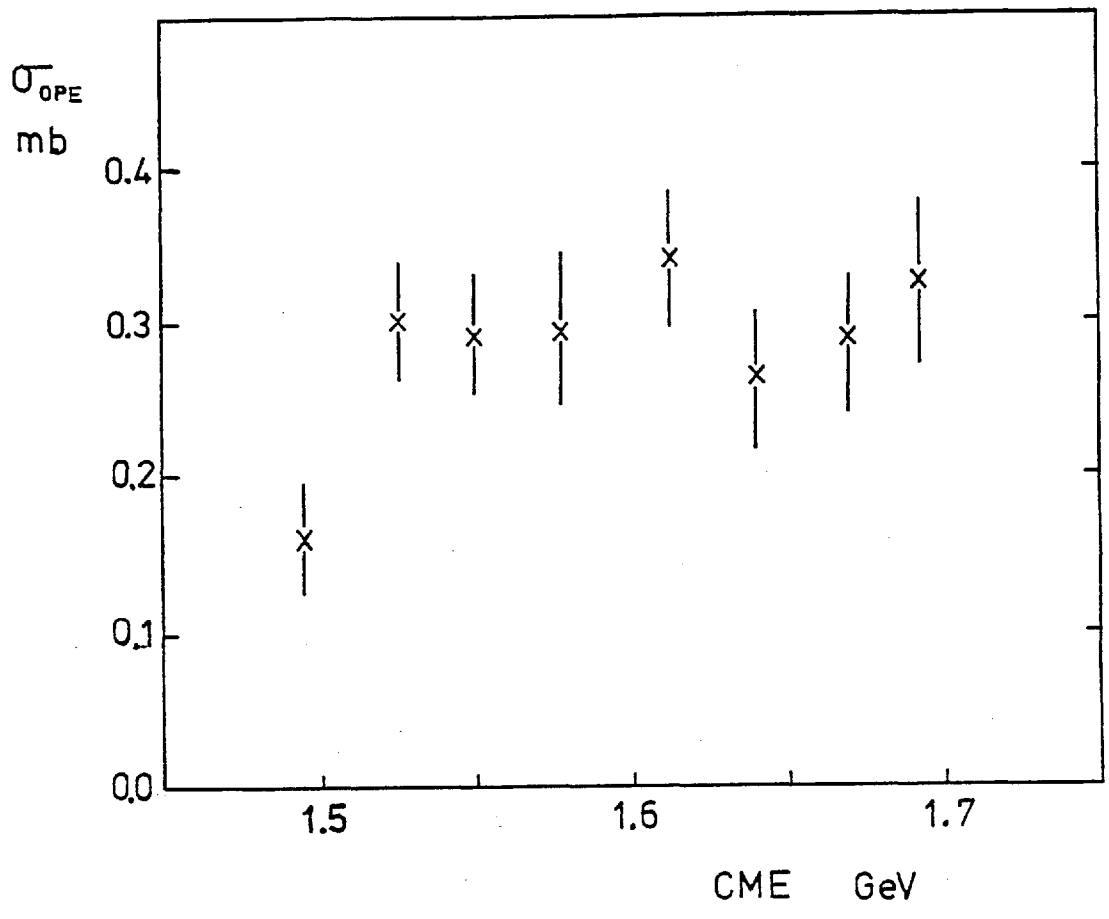

Figure VII.6 I=2 O.P.E. contributions to $\pi^+p \to \pi\pi N$ cross-sections

effect becomes less significant at our highest energies.

The fitted values of the parameters a , r_o are given in Table VII.7. In the effective range expression, the parameters are taken to be energy-independent; if the parametrisation is meaningful then the fitted values should be similar at the different energies. Table VII.7 shows that r_o varies from energy to energy, but not systematically and has large errors; this is consistent with r_o being a poorly determined constant. The scattering length, a, is better determined. In $\pi\pi$ analyses, the scattering lengths a_ℓ^I (ℓ = angular momentum, I = isospin of given $\pi\pi$ state) are defined by

$$a_\ell^I = \lim_{m^2_{\pi\pi} \to 4\mu^2_+} \frac{\delta_\ell^I}{q_{\pi\pi}^{2\ell+1}} \qquad 7.22$$

see for example reference 63. The symbols are all as defined earlier in this chapter.

In our case $\ell=0$, $q_{\pi\pi} \equiv k$, so comparison of 7.22 with 7.11 shows that

$$a \equiv -a_o^2 \qquad 7.23$$

Figure VII.7 shows our values of a compared with other experimental values, and with the theoretical prediction of Weinberg. The experimental values and theoretical predictions are discussed in references 63 and 64, the original references for each value shown on the figure are numbered in the figure. Most experimental values are larger than the theoretical

Centre of mass Energy (GeV)	Effective range r_o (fermis)	Scattering length a (fermis)
1.495	1.10 ±2.64	.179 ±.044
1.526	-1.24 ±1.46	.291 ±.054
1.551	-0.60 ±1.04	.254 ±.033
1.577	2.45 ±1.31	.167 ±.028
1.612	1.02 ±1.11	.207 ±.036
1.640	3.93 ±1.52	.123 ±.023
1.668	-1.18 ±0.88	.248 ±.043
1.693	0.83 ±1.0	.186 ±.034
Weighted mean	0.77 ±1.41	.208 ±.037

Table VII.7

Fitted values of a, r_o at each energy, and mean values

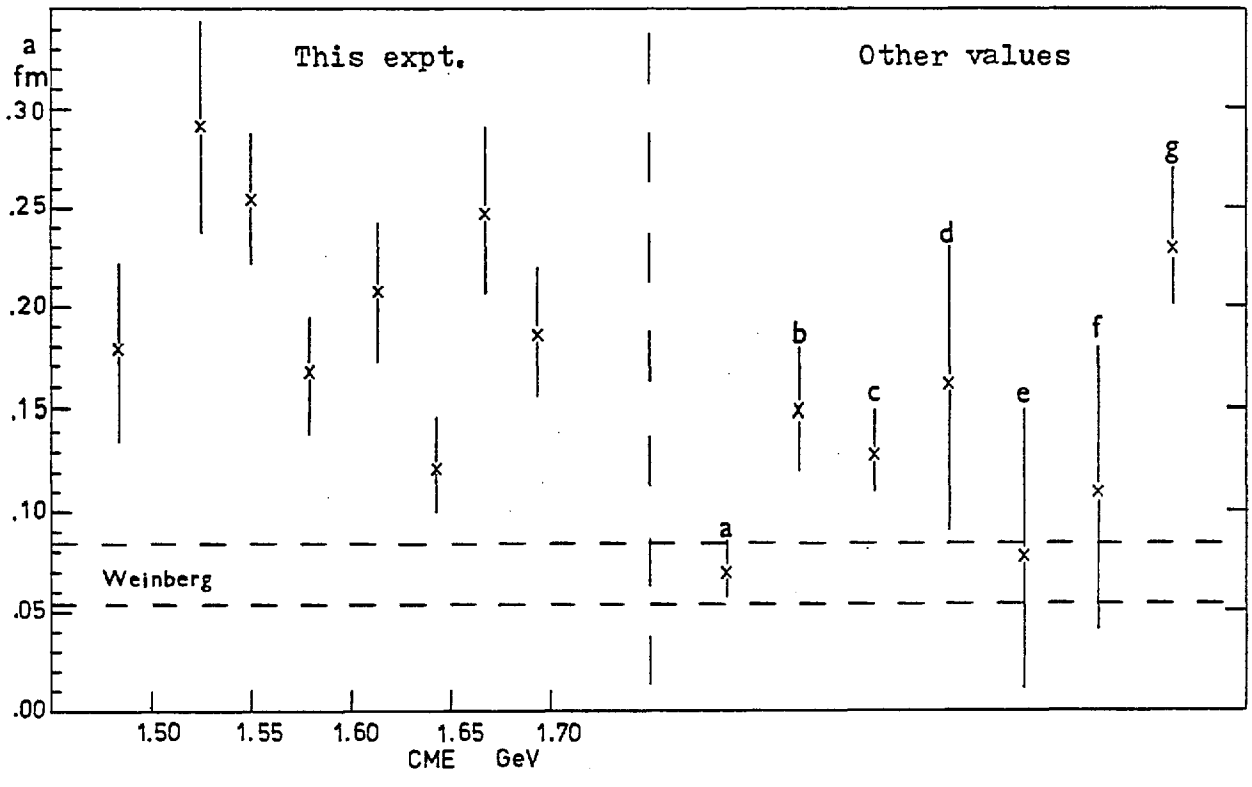

I=2 $\pi\pi$ scattering lengths

A range of values derived from Weinberg's current algebra model (ref. 68), and corrections to it is shown. The value marked 'a' is also a theoretical calculation by Morgan and Shaw (ref. 64a) quoted in ref. 64.

The remaining values are experimental determinations

b - ref. 67a, Cohen et al

c - ref. 66, Losty et al

d - ref. 67b, Villet et al

e - ref. 67b, as d but with one suspect value removed by them

f - calculated by Morgan (ref. 64b) from the results of Hoogland (ref. 55)

g - ref. 65, Prukop et al

Figure VII.7

I=2 $\pi\pi$ scattering length values

prediction, as are ours. Our values are consistent with the assumption of a constant value, and they are consistent with or slightly larger than the other experimental values. Table VII.7 also shows a strong correlation between a and r_o; a increases as r_o decreases.

Mean values with standard deviations of a and r_o are given at the foot of Table VII.7. The numbers of events at different energies varied, so in calculating these means, the value at each energy was given a weight, obtained by multiplying the number of $\pi^+\pi^+n$ events at that energy by the fraction of $\pi^+\pi^+n$ cross-section taken by I=2 O.P.E. The weights were calculated from the $\pi^+\pi^+n$ channel alone because it takes 4/5 of our I=2 O.P.E. cross-section. These mean values were used to calculate the phase shift δ_o^2 for $\pi\pi$ masses up to 700 MeV, shown in Table VII.8 and Figure VII.8. The figure also shows δ_o^2 calculated by other experiments. At the higher $\pi\pi$ masses, the effective range potential approximation is insufficiently accurate, but we had no need to fit events with $m_{\pi\pi} > 500$ MeV, so this does not matter.

As we have few low $\pi^+\pi^+$ mass events, and the I=2 O.P.E. was introduced primarily to improve the partial wave analysis, these results are very satisfying. The parameter values at different energies are sufficiently consistent to show that they are meaningful, and not just fitting random fluctuations of the data. The scattering length is consistent with that obtained by other analyses, and as it was obtained in a different way, it supports the results of those analyses. The I=2 O.P.E. part of the analysis was successful, and adds to

$m_{\pi\pi}$ (MeV)	δ_o^2 (degrees)
280	-0.7 ± 0.1
300	-3.3 ± 0.6
350	-6.5 ± 1.4
400	-9.0 ± 2.3
450	-11.2 ± 3.5
500	-13.5 ± 4.8
550	-15.8 ± 6.6
600	-18.1 ± 8.8
650	-20.6 ± 11.5
700	-23.2 ± 14.9

Table VII.8

s-wave I=2 phase shift calculated from mean a and r_o

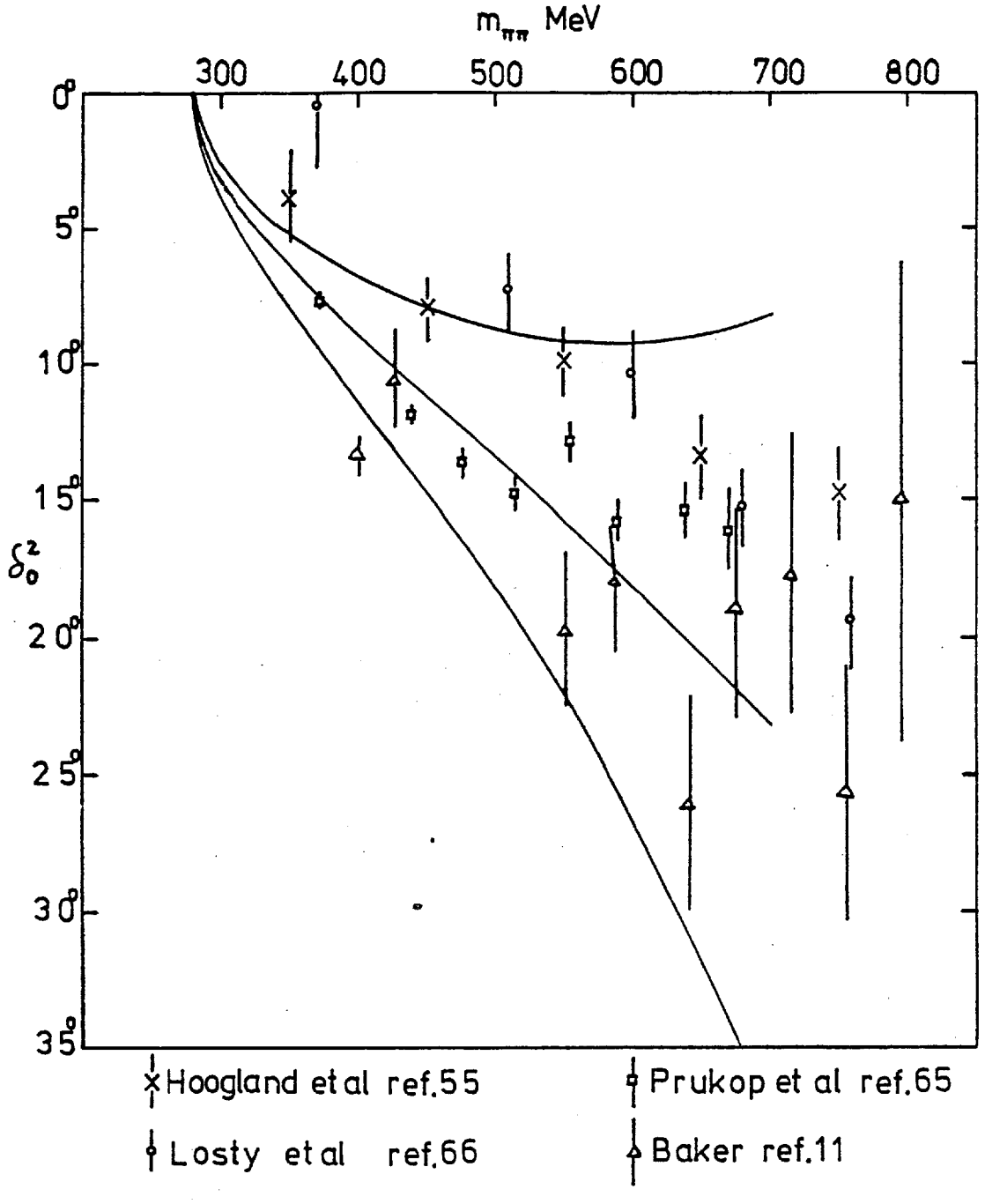

The central continuous line gives the phase shift calculated from the effective range potential formula using our mean values of a and r_o. The upper and lower curves show one standard deviation errors.

Figure VII.8

I=2 S-wave phase shifts, δ_o^2

confidence in the overall results of the analysis.

VII.5 Discussion of partial wave analysis results

VII.5.1 Discussion of the results of this analysis

The results without O.P.E. were sensible, and the refit with O.P.E. has improved the projections, given better continuity, and provided a satisfactory description of the I=2 $\pi\pi$ state. There remains the task of examining both sets of Argand diagrams and σ^{JP} plots to produce a list of resonance parameters. That list can then be compared with the results of other analyses and with theory.

Our K-matrix program, already mentioned, was written when 4-variable maximum likelihood solutions were only available at four energies. (These were the results presented by Rob Stevens in his thesis, reference 9.) It was found that four energies were not enough for a K-matrix fit, and also that more waves were needed in the analysis. The author of this thesis therefore concentrated on analysing more energies, using more waves, and including an O.P.E. contribution. The K-matrix program should now be used on the results, but as this has not yet been done, resonance parameters had to be found by eye.

The σ^{JP} plots, Figures V.6.a, V.6.b, VII.4 and VII.5 were searched for bumps, and Breit-Wigner shapes were drawn in by hand in places where bumps coincided with rapid

movement in the Argand diagrams. As an extra check, a linear background was estimated in each σ^{JP} plot, the plots were redrawn with this background subtracted, and Breit-Wigners were drawn in again. Masses were also estimated from the Argand diagrams. Although σ^{JP} plots from the non-O.P.E. analysis were examined together with the O.P.E. analysis σ^{JP} plots, the Breit-Wigners were drawn on the O.P.E. plots as the O.P.E. analysis results were more continuous. Estimated masses and widths are given in Table VII.9 - where more than one resonance is indicated in a wave, the first is marked with a prime, the second with two primes.

A good resonance candidate should be visible in the cross-section plots and in the Argand diagrams, and it should be visible in the non-O.P.E. and the O.P.E. analyses. If tying to the resonance in CHI gives the preferred combination or a similar one and a good χ^2, that is additional evidence in its favour. If the resonance mass lies at the same energy in different decay channels on the Argand diagrams, that too gives it support. To distinguish obvious resonances from less certain or possible ones, a star rating system (the more stars the better) is used. Four stars are given to resonances seen clearly in O.P.E. and non-O.P.E., in σ^{JP} plots and in Argand diagrams, but only if the resonance parameters are well determined. Good resonances whose parameters are not so well determined because different methods give different values, or because they are near the top of our energy range, are given three stars. Resonances whose parameters are poorly determined are given two stars, and resonances whose existence is possible, but open to serious doubt, are given one star.

In addition to resonance masses and widths, we can obtain fractional widths x_r and coupling signs from the Argand diagrams. A relativistic Breit-Wigner (discussed in section VI.3.2) in an inelastic channel r describes a circle of diameter $\sqrt{x_e x_r}$ on the Argand diagram. A set of Argand diagrams with errors drawn in were produced, using a diameter of 13cm. so that circles could then be drawn in easily by use of a template. Table VII.10 gives the diameters of circles for every wave where they could be drawn. The sign in each wave is given with the diameter; circles lying above the origin are given a positive sign, circles below the origin a negative sign. Uncertain signs are followed by a question mark, and indeterminate signs are represented by a question mark alone.

A discussion of the considerations that went into the making of Tables VII.9 and VII.10 is presented here; comparison with other experiments and considerations of theory come in the next sections.

S31

Both σ^{JP} plots show one clear peak in S31, between 1612 and 1640 MeV, closer to 1612. The Δ SD31 and ρ_1SS31 Argand diagrams show anti-clockwise loops with fast motion before energy 6 and maximum amplitude at energies 6 and 7. These are typical indications of a clear Breit-Wigner resonance, with little background, just above energy 6. The resonance width can also be easily determined from the σ^{JP} plots. This resonance therefore appears in Table VII.9 with four stars.

The poor determination of phases at the low energies does not affect the resonance parameters. Both these waves give the preferred combination and a very good χ^2 when tied to CHI.

N*SS31 and ρ_3SD31 are much smaller; they are not particularly useful in determining resonance parameters, nor can too many conclusions be drawn in the N*SS31 due to the change after the O.P.E. refit. Diameters of estimated circles in all 4 waves are given, with signs, in Table VII.10. This analysis gives the clearest determination yet of the ρ_1SS31 sign. The signs of N*SS31 and ρ_3SD31 are reasonably well determined in the O.P.E. fits, but the non-O.P.E. fits do not confirm these signs, so they are given question marks. The S31 wave in our energy range is almost an analyst's dream: one strong peak, a clear signal in two isobar modes, agreement between σ^{JP} plots and Argand diagrams, and between the non-O.P.E. and O.P.E. analyses. Unfortunately, no other wave has all these desirable properties.

P31

This wave has a small cross-section throughout our energy range, but shows interesting structure, so enlarged cross-section plots were given in Figures V.6.a and VII.5. Both plots show a peak at energy 3, and all Argand diagrams show rapid motion at point 3. This effect looks like a narrow resonance, its estimated parameters are given in Table VII.9. Runs of CHI tied to this resonance gave solutions similar to the preferred combination, except in ρ_3, and surprisingly good χ^2 values considering how narrow

the suggested resonance is. The ρ_1PP31 CHI run gave the third best χ^2 of all the ρ waves. The Argand diagrams do however look confused, so a χ^2 test was made to compare the hypotheses of a Breit-Wigner resonance and of an appromimately linear background. (The O.P.E. fit σ^{JP} values were used.)

A Breit-Wigner fit to the cross-section requires three parameters; mass, width, and an overall scale. The scale was allowed for by a parameter that defined the total $\pi\pi$N P31 cross-section at the resonance mass. The cross-sections at the first five energies were used in a χ^2 fit, so that there were two degrees of freedom. The best fit was obtained with Mass = 1523 MeV, Width = 40 MeV, cross-section at resonance mass = 0.94 mb. This gave a value

$$\chi^2/\text{N.D.F.} = 2.3/2$$

A straight line fit was then made to the same five points, and this gave a minimum χ^2 value of

$$\chi^2/\text{N.D.F.} = 16.5/3$$

This test shows that a Breit-Wigner describes the cross-sections far better than a linear background, and that the parameter values estimated by eye, given in Table VII.9 are fairly well-determined. The resonance is therefore given three stars in Table VII.9.

Above this resonance energy, the cross-section falls, then rises again. The top point in the non-O.P.E. plot shows the discontinuous behaviour discussed in Chapter V. The rise in cross-sections, together with anti-clockwise motion on

the Argand diagrams in energies 6 to 9 is indicative of a second resonance near the top of our energy range. Circles drawn on the Argand diagrams support this resonance, but CHI runs tied to such a possible resonance only gave good results in the ΔPP31 wave. We cannot be sure of the meaning of this effect until higher energies are analysed; it could be the tail of a wide P31 resonance at a higher energy, so it is tentatively put in Table VII.9 with one star.

P33

Both ΔPP33 and N*PP33 show clearly resonant Argand diagrams. The σ^{JP} plots show large cross-sections, indeed they considerably exceed the elastic predictions at the top two energies. Attempts to draw a single circle in each Argand diagram met with some difficulty, and a single Breit-Wigner drawn in the σ^{JP} plots disagreed with the cross-section at energy 7 in both σ^{JP} plots. The data is much better described by two resonances, one near 1600 MeV, the other near 1700 MeV. A K-matrix analysis should be performed to check this suggestion of two resonances, but there is considerable theoretical support for the suggestion, as will be discussed in Section VII.5.3. On the basis of the Argand diagrams and σ^{JP} plots alone, the lower resonance deserves only one star, but because of the theoretical support it is given two stars in Table VII.9. The inclusion of this lower mass resonance affects the estimate of the higher one's width, and this together with its proximity to the top of our energy range allow the higher mass resonance only three stars though it is clearly seen.

CHI runs tied to both resonances in ΔPP33 and N*PP33 gave very good χ^2 values, our analysis was clearly right to include the N* isobar. The ρ channels are much smaller, though both show clockwise motion in the upper energies. The ΔPF33 Argand diagram (see Figure VII.9) has small amplitudes but it shows very clear anti-clockwise motion, and a CHI run tied to it gave the preferred combination and a reasonable χ^2. Two circles were drawn on the Argand diagram, though one may have been sufficient - this is noted in Table VII.10. The PP33 second resonance circle lay to the left of the origin, and the ΔPF33 circle lay to the right, so their signs could not be determined, but it was very clear that the two waves have the opposite sign; the theoretical consequences of this will be discussed later. Two circles were also drawn on the ρ_3PF33 Argand diagram. ρ_3PP33 was difficult to fit circles to, whereas ρ_1PP33 showed two circles, Table VII.10 includes comments about the difficulties. To clarify the conclusions about 2 resonances and relative signs, Figure VII.9 shows enlarged sections of the relevant Argand diagrams.

D33

This wave is clearly resonant, the ΔDS33 wave was used to fix the overall phase at each energy in the Argand diagrams. The σ^{JP} plots show a wide peak; the non-O.P.E. plot is discontinuous at the last energy as in other waves. The ρ_3DS33 wave becomes smaller after the O.P.E. refit as was the case with N*SS31. The ΔDD33 wave becomes more continuous after the refit; it gave good results in the CHI run tied to it. ρ_1DD33 becomes larger and is also a good wave to use in CHI. ρ_3DD33 looks more continuous after the refit, and gives the best χ^2 of the admittedly poor χ^2

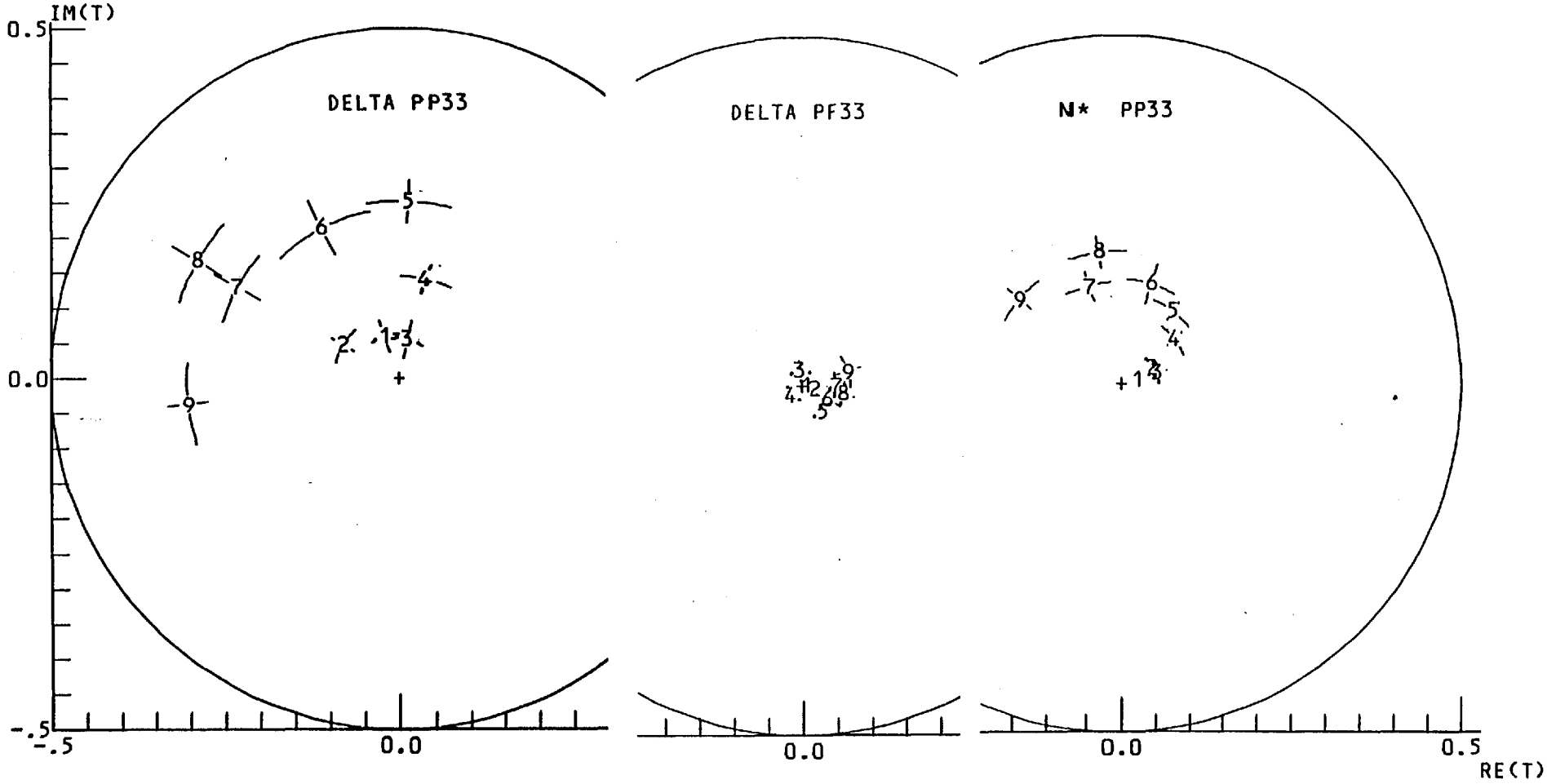

Figure VII.9 Enlarged sections of P33 Argand diagrams

values given by the ρ_3 waves.

The width of the cross-section peak, and the dips in both σ^{JP} plots at energy 6 make it difficult to determine the mass of this resonance. The CHI runs with a variety of masses and widths showed little sensitivity to changes in these parameters, so the mass was eventually taken from the ΔDS33 Argand diagram where the maximum amplitude was apparently between energies 6 and 7. Because of these problems, the resonance is given only three stars. The dip in σ^{JP} at energy 6 is worthy of comment because it is seen in both σ^{JP} plots, particularly as the Argand diagrams are consistent with a loop at energy 7, and a second smaller one between energies 4 and 5. The dip may be due to a statistical fluctuation, though it would be surprising to see such a fluctuation looking so similar in both the non-O.P.E. and the O.P.E. results. It could be due to the introduction of more waves at energy 6, but other waves could then be expected to see a similar dip, and none do. It could even possibly indicate a second resonance close to the the three-star one. We have therefore made a note about the dip in Table VII.9.

D35

This wave is small at all energies except 6 and 7 in the non-O.P.E. solution; in the O.P.E. solution the cross-section becomes even larger at energy 7, and at energy 6 it falls but is still larger than at the other energies. The ΔDD35 was fitted at all energies and D35 was introduced

in the other isobars at energy 6, but the sudden rise in cross-section can only be partly attributed to the additional waves, as they are small, and the increase in amplitude occurs in ΔDD35. At energy 8, the cross-section again falls to its value at energy 5, showing that the additional waves have little effect, though this fall may be due, at least in part, to the introduction of F37 waves at energy 8. It is worth recalling that our elastic Legendre coefficients also showed considerable D35 structure.

Statistical fluctuations alone are unlikely to explain this effect, because it is seen to some extent in two energies in the non-O.P.E. fit and in the O.P.E. refit. It is also most unlikely that a background change alone could produce this large cross-section. The $N^*(1520)\pi$ production threshold lies close to these energies (at 1660 MeV) so threshold effects could be invoked to explain the sudden rise in cross-section. A CHI run tied to a possible ΔDD35 resonance chose the preferred combination, and gave an acceptable χ^2, so the existence of a resonance is clearly possible. A narrow resonance, with one star, is given in Table VII.9, but a threshold effect combined with a large background may be able to explain this effect. A refit of our data with an additional N*(1520) isobar would be helpful here.

F35

This wave was used at energies 6, 7, 8, 9; the Argand plots are small. An unexpectedly high cross-section seen at energy 6 in the O.P.E. refit is presumably due to statistical fluctuation, because it is seen at only one energy, and only in the refit. Apart from this one point, the σ^{JP} plots show a fairly steady rise in cross-section consistent with their

Resonance	Mass (GeV)	Width (GeV)	Rating	Comments
S31	1620	120	****	
P31'	1520	50	***	
P31"	1680	90	*	May be the tail of a higher mass resonance
P33'	1620	90	**	
P33"	1680	150	***	
D33	1650	160	***	May be split
D35	1640	40	*	

Table VII.9

Resonance parameters and ratings

Wave	Sign, $\sqrt{x_e x_r}$	Comments ("Poor" means a wave where it was difficult to draw a circle to fit several points)
ΔSD31	-.17	
ΔPP31'	+?.06	
ΔPP31"	+?.08	
ΔPP33'	+ .11	
ΔPP33"	?.12	
ΔPF33'	-?.03	It is also possible to draw
ΔPF33"	+ .03	a single circle : +?.04
ΔDS33	+ .09	
ΔDD33	+ .08	Sign uncertain on O.P.E. results,
ΔDD35	- .06	taken from non-O.P.E.
N*SS31	+?.05	Poor
N*PP31'	-?.05	Poor
N*PP31"	- .06	
N*PP33'	+ .08	The best circle in these Argand
N*PP33"	+ .08	diagrams
N*DD33	+?.04	
ρ_1SS31	+ .19	
ρ_1PP31'	?.06	
ρ_1PP31"	- .08	
ρ_1PP33'	?.03	
ρ_1PP33"	?.04	
ρ_1DD33	+ .08	
ρ_3SD31	?.04	Poor
ρ_3PP31'	?.08	
ρ_3PP31"	?.08	
ρ_3PP33'	?.05	Very poor
ρ_3PP33"	+?.03	
ρ_3PF33'	?.03	
ρ_3PF33"	?.04	
ρ_3DS33	?.04	
ρ_3DD33	+?.09	

Table VII.10

Signs and diameters on Argand diagrams

lying on the tail of a wide resonance whose mass lies above our energy range.

F37

This wave was included only at energies 8 and 9. It is small at energy 8, and larger at energy 9, particularly in the $^{\Delta}$FF37 wave, but nothing much can be made of this until more energies are analysed; it is most probably showing the tail of a resonance above our energy range.

VII.5.2 Comparison with other analyses

It would be tedious to compare our results with those of all other analyses. Of earlier analyses of our own data, Gopal (ref. 1), Stark(ref. 12) and Stevens (ref. 9) will suffice. Gopal analysed the 3-body channels, using decay data only, at energies 6, 7, 8, 9. (Vaughan Tayler (ref. 2) performed a similar analysis.) Stark extended Gopal's analysis to include data at 1.1 GeV/c and 1.2 GeV/c incident momenta. Rob Stevens performed our first 4-variable fits at 4 energies, but his results must be treated with caution because of the error in the N*DD3 wave (though other waves were not seriously affected by this error). Other $\pi\pi$N analyses that must be compared with ours are SLAC-LBL (ref.15) and Saclay (ref. 16); details of the Saclay analysis are also given in Dolbeau's thesis (ref. 34). The Oxford $\pi\pi$N analysis (refs. 7 and 8) deserves some mention because we have used their data. Novoseller's refit of the SLAC-LBL results, with O.P.E. effects included (refs. 53,54) is not directly

comparable with our results because he refitted data only above 1.63 GeV (above the SLAC-LBL gap) and only obtained reliable phases above 1.81 GeV. SLAC-LBL and Saclay have performed K-matrix analyses of their $\pi\pi N$ results, the results of these K-matrix fits will be referred to as both groups believe that the most reliable resonance parameters are obtained in this way.

Of elastic analyses, CERN (refs. 69,70,71) and Saclay (refs. 72,73,74) are the best suited for making comparisons; they are recent and comprehensive analyses. Other more recent elastic analyses have either used special techniques or concentrated on higher energies, see for instance the proceedings of the 1976 Oxford Conference on Baryon Resonances (ref. 13). The CERN and Saclay elastic predictions have been included on our σ^{JP} plots, and will be referred to frequently, the other more recent analyses will be referred to when necessary.

S31

Everyone sees a resonance near 1650 MeV. Compared to this analysis, Gopal and Stark found a smaller branching ratio into $\Delta\pi$ and $\rho\pi$, and a larger one into $N^*\pi$, but this may be because they analysed too few waves, and did not use all 4 variables in their analyses. The CERN and Saclay elastic predictions are in good agreement, and our results lie between theirs. It is noticeable that both K-matrix analyses lower the mass to 1580 MeV. As Novoseller points out, the K-matrix method tends to alter the resonance parameters

from the elastic phase shift results. We would add that in some cases this is because two resonances lie close together in the same wave, so the K-matrix analysis finds a different resonance.

P31

The elastic analyses do not claim any resonances in our region. Gopal found strong structure near 1 GeV/c, Stark did not. Stevens also found strong structure, and the Oxford analysis found this wave to be strongly inelastic at the lower energies. SLAC-LBL and the earlier Saclay work found little P31 structure, perhaps because they constrained their results to be similar to the elastic predictions. (though Oxford did this too). Dolbeau's thesis claimed a low mass P31, and the Saclay K-matrix analysis confirmed it. It is somewhat worrying that most of the evidence for this resonance comes from data taken in one experiment, the low-energy Oxford data, though our 800 MeV/c data contributes to the 750 MeV/c bin and predominates in the 800 MeV/c bin, without altering Saclay's conclusions.

Our suggestion of a possible resonance near 1700 MeV is not supported by any other analysis, but analyses at higher energies find a wide P31 resonance somewhere between 1780 and 1950 MeV. Our higher energy data must be analysed to check if we see a separate resonance, or if, as seems probable, we just see the tail of the higher mass P31.

P33

The P33(1690) resonance is now well-established, though its parameters are not well-determined. Of the analyses being discussed, only the Saclay elastic analysis does not find it, and Stevens failed to see it clearly. Gopal found increases in cross-section at our energies 6 and 9, and he found that PF33 waves were needed as well as PP33. No other analysis claims two resonances in this region, but elastic analyses agree on a mass close to 1690 MeV, whereas the K-matrix fits find it at 1609 MeV (SLAC-LBL, but 1609 MeV is in their data gap) or 1560 MeV (Saclay). The SLAC-LBL value could possibly be due to a shift similar to that found in S31, but the Saclay value is too far for this, and they think it is a new resonance. There may well be a very inelastic resonance near 1600 MeV in addition to the P33(1690). The presence of a significantly non-zero PF33 coupling also supports this conclusion as will be discussed in the next section. It is also interesting to note that the SLAC-LBL "by eye" search located a resonance at 1900 MeV. This could have been a misplacement of the 1690 resonance, or an observation of the tail of the P33(2130), but is most likely to be yet another P33 resonance, the P33(1950) mentioned by some analyses at the Oxford conference.

This is a difficult wave to sort out - theory suggests that it should contain several resonances, so it requires careful analysis. Our use of very accurate normalisation constants and of the N* isobar should ensure that our results are reliable, but an analysis of our higher energies, and a K-matrix analysis are still needed.

D33

The D33 resonance is wide; its mass is still not accurately determined. Elastic analyses give a mass between 1650 and 1720 MeV. SLAC-LBL give 1725 (by eye) or 1650 (K-matrix) MeV. The Saclay K-matrix fit gives 1600 MeV. Gopal saw resonant behaviour, Stark suggested a mass of 1650 MeV, as did Stevens, and this analysis finds the same mass. The Saclay elastic analysis found behaviour similar to our dip, several possible reasons for this dip were given in the previous section. The Saclay K-matrix gave a low mass for the resonance when the Saclay elastic data were used, and also when run with the CERN elastic data, which do not show a dip; the suggestion of a second resonance is unlikely, but would explain this Saclay result.

D35

Analyses of our data have always seen a narrow resonance - like D35 structure. Gopal suggested a mass of 1640 MeV and a width of 80 ± 20 MeV. Stark's results showed a smaller and narrower σ^{JP} peak. Stevens found that the addition of the ΔDD35 wave to his earlier set of waves improved his fits dramatically. Gopal and Stark pointed out that the Saclay elastic results available at the time (ref. 72) also suggested a narrow resonance in this region; the Saclay elastic results shown in our σ^{JP} plots do indeed show a peak near 1600 MeV, but they disagree seriously with the CERN elastic results. The latest Saclay results (ref. 74) do not claim a resonance, nor does the CERN analysis. SLAC-LBL

did not fit this wave at all, but their technique of testing waves and rejecting those not needed at adjacent energies could easily lead to the rejection of a narrow resonance. The first energy at which the Saclay $\pi\pi$ N analysis included the D35 wave was 1640 MeV. They found a σ^{JP} of 0.7 mb at 1640, but only 0.1 mb at their next two energies (1668 and 1695 MeV). The Saclay results therefore appear to confirm ours, and it is a pity that they did not include this wave at lower energies.

F35

Elastic analyses agree on a wide F35(1890) resonance. SLAC-LBL find this resonance too, though their K-matrix fit gives it a mass of 1813 MeV. We do not reach this energy, but like the Saclay $\pi\pi$N analysis we apparently see the tail of the 1890.

F37

The 4 star resonance at mass 1950 MeV, with width 220 MeV, is seen by all elastic analyses, and by SLAC-LBL. Our σ^{JP} values at the top two energies are somewhat larger than the SLAC-LBL values, but appear to be consistent with them.

VII.5.3 Comparison with theory

A brief description of the theories relevant to these results is now necessary. Detailed descriptions can be found in references 13 and 14 which also give many references to

the original work. No complete theory of the strong interaction exists, so patterns that may help build up such a theory are sought through Group Theory. The symmetry group SU(3) successfully describes groupings of particles (multiplets) and higher symmetries are being sought in attempts to describe larger multiplets and their behaviour. $SU(6)_W \supset O(3)$ appears to be such a symmetry; its development will be described and our results will be compared with it.

SU(3) is generally explained as representing three fundamental particles, quarks; the up, down, and strange quarks. These are written u, d, s or if the nature of the quark does not matter, just q.† Each quark has a corresponding anti-quark, written $\bar{q}$. Mesons are built up of a quark and an anti-quark : $q\bar{q}$, whereas baryons are built up of three quarks : qqq. The combination of one of three possible quarks with one of three possible anti-quarks is written using Group-theoretical notation :

$$3 \otimes \bar{3} = \{1\} \oplus \{8\}$$

which means that mesons come in singlets and octets. Baryons are similarly written :

$$3 \otimes 3 \otimes 3 = \{1\} \oplus \{8\} \oplus \{8\} \oplus \{10\}$$

so they come in singlets, octets, and decuplets. A π^+p resonance can only be an $I=\frac{3}{2}$ member of a decuplet. π^-p can

---

† The existence of a fourth quark - the charmed quark c - is now certain, and two more - t and b - may be in the offing. The additional quark (or quarks) extend SU(3) to SU(4) (or SU(6)), but this does not need to be taken into account here because π^+p experiments at our energies do not show any effects connected with charm.

produce members of decuplets ($\Delta, I=\frac{3}{2}$) and also N*, $I=\frac{1}{2}$ particles which are members of octets.

The next step is to include the spin of the quarks in the Group Theory descriptions. Quarks are treated as spin-$\frac{1}{2}$ objects; this automatically gives integral spin to mesons and $\frac{1}{2}$ integral spin to baryons. (The assignment of spin-$\frac{1}{2}$ to quarks itself causes spin statistics problems but these are not relevant to the present discussion.) To make the theory relativistic (and workable) W-spin, described by the group $SU(2)_W$ is used. This gives the group $SU(6)_W$

$$SU(3) \otimes SU(2)_W = SU(6)_W$$

Baryons are now written

$$6 \otimes 6 \otimes 6 = \{20\} \oplus \{56\} \oplus \{70\} \oplus \{70\}$$

These larger multiplets can be broken down into SU(3) multiplets with spin. The {56} is

$$\{56\} = \{10,4\} \oplus \{8,2\}$$

here 10 = SU(3) decuplet

4 = 2S+1, so $S = \frac{3}{2}$; this is a spin $\frac{3}{2}$ decuplet

and 8 = SU(3) octet

2 = 2S+1, so this is a spin $\frac{1}{2}$ octet

Similarly $\{70\} = \{8,4\} \oplus \{10,2\} \oplus \{8,2\} \oplus \{1,2\}$

Thus 56-plets and 70-plets can be detected by a $\pi^+ p$ experiment, but only a few of their members will be seen. The advantage of $\pi^+ p$ experiments is that beam and target can be easily produced, and only the $I=\frac{3}{2}$ channel need be

analysed, so a careful analysis with high statistics can be performed.

As the spin of a baryon can be greater than $\frac{3}{2}$, it must be possible to have angular momentum L between the quarks. This is described by the group O(3), so baryons (and mesons) are described in terms of $SU(6)_W \otimes O(3)$, giving multiplets of the type $\{n, L^P\}$, where n is the $SU(6)_W$ multiplet number, and p is the parity of the state. The total spin of the baryon, J, is given by the vector addition $\underline{J} = \underline{L} + \underline{S}$. Apart from orbital excitations ($L > 0$), radial excitations which provide recurrences of the same $\{n, L^P\}$ multiplets are possible. Excitations are denoted by a subscript N at the end of the multiplet description, N giving the excitation level. The SU(3) octet of stable baryons and the $\frac{3^+}{2}$ decuplet fit well into a $\{56, 0^+\}$ supermultiplet. The low-lying negative parity baryons make up a $\{70, 1^-\}$ supermultiplet.

This scheme successfully describes the static properties of many known baryons, though some mixing of multiplets is apparent. One would then like to use these groups to describe interactions and decays. Some good predictions can be obtained from $SU(6)_W$, but others are bad. Basically, in decays $SU(6)_W$ involves the conservation of S_z, the quark spin component along the decay axis. L_z is therefore also conserved, so all decays are forced to have $\Delta L_z = 0$. In fact, quarks can have transverse momentum, so that $\Delta L_z = \pm 1$ decays can occur. Various broken $SU(6)_W$ models allowing $\Delta L_z = \pm 1$ and 0

have been suggested, and analyses such as this one are needed to decide which models are acceptable. Two such models deserve particular mention.

ℓ-broken SU(6)w

In a hadron decay, two possible values of the orbital angular momentum ℓ between the two final particles are generally possible. In the simple $SU(6)_W$ model, these two states ℓ_+, ℓ_- are linked. The breaking of this link, so that separate couplings can be calculated for ℓ_+ and ℓ_- gives ℓ-broken $SU(6)_W$. The relative phase of ℓ_+ and ℓ_- states can then be as predicted by $SU(6)_W$ - this is the "$SU(6)_W$-like" solution, but the phase can now also be opposite - the "anti-$SU(6)_W$" solution.

The Melosh transformation

Up to now, the discussion has been in terms of quarks that make up the hadrons - "constituent" quarks. This provides a very simple model of mesons and baryons. Decays of hadrons can however be described in terms of current algebra which uses a different SU(3) whose representations are "current" quarks. To describe a transition from hadronic state A to hadronic state B, we therefore use the matrix element

$$< B_{const.} | Q | A_{const.} > \qquad 7.24$$

It is however much easier to calculate terms such as

$$< B_{current} | Q | A_{current} > \qquad 7.25$$

Here, Q is the axial charge used in current algebra; according to $SU(6)_w$ it can only have a $\Delta L_z = 0$ part. The constituent and current quarks are representations of different algebras, and the Melosh approach is to write a transformation V such that

$$| A_{const.} > = V | A_{current} > \qquad 7.26$$

The general properties of V can be examined, or specific expressions can be tried. It is sufficient here to note that 7.24 can be rewritten

$$\begin{aligned} <B_{const.}| Q | A_{const.}> &= <B_{current}| V^{-1} Q V | A_{current}> \\ &= <B_{current} | \tilde{Q} | A_{current}> \qquad 7.27 \end{aligned}$$

The transformed $\tilde{Q}$ can keep its $\Delta L_z = 0$ part, and also gain a $\Delta L_z = \pm 1$ part. If one part or the other dominates, then we have "$SU(6)_w$-like" or "anti-$SU(6)_w$" behaviour. This approach validates the previously arbitrary breaking, and allows current algebra calculations to be made. Rosner and Faiman (refs. 75 and 76) for example have calculated the signs expected in decays of the $\{70, 1^-\}$ and $\{56, 2^+\}$ depending on whether they are "like" or "anti". Such predictions can be used to compare possible multiplets with our results.

Negative parity states

S31(1620) and D33(1650) fit well into the $\{70, 1^-\}$. Table VII.11 compares the $SU(6)_w$ predictions of Faiman and Rosner (refs. 75 and 76) with our signs for $\pi\Delta$ and ρN decays; it is seen that our results favour "anti-$SU(6)_w$", as do the

results of other analyses. It would be useful to check the $N^*\pi$ decays too, but $SU(6)_W$ calculations for these are not yet available.

Experimental determinations of ρN signs have long been an embarassment to $SU(6)_W$ predictions. ρN Argand diagrams in our energy range do not show clear loops as do $\Delta\pi$ Argands, this is presumed to be caused by ill-understood effects which are due to the ρN channel being below the ρ production threshold. Even where ρN signs are determined though, they are often poorly determined, and can be in conflict with $SU(6)_W$ predictions. This analysis makes a significant contribution to knowledge of the negative parity ρN states. We determine the $\rho_1 SS31$ sign to be clearly positive - neither SLAC-LBL nor Saclay were sure of this sign. We also determine the $\rho_1 DD33$ sign to be clearly positive, and the $\rho_3 DD33$ sign to be probably positive. Neither SLAC-LBL nor Saclay included these waves in their analyses. All three signs agree with $SU(6)_W$, but do not distinguish between "like" and "anti".

In addition to $SU(6)_W$ predictions, fits can be made. Hey et al have made $SU(6)_W$ fits, based on the Melosh transformation, to available experimental results, and thence predicted other values. Their original paper (ref. 51a) was expanded (ref. 52a) and then updated at the Oxford conference (ref. 13) in the light of additional experimental results. Their fitted signs for the $\Delta\pi$ channels, and their predicted signs for ρN are given in Table VII.11. The ρN predictions are made on the basis of a fit to ρN couplings that Hey et al considered to be reliable at the time of the Oxford Conference, and none of the waves in Table VII.11 were included in that fit.

Hey et al did not give their predictions for ρ_1DD33, ρ_3SD31, ρ_3DD33, so their predicted signs have been calculated by the author from the updated parameters given at Oxford, and from other parameters and formulæ given in references 51a and 51b. The fits made by Hey et al contain more theoretical input than the $SU(6)_w$ predictions and predictions made from these fits are sensitive to the experimental input. It is therefore a significant success of these fits that they correctly predict all the three $\{70, 1^-\}\rho N$ signs that we have determined, and our determination of these signs is a valuable experimental result.

The D35(1640) resonance is a considerable embarassment for theory. The lowest multiplets it can come from are $\{70, 3^-\}$ or $\{56, 1^-\}$. Unfortunately, conventional models do not expect these multiplets to have masses below 2 GeV. At the 1976 Oxford conference (ref. 13), Cutkosky presented strong evidence for a ΔD35(1925) resonance, and proposed a dual string model to allow a lower mass for the $\{56, 1^-\}$ multiplet, so that the ΔD35(1925) could fit into it. This model, dubbed the "Polish bag", could perhaps be stretched to even lower masses allowing our D35(1640) to fit into it. Two consequences would arise. Firstly, the D35(1925) would have to belong in a radially excited $\{56, 1^-\}$ or in a $\{70, 3^-\}$. Hey pointed out at Oxford that masses of a $\{70, 3^-\}$ could lie below 2 GeV, so the D35(1925) could after all be assigned to this multiplet. (The alternative of an excited Polish bag appeals to this author.) Secondly, a $\{56, 1^-\}$ would require additional low mass ΔS31 and ΔD33 resonances. The possible second ΔD33

Resonance/wave	Predictions			Saclay sign	I.C./ W.C. sign
	$SU(6)_W$-like	Anti-$SU(6)_W$	Hey et al fit		
Δ SD31	+	-	-	-	-
Δ DS33	-	+	+	+	+
Δ DD33	+	+	+	+?	+?
ρ_1SS31	+	+	+	+?	+
ρ_1DD33	+	+	+	n/a	+
ρ_3SD31	+	-	-	-	?
ρ_3DS33	-	+	+	+?	?
ρ_3DD33	+	+	+	n/a	+?

Sign convention of Hey et al (ref. 51)

Uncertain signs are followed by a question mark, very doubtful ones are given by a ? alone

n/a - wave not included in Saclay analysis

Table VII.11

Comparison of $\{70, 1^-\}$ signs with predictions

resonance in our energy range would fit such a scheme very nicely, but there is no sign of an additional $\Delta S31$.

The Δ D35(1640) is therefore a serious challenge to theory, and it may be preferable to dismiss it as a threshold effect unless other analyses confirm it, or this analysis is repeated with allowance for the N*(1520) isobar and still sees this resonance.

Positive parity states

Our mass range lies above that of the $\{56, 0^+\}$ ground level multiplet, and in the region of the $\{56, 2^+\}$ multiplet or slightly below it. These two are well established, but other multiplets are also needed to explain some resonances that lie in this mass range. In order to discuss this situation, N* resonances must be considered as well as Δ resonances, so results of analyses discussed in the previous section, and values from the Particle Data Group tables (ref. 50) will be frequently mentioned. Possible multiplets in our mass range are radial excitations of the $\{56, 0^+\}$ - these are $\{56, 0^+\}_2$ and $\{56, 0^+\}_4$ - and also $\{56, 2^+\}$, $\{70, 0^+\}$, $\{70, 2^+\}$. Results from the Oxford conference show that the $\{70, 2^+\}$ has masses of 2 GeV or above. Hey et al are strongly opposed to suggestions of "non-minimal" multiplets such as the $\{70, 0^+\}$ (and the $\{56, 1^-\}$) but they may be wrong. The first column of Table VII.12 lists the possible multiplets, and the members each requires. Only $\Delta\pi$ decays are included because no predictions are available for $N^*\pi$, and our ρN signs are uncertain.

The known P11(1470) and P11(1780) resonances appear to be members of two radially excited $\{56, 0^+\}$ multiplets. Their signs, determined by the SLAC-LBL analysis prevent them from being members of the $\{70, 0^+\}$. The second and third columns of Table VII.12 give the $\Delta\pi$ decay sign predictions for "$SU(6)_W$-like" and "anti-$SU(6)_W$" dominance; the calculations of Faiman and Rosner have been used (ref. 75). The fourth column shows the SLAC-LBL K-matrix results, the fifth shows the Saclay K-matrix results, the sixth shows our results, and the seventh contains comments. The assignments of each particle will be discussed here, the signs given by SLAC-LBL and Saclay have all been flipped to agree with the convention of Hey et al, which is the same as ours and Faiman and Rosner's. Uncertain signs are followed by a question mark and unknown signs are represented by a question mark alone.

As the two P11 resonances establish two $\{56, 0^+\}$ radial excitations, two P33 resonances with positive signs are required. These must be the ΔP33(1560-1620) and the ΔP33(1900-1950), whose signs are clearly determined. In a simple experimental model, one would expect our radially excited $\{56, 0^+\}_2$ P33 to decay into P11(1470)π , just as the ground state P33(1230) decays into P11(938)π . This is very clearly seen in our $N^*\pi$ Argand diagrams, indeed the N*PP33 wave gave better results in CHI than any other wave. The $\{56, 2^+\}$ P33 resonance should also lie in our energy range or a little above it. The first column of Table VII.12 shows that it will have a PF33 decay, whereas $\{56, 0^+\}$

members will not. We do indeed see a PF33 signal - small, but with small errors - we believe that a signal of this size is real because we have used very accurate normalisation constants. A CHI run tied to the Δ PF33 wave gave the preferred combination and a χ^2 that is good for a small wave; see Table VII.3.a for details of this run. We therefore conclude that ΔPF33 clearly shows a resonance, which must be a $\{56, 2^+\}$ member, and must have a corresponding Δ PP33 with a negative sign. One would expect this to be our PP33(1680) which shows an uncertain sign, but may be negative, unlike the ΔPP33(1620). Analysis of our higher energies would be useful as the higher PP33 may have a mass slightly above the present energy range, and may show its sign more clearly at these higher energies.

The P33 situation is not entirely clear; the two resonances lie so close together that they may undergo some multiplet mixing. The possibility of drawing two loops in the PF33 waves could then be explained by mixing instead of merely being attributed to large errors in a small wave. SLAC-LBL and Saclay did not allow for the $N^*\pi$ channel, so their PP33 results are bound to differ from ours. Both these analyses find a PP33 near 1600 MeV with a positive sign - neither analysis sees a negative sign near 1700 MeV, though both show a clear doubling back in their Argand diagrams at this energy. There is also a problem with the $\{56, 2^+\}$ P33 signs. The $\{56, 2^+\}$ is generally believed to be "$SU(6)_W$-like" because of the F15 decay signs. ρ N signs do not agree with "like" or "anti", but they are even more uncertain than the ρN signs of the $\{70, 1^-\}$. Photoproduction experiments seem

to require the $\{56, 2^+\}$ to be "anti-$SU(6)_w$" - see Hey's talk at Oxford (ref. 13). Our Argand diagrams, and those of Saclay show clearly that the signs of ΔPP33 and ΔPF33 are out of phase at all energies analysed. This requires the $\{56, 2^+\}$ to be "anti-$SU(6)_w$", and it appears that no arguments about mixing or resonances lying close together can change this. Even if the mass of the second P33 lies somewhat above our energy range and above Saclay's highest energy (1738 MeV), the relative phases of the two waves would have to change by more than $\frac{\pi}{2}$ in a very small energy range to give "$SU(6)_w$-like" behaviour. It may be that neither $\Delta L_z = 0$ nor $\Delta L_z = \pm 1$ dominate in this multiplet.

Further evidence for there being two P33 resonances close together comes from Hey et al (ref. 51b) and also Burkhardt and Pulido (ref. 76) who examine our P33 $N^*\pi$ results. Both find that the P33 is about 3 times as large as they require for a $\{56, 0^+\}_2$. If the experimental results are interpreted as two resonances, not one wide one, this problem should be immediately resolved.

Our analysis sees no other $\{56, 2^+\}$ members, except for the tails of F35 and F37 but, for completeness, the members seen by SLAC-LBL and Saclay are included in Table VII.12.

This leaves our P31 resonance or resonances still not assigned. The P31 (1520) mass is too low for the $\{56, 2^+\}$ and its sign, though not very well determined, also disagrees with the $\{56, 2^+\}$. The P31 (1520) therefore has to be

assigned to $\{70, 0^+\}$. Saclay also make this assignment, and find a low mass P13(1550) to go into the $\{70, 0^+\}$. This leaves a missing P11, which Saclay suggest is mixed with the Roper - P11(1470) - and difficult to see. The Saclay elastic analysis claims that the Roper is split, with components of masses 1413 MeV and 1532 MeV. The higher mass P11 would then fit very well with the P13(1550) and the P31(1520-1550). The Particle Data Group mini-review on N's and Δ's in reference 50 discusses this splitting, and mentions the possibility of a P13(1530). The $\{70, 0^+\}$ clearly needs closer examination, but the combined evidence for it is strong. The only place another P31 can belong is in the $\{56, 2^+\}$, and this is already clearly filled by the P31(1780-1950). The uncertainty in this resonance's parameters is large, and our higher mass P31 can easily be the tail of this resonance; analysis of our higher energy data should clarify the matter.

What can we conclude about $SU(6)_W$ multiplets and the resonances in Table VII.10? For the $\{70, 1^-\}$, we confirm its anti-$SU(6)_W$ nature, and our S31 and D33 resonances clearly belong in it. We note a possible D35 and suggest, with some diffidence, that it be placed in a $\{56, 1^-\}$. The D35 may however be the result of large background and a threshold effect. We see the $\{56, 0^+\}_2$ and some of the $\{56, 2^+\}$ - their P33 members appear to be mixed, but both seem to exist. Our P31(1520) adds to the significant evidence accumulating in favour of a $\{70, 0^+\}$. Finally, our suggested P31(1680) is almost certainly just the tail of the P31 somewhere between 1780 and 1950 MeV.

Multiplet members	Predicted signs		Experimental signs & masses			Comments
	$SU(6)_w$-like	anti-$SU(6)_w$	SLAC-LBL	Saclay	I.C./W.C.	
$\{56, 0^+\}_2$						
PP11	+	+	1381 +	1340 +		see note about the Roper resonance.
PP33	+	+	1609 +	1540 +	1620 +	
$\{56, 0^+\}_4$						
PP11	+	+	1708 +	1710 -?		
PP33	+	+	maybe the 1900+ seen by eye	o/e	o/e	A P33 with mass 1900-1950 is seen by several analyses.
$\{70, 0^+\}$						
PP11	-	-	n/s	may be mixed with the Roper		see note about the Roper resonance
PP31	+	+	n/s	1550 -?	1525 +?	
PP13	+	+	n/s	1530 -?		
$\{56, 2^+\}$						
PP13	-	-	1716s/u	1750 -		
PF13	+	-	n/a	n/a		
FP15	-	+	1668 -	1650 -		
FF15	+	+	1668 +	1650 +		
PP31	-	-	n/s	1800 +?		
PP33	-	-	n/s	not seen separately from PP33 1540	1690?	Saclay & SLAC-LBL see a squiggle here.
PF33	-	+	n/a	1540 -?	1690?	Sign undetermined, but opposite to PP33.
FP35	+	-	1813s/u	o/e	o/e	
FF35	+	+	1813 +	o/e	o/e	
FF37	+	+	1924 +?	o/e	o/e	

Symbols

n/a not included in this analysis

o/e outside energy range

n/s not seen

s/u sign unavailable, because $\Delta\pi$ channel not analysed

Notes

1/ the signs of SLAC-LBL and Saclay have all been flipped, to conform with the conventions of Hey et al, and Faiman and Rosner

2/ I.C./W.C. only analyse $I=\frac{3}{2}$ waves

3/ The Roper P11(1470) may well be split into two resonances, see text for details

4/ Doubtful signs are followed by a ?, Very doubtful ones are given by ? alone

Table VII.12

Positive parity multiplets and their $\Delta\pi$ decays

The $\{56, 2^+\}$ cannot be firmly said to be "$SU(6)_w$-like", or "anti-$SU(6)_w$". It would be useful to check ρ signs in this multiplet, and also in $\{56, 0^+\}_2$ and $\{70, 0^+\}$, once definite theoretical predictions are available. $N^*\pi$ decay signs should also be checked. Analysis of our higher energy data would be interesting, but the analysis described here is itself a significant contribution to work on the baryon spectrum.

VII.6 Concluding Remarks

This work started with film measurement and analysis, followed by an elastic data analysis which provided data on backward elastic cross-sections, and allowed the accurate determination of cross-sections in π^+p induced states. The results of two energies were used to bridge the gap between other data which was then subjected to a $\pi\pi N$ 4-variable maximum likelihood partial wave analysis. As opposed to the claims made by the Saclay group (ref. 16a) we found that analysis of the $I=\frac{3}{2}$ data alone can be successful; such results can then be used to check the results of a joint $I=\frac{3}{2}$ and $I=\frac{1}{2}$ analysis, or they can be used as input to such an analysis.

We have analysed $\pi^+\pi^+n$ data properly, using an N^* isobar, and including One Pion Exchange terms, not an I=2 isobar. Many fits from random starts were made, without rejecting apparently small waves, and using very accurate normalisation integrals. The continuum ambiguity has been discussed, and we suggested that its seriousness has been

overestimated. A continuity analysis was used to pick a unique combination of solutions at different energies, and this continuity analysis was also used to check for resonant waves. Unitarity corrections to the isobar model have been shown not to be serious.

Resonances were sought in the final Argand diagrams and cross-section plots, then compared with other experimental results and with theory. The $\{70, 1^-\}$ supermultiplet is seen clearly and is definitely "anti-$SU(6)_W$". A possible D35 resonance is noted, but other explanations for the behaviour of this wave are given. Some members of the $\{56, 2^+\}$ supermultiplet are seen, but it is not clear whether it is "anti-$SU(6)_W$" or "$SU(6)_W$-like". The $\{56, 0^+\}_2$ supermultiplet is also seen, and we find a P31(1525) resonance which requires the existence of a $\{70, 0^+\}$ supermultiplet.

Our O.P.E. results were self-consistent, the scattering length a_0^2 was found to be inconsistent with theory, but consistent with other experimental determinations. The phase shifts δ_0^2 agree at low $\pi\pi$ masses with other experiments.

The achievements of this work can be favourably compared with a list describing the "ideal $\pi N \to \pi\pi N$ analysis", given by another Ph.D. student, D.E. Novoseller, in his recent Ph.D. thesis (ref. 53).

(a) "Include all $\pi\Delta$, ρN, εN low partial waves"
We have analysed only $\pi^+ p$ data, so εN waves were not needed, but we have included all the $\pi\Delta$ and ρN waves.

(b) "Include the effects of various πN^* isobar contributions"

We have included the Roper N*(1470) isobar, the only important one in our range of energies.

(c) "Include proper barrier factors for the isobar production amplitude"

We have not done this, but Rob Stevens, in the Ph.D. thesis immediately preceding this one (ref. 9) showed that q^{ℓ} barrier factors were satisfactory at our energies.

(d) "Include the π-exchange input for the high partial waves"

We have treated this problem differently from Novoseller, but have included O.P.E., and have shown it to be successful.

(e) "Incorporate subenergy unitarity"

We have not done this, but we quote K.W.J. Barnham who has used our data to show that this effect is small.

(f) "Include the effect of I=2 $\pi\pi$ scattering"

We have used O.P.E. to do this.

(g) "Include corrections due to electromagnetic mass differences"

We feel that this cannot at present be justified. Even with our accurate normalisation integrals and good $\pi^{+}p$ statistics, we cannot hope for accuracy at a level where electromagnetic mass differences can have a noticeable effect. This does however bring out an important point - better results need higher statistics. Novoseller suggests a factor of 20 more data, but where is this to come from? A few groups still have unmeasured πp film, at our energies, but this would not even double present statistics. Taking 3-body data in any apparatus other

than a bubble chamber and analysing it is extremely difficult. Even if we were to ask for a factor of three more data, where are we to get it? $SU(6)_W$ has not yet been investigated to theorists' satisfaction, but experimental work has long since bypassed it, and bubble chambers have been closed down or assigned to other work. Perhaps the new Japanese K.E.K. bubble chamber will be used to take the required film, but who will measure it?

The work we have done compares favourably with Novoseller's list, but much could still be done. Using our present data, we could analyse higher energies, add another N* isobar, and perform a K-matrix analysis. An amalgamation of world data could be analysed by $\pi\pi$N analysts from various groups, and more data would be welcome. Perhaps even, a theoretical breakthrough will explain present results completely and obviate the need for further experimental work. For the present - we have done more than we dreamt of doing.

Appendix A

Argand diagrams with errors for all waves fitted, obtained from the original non-O.P.E. fits.

Points 1-9 denote solutions at the following energies (in GeV)

1 - 1.439	2 - 1.495	3 - 1.526
4 - 1.551	5 - 1.577	6 - 1.612
7 - 1.640	8 - 1.668	9 - 1.693

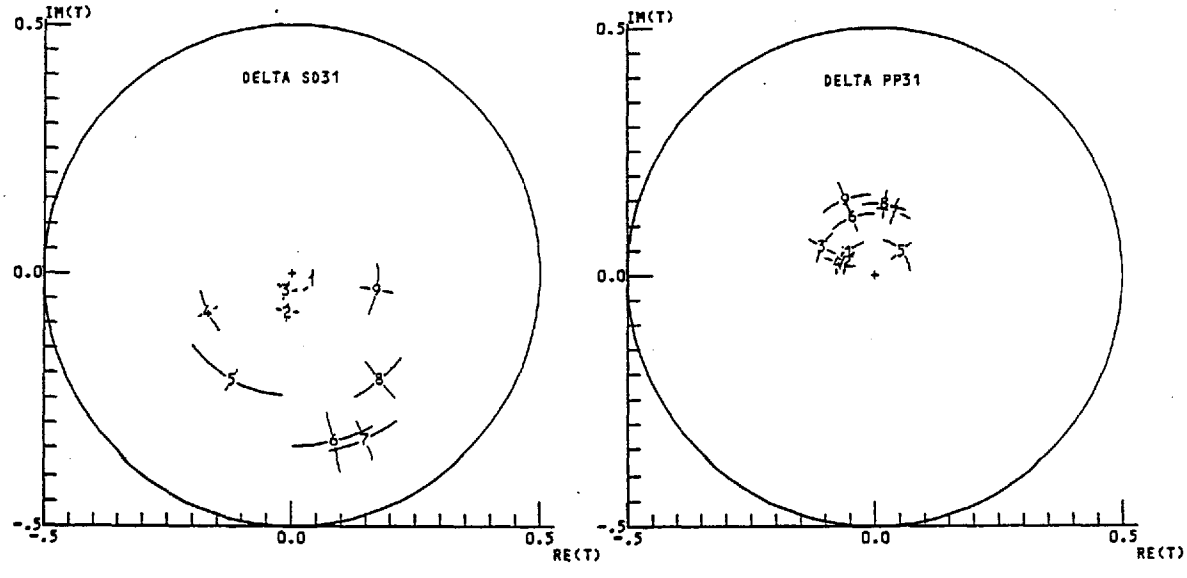

non O.P.E.

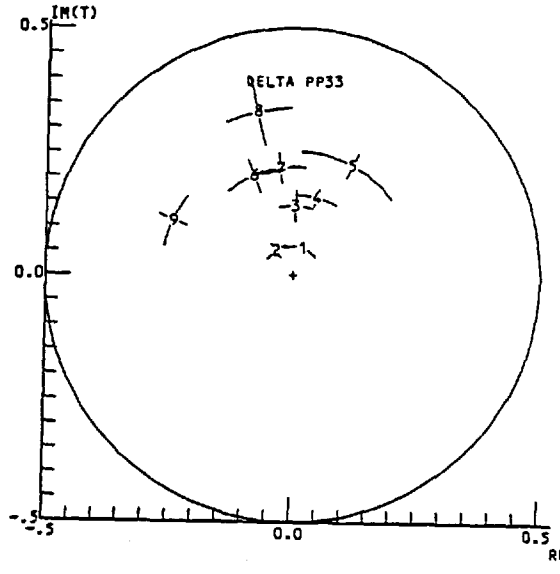
IM(T)
0.5
0.0
-.5
DELTA PP33
-.5
0.0
0.5
RE(T)

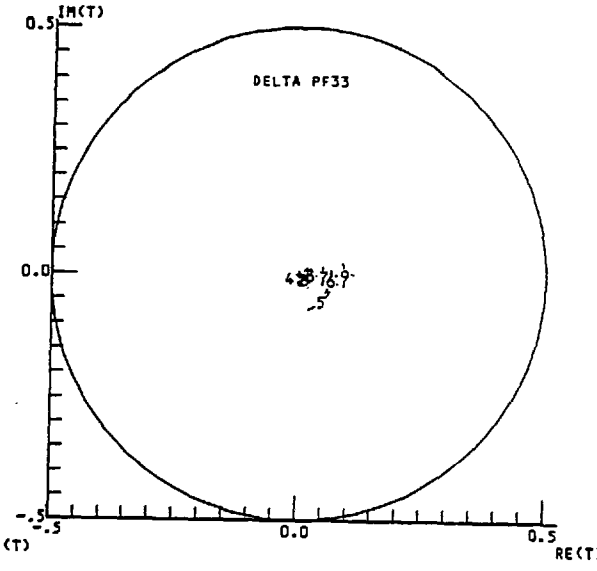
IM(T)
0.5
0.0
-.5
DELTA PF33
-.5
0.0
0.5
RE(T)

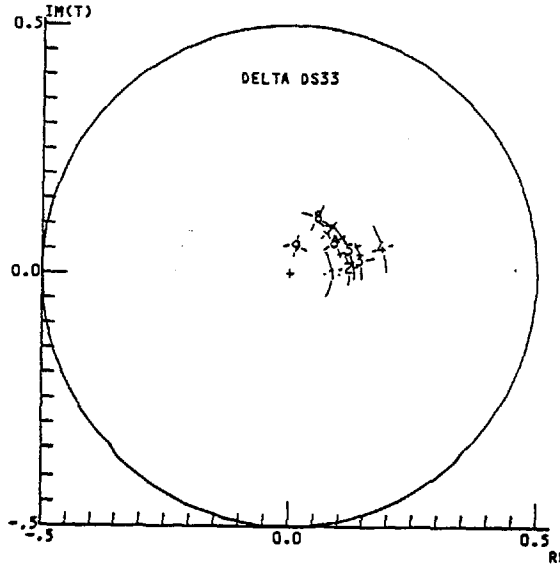
IM(T)
0.5
0.0
-.5
DELTA DS33
-.5
0.0
0.5
RE(T)

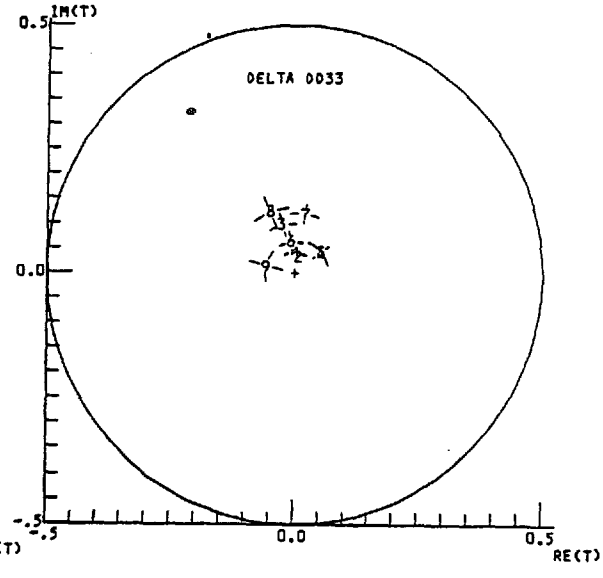
IM(T)
0.5
0.0
-.5
DELTA DD33
-.5
0.0
0.5
RE(T)

non O.P.E.

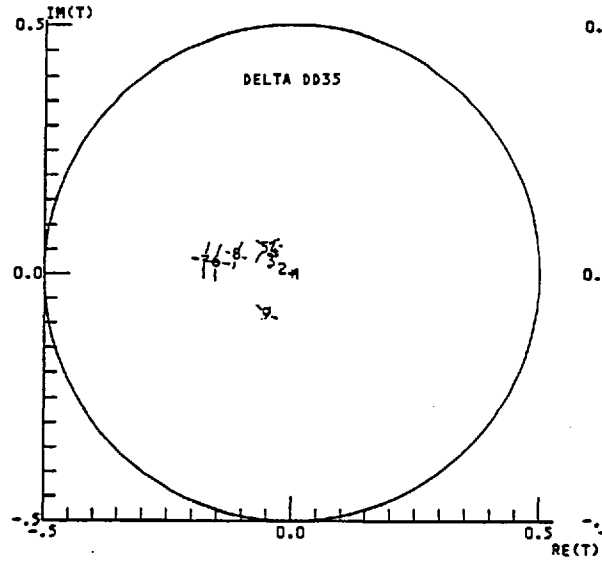
IM(T)
0.5
0.0
-.5
DELTA DD35
-.5
0.0
0.5
RE(T)

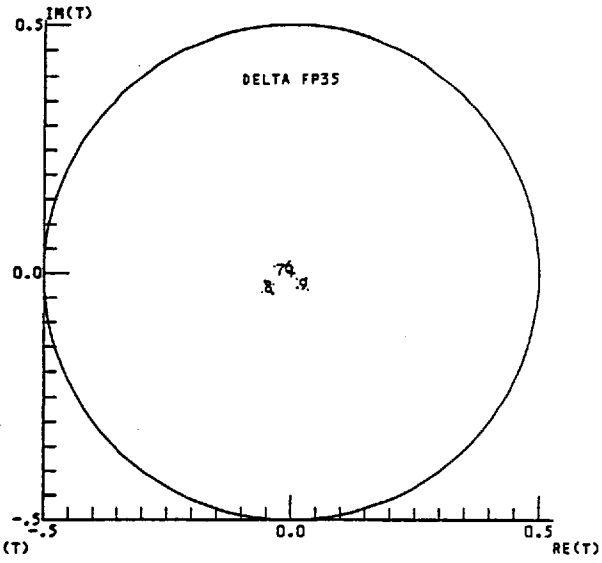
IM(T)
0.5
0.0
-.5
DELTA FP35
-.5
0.0
0.5
RE(T)

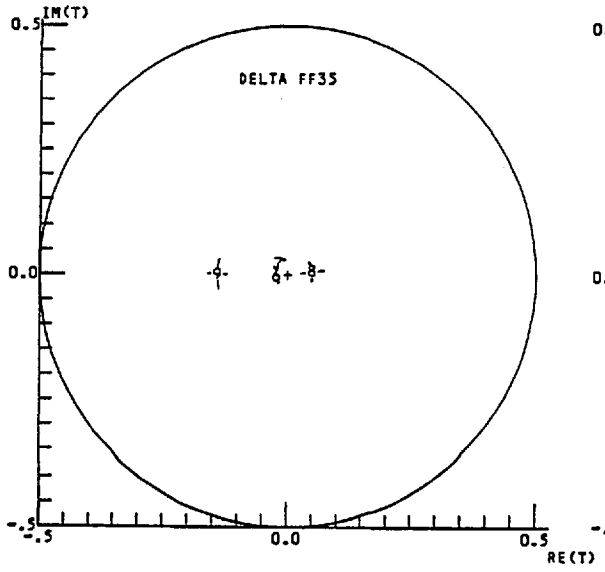
IM(T)
0.5
0.0
-.5
DELTA FF35
-.5
0.0
0.5
RE(T)

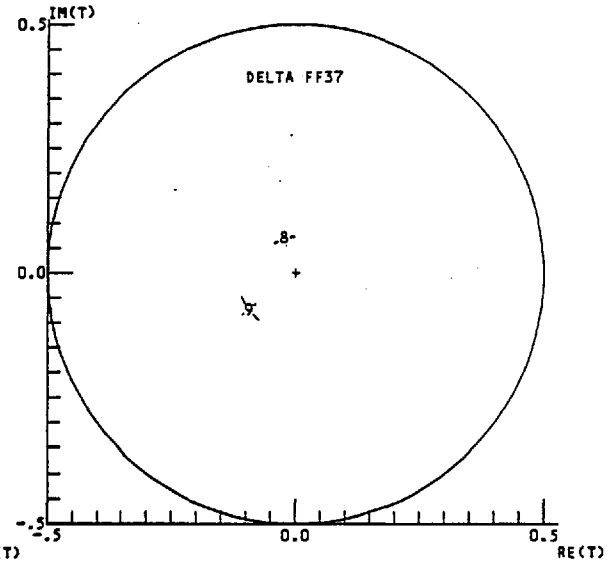
IM(T)
0.5
0.0
-.5
DELTA FF37
-.5
0.0
0.5
RE(T)

non O.P.E.

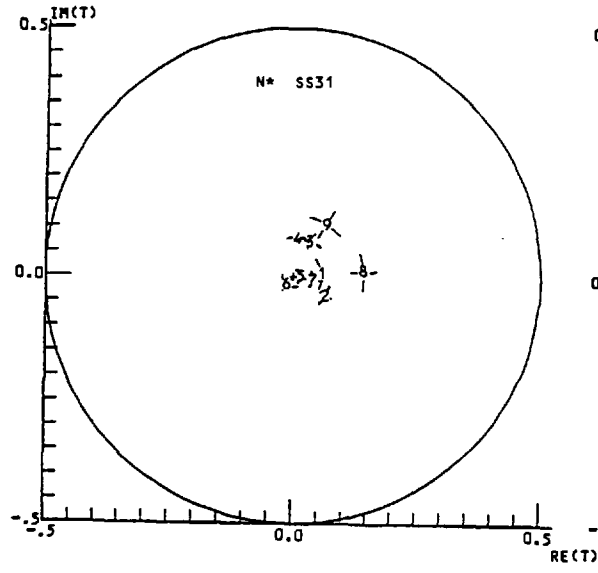
IM(T)
0.5
0.0
-.5
N* SS31
-.5
0.0
0.5
RE(T)

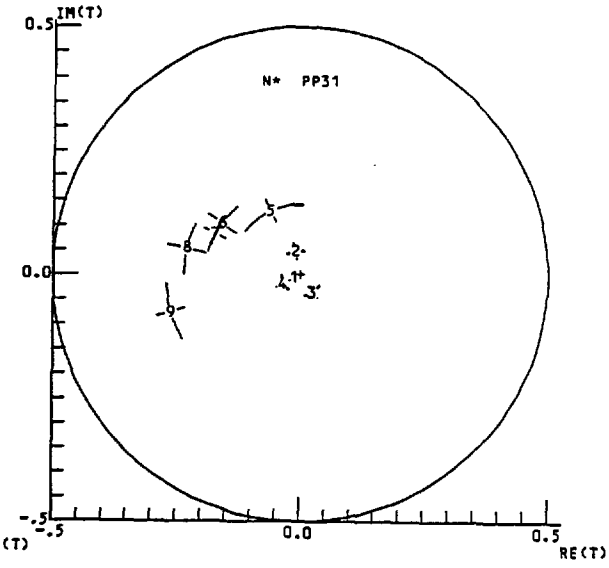
IM(T)
0.5
0.0
-.5
N* PP31
-.5
0.0
0.5
RE(T)

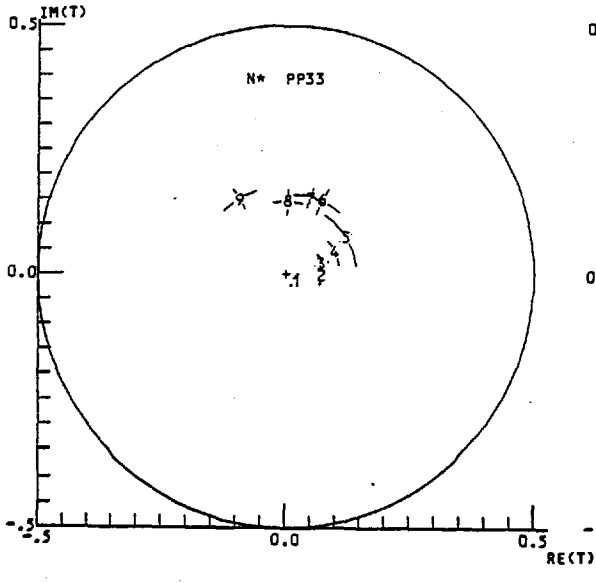
IM(T)
0.5
0.0
-.5
N* PP33
-.5
0.0
0.5
RE(T)

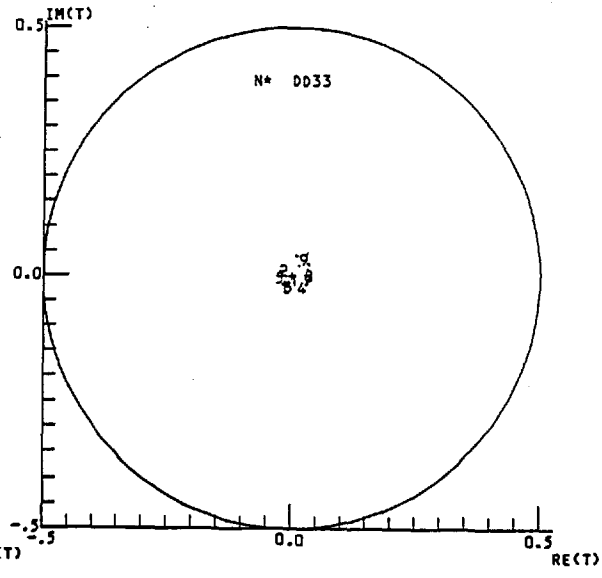
IM(T)
0.5
0.0
-.5
N* DD33
-.5
0.0
0.5
RE(T)

non O.P.E.

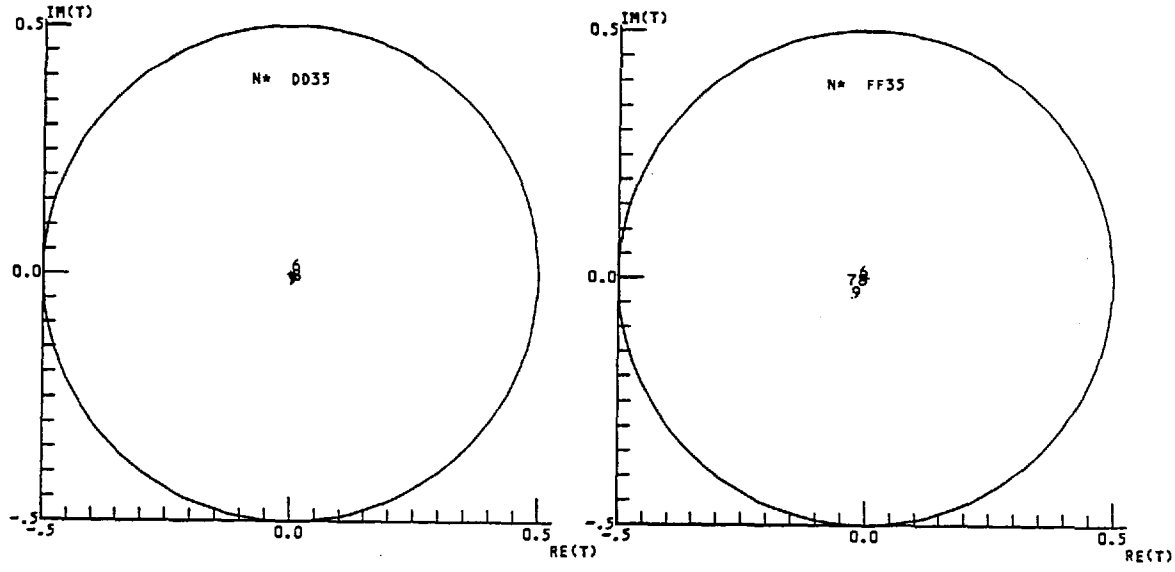
IM(T)
N* DD35
0.5
0.0
-.5
-.5
0.0
0.5
RE(T)
IM(T)
N* FF35
0.5
0.0
-.5
-.5
0.0
0.5
RE(T)

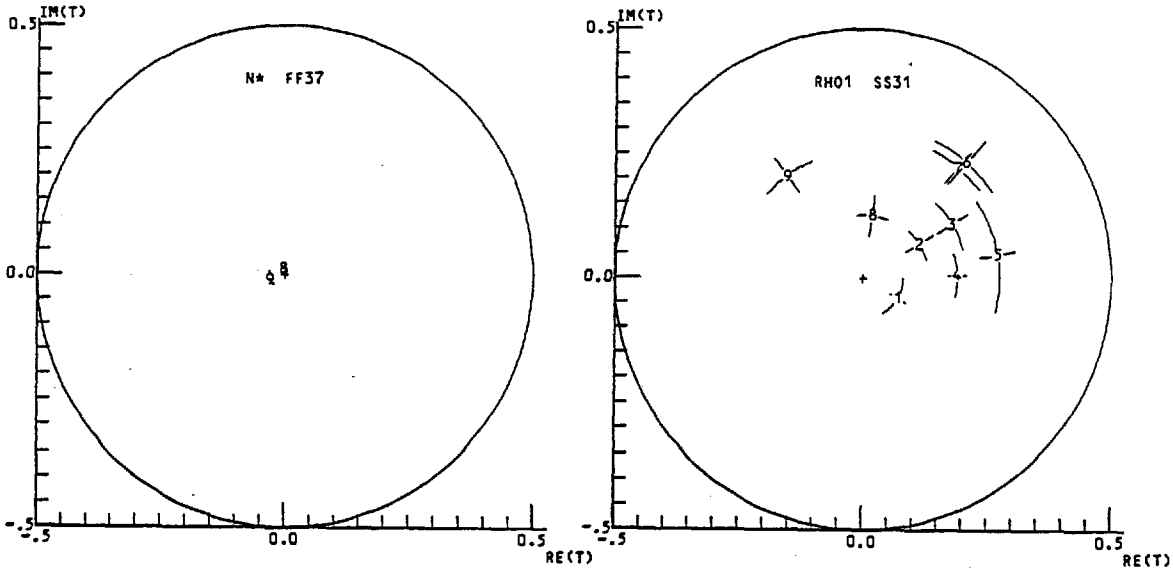
IM(T)
N* FF37
0.5
0.0
-.5
-.5
0.0
0.5
RE(T)
IM(T)
RH01 SS31
0.5
0.0
-.5
-.5
0.0
0.5
RE(T)

non O.P.E.

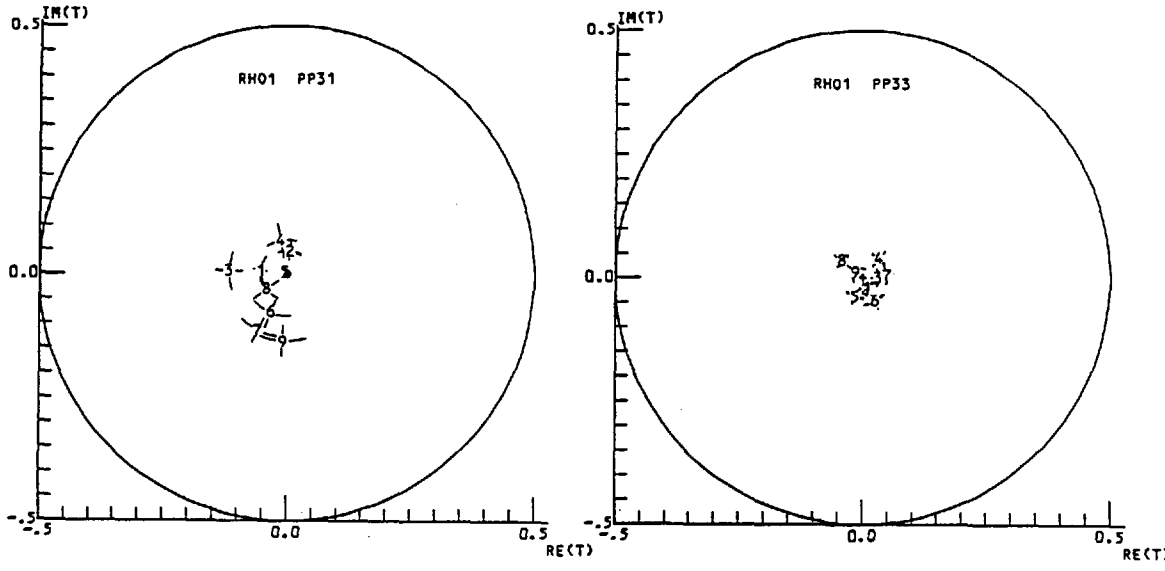
IM(T)
0.5
0.0
-.5
RHO1 PP31
RE(T)
-.5
0.0
0.5
IM(T)
0.5
0.0
-.5
RHO1 PP33
RE(T)
-.5
0.0
0.5

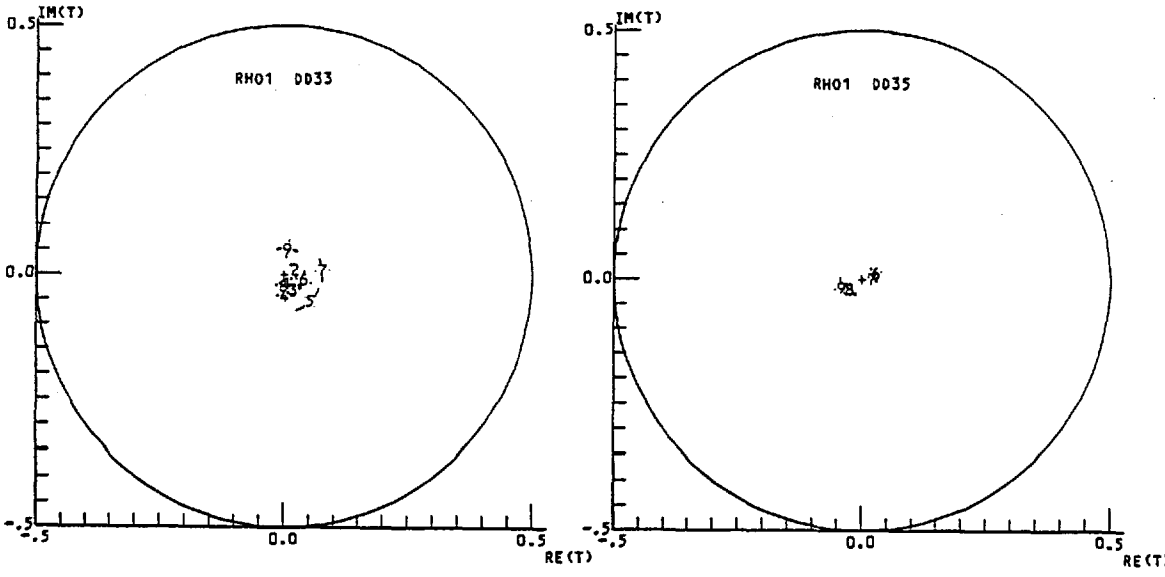
IM(T)
0.5
0.0
-.5
RHO1 DD33
RE(T)
-.5
0.0
0.5
IM(T)
0.5
0.0
-.5
RHO1 DD35
RE(T)
-.5
0.0
0.5

non O.P.E.

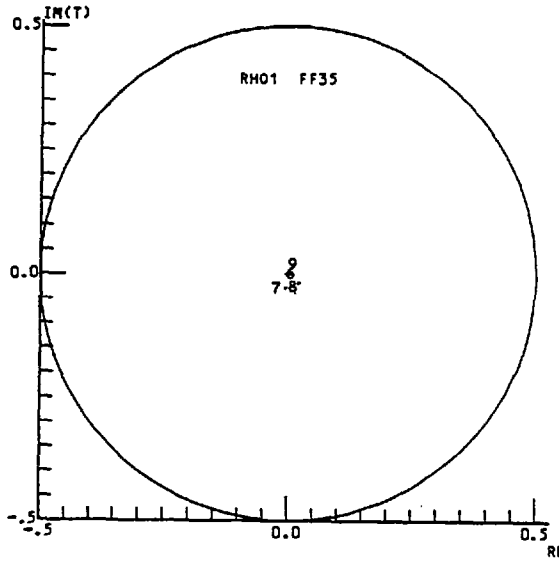
IM(T)
0.5
0.0
-.5
RH01 FF35
-.5
0.0
0.5
RE(T)

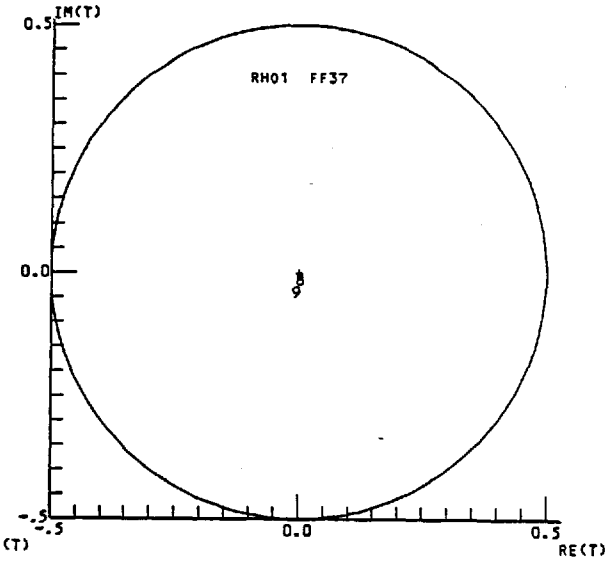
IM(T)
0.5
0.0
-.5
RH01 FF37
-.5
0.0
0.5
RE(T)

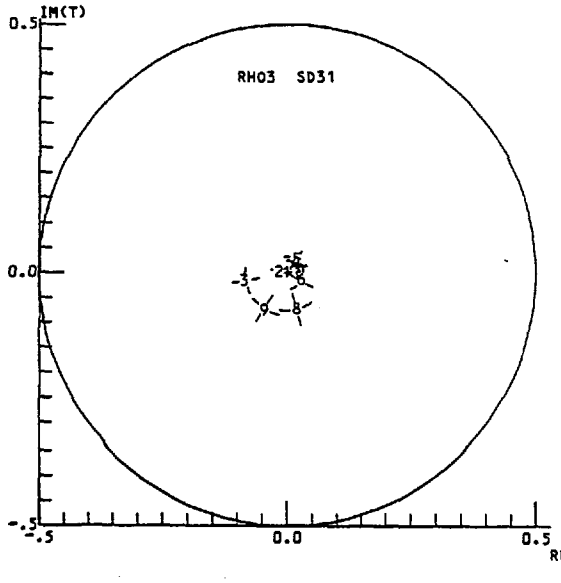
IM(T)
0.5
0.0
-.5
RH03 SD31
-.5
0.0
0.5
RE(T)

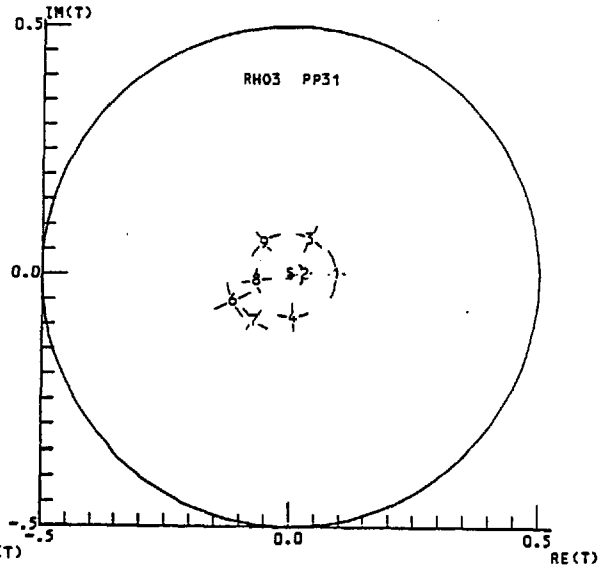
IM(T)
0.5
0.0
-.5
RH03 PP31
-.5
0.0
0.5
RE(T)

non O.P.E.

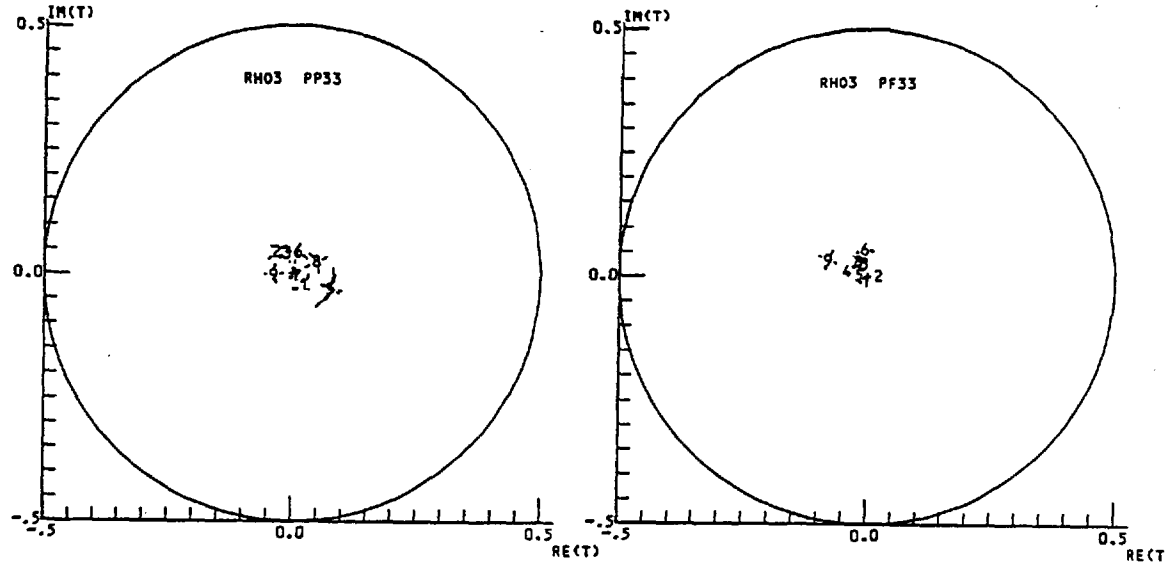
IM(T)
0.5
0.0
-.5
RH03 PP33
RH03 PF33
-.5
0.0
0.5
RE(T)

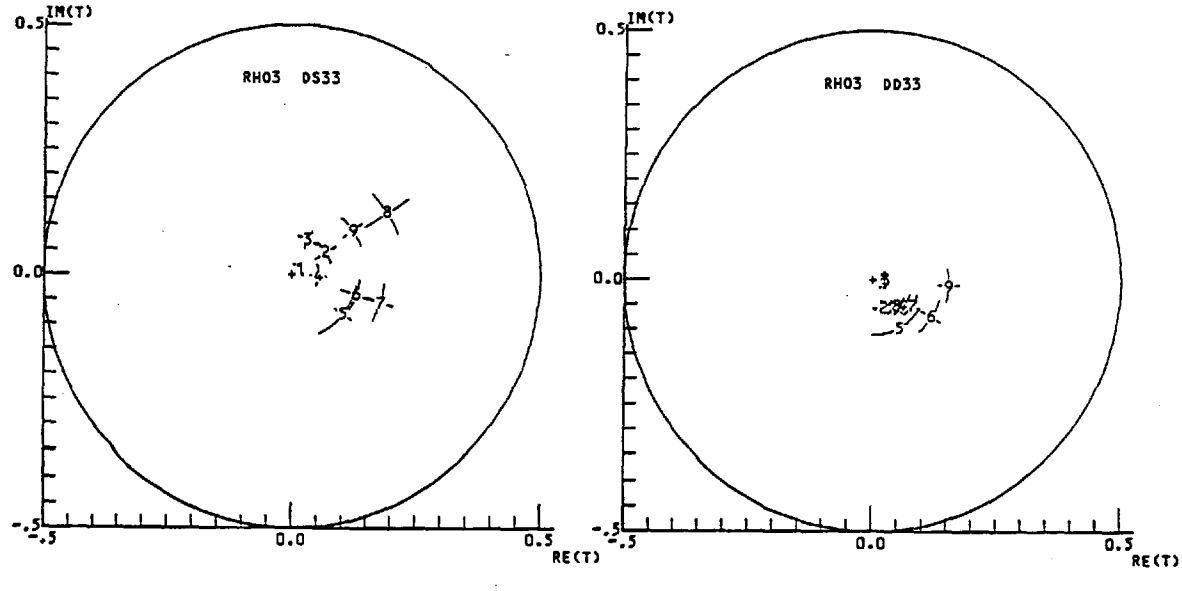
IM(T)
0.5
0.0
-.5
RH03 DS33
RH03 DD33
-.5
0.0
0.5
RE(T)

non O.P.E.

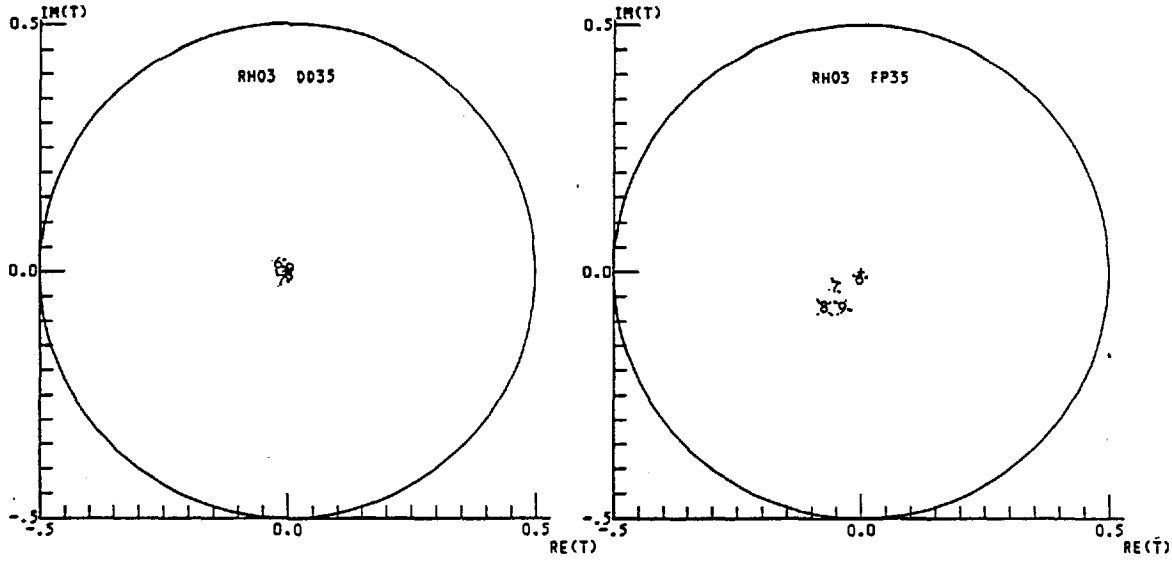
IM(T)
0.5
0.0
-.5
RH03 DD35
RE(T)
RH03 FP35

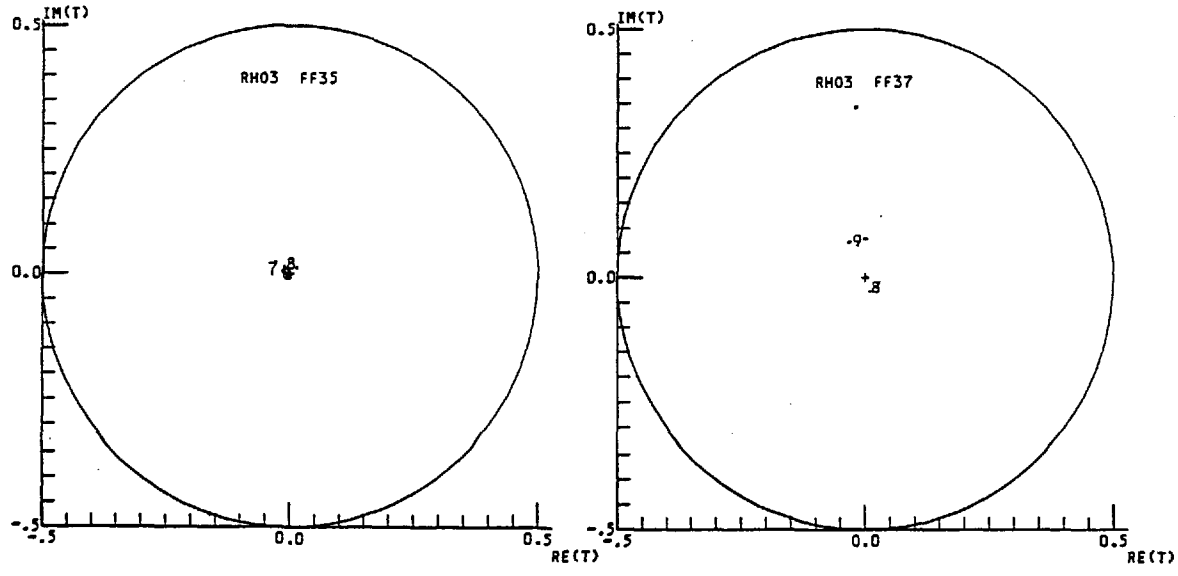
IM(T)
0.5
0.0
-.5
RH03 FF35
RE(T)
RH03 FF37

non O.P.E.

Appendix B

Argand diagrams with errors for all waves fitted, obtained from the refits with O.P.E.

Points 1-9 denote solutions at the following energies (in GeV)

1 - 1.439	2 - 1.495	3 - 1.526
4 - 1.551	5 - 1.577	6 - 1.612
7 - 1.640	8 - 1.668	9 - 1.693

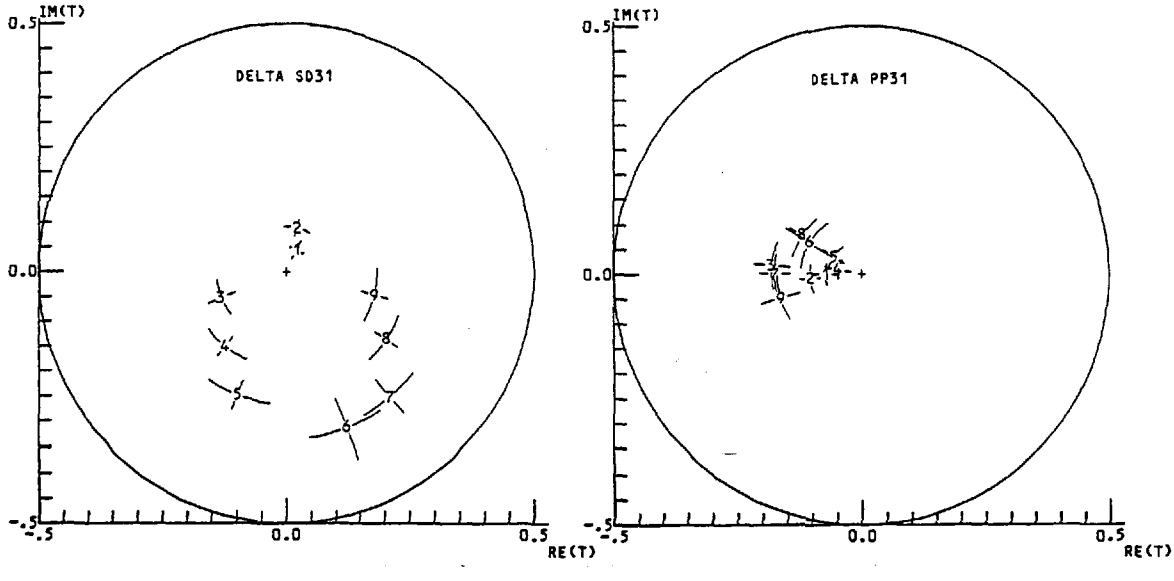

O.P.E. refit

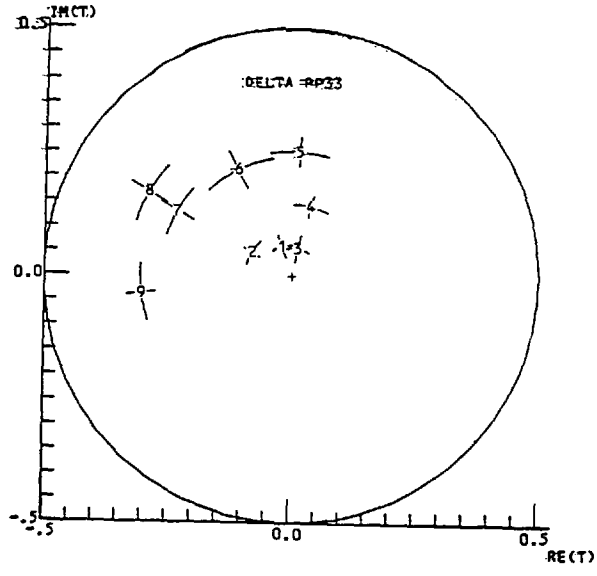
IM(T)
DELTA PP33
0.5
0.0
-.5
-.5
0.0
0.5
RE(T)

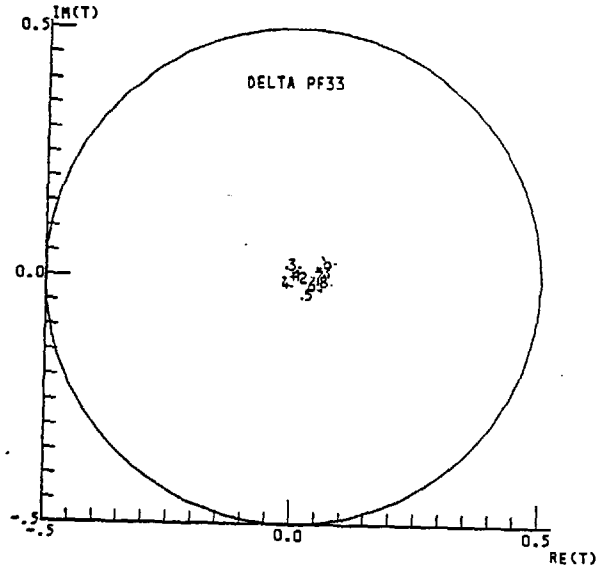
IM(T)
DELTA PF33
0.5
0.0
-.5
-.5
0.0
0.5
RE(T)

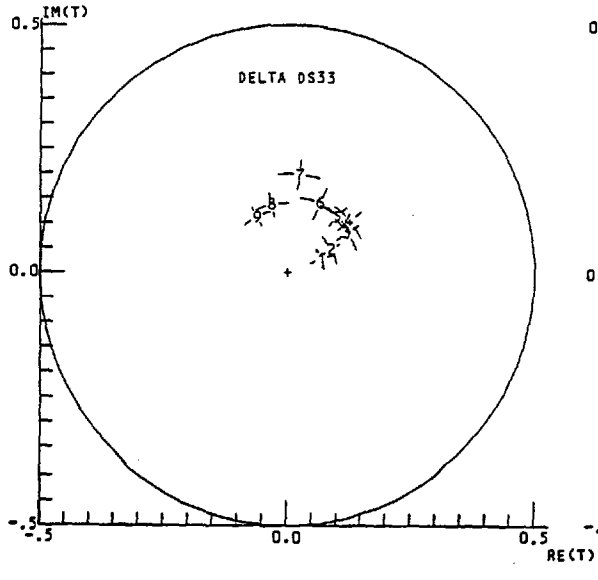
IM(T)
DELTA DS33
0.5
0.0
-.5
-.5
0.0
0.5
RE(T)

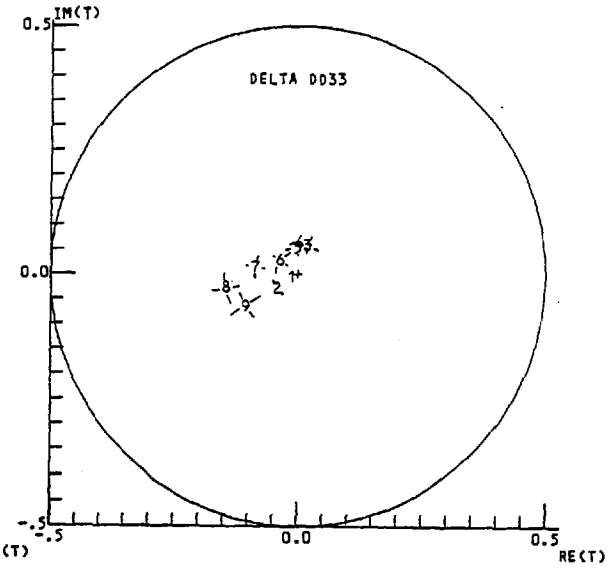
IM(T)
DELTA DD33
0.5
0.0
-.5
-.5
0.0
0.5
RE(T)

O.P.E. refit

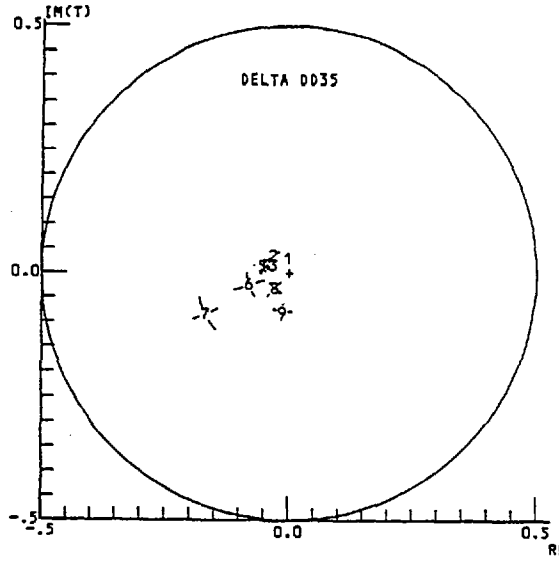
IM(T)
0.5
0.0
-.5
DELTA DD35
-.5
0.0
0.5
RE(T)

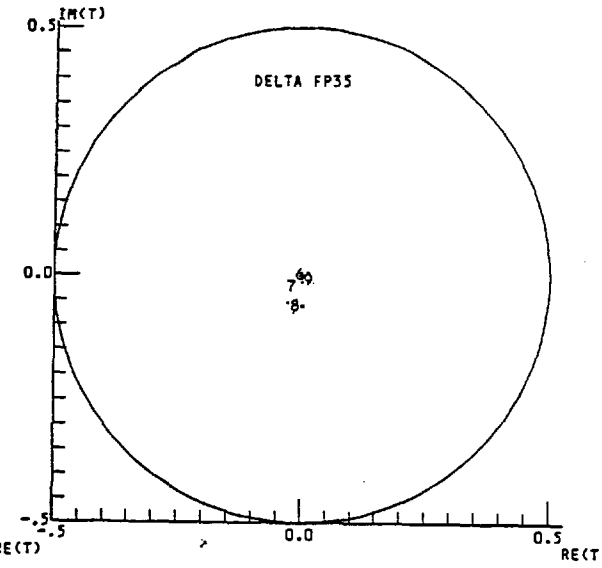
IM(T)
0.5
0.0
-.5
DELTA FP35
-.5
0.0
0.5
RE(T)

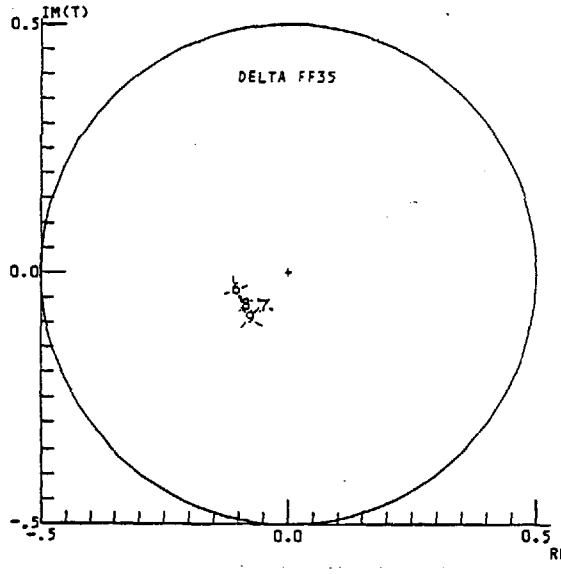
IM(T)
0.5
0.0
-.5
DELTA FF35
-.5
0.0
0.5
RE(T)

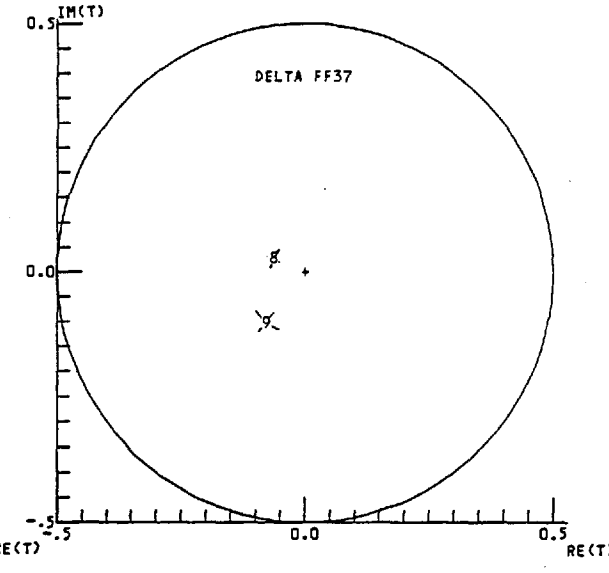
IM(T)
0.5
0.0
-.5
DELTA FF37
-.5
0.0
0.5
RE(T)

O.P.E. refit

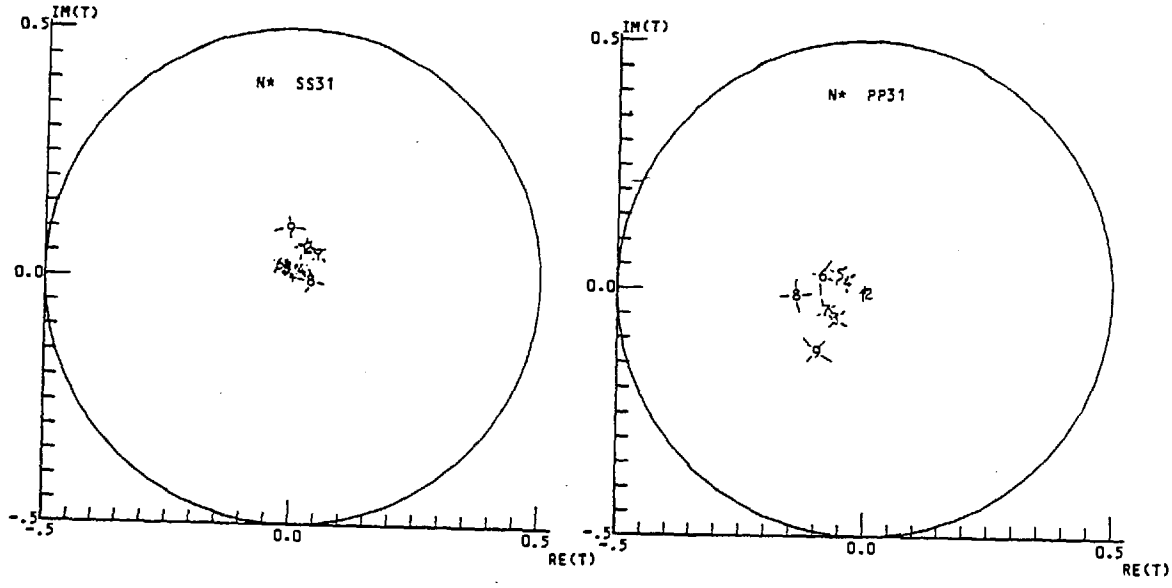

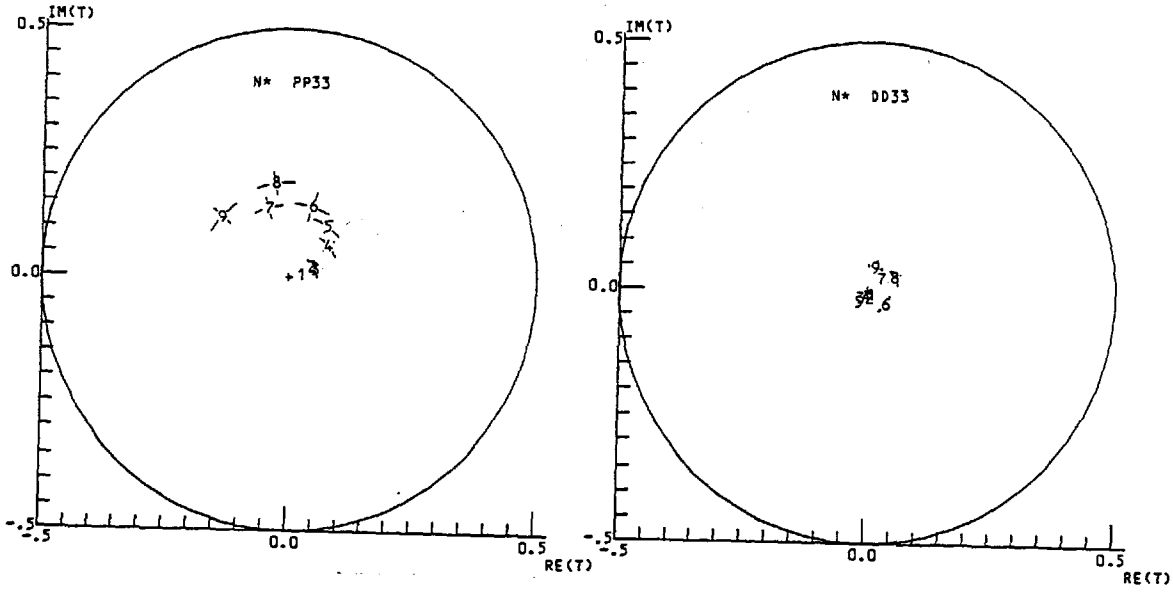

O.P.E. refit

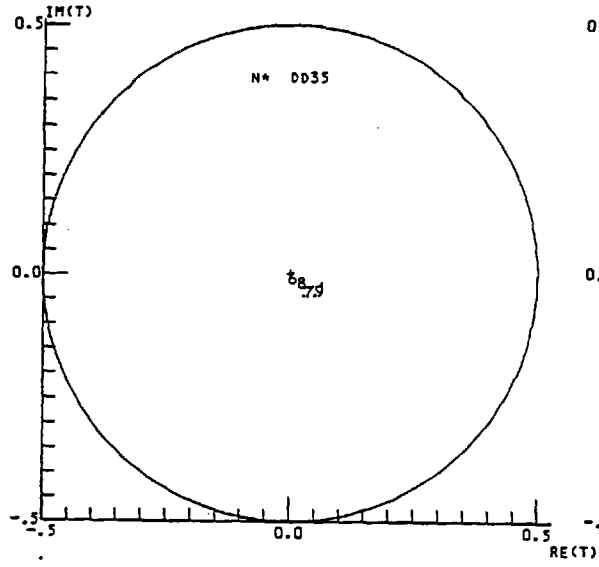
IM(T)
0.5
0.0
-.5
N* DD35
-.5
0.0
0.5
RE(T)

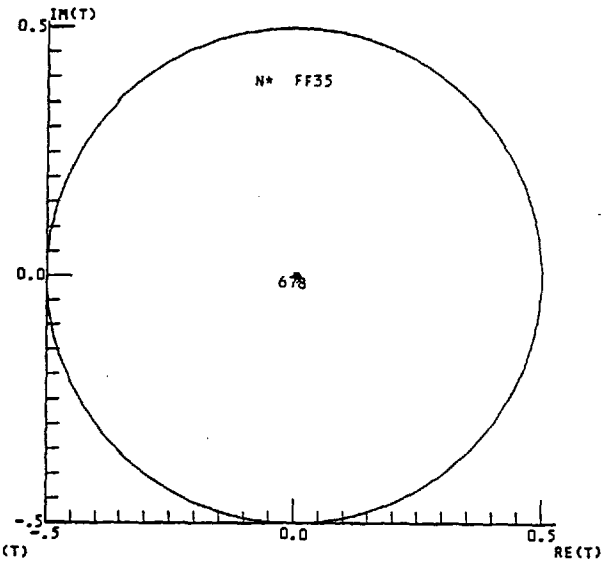
IM(T)
0.5
0.0
-.5
N* FF35
-.5
0.0
0.5
RE(T)

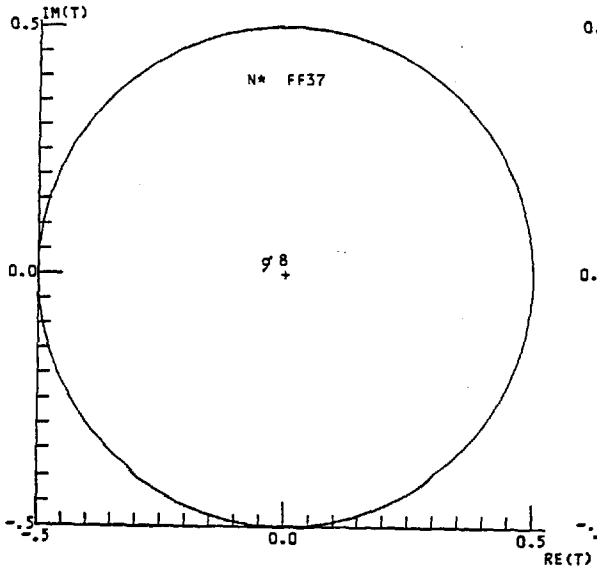
IM(T)
0.5
0.0
-.5
N* FF37
-.5
0.0
0.5
RE(T)

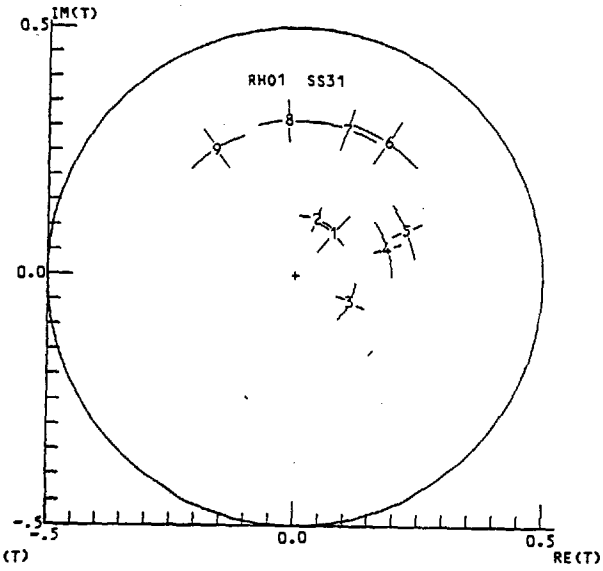
IM(T)
0.5
0.0
-.5
RH01 SS31
-.5
0.0
0.5
RE(T)

O.P.E. refit

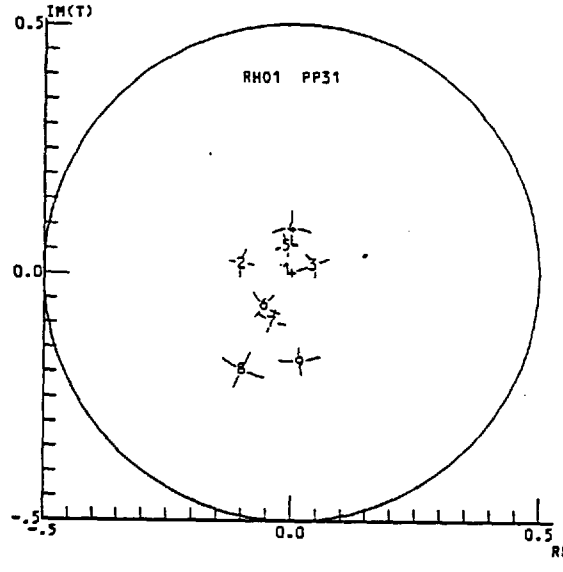
IM(T)
0.5
0.0
-.5
RHO1 PP31
-.5
0.0
0.5
RE(T)

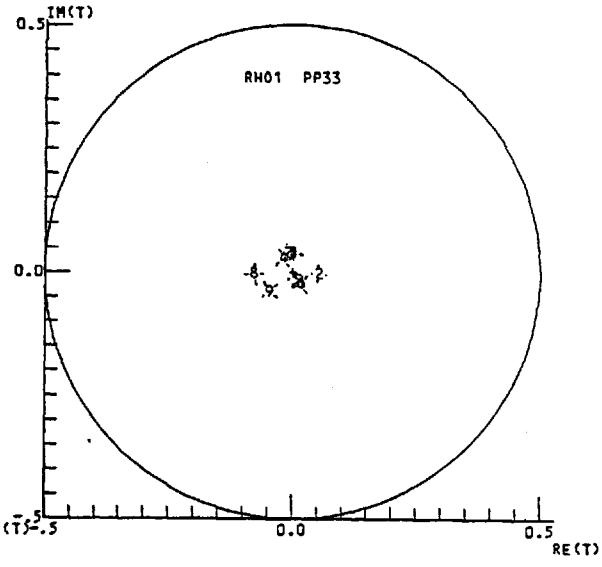
IM(T)
0.5
0.0
-.5
RHO1 PP33
-.5
0.0
0.5
RE(T)

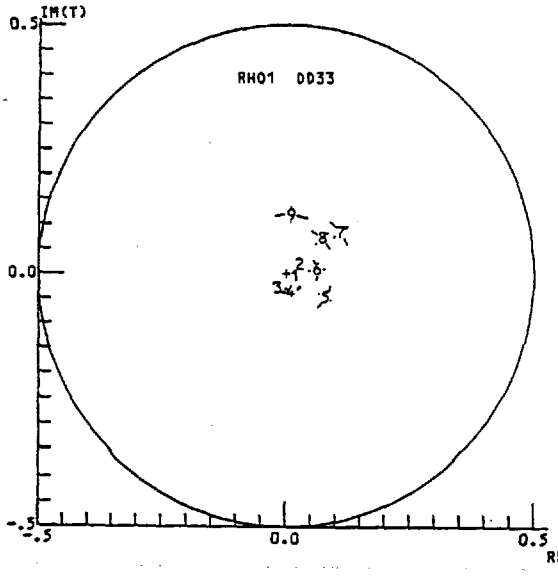
IM(T)
0.5
0.0
-.5
RHO1 DD33
-.5
0.0
0.5
RE(T)

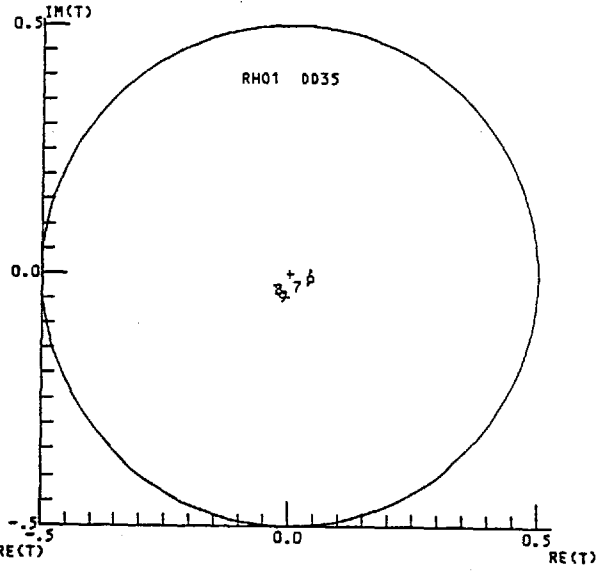
IM(T)
0.5
0.0
-.5
RHO1 DD35
-.5
0.0
0.5
RE(T)

O.P.E. refit

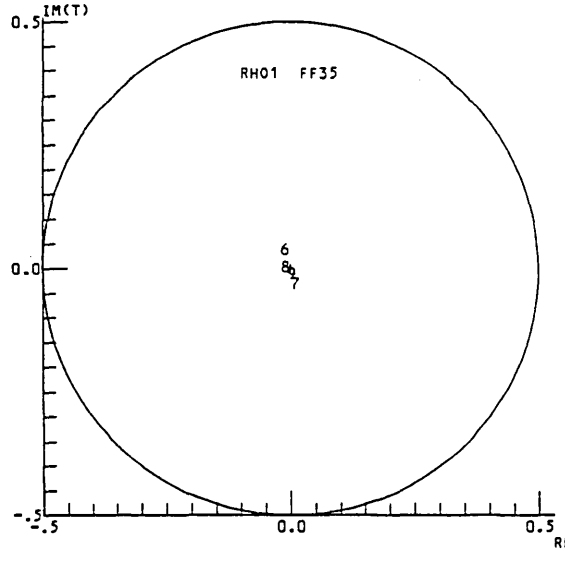
IM(T)
0.5
0.0
-.5
RH01 FF35
-.5
0.0
0.5
RE(T)

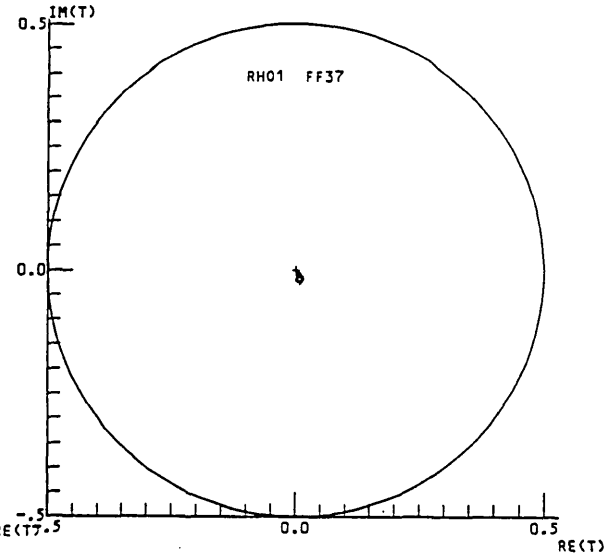
IM(T)
0.5
0.0
-.5
RH01 FF37
-.5
0.0
0.5
RE(T)

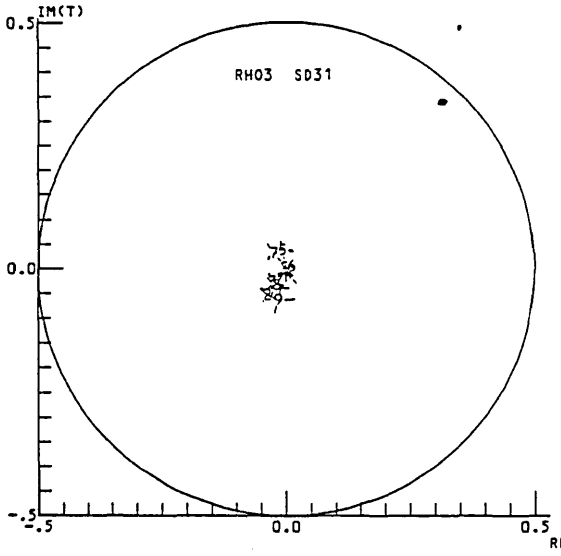
IM(T)
0.5
0.0
-.5
RH03 SD31
-.5
0.0
0.5
RE(T)

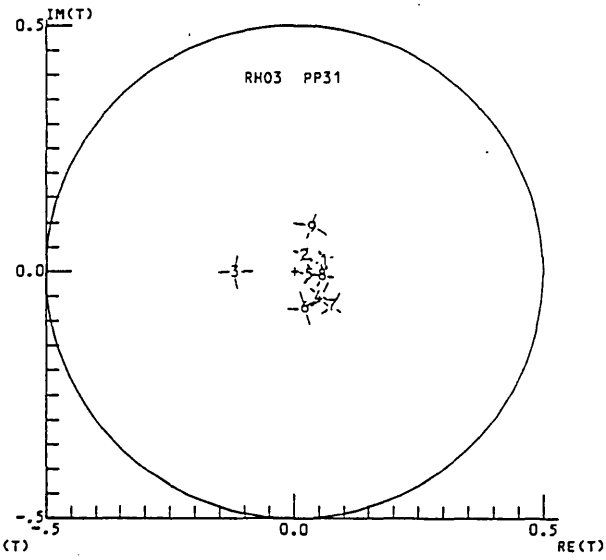
IM(T)
0.5
0.0
-.5
RH03 PP31
-.5
0.0
0.5
RE(T)

O.P.E. refit

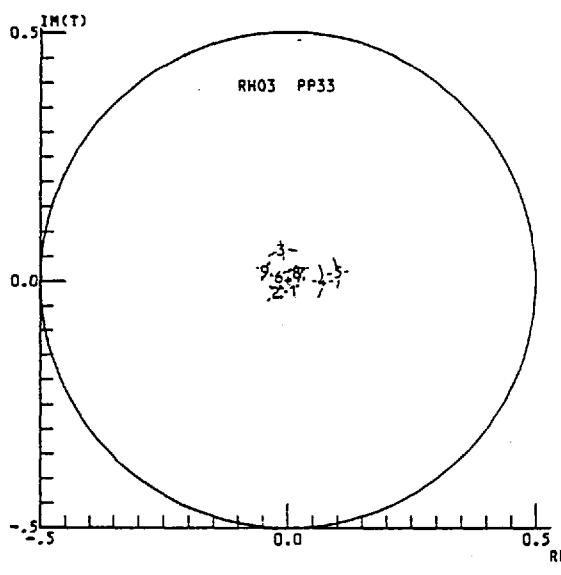
IM(T)
0.5
0.0
-.5
RHO3 PP33
-.5
0.0
0.5
RE(T)

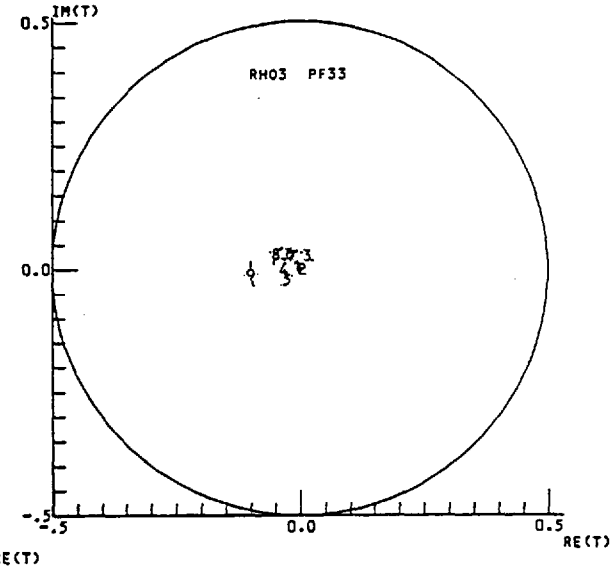
IM(T)
0.5
0.0
-.5
RHO3 PF33
-.5
0.0
0.5
RE(T)

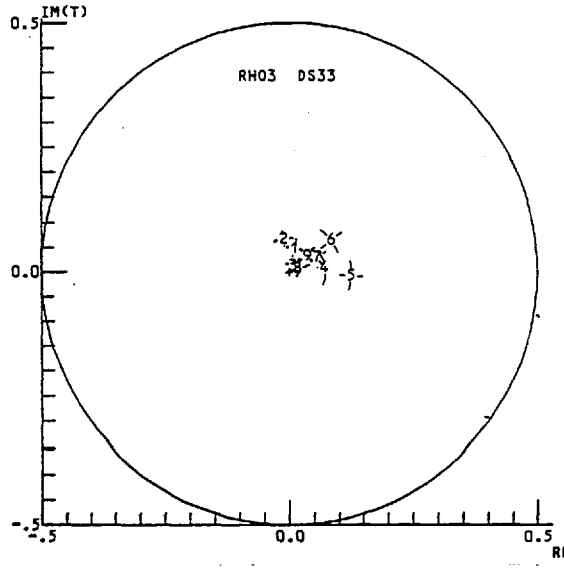
IM(T)
0.5
0.0
-.5
RHO3 DS33
-.5
0.0
0.5
RE(T)

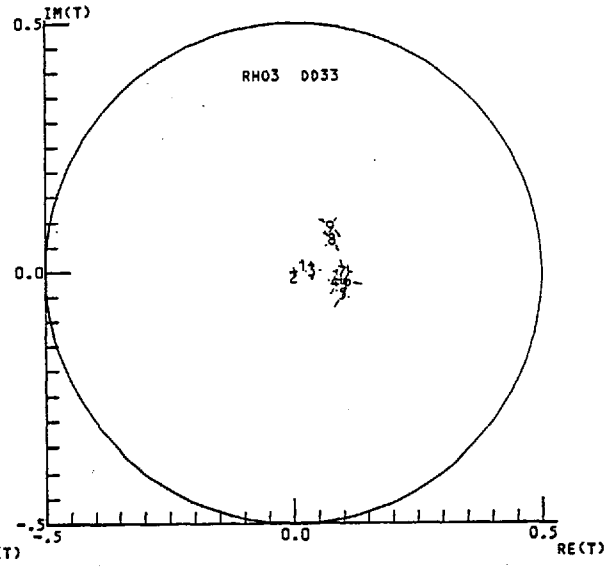
IM(T)
0.5
0.0
-.5
RHO3 DD33
-.5
0.0
0.5
RE(T)

O.P.E. refit

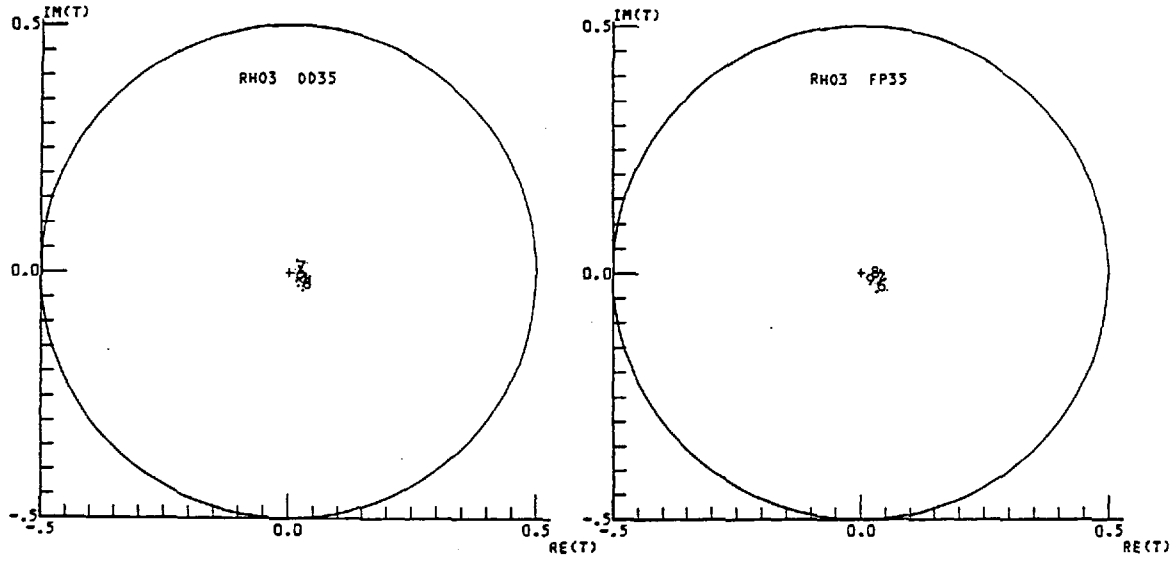
RH03 0035
RH03 FP35
IM(T)
RE(T)
0.5
0.0
-.5

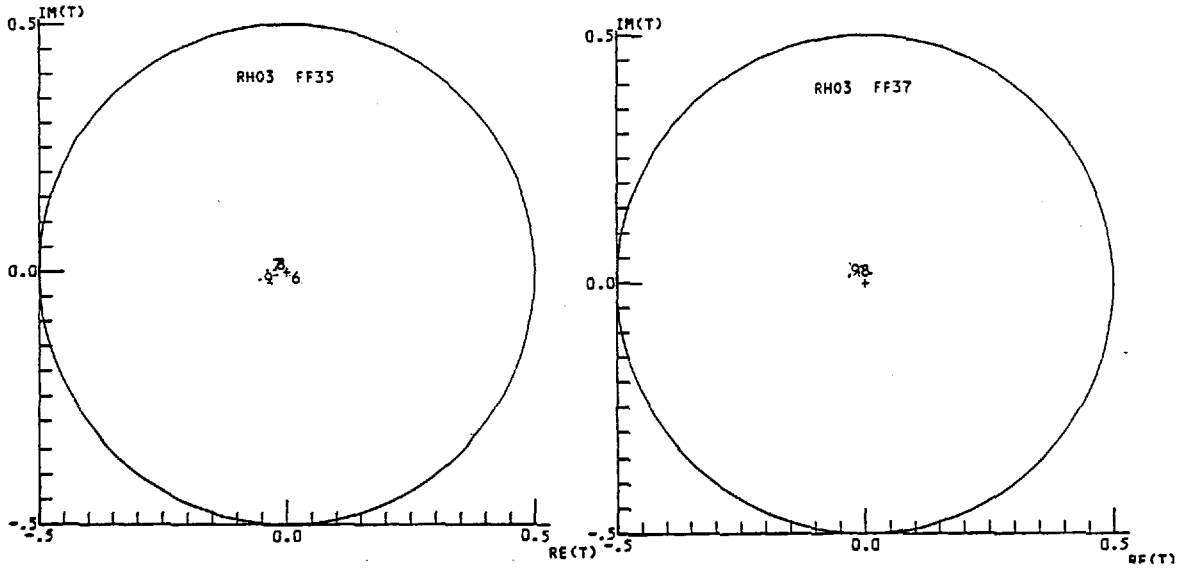
RH03 FF35
RH03 FF37
IM(T)
RE(T)
0.5
0.0
-.5

O.P.E. refit

References

1 G.P. Gopal, Ph.D. Thesis, Imperial College, London, October 1970. Rutherford publication HEP/T/9.

2 V. Tayler, Ph.D. Thesis, Westfield College, London, May 1971. Rutherford publication HEP/T/16

3 S.L. Baker et al. Positive Pion-Proton Elastic Scattering at 895, 945, 995 and 1040 MeV/c. Nuclear Physics B 18(1970)29

4 S.L. Baker et al. A constrained phase-shift analysis of π^+p data in the mass range 1600 to 1700 MeV. N.P.B 30(1971)116

5 S.L. Baker et al. Single pion production in π^+p interactions at 895, 945, 995 and 1040 MeV/c. N.P. B41 (1972) 91

6 M.G. Bowler et al. π^+p elastic scattering between 0.6 and 0.8 GeV/c. N.P. B37 (1972) 133

7 M.G. Bowler and R.J. Cashmore. Single pion production in π^+p interactions between 0.6 and 0.8 GeV/c. N.P. B17 (1970) 331
(This paper has a mistake in the cross-sections at 0.65 GeV/c. Ref. 6 gives the correct values)

8 R.J. Cashmore, D. Phil. Thesis, University of Oxford, 1969

9 R.A. Stevens, Ph.D. Thesis, Imperial College, London, November 1974

10 A.P. White, Ph.D. Thesis, Westfield College, London, 1978

11 R.D. Baker, Ph.D. Thesis, Cambridge University, August 1972. Rutherford publication HEP/T/31
O.P.E. results from the above also published in :
N.P. B90 (1975) 296

12 J.W. Stark, Ph.D. Thesis, Imperial College, London, August 1972

13 Proceedings of the Topical Conference on Baryon Resonances, Oxford, July 1976. Published by the Rutherford Laboratory, editors R.T. Ross and D.H. Saxon

14 J.L. Rosner. The Classification and Decays of Resonant Paticles. Physics Reports 11C (1974), Number 4 (pages 189-326)

15 The results of the SLAC-LBL $\pi\pi N$ analysis have been published over a period of time in the following :

a/ D.J. Herndon et al. A Parial-Wave Analysis of the Reaction $\pi N \to \pi\pi N$ in the c.m. Energy Range 1300-2000 MeV Phys. Rev. D 11 (1975) 3183

b/ R.J. Cashmore et al. Baryon Resonance Couplings in the Reactions $\pi N \to \pi\Delta$ and $\pi N \to \rho N$: Comparison with Theory and related Reactions. N.P. B 92 (1975) 37

c/ R.S. Longacre et al. N^* Resonance Parameters and K-matrix fits to the Reactions $\pi N \to \Delta\pi + \rho N + \varepsilon N$. Phys. Lett. B 55B (1975) 415

d/ A.H. Rosenfeld et al. A Partial Wave Analysis of $\pi N \to \pi\pi N$ at Center-of-Mass Energies Below 2000 MeV. Phys. Lett. B 55B (1975) 486

16 The results of the Saclay $\pi N \to \pi\pi N$ analysis have been published in the following, and also in ref. 34

a/ J. Dolbeau et al. Energy-Independent Partial-Wave Analysis of the Reactions $\pi^{\pm} p \to N\pi\pi$ in the c.m. Energy Range 1.36 - 1.76 GeV. N.P. B108 (1976) 365

b/ R.S. Longacre and J. Dolbeau. Comparison Between $\gamma N \to \pi N$ and $\pi N \to \rho N$ in the Resonance Region up to $\sqrt{s}$ = 1.75 GeV via the V.D.M. Phys. Lett. 58B (1975) 455

c/ R.S. Longacre and J. Dolbeau. K-matrix Fits to $N\pi \to N\pi$ and $N\pi\pi$ in the Resonance Region s = 1380 to 1740 MeV. N.P. B122 (1977) 493

17 R.J. Cashmore et al. Ambiguity Resolved: A single Continuous Solution for $\pi N \to \pi\pi N$ Below 2000 MeV.
The work described in this paper was included in ref. 15d, but was originally published as a separate preprint. SLAC-PUB-1387(Rev.), LBL 2634(Rev.)

18 Programs TELESCOPE and HPDEDT, internal Imperial College write-ups.

19 Program ADDER (Automatic Derivation of Data for Excellent Reproduction), internal I.C. write-ups.

20 CERN T.C. Program Library

21 SMOG and BINDG - these are part of the Imperial College measuring system set of programs - Imperial College internal communication.

22 A.A. Carter et al. Pion-Nucleon Total Cross-sections from 0.5 to 2.65 GeV/c
Phys. Rev. 168 (1968) 1457

23 Harwell subroutine library write-ups AERE-R7477

24 Cross-section values were taken from the CERN-HERA compilation by E. Bracci et al CERN/HERA 72-1 (1972)
Original sources referred to are :-

a/ J.A. Helland et al		PR 134B (1964) 1062
b/ R. Barloutaud et al		NC 26 (1962) 2049
	and	NC 27 (1963) 238
c/ Foelsche et al		PR 134B (1964) 1138
	and	36, CERN 62
d/ Detoeuf et al		P.R.L. 16 (1966) 860
e/ J. Debaisieux et al		NPB 5 (1968) 147
	and	NP 63 (1965) 273
f/ J.L. Broderick et al		PR 158 (1967) 1331
g/ J. Kopp et al		PR 123 (1961) 301
h/ Grossmann et al		PR 178 (1969) 2109
i/ Daronian et al		NC 41A (1966) 503
j/ Carayannopoulos et al		PR 138B (1965) 433
k/ Crawford Jr. et al		PR 128 (1962) 368

25 One cross-section value was taken from the LBL compilation by D.M. Chew et al LBL-53 (1973)
a/ M. de Beer et al NP B12 (1969) 617

26 Kalmus et al. Phys. Rev. D2 (1970) 1824
and Phys. Rev. D4 (1971) 676
Values from the first publication are given in the compilations, refs 24 and 25.

27 R.E. Rothschild et al - Proton Elastic Scattering at 180° from 0.60 to 1.60 GeV/c. Phys. Rev. D5 (1972) 499

28 R.D. Tripp, CERN Yellow Report 65-7

29 S.J. Lindebaum and R.J. Sternheimer, P.R. 109 (1958) 173
and P.R. 123 (1961) 333

30 B. Deler and G. Valladas. Nuovo Cimento 45 (1966) 1077
P. Chavanon et al N.C. 63 (1969) 1035

31 H.P. Stapp. P.R. 103 (1957) 425

32 REDUCE-2, A.C. Hearn, University of Utah. This is a program, written in LISP, to automatically manipulate and simplify algebraic expressions, available on the RHEL IBM 360 computers

33 D.J. Herndon, P. Söding, R.J. Cashmore. A Generalized Isobar Model Formalism. Phys. Rev. D11 (1975) 3165 (This paper is often referred to as C.H.S.)

34 J. Dolbeau, Ph.D. Thesis, Orsay, 1975. Note CEA-N-1840

35 J.D. Jackson, N.C. 34N. 6 (1964) 1644

36 S. Glashow and A.H. Rosenfeld. P.R.L. 10 (1963) 192

37 L. Miller, Ph.D. Thesis, University of California, Berkeley, November 1971 LBL-38

38 Y. Goradia. The Overlap Integrals in the Isobar Model for $a+b \to j+k+l$. Virginia Polytechnic Institute and State University, preprint 1977

39 R. Fletcher, FORTRAN subroutines for minimization by quasi-Newton methods. A.E.R.E. Report 7125 (1972)

40 J. Orear, Notes on statistics for Physicists. August 1958, UCRL-8417

41 "Modern Computing Methods", no. 16 in the N.P.L. series of Notes on Applied Science. Published by H.M.S.O. London, Second Edition, 1961

42 R.G. Roberts, Phenomenology of $\pi N \to \pi N^*$ below 1 GeV. Ann. of Physics 44 (1967) 325

43 P. Eberhard and M. Pripstein, P.R.L. 10 (1963) 351

44 R. Aaron and D. Amado, P.R.L. 31 (1973) 1157

45 G. Smadja, LBL-382 (1971)
Y. Goradia and T.A. Lasinski, LBL-3626 (1975)
Y. Goradia, LBL-3628 (1975)

46 See review article by I.J.R. Aitchison, Daresbury Study Weekend series no. 8 DL/R34 (1975)

47 A. Martin, The Phase and Modulus of the Scattering Amplitude. New Phenomena in Subnuclear Physics, A. Zichichi Ed. Academic Press 1975 (also CERN preprint Ref. TH.2077-CERN)

48 H. Burkhardt, Serious Ambiguities in Inelastic Phase-shift Analysis. Invited talk at the Triangle Seminar, Smoleniče, Czechoslovakia, November 1973. CERN publication Ref. TH. 1784-CERN

49 D. Atkinson et al, N.P.B. 109 (1976) 322

50 Particle Data Group, T.G. Trippe et al., Rev. Mod. Phys. 48, No.2, Part II (April 1976)

51 a/ A.J.G. Hey et al, N.P.B. 95 (1975) 516
b/ R.J. Cashmore et al, N.P.B. 98 (1975) 237

52 J.L. Basdevant et al, N.P.B. 72 (1973) 413
J.P. Baton et al, Phys. Letters 33B (1970) 528

53 D.E. Novoseller, Ph.D. Thesis, California Institute of Technology, Pasadena, May 1977

54 D.E. Novoseller, California Institute of Technology preprints CALT-68-596 and CALT-68-608, June 1977

55 W. Hoogland et al, N.P.B. 126 (1977) 109
(This is an updated version of W. Hoogland et al, N.P.B. 69 (1974) 266)

56 C. Goebel, Phys. Rev. Lett. 1 (1958) 337

57 G. Chew and F.E. Low, P.R. 113 (1959) 1640

58 G. Wolf, P.R.L. 19 (1967) 925

59 G. Wolf, P.R. 182 (1969) 1538

60 H.P. Dürr and H. Pilkuhn, N.C. 40A (1965) 899

61 References 7 and 66 for example use this parametrisation. For a discussion of this parametrisation see text books, such as Quantum Mechanics, L.I. Schiff, McGraw-Hill, 1949

62 E. Byckling and K. Kajantie, Particle Kinematics, Wiley, 1973

63 J.L. Petersen, The $\pi\pi$ Interaction. CERN Yellow Report, 77-04, 1977

64 Pion-Pion Interactions in Particle Physiscs. B.R. Martin, D. Morgan and G. Shaw. Academic Press, 1976.
This book gives many $\pi\pi$ I=2 references, two that are used in this thesis are
a/ D. Morgan and G. Shaw P.R. D2 (1970) 520

b/ D. Morgan, in the Proceedings of the XVIIth International Conference on High Energy Physics, London

65 J.P. Prukop et al, P.R. D10 (1974) 2055

66 M.J. Losty et al, N.P.B. 69 (1974) 185

67 Values of the I=2 S-wave $\pi\pi$ scattering length were obtained from the following in addition to references given separately
a/ D. Cohen et al, P.R. D7 (1973) 661
b/ G. Villet et al, Saclay preprint D.Ph.P.E. 76-09 (1976)

68 S. Weinberg, P.R.L. 17 (1966) 616

69 Donnachie et al, P.L. 26B (1968) 161

70 R.G. Kirsopp, Ph.D. Thesis, 1968

71 S. Almehed and C. Lovelace, N.P.B. 40 (1972) 157

72 P. Bareyre et al, P.R. 165 (1968) 1730

73 R. Ayed et al, P.L. 31B (1970) 598

74 R. Ayed and P. Bareyre, Communication to 2nd Aix-en-Provence International Conference on elementary particles, 1973

75 a/ D. Faiman and J. Rosner, P.L. 45B (1973) 357
b/ D. Faiman N.P.B. 77 (1974) 443. This makes a change to a sign convention given in a/

76 H. Burkhardt and J. Pulido, Baryon Decays to Radially Excited States in the Quark Model,
preprint : University of Nottingham UNAM-78-31
University of Birmingham BUMP-78-31